Max-Planck-Institut
für Plasmaphysik

D-85748 Garching, Germany
EURATOM-Association

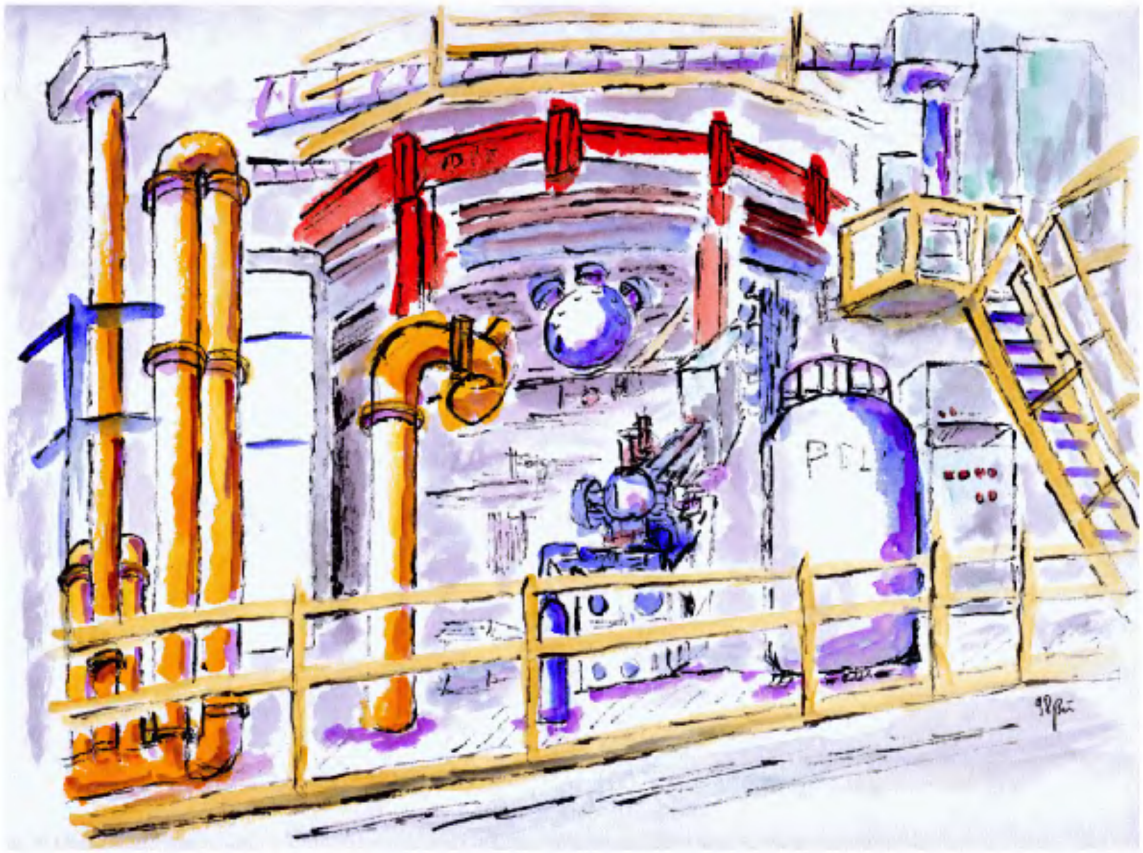

Summer University for Plasma Physics

September 27 – October 1, 2004

Garching/Munich, Germany

Edited by Axel Könies and Karl Krieger

Contributions from:
H. W. Bartels, H.-S. Bosch, R. Brakel, D. Hartmann, D. H. H. Hoffmann, W. Jacob, R. Kleiber, A. Könies, K. Krieger, H. Lesch, R. Neu, A. Peeters, R. Schneider, B. Scott, W. Suttrop, H. Zohm

Cover: ASDEX Upgrade, watercolours by Dr. Klaus Büchl

List of authors

Dr. Hans-Stephan Bosch
Dr. Wolfgang Jacob
Dr. Karl Krieger
Dr. Rudolf Neu
Dr. Arthur Peeters
Dr. Bruce Scott
Dr. Wolfgang Suttrop
Prof. Dr. Hartmut Zohm

Max-Planck-Institut für Plasmaphysik
Boltzmannstr. 2
D-85748 Garching

Dr. Rudolf Brakel
Dr. Dirk Hartmann
Dr. Ralf Kleiber
Dr. Axel Könies
Dr. Ralf Schneider

Max-Planck-Institut für Plasmaphysik
Wendelsteinstr. 1
D-17491 Greifswald

Dr. Hans-Werner Bartels

ITER Joint Central Team
Garching Working Site
Boltzmannstr. 2
D-85748 Garching

Prof. Dr. Dr. Dieter H. H. Hoffmann

Institut für Kernphysik
Universität Darmstadt
Schloßgartenstr. 9
D-64289 Darmstadt

Prof. Dr. Harald Lesch

Institute for Astronomy and Astrophysics
University of Munich
Scheinerstr. 1
D-81679 München

Contents

Chapter 1

Basic Nuclear Fusion

Hans-Stephan Bosch

1.1 Introduction

Any energy production from nuclear reactions is based on differences in the nuclear binding energy. Figure 1.1 shows the nuclear binding energy per nucleon (proton or neutron). It has been derived from measurements of the masses of the nuclei, when it was observed that the masses of nuclei are always smaller than the sum of the proton and neutron masses which constitute the nucleus. This mass difference corresponds to the nuclear binding energy according to Einstein's energy-mass relation $E = \Delta m \cdot c^2$. An explanation of the structure of figure 1.1 was given by C. F. von Weizsäcker in 1935. Starting from the very limited range of the strong nuclear force he assumed that each nucleon just influences its nearest neighbours. The binding energy per nucleon would thus be constant. The smaller binding energies for smaller nuclei are due to the relatively large surface to volume ratio. The nucleons at the surface have missing partners and thus their contribution to the total binding energy of the nucleus is reduced. The decrease of binding energy per nucleon for nuclei beyond $A \approx 60$ is due to the repulsive coulomb force of the large amount of positive protons.

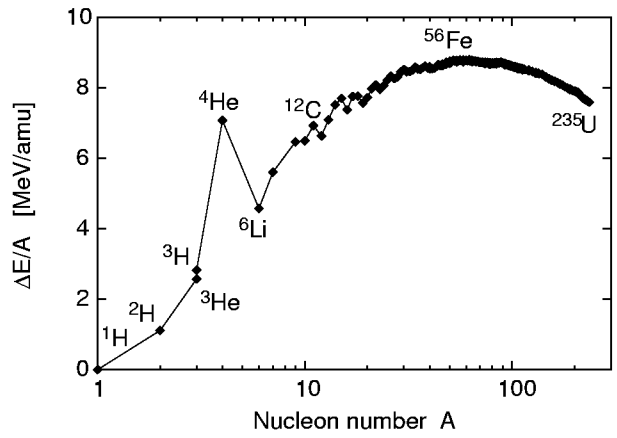

Figure 1.1: Nuclear binding energy per nucleon as a function of the nucleon number A

The finer structures in figure 1.1 are due to quantum mechanical effects, i.e. at certain so-called 'magic' proton and neutron numbers the nucleus formed is a very stable configuration. This is roughly comparable to the stable electron configurations of the noble gases, where electron shells are completed. The first magic number is 2, which is manifested as a most remarkable example of a local maximum in figure 1.1, i.e. the helium nucleus with 2 protons and 2 neutrons. From figure 1.1 it is clear that there are two ways of gaining nuclear energy:

1. By transforming heavy nuclei into medium-size nuclei: This is done by fission of uranium, which is not a topic of these lectures.

2. By fusion of light nuclei into heavier ones: in particular the fusion of hydrogen isotopes into stable helium offers the highest energy release per mass unit. Doing this in a controlled manner has been the goal of fusion research for about 40 years. Most of the following lectures are dedicated to this goal.

The energy release per nucleon is of the order of 1 MeV ($= 10^6$ eV) for fission reactions and in the order of a few MeV for fusion reactions. This is 6–7 orders of magnitude above typical energy releases in chemical reactions, which explains the effectiveness and potential hazard of nuclear power.

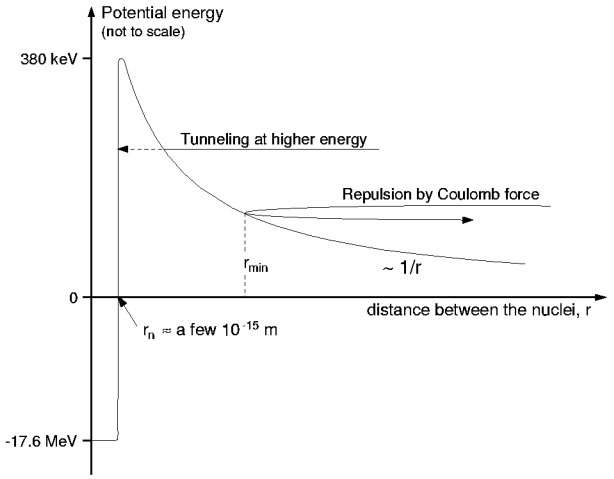

Figure 1.2: Schematic representation of the potential energy U of two nuclei as a function of their distance. The energies quoted are for a system of D ($=^2$H) and T ($=^3$H).

All the nuclear reactions are mostly governed by the strong nuclear force acting over very small distances in the order of the radius of the nuclei, but for distances above a few fermi (i.e. 10^{15} m) the repulsive Coulomb force between the positively charged nuclei becomes dominant. The potential energy of two nuclei as a function the distance between the nuclei is shown in figure 1.2. The depth of the deep well at small radii is determined by the binding energy, discussed before, while the barrier at a few fermi is given by the Coulomb potential of $Z_1 Z_2 e^2/4\pi\epsilon_0 r_m$ which is much smaller, but still poses a principal problem. For alpha-particle decay (where a ^{4}He nucleus separates itself out of a positive nucleus) as well as for fusion of lighter nuclei, this diagram demands a particle energy of the order of 500 keV, and this would make fusion processes almost impossible. However, is was known since the end of the last century, that α-particle decay occurs at room temperature, and in 1928 Gamov [1] explained this by the tunneling effect, which in turn also allows fusion reactions to occur at temperatures far below the Coulomb barrier:

Due to quantum mechanical effects the minimum distance between the two nuclei is not fixed (as it is indicated by the repulsion in fig. 1.2), but there is a finite probability for the nuclei to get closer, and eventually "tunnel" through the Coulomb barrier, as indicated by the dotted line in figure 1.2. In terms of wave functions, the amplitude is not zero for $r \leq r_{min}$, but it is finite and decays slowly for smaller radii. Therefore it can still be finite for $r \leq r_n$, i.e. the particles have a possibility to approach close enough for a fusion reaction to occur. This tunneling probability is a strong function of the relative velocity v of the reacting particles with charge Z_1, Z_2,

$$P_{tunneling} \sim exp - \frac{2\pi Z_1 Z_2 e^2}{\hbar\, v}.$$

This equation shows that reaction partners with small mass (and charge Z) are preferred, and that the rection probability increases strongly with the temperature ($\sim$ relative velocity v).

In the light of the above discussion it becomes clear why fission energy has been much more readily obtained than fusion energy: fission is triggered by thermal neutron capture, i. e. no force prevents the neutron from entering the uranium nucleus at room temperature and causing a fission reaction.

1.2 Energy production on the sun

Though still a somewhat exotic topic on earth, nuclear fusion is **the** energy source of our universe. The light of all stars is generated by fusion reactions. On the sun the main reactions are the following:

$$\begin{aligned} p + p &\longrightarrow D + e^+ + \nu_e \\ D + p &\longrightarrow {}^3He + \gamma \\ {}^3He + {}^3He &\longrightarrow {}^4He + 2p \end{aligned}$$

where p denotes a proton, D a deuteron, a heavy hydrogen isotope with one proton and one neuteron, ${}^3He$, ${}^4He$ are helium isotopes, γ stands for a high-energy photon, e^+ for a positron (anti-electron), and ν_e for an electron neutrino.

A very important feature of the energy production on the sun is the need for the weak interaction which transforms protons to neutrons (β^+-decay), in the first of the above listed reactions. All weak interaction processes involve the emission of neutrinos (thereby keeping the lepton number constant). As the weak interaction is very slow, it causes the long lifetime of the sun and it is an essential condition for our evolution .

Further reactions which are important at temperutures above about 1 keV, produce ${}^7_4Be$, ${}^7_3$Li, ${}^8_5$B and ${}^8_4$Be, which decays into 2 ${}^4_2$He nuclei. Also in these reactions neutrinos are produced, however with a higher kinetic energy than those from the pp-reactions mentioned above.

These neutrinos ignore both the strong and electromagnetic interactions and therefore it is extremely hard to detect them experimentally. Almost all neutrinos produced in the

sun travel through it without interaction and thus carry information from the reactions in the core of the sun. It was not till 1992 that the European GALLEX collaboration detected the low energy solar neutrinos from the main energy-producing reactions (pp-chain) listed above. This was the first experimental validation of our theoretical model of energy production in the stars.

For much higher temperatures (T $\geq$ 2 keV), i.e. in stars which with higher mass than the sun, fusion of four protons to $^4_2$He can also occur in a catalytic process based on ^{12}C. In this so-called Bethe-Weizsäcker cycle oxygen, nitrogen and ^{13}C are only present in intermediate stages, and the net reaction again is 4 p $\rightarrow$ ^{4}He + 2 e^+ + 2 ν_e.

1.3 Fusion on earth

The fundamentals of fusion research are well described in great detail in two (german) books by J. Raeder [4] and U. Schumacher [5].

For energy production on earth the weak interaction has to be avoided since it would lead to unacceptably small reaction rates. The sun (and all other stars) overcome this problem by their huge mass, but a fusion reactor has to be considerably smaller in size than a star.

Possible candidates for using fusion energy on earth are the following reactions (T denoting tritium, the heaviest hydrogen isotope with 2 neutrons):

D	+	D	$\longrightarrow$	^{3}He	+	n	+	3.27 MeV	(50 %)
			or	T	+	p	+	4.03 MeV	(50 %)
D	+	^{3}He	$\longrightarrow$	^{4}He	+	p	+	18.35 MeV	
D	+	T	$\longrightarrow$	^{4}He	+	n	+	17.59 MeV	
p	+	^{11}B	$\longrightarrow$	3 ^{4}He			+	8.7 MeV	

Because the kinetic energy of the reactants is much lower than the energy gained in the reaction, the distribution of the reaction energy onto the two product particles is inverse proportional to their mass, i.e. $E_1/E_2 = m_2/m_1$. In the DT-reaction, e.g. the α-particle has an energy of 3.54 MeV, and the neutron has 14.05 MeV. The first four reactions (for which the cross sections are shown in fig. 1.3) can be summarized as

$$3D \longrightarrow {}^4\text{He} + p + n \quad + 21.6 \text{ MeV},$$

and therefore rely on deuterium as fuel only. Since the weight fraction of deuterium in water is $3.3 \cdot 10^{-5}$, the energy content of water is about 11.5 GJ per litre, which is about 350 times larger than the chemical energy density of gasoline. This demonstrates the huge potential afforded by nuclear fusion as an energy source.

All the reaction cross sections in figure 1.3 show a steep increase with the relative energy, as discussed before, but the D-T reaction

$$D + T \longrightarrow {}^4\text{He} + n \quad + 17.6 \text{ MeV}$$

has by far the largest cross-section at the lowest energies. This makes the D-T fusion process the most promising candidate for an energy-producing system. The special role

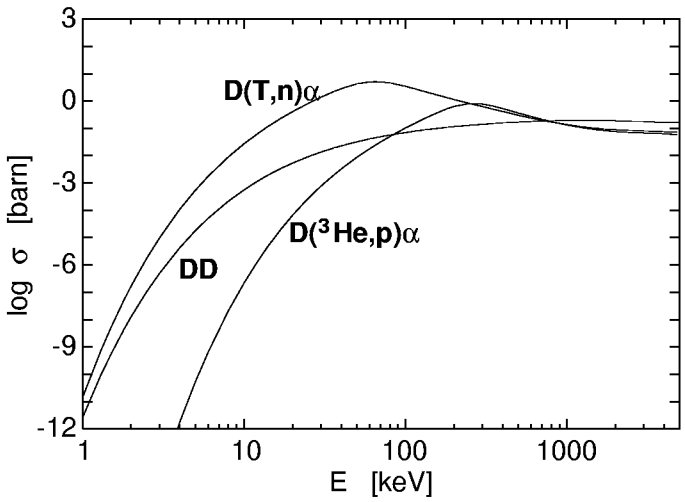

Figure 1.3: Measured cross-sections for different fusion reactions as a function of the center of mass energy [3]. The curve labeleld DD shows the sum of the cross sections for both branches of this reaction. Reaction cross sections are usually measured in barn, where 1 barn = 10^{-28} m^2.

of D-T reactions becomes clear from the energy levels of the unstable ^5He nucleus shown in figure 1.4. It has an excited state just 64 keV above the sum of the masses of deuterium and tritium. The D-T fusion cross-section therefore reaches its maximum at this energy difference, due to the resonance-like reaction mechanism. The DD reactions (figure 1.4, left part) show no such resonances, and their cross sections are solely governed by the tunneling probability, showing a smooth increase without any maximum, while the D^{3}He reaction also has a resonance at about 270 keV in the ^{5}Li system, not shown here.

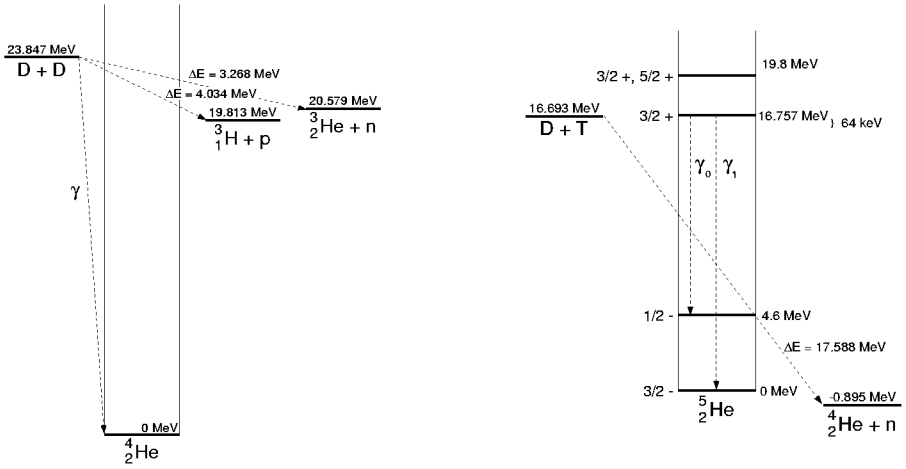

Figure 1.4: Energy diagram of the ^{4}He nucleus (left), and of the unstable ^{5}He nucleus (right), where the resonance at 16.76 MeV dominates the reaction cross section. The numbers left of the level scheme indicate the J-value and parity of the respective level.

To be a candidate for an energy-producing system, the fusion fuel has to be sufficiently abundant. As mentioned earlier, deuterium occurs with a weight fraction of $3.3 \cdot 10^{-5}$ in water. Given the water of the oceans, the static energy range is larger than the time the sun will continue to burn (a few billion years).

Tritium is an unstable radioactive isotope. It decays to

$$T \longrightarrow {}^3He + e^- + \bar{\nu}_e$$

with a half-life of 12.3 years. Note the previously mentioned neutrino production of this β^- decay. Owing to the unstable character of tritium no significant amounts exist, but tritium can be produced with nuclear reactions of the neutrons from the D-T reaction and lithium:

$$\begin{aligned} n + {}^6Li &\longrightarrow {}^4He + T &&+ 4.8 \text{ MeV} \\ n + {}^7Li &\longrightarrow {}^4He + T + n\prime &&- 2.5 \text{ MeV} \end{aligned}$$

The reaction with ^7Li is particularly important because it does not consume a neutron and opens the possibility for self-sufficient tritium production in a fusion reactor, i.e. each fusion neutron will produce at least one new tritium nucleus.

The ultimate fusion fuel will thus be deuterium and lithium. The latter is also very abundant and widespread in the earth's crust and even ocean water contains an average concentration of about 0.15 ppm (1 ppm = parts per million). Table 1 summarizes the estimated world energy resources.

Present world annual primary energy consumption	3×10^{11} gigajoules	
Resources		
Coal	10^{14}	300 years
Oil	1.2×10^{13}	40 years
Natural Gas	1.4×10^{13}	50 years
^{235}U (fission reactors)	10^{13}	30 years
^{238}U and ^{232}Th (breader reactors)	10^{16}	30000 years
Lithium (D-T fusion reactors) :		
Land	10^{16}	30000 years
Oceans	10^{19}	3×10^7 years

Table 1. Estimated world energy resources. The figures are only indicative, being dependent on prices and subject to uncertainty because of incomplete exploration.

1.4 Thermonuclear fusion

As discussed before, for a fusion reaction to occur, the two nuclei have to 'touch' each other since the range of the nuclear force is of the order of the dimensions of the nuclei. The repulsive Coulomb force counteracts all attempts to bring them close together. This is what the difficult research on nuclear fusion is all about: how can the two reaction partners be brought into contact?

The simplest approach to realizing the fusion reactions would be to accelerate the reactants to about 100 keV and bring them to collision. This does not lead to a positive energy balance, since the elastic Coulomb scattering as another reaction type has a

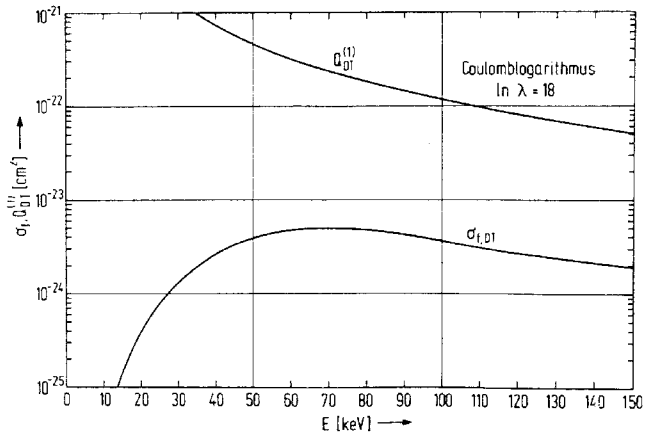

Figure 1.5: Comparison of the D-T fusion cross-section $\sigma_{f,DT}$ and the cross-section for momentum exchange by Coulomb scattering Q_{DT} in a fusion relevant plasma

much larger cross-section, as shown in figure 1.5. Thus the two particle beams would just scatter and diverge after one interaction.

A way of overcoming this problem is to confine a thermalized state of deuterium and tritium particles at energies of about 10 keV. Since the average energy of particles at a certain temperature is about kT, where k is the Boltzmann constant, temperatures are often given in electron volt units (1 eV $\hat{=}$ $1.16 \cdot 10^4$ ^oC). At energies of 10 keV the hydrogen atoms are completely ionized and form a plasma of charged ions and electrons. The basic physics of plasmas is discussed in chapter 2. For now it should suffice to observe that in a plasma the particles thermalize as a result of many Coulomb scattering processes and thus entail a Maxwellian velocity distribution:

$$f(v) = n \left(\frac{m}{2\pi kT}\right)^{3/2} \cdot \exp\left(-\frac{mv^2}{2\ kT}\right)$$

where f is the number of particles in the velocity interval between v and $v + dv$, n is the density of particles, m is their mass, nd kT is their temperature.

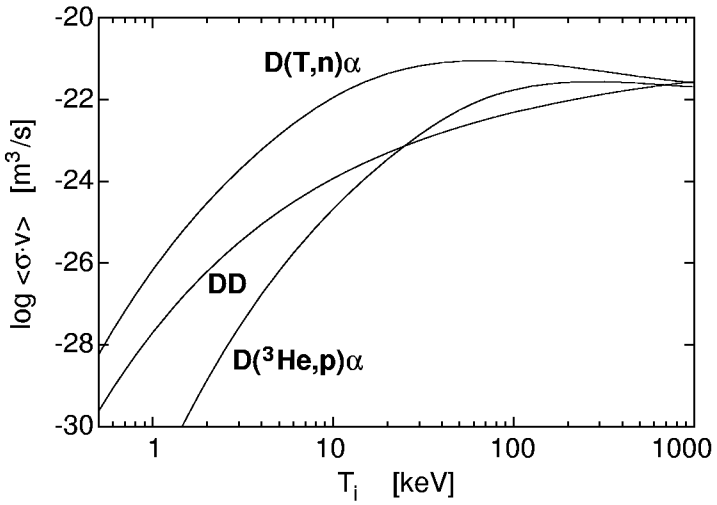

Figure 1.6: Reaction parameter $< \sigma\ v >$ as a function of ion temperature T_i for different fusion reactions [3].

The reaction rate per unit volume, R, can be written as

$$R = n_D \cdot n_T \cdot < \sigma\ v >$$

with v now being the relative particle velocity and $< \sigma\ v >$ being the reaction parameter, i. e. the average of the product of cross-section times velocity.

Calculation of the reaction parameter requires integration over the distribution function of deuterium and tritium. After some numerical transformations one obtains

$$< \sigma\ v >= \frac{4}{(2\pi m_r)^{1/2}(kT)^{3/2}} \int \sigma(\epsilon_r) \cdot \epsilon_r \cdot \exp\left(-\frac{\epsilon_r}{kT}\right)\ d\epsilon_r$$

where m_r is the reduced mass, and ϵ_r the relative kinetic energy.

Figure 1.6 shows the reaction parameter for some important fusion reactions. At temperatures of interest the nuclear reactions come predominantly from the tail of the distribution. This is illustrated in figure 1.7, where the integrand of the last equation is plotted versus ϵ_r/T together with the two factors $\sigma(\epsilon)$ and $\epsilon \cdot \exp(-\epsilon/kT)$ for a D-T plasma at a temperature of 10 keV.

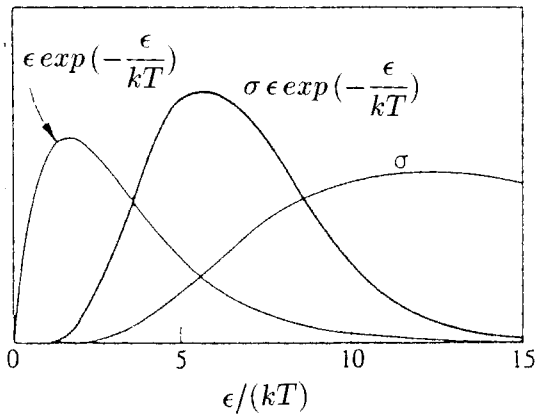

Figure 1.7: Graph of integrand of the reaction parameter equation and of its two factors $\sigma(\epsilon)$ and $\epsilon \cdot \exp(-\epsilon/kT)$ versus the normalized energy ϵ/T for a D-T plasma at T = 10 keV.

Thermalization is thus not just a way of handling the large cross-sections for elastic Coulomb scattering, it also considerably increases the reaction rate considerably in relation to beam experiments with single particle energies.

1.5 Ignition

In the following the condition which a thermalized D-T plasma has to satisfy to serve as an energy producing system is investigated. Historically, in 1957 John D. Lawson deduced a criterion for a positive energy balance using quantities such as the thermal cycle efficiency η of power reactors [2]. Today the approach has changed slightly to a more physics oriented condition: the aim is an ignited plasma where all energy losses are compensated by the α-particles from the fusion reactions, which transfer their energy of 3.5 MeV to the plasma while slowing down. The neutrons cannot be confined and leave the plasma without interaction.

Transport processes such as diffusion, convection, charge exchange and others are empirically described by an energy confinement time τ_E leading to the power loss term $3\mathrm{nkT}/\tau_E$ with 3nkT as the inner thermal plasma energy (n is the electron density).

Note that this is twice the ideal gas value since every hydrogen atom is split into two particles (electron and nucleus). Another loss mechanism is the bremsstrahlung, which becomes particularly important at high temperatures and impurity concentrations. The power loss due to bremsstrahlung can be written as

$$P_{bremsstrahlung} = c_1 \cdot n^2 \cdot Z_{eff} \cdot (kT)^{1/2}$$

with c_1 being the bremsstrahlungs constant ($c_1 = 5.4 \cdot 10^{-37}$ $Wm^3keV^{-1/2}$), and Z_{eff} the effective charge of the plasma, including all (impurity) species : $Z_{eff} = \Sigma_z n_z Z^2/n$.

The energy balance now reads

$$\left(\frac{n}{2}\right)^2 < \sigma v > \cdot \epsilon_\alpha = 3nkT/\tau_E + c_1 n^2 Z_{eff}(kT)^{1/2}$$

and this can be rewritten to the ignition condition

$$n\tau_E = \frac{12\ kT}{< \sigma v > \epsilon_{alpha} - 4c_1 Z_{eff}(kT)^{1/2}}$$

where ϵ_{alpha} is the energy of the α-particle, 3.54 MeV. This equation shows that the product of the particle density and energy confinement time is only a function of the plasma temperature, with a minimum at about 13 keV. In the range of 10 keV the reaction parameter $< \sigma v >$ is roughly proportional to T^2, which motivated the definition of the so-called fusion product

$$n\tau T = \frac{12\ kT^2}{< \sigma v > \epsilon_{alpha} - 4c_1 Z_{eff}(kT)^{1/2}}$$

which has a flat minimum of about $35 \cdot 10^{20}\ s/m^3 \cdot keV$ around 10 keV. The fusion product dictates the strategy for developing fusion power as an energy producing system: One has to attain temperatures of around 10 keV (about 100 million °C) and achieve the required density and energy confinement time simultaneously. There are two distinct approaches:

1. The hot plasma is confined by strong magnetic fields leading to maximum densities of about $1.5 \cdot 10^{20}\ m^{-3}$, which is $2 \cdot 10^5$ times smaller than the atom density of a gas under normal conditions. With these densities, the energy confinement time required is in the range of 2 to 4 seconds. This approach, which is the main line in fusion research, will be covered by most of the following lectures, and is introduced in the next section.

2. The other extreme is to maximize the density. This can be done by strong, symmetric heating of a small D-T pellet. The heating can be done with lasers or particle beams and leads to ablation of some material causing implosion due to momentum conservation. It is clear that the energy confinement time is extremely short in this concept: it is the time required for the particles to leave the hot implosion center. Since it is the mass inertia which causes the finiteness of this time, this approach to fusion is often called 'inertial fusion'. The density required is about 1000 times the density of liquid D-T; the pressure in the implosion center reaches (at temperatures of 10 keV) that in the center of the sun. A detailed description of the actual status in this area can be found in references [7] and [8].

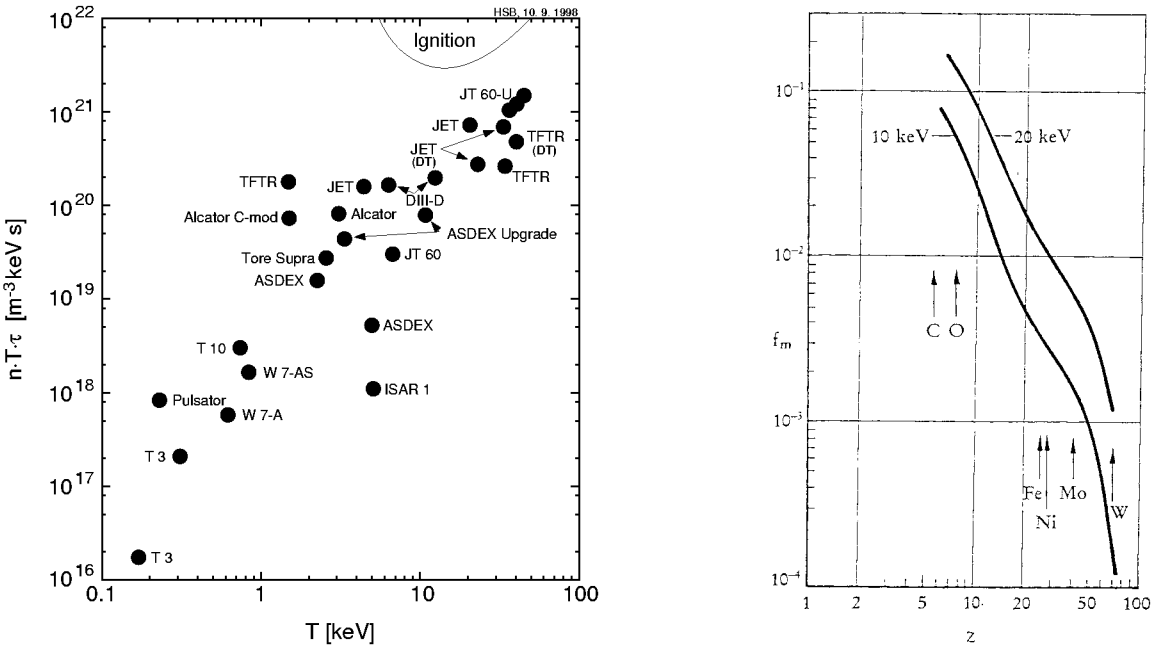

Figure 1.8: Diagram of $nT\tau$ values versus T obtained in different experiments (left) and maximum tolerable impurity concentrations in a plasma to reach ignition (right).

Figure 1.8 (left) illustrates the progress of nuclear fusion research in approaching the required $n\tau T$ condition. Today a factor 7 is missing for ignition, whereas in the mid-sixties the best experiments fell short of the required conditions by more than 5 orders of magnitude. However, it has to be kept in mind that achieving ignited plasmas is not sufficient for building fusion reactors. In addition, this plasma state has to be maintained for very long times to allow continuous energy production. One of the most difficult problems will be the interaction of the edge plasma with the surrounding structures and the removal of helium ash. Consequently, edge plasmas constitute an increasingly important research topic.

Impurities from the walls worsen the ignition condition in two ways. They dilute the fuel concentration and even in small amounts they can significantly enhance the radiation losses. Figure 1.8 (right) shows the maximum tolerable impurity concentration to reach ignition. Depending on the charge it ranges from a few % for light atoms to the few 10^{-4} level for high Z materials.

1.6 Magnetic confinement

As discussed in chapter 2, plasmas can be confined by magnetic fields, but in linear configurations the end losses are by far too large to reach the necessary energy confinement time τ_E of the order of some seconds. These end losses can be completely avoided in a toroidal system, but in a simple toroidal system with purely toroidal magnetic field, the magnetic field curvature and gradient (approximately as in Figure 2.9) result in a vertical drift which is in opposite directions for ions and electrons. The resulting electric field causes an outward $\vec{E} \times \vec{B}$ drift of the whole plasma, and therefore such a simple magnetic

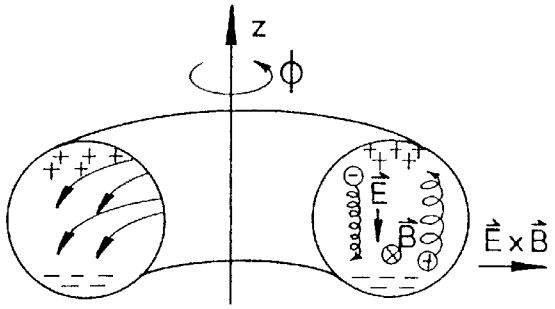

Figure 1.9: Vertical drifts and associated $\vec{E} \times \vec{B}$ in a toroidal field.

field configuration will be unstable. To avoid this charge separation, it is necessary to twist the magnetic field lines by additional magnetic field components. Then, single field lines map out so-called flux surfaces. On these flux surfaces, plasma transport is fast, as it is always parallel to $\vec{B}$, and therefore plasma parameters usually are constant on a given flux surface. Perpendicular to the flux surfaces, transport is hindered because particle motion perpendicular to $\vec{B}$ is restricted by the Lorentz force, and therefore plasma parameters can vary strongly in this direction.

Two different principles for twisting the magnetic field lines have been invented in the '50s, and are under investigation worldwide:

1.6.1 The stellarator

The stellarator was invented in 1951 by Lyman Spitzer, Jr. in Princeton. In a stellarator the twist of the field lines is created by external coils wound around the plasma torus, as shown in Figure 1.10. Due to these external currents the plasma shape is not circular, but shows some indentation. In this case, with four coils (neighbouring coils carry opposite current), the plasma has an oval shape.

These external coils have the advantage that the current can be controlled from outside, and can flow continously, but the configuration shown in Figure 1.10, is very difficult from the engineering point of view. Therefore such "classical" stellarators nowadays have been replaced by "modular" stellarators, where the planar toroidal coils and the helical coils have been replaced by one complex, but modular system of non-planar coils, as will be discussed in the chapters 7 and 8.

1.6.2 The tokamak

The second approach is the tokamak proposed by two Russian physicist, TAMM and SAKHAROV, in the year 1952 and realized by ARTSIMOVICH. The word *tokamak* itself is derived from the Russian words for toroidal chamber with magnetic field. The tokamak concept is outlined in figure 1.11 The toroidal magnetic field is provided by simple magnets and the necessary twist is produced by the plasma itself, by means of an electric current in the plasma which gives rise to the poloidal component of the twisted magnetic field. The current also serves for plasma build-up and heating. This current is produced by induction, the plasma acting as the secondary winding of a transformer. Tokamaks have proved to be very successful in improving the desired fusion plasma conditions

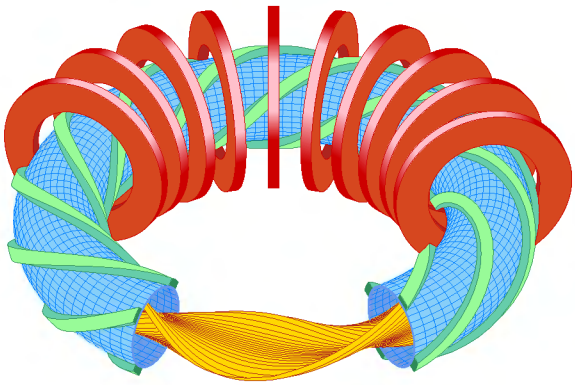

Figure 1.10: Schematic view of a stellarator with four helical coils wound onto the vacuum vessel.

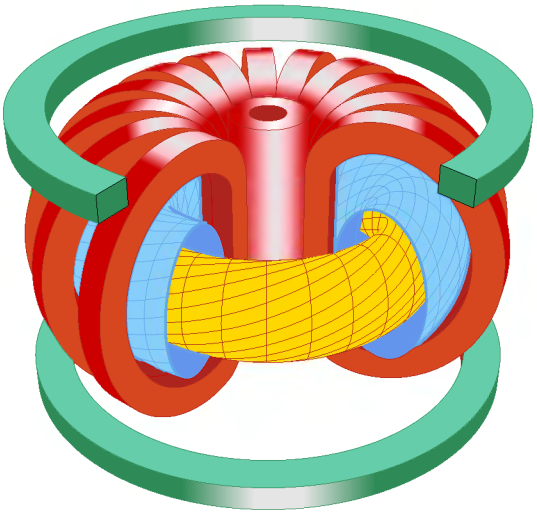

Figure 1.11: Tokamak concept. The innermost cylindrical coil is the transformer coil for inducing a plasma current. The toroidal coils above and below the machine create a vertical field for plasma shaping and position control.

and the today's best experiments are based on the tokamak principle. Of course, a transformer can induce the (dc-) plasma current only during a finite time, while, as mentioned before, a stellarator may principally run steady-state. For truely continuous tokamak operation, alternative current drive methods are being developed. Another disadvantage of the required large plasma current is the potential danger of so-called disruptions: uncontrolled very fast ($\sim 10\,\mathrm{ms}$) plasma current decays which can give rise to large forces on the machine.

A recent review on the status of tokamak research is given in [6].

1.6.3 The fusion reactor

The basic geometry of fusion reactors will be a torus (ring) for magnetically confined plasmas. A schematic cross-section of such a reactor is shown in figure 1.12. The hot plasma is surrounded by the first wall and blanket. The latter is filled with lithium to produce the tritium, as discussed before, and the majority of thermal energy of the plant is delivered here by neutron moderation. A shield is provided behind the blanket to stop the neutrons not captured by the blanket in order to reduce the heat and radiation loads to the cold structures of the superconducting magnets. The application of superconduction is mandatory for fusion reactors to obtain a positive energy balance.

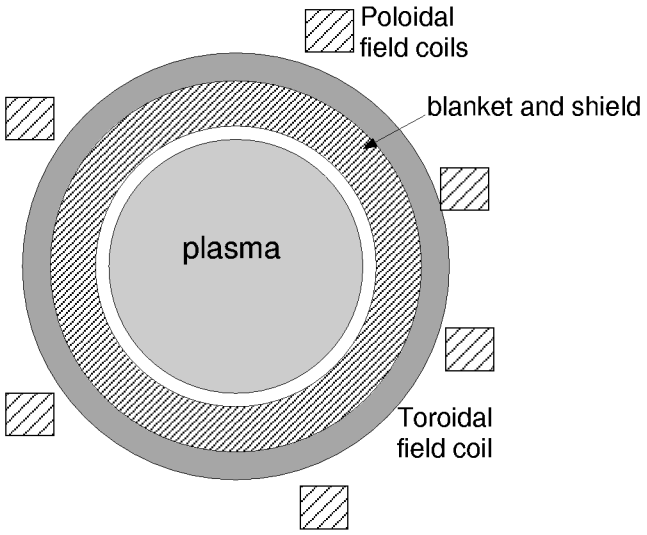

Figure 1.12: Layout of principal components in a conceptual fusion reactor.

1.7 Muon-catalyzed fusion

The real issue in achieving nuclear fusion is to overcome the repulsive Coulomb forces of light nuclei. The 'conventional' approach is strong heating to reach the ignition conditions described above. Another, more exotic, way is to screen the electric charge by replacing the electron in the hydrogen atom with a muon [9]. This idea was first proposed by A.D. Sacharov in 1948. A muon is an elementary particle, a so-called lepton ('light' particle). This muon has the same properties as an electron, the only difference being that its mass is 200 times larger. Due to its larger mass the muon decays with a half-life of $1.5 \cdot 10^{-6}$ seconds:

$$\mu^- \longrightarrow e^- + \bar{\nu}_e + \nu_\mu$$

Muons can be produced in accelerators which provide collisions between accelerated protons and some other material. In these collisions many pions are produced. A pion is the lightest elementary particle participating in the strong interaction (so-called hadrons). The three types of pions (π^-, π^+ and π^0) are produced in equal amounts. A negative muon is formed from the decay of a negative pion:

$$\pi^- \longrightarrow \mu^- + \bar{\nu}_\mu$$

In a D-T mixture the muon slows down very fast ($\approx 10^{-9}$ s) and forms a $D\mu$ or $T\mu$ atom with a small Bohr radius of

$$a_\mu = a_e \cdot m_e/m_\mu \approx 2.5 \cdot 10^{-13}\ m$$

This reduced atomic radius is the key point for possible catalyzed nuclear fusion: if a $D\mu T$ molecule is formed, it takes just 10^{-12} s until quantum mechanical tunnelling triggers a fusion reaction:

$$D\mu T \longrightarrow {}^4He + n + \mu^- \quad + \ 17.6\ MeV$$

There are two limiting factors in this approach: the first is the time needed to form a $D\mu T$ molecule. This time can be influenced by some resonance mechanisms. The second limitation comes from the 0.6% probability that the muon will stick to the helium atom

after the fusion reaction and will thus be lost for catalyzing more fusion reactions during its lifetime. Recently, experiments obtained fusion rates of more than 100 reactions per muon. For a pure energy producing system this rate is not sufficient, since about 3 GeV ($= 3 \cdot 10^9$ eV) is needed to produce one negative muon.

Acknowledgement The author acknowledges the work of H.W. Bartels and G. Pautasso, who prepared the basis of this manuscript for earlier Summer Universities.

Bibliography

[1] G. Gamov; *Zur Quantentheorie des Atomkernes*, Zeitschrift für Physik **51** (1928), p. 204–212.

[2] J. D. Lawson; it Some Criteria for a Power Producing Thermonuclear Reactor, Proceedings of the Physical Society **B70** (1967), p.6.

[3] H.-S. Bosch, G. M. Hale; *Improved Formulas for Fusion Cross-Sections and Thermal Reactivities*, Nuclear Fusion **32** (1992), p. 611–631.

[4] J. Raeder et al.; *Kontrollierte Kernfusion*,
Teubner Verlag, Stuttgart (1981).

[5] U. Schumacher; *Fusionsforschung*,
Wissenschaftliche Buchgesellschaft, Darmstadt (1993).

[6] J. G. Cordey, R. J. Goldston, R. R. Parker;
Progress toward a Tokamak Fusion Reactor, Physics Today, January 1992, p. 22–42.

[7] J. D. Lindl, R. L. McCrory, E. M. Campbell;
Progress Toward Ignition and Burn Propagation in Inertial Confinement Fusion,
Physics Today, September 1992, p. 32–40.

[8] W. J. Hogan, R. Bangerter, G. L. Kulcinski;
Energy from Inertial Fusion, Physics Today, September 1992, p. 42–50.

[9] S. E. Jones; *Muon-Catalysed Fusion Revisited*, Nature **231** (1986), p. 127–133.

Chapter 2

Basic Plasma Physics

Axel Könies

Monika Bessenrodt-Weberpals, Hugo de Blank,

Ralf Schneider

2.1 Introduction

A plasma is a hot gas consisting of charged and neutral particles which exhibit collective behaviour.

The name *plasma* goes back to Langmuir (1929) who discovered electromagnetic oscillations in rarefied gases which he called *"plasma oscillations"*.

The plasma is often referred to as the fourth state of matter (solid – liquid – gas – plasma). This concept arises from a thermodynamic description but is not completely rigorous. The variation of the basic macroscopic physical quantities like density n and temperature T determines the properties of the matter in the plasma state (see Fig. 1). However, the transition from the liquid, gaseous or solid state into the plasma state is not abrupt but continuous. In a gas, for example, more and more of the atoms become ionized with rising temperature and a plasma forms.

We know now that 99% of the matter in the universe is in the plasma state. Plasma can be found in the interior of the stars as well as in the interstellar space and in the core of the planets. Plasma also occurs in gas discharges ("neon light", lightning) as part of our daily live.

The transition from weakly interacting neutral particles to charged particles which interact over the long range Coulomb force may alter the properties of the particle system considerably. Therefore, many-body-interaction plays an important role. The possible charge separation gives rise to electromagnetic oscillations or waves in a plasma.

Note, that today the term plasma is understood in a very broad sense and may be applied to all systems with consist of charged particles as eg. electrons in a solid or, even more

general, systems where the bound states of the constituents are broken. The quark-gluon-plasma with its "color" charged constituents, occurring shortly after big bang or at high energy nucleus-nucleus collisions, is a famous example for this concept. (15)

In the course of this lessons we will focus on plasmas made up of ions and electrons which interact over the Coulomb force and which are globally neutral. We will briefly discuss the types of plasmas in the next passage. Then, we go over to the plasma parameters which provide a more quantitative access to the several types of plasmas shown in Fig. 1. We will discuss the fundamental concepts of plasma physics, namely the Debye screening the plasma frequency and the so-called quasi-neutrality. Further we will touch plasma collisions and we will end the lecture discussing the plasma motion in a magnetic field which is of paramount importance for plasmas in magnetic fusion devices.

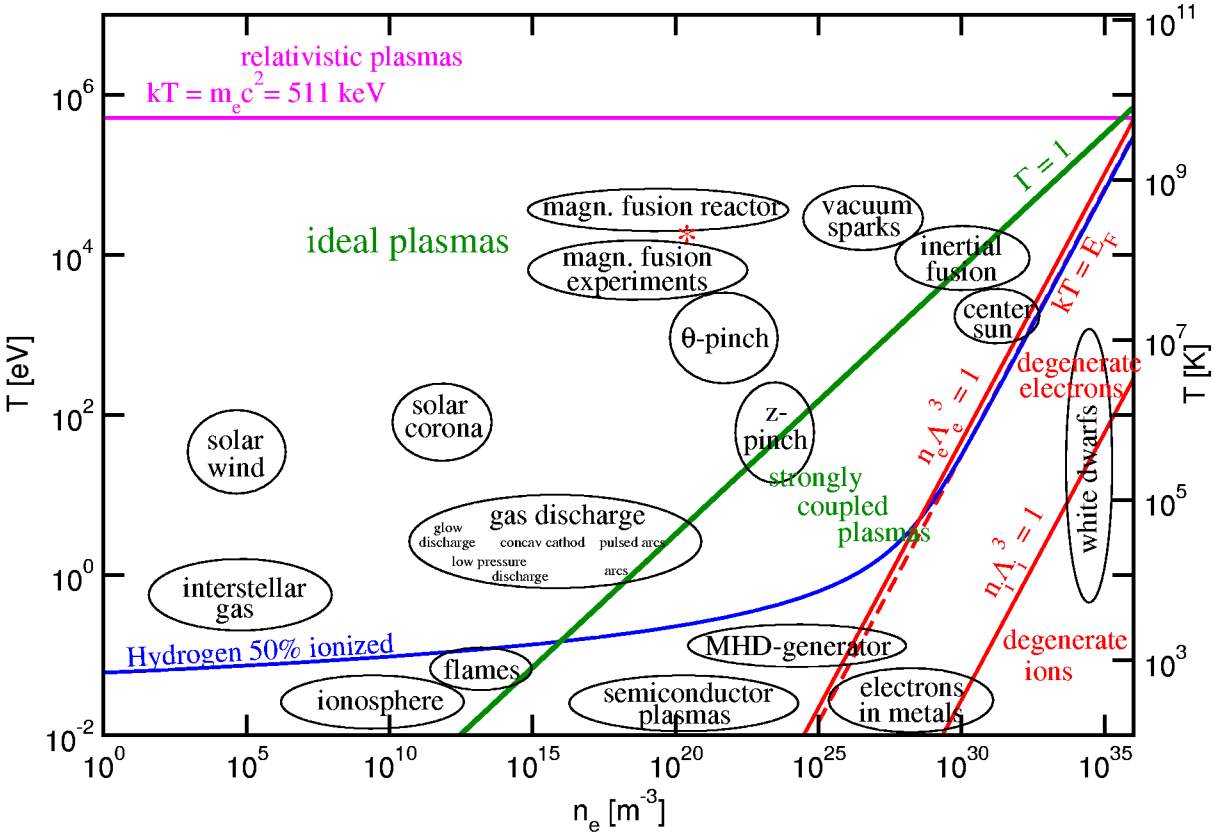

Figure 2.1: *Temperatures and densities of astrophysical and laboratory plasmas. The asterisk indicates the fusion relevant parameters used in the examples:* $T = 10^4\,\mathrm{eV}$, $n_e = 10^{20}\,\mathrm{m}^{-3}$, $B = 5\,\mathrm{T}$.

2.2 Types of plasmas

2.2.1 Astrophysical plasmas

There are a variety of astrophysical plasmas in nature. They cover a wide range of densities and temperatures. Here, we will mention only a few of them. (see Chapter 14)

The interior of the sun and the stars consists of a very dense and very hot plasma where light atomic nuclei fuse to heavier ones and release the access of binding energy according to Einsteins famous formula $E = mc^2$. (see Chapter 1)The plasma density and the plasma temperatures drop the closer one comes to the surface, thus the stellar atmosphere has completely different properties. The solar corona which is even more outside is a dilute magnetized plasma of several million degrees.

The sun emits an extremely dilute supersonic plasma, the solar wind, into its planet system. Near the earth the solar wind has $n_e \approx 5\,\mathrm{cm}^{-3}$ and $T_e = 10^5\,\mathrm{K}$. Because of its high temperature, the plasma has still a high conductivity.

By interaction with the electromagnetic radiation from the sun the atoms of the upper atmosphere become partly ionized. We call this plasma which expands from about 60 km to 2000 km altitude the ionosphere.

A completely other type of plasmas are the degenerate plasmas within white dwarfs or neutron stars showing extremely high densities and thus behaving differently from the typical ideal plasmas we know from the majority of the Laboratory plasmas.

2.2.2 Laboratory plasmas

The tradition of laboratory plasma physics starts with the investigation of the weakly ionized plasmas of flames in the 18th century. Typical applications nowadays are plasma-aided welding and combustion for this type of plasma.

Since the plasma may carry an electric current, plasma discharges of various types are investigated in fundamental research and applied in industry. Low-pressure discharges like glow discharges carry small currents with cold electrodes. They serve for lightening, for gas lasers like the CO_2 laser or the HeNe laser, and for the wide-spread applications of plasma etching and deposition .

High-pressure discharges like arcs may carry larger currents and thereby attain higher temperature. They may also serve for lightening like the well-known high-pressure mercury lamp, for switches, and for plasma-material processing like melting, cutting, and welding.

In order to gain fusion energy in laboratories, high-temperature plasma physics has been started as a classified project around 1950. In 1958, the UN conference on the peaceful use of atomic energy has led to a declassification of fusion research (see Chapter 1).

Note: The free electrons in metal behave similar to a high-density, low-temperature plasma (see Figure 2.1).

2.3 Plasma parameters

To distinguish between different plasma states, let us look at the n-T diagram (see Figure 2.1). The different physical behavior is ordered by the four characteristic energies, namely the thermal energy $E_{th} = \frac{3}{2}k_BT$, the Fermi energy $E_F = (\hbar^2/2m_e) \cdot (3\pi^2 n)^{2/3}$, the electrostatic interaction energy $E_{el} = e^2/(4\pi\varepsilon_0 r)$, and the energy of Bohrs ground state $E_I = m_e e^4/(8\varepsilon_0^2 h^2)$. For simplicity, let us concentrate on hydrogen with charge $q = e$.

2.3.1 Ionization

First, with $E_{th} \approx E_I$ we can estimate the temperature T_I necessary for ionization from

$$\tfrac{3}{2}k_BT_I = m_e e^4/(8\varepsilon_0^2 h^2)$$

we get

$$T_I = \frac{m_e e^4}{8\varepsilon_0 h^2 k_B} \cdot 2/3 = 9\,\mathrm{eV}\,. \tag{2.1}$$

Above this temperature, hydrogen plasmas are partially to fully ionized.

More exactly, the degree of ionization in a plasma in thermodynamic equilibrium is given by the Saha equation [13]

$$\frac{n_z n_e}{n_{z-1}} = 2\frac{Z_z(T)}{Z_{z-1}(T)}\left(\frac{m_e k_B T}{2\pi\hbar^2}\right)^{3/2} \exp\left(-\frac{E_{I,z}}{k_B T}\right) \tag{2.2}$$

with n_z being the density of the z-th ionization stage and Z_z the corresponding partition function. From Figure 2.1, you can read the situation in a hydrogen plasma whose ionization degree is 50%. This shows that the hydrogen plasma is almost completely ionized at $k_BT > 1/10\ E_I$. The Saha equation may be applied for low ionization stages and high-density plasmas where collision processes dominate over radiative transitions and thereby determine the equilibrium. For high-ionized atoms like heavy impurities in a fusion plasma, the full set of rate equations has to be solved including both collisional and radiative transitions (see also Chapter 13).

2.3.2 Degeneracy and thermal wave length

The electrons which are Fermions and thus obey the Pauli principle, have actually to be described by a Fermi distribution of the energy. However, in a wide range of plasma parameters ($E_{th} \gg E_F$) the Maxwell-distribution is an excellent approximation. This is the case for magnetic fusion plasmas, the sun, flames, gas discharges, interstellar plasmas ...

With increasing density or for low temperatures, if the Fermi energy approaches the thermal energy (see Figure 2.1),

$$k_BT \approx E_F = \frac{\hbar^2}{2m}\left(3\pi^2 n\right)^{2/3}.$$

the electron gas becomes more and more degenerate. That means that the quantum statistical behavior of the electrons does play a role and the Fermi distribution has to be used.

We can express the influence of the quantum character of the particles also using the ratio of the length scales of the thermal (de Broglie) wave length of the particles

$$\Lambda_c = \frac{h}{\sqrt{2\pi m_c k_B T_c}} \tag{2.3}$$

to their average distance (also called Wigner-Seitz-Radius)

$$r_0 = \left(\frac{4\pi}{3} n\right)^{-1/3}. \tag{2.4}$$

The criterion of non-degeneracy for a particle species c is then given by

$$n_c \Lambda_c^3 \gg 1 \tag{2.5}$$

which is true if the de Broglie wave length is much less than the average particle distance.

2.3.3 Relativistic effects

If the thermal energy of the electrons is of the order of the energy corresponding to the electron rest mass.

$$E_{th} \approx m_e c^2,$$

at a temperature of approximately 511 keV, we have a relativistic plasma (see Figure 2.1).

The plasma is called a relativistic degenerate plasma if the Fermi energy is of the order $m_e c^2$.

2.3.4 Ideal and non-ideal plasmas

If the thermal energy of a charged species (e.g. electrons) is much larger than that of their Coulomb interaction then the interaction can be neglected and the plasma can be regarded an ideal gas of charged particles and is called an ideal plasma.

If the interaction of the charged particles starts to effect the plasma behavior we call it a non-ideal plasma. To get a quantitative estimate, let us define the ratio of the Coulomb energy at the average distance to the thermal energy

$$\Gamma = \frac{Ze}{4\pi\epsilon_0 r_0 k_B T} \tag{2.6}$$

The parameter Γ allows the classification of the degree to which the Coulomb interaction determines the plasma behavior. ($\Gamma \ll 1$ almost ideal, $\Gamma < 1$ weakly non-ideal and $\Gamma > 1$ strongly non-ideal)

Figure 2.2: *Schematic illustration of charge separation in a plasma.*

At this point we introduce the Landau length λ_L at which the thermal energy equals the electrostatic energy:

$$\lambda_L = \frac{e^2}{4\pi\varepsilon_0 k_B T}. \tag{2.7}$$

This quantity will reappear in the calculation of the plasma resistivity.

There may be defined another parameter which estimates the particle-particle interaction, namely the ratio of the Landau length and the thermal wave length:

$$\xi_c = \sqrt{2\pi}\frac{\lambda_L}{\Lambda_c} = 2\sqrt{\frac{E_I}{k_B T}} \tag{2.8}$$

If the plasma parameter ξ is of the order of one then in microscopic scattering processes the quantum mechanical interaction does play an important role and the Born series approximation can not be applied.

2.4 Plasma fundamentals

2.4.1 Quasi-neutrality

First, let us look deeper at electrostatic properties of plasmas. Indeed, plasmas are usually electrically *quasi-neutral*, i.e. local concentrations of charge or external potential are shielded out in a distance short compared with the typical system length. A simple estimate shows that a small charge separation causes a large restoring electric field. Consider a non-zero charge density $\rho_E = e(n_i - n_e)$ caused by a small separation x of the electrons from the ions (see Figure 2.2). Application of Poisson's equation $\boldsymbol{\nabla}\bullet\boldsymbol{E} = \rho_E/\varepsilon_0$ yields ($\boldsymbol{\nabla}\bullet\boldsymbol{E} \approx E/x$),

$$E \approx \frac{n_e e\, x}{\varepsilon_0}. \tag{2.9}$$

A fully ionized plasma at 5 eV and atmospheric pressure has an electron density of $n_e = 6 \times 10^{22}\,\mathrm{m}^{-3}$. A charge separation of $x = 1\,\mathrm{mm}$ would lead to a very strong electric field $E = 1 \times 10^{12}\,\mathrm{V/m}$ and an electric potential $\phi = 5 \times 10^8\,\mathrm{V}$ over 1 mm. In fact, finite electric fields can be generated by very small deviations of the densities from quasi-neutrality.

2.4.2 Plasma frequency

The strong restoring electric field associated with deviations from quasi-neutrality causes a harmonic oscillation (Langmuir, 1929). In the absence of a magnetic field, electrons

react to the electric field of equation (2.9) with

$$m_e \frac{d^2x}{dt^2} = -e\,E = -\frac{n_e e^2\,x}{\varepsilon_0}.$$

The solution of this equation is an oscillation with the characteristic electron *plasma frequency*

$$\omega_{p,e} = \left(\frac{n_e e^2}{\varepsilon_0\, m_e}\right)^{1/2}. \tag{2.10}$$

The ions do not participate in these oscillations because of their high mass. The plasma frequency is temperature-independent. For typical fusion plasma densities ($10^{20}\,\mathrm{m}^{-3}$) it is $\nu_{p,e} \approx 100\,\mathrm{GHz}$. Above this frequency, electromagnetic waves can propagate, while for $\omega < \omega_p$ they are absorbed (see also Chapter 6). Analogously, the ion plasma frequency is defined as

$$\omega_{p,i} = \left(\frac{n_i Z^2 e^2}{\varepsilon_0\, m_i}\right)^{1/2} \tag{2.11}$$

and the total plasma frequency

$$\omega_p^2 = \omega_{p,e}^2 + \omega_{p,i}^2\,. \tag{2.12}$$

2.4.3 Debye shielding

Usually, ions are surrounded by electrons which screen the ion charge. Only at small distances a deviation from charge neutrality may be observed. In the presence of an electric potential ϕ, the electron and ion densities in thermal equilibrium are modified according to Boltzmann's distribution $\sim \exp(-E/k_BT) = \exp(-q\phi)/k_BT$ with $q = \pm e$. Integration over all velocities yields $\tilde{n}_q = n_q \exp(-q\phi/k_BT)$, where n_q are the densities for $\phi = 0$. For small exponents, this can be approximated by $\tilde{n}_q = n_q(1 - q\phi/k_BT)$. For singly charged ions, Poisson's equation $\nabla^2\phi = -\rho_E/\varepsilon_0$ in spherical geometry reads

$$\frac{1}{r^2}\frac{d}{dr}(r^2\frac{d\phi}{dr}) = \frac{e(\tilde{n}_e - \tilde{n}_i)}{\varepsilon_0} = \frac{n_e e}{\varepsilon_0}\,\frac{e\phi}{1/k_BT_e + 1/k_BT_i}\,, \tag{2.13}$$

where the plasma approximation $n_e = n_i$ is used. With the definition of the *Debye length*

$$\lambda_{D,q} = \left(\frac{\varepsilon_0\, k_B T_q}{2 n_e e^2}\right)^{1/2}, \tag{2.14}$$

and the total Debye length

$$\lambda_D^{-2} = \lambda_{D,e}^{-2} + \lambda_{D,i}^{-2} \tag{2.15}$$

the solution of equation (2.13) gives the screened potential

$$\phi(r) = \frac{e}{4\pi\varepsilon_0}\,\frac{\exp\left(-r/\lambda_D\right)}{r}. \tag{2.16}$$

The Debye length describes the range of an electric potential inside a plasma, which is much smaller than the range in vacuum.

A more heuristic deviation of the Debye length is the following: small charge separations arise as a result of thermal fluctuations. In a plasma the thermal energy density of the electrons per degree of freedom is $E_f = \frac{1}{2} n_e k_B T$. The electrostatic energy density results from a separation of charge over a length x (see Figure 2.2 and equation (2.9)) as $E_e = \frac{1}{2}\varepsilon_0 E^2 = \frac{1}{2}\varepsilon_0 (n_e e x/\varepsilon_0)^2$. The comparison of E_f and E_e shows that substantial separation of charge can only occur over lengths of up to $x \approx (\varepsilon_0 k_B T/n_e e^2)^{1/2}$, which is again the Debye length λ_D given in equation (2.14).

Averaged over many λ_D, the electron and ion charge densities are equal, i.e. $n_e = n_i$. The thermal electron velocity $v_{th,e} = \sqrt{3k_B T_e/m}$ is found from equations (2.10) and (2.14) to be

$$v_{th,e} = \sqrt{3}\,\lambda_{D,e}\,\omega_{p,e}\,.$$

Therefore, $1/\omega_{p,e}$ can be interpreted as the time that a thermal electron needs to pass the Debye length. One important consequence is, as mentioned before, that electromagnetic waves with frequencies below $\omega_{p,e}$ cannot propagate in plasmas since their electric fields are screened by the Debye shielding. Instead the waves are reflected. For larger frequencies, the inertia of the electrons allows the propagation of the waves. This is the reason why metals reflect visible light but not x-rays.

The definition of an ideal plasma (see Section 2.3.4) is equivalent to the call for a large number of particles in a Debye sphere, called the *plasma parameter* N_D:

$$N_D = \tfrac{4}{3}\pi\, n\, \lambda_D^3 \gg 1\,.$$

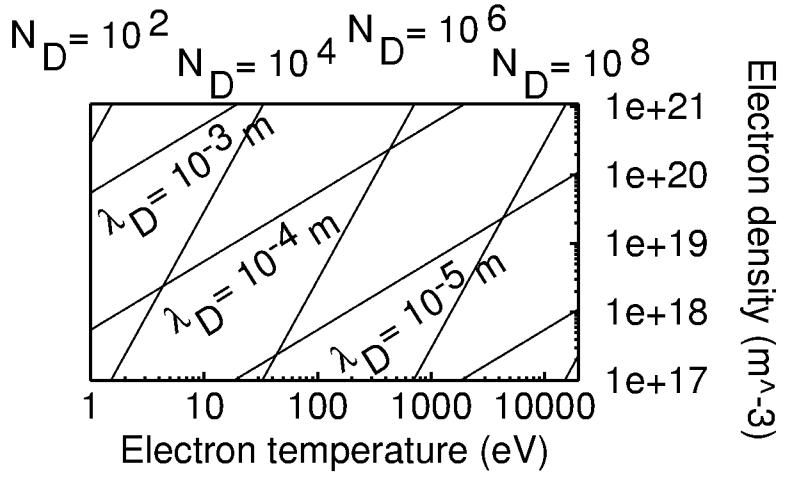

Figure 2.3: *Values of the Debye length λ_D and the plasma parameter N_D plotted against electron temperature and electron density.*

2.5 Particle collisions

2.5.1 Coulomb collisions and Rutherford scattering

Collisions in the plasma play an important role for all collective effects like e.g. resistivity in the plasma. When an electron collides with a neutral atom, no force is felt until the electron is close to the atom; these collisions are similar to billiard-ball collisions. However, when an electron collides with an ion, the electron is gradually deflected by the long-range Coulomb field of the ion. Nonetheless, an effective cross-section may be derived. We will do it in a classical picture without considering quantum mechanical or relativistic corrections.

We will consider here the scattering of an electron at an ion. Because of the large ratio of ion to electron mass we can assume the ion location in the centre of mass of the two-particle system (see 2.4).

In the absence of Coulomb forces, the electron could have a distance of closest approach called the *impact parameter* ρ.

For the Coulomb interaction of two charges e_1 and e_2, the potential reads $U(r) = \alpha/r$ with $\alpha = e_1 e_2/(4\pi\varepsilon_0)$. Having in mind (2.4) and following textbooks from theoreti-

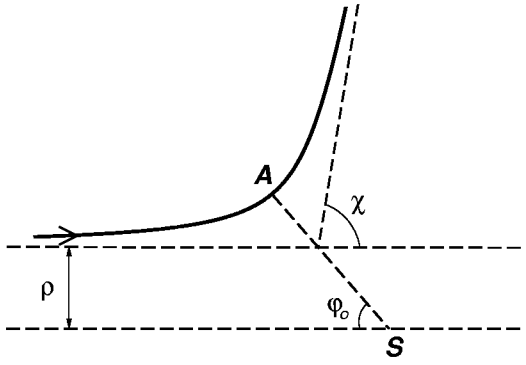

Figure 2.4: *Rutherford scattering; S is the centre of mass of the scattering partners. As the Coulomb force is a central force, the orbit is symmetric with respect to A and therefore* $\chi = |\pi - 2\phi_0|$

cal mechanics [17] we introduce cylindrical coordinates and employ the conservation of energy:

$$E = \frac{m\dot{r}^2}{2} + \frac{L^2}{2mr^2} + U(r) \tag{2.17}$$

and angular momentum:

$$L = mr^2\dot{\phi} \tag{2.18}$$

Let us assume that the electron has the relative velocity v_∞ if it is at a very large distance from the scattering centre (ion). Then, obviously, the energy must be equal to $E = \frac{mv_\infty^2}{2}$ and the angular momentum $L = m\rho v_\infty$ For very long times the particle should again go to infinity. All together this gives

$$\phi_0 = \int_{r_{min}}^{\infty} \frac{\rho\frac{dr}{r^2}}{\sqrt{1 - \frac{\rho^2}{r^2} - \frac{2U}{mv_\infty^2}}} \tag{2.19}$$

The distance of closest approach r_{min} is reached when $\dot{r}$ is zero, i.e. when the kinetic energy of the particle has been converted to energy in the effective potential $U(r) + L^2/(2mr^2)$. $r = r_{min}$ is a root of the denominator in eq. (2.19). Integration gives

$$\rho^2 = \frac{\alpha^2}{m^2 v_\infty^4} \cot^2 \frac{\chi}{2} = \rho_0^2 \cot^2 \frac{\chi}{2} \tag{2.20}$$

As we have usually an ensemble of particles which undergo the scattering we define the cross-section σ as

$$d\sigma = \frac{dN}{n}\,, \tag{2.21}$$

where N shall denote the number of particles being scattered by angles between χ and $\chi + d\chi$, while n is the number of particles per area unit. Assuming a homogeneous beam, we have $dN = n 2\pi\rho d\rho$. Expressing this in terms of the solid angle Ω gives

$$d\sigma = \frac{\rho}{\sin\chi} \left|\frac{d\rho}{d\chi}\right| d\Omega\,. \tag{2.22}$$

Finally, the Rutherford cross-section becomes:

$$d\sigma = \left(\frac{\alpha}{2mv_\infty}\right) \frac{d\Omega}{\sin^4 \frac{\chi}{2}} \tag{2.23}$$

We can see that the number of collisions with small angles is larger than those of large angles. Furthermore, the value for the cross section diverges for large impact parameters ρ or small angles χ like χ^{-4} with the consequence of an infinite total cross-section. This is due to of the infinite long range of the Coulomb interaction.

From the cross section we can infer an approximate expression for the electron-ion collision time if we define the collision time as proportionality constant between the initial parallel momentum of the electron and its change during collisions with ions at all possible impact parameters ρ:

$$\frac{d}{dt} \langle \Delta p_\parallel \rangle = -\nu_{ei} p_\parallel \tag{2.24}$$

The initial parallel momentum is $p_\parallel = p = mv_\infty$ while $p_\parallel^f = p\cos\chi$, as it can easily inferred from Fig. 2.4. Using trigonometric relations and eq.(2.20) we get:

$$\Delta p_\parallel = p(\cos\chi - 1) = -2p \frac{1}{1 + \cot^2 \frac{\chi}{2}} = -2p \frac{1}{1 + \left(\frac{\rho}{\rho_0}\right)^2} \tag{2.25}$$

In the following we will denote v_∞ by v for brevity. For the net change of momentum per time unit of the electron we have to consider all ions that the incoming electron can encounter in this time unit:

$$\frac{d}{dt} \langle \ldots \rangle = 2\pi n_i v \int_0^{\rho_{max}} \rho d\rho \ldots\,. \tag{2.26}$$

The upper limit should actually be taken to be infinity. We will see, however, that the integral diverges for $\rho_{max} \to \infty$ which is the well known Coulomb divergence which is due

the the infinite long range of the interaction. The problem can be solved considering the screening of the particle-particle interaction by the other charges in the system. This is done by the exponentially decaying Debye-potential we have derived in the last section. The typical radius of the interaction is the Debye-length. Therefore, we take this length as the upper cut-off and we obtain:

$$\frac{d}{dt}\left\langle \Delta p_{\parallel} \right\rangle = -\frac{4\pi n_i}{mv^2}\alpha^2 \frac{1}{2}\left\{ \ln\left| \rho_{max}^2 \left[1 + \left(\frac{\rho_0}{\rho_{max}} \right)^2 \right] \right| - \ln\left|\rho_0^2\right| \right\}, \tag{2.27}$$

which gives

$$\frac{d}{dt}\left\langle \Delta p_{\parallel} \right\rangle \approx -\frac{n_i Z_i^2 e^4}{4\pi\epsilon_0 m v^2} \ln\frac{\lambda_D}{\rho_0} = -\frac{n_i Z_i^2 e^4}{4\pi\epsilon_0 m v^2} \ln\Lambda\,, \tag{2.28}$$

if we consider that the Debye length $\rho_{max} = \lambda_D$ is much larger than ρ_0. The latter condition is true if the number of particles in a Debye sphere is large, i.e. if we have an ideal plasma. This is the case for magnetic fusion and a lot of astrophysical plasmas. The expression $\ln\Lambda = \ln(\lambda_D/\rho_0)$ is called the Coulomb logarithm.

The cross sections and collision times are most important for the behavior of the plasma. In the next section we will relate it to the resistivity by very simple physical arguments. Note, however, that the derivation we gave here is heuristic and not rigorous at all. An average over the velocity distribution had actually to be included in the derivation. This is shown in chapter 5.

The rigorous derivation should start from a kinetic equation. There are a lot of approaches to non-equilibrium processes which give quantum mechanical expressions for cross sections or collision times. These expressions usually include the collective effects like screening which we had to introduce artificially by the cut-off parameter. The expression we have obtained here turns out to be the first order Born approximation of a quantum mechanical cross section. This makes clear that the approximation is valid for high energies of the electron only, i.e. when the thermal energy of a particle is much larger than the Coulomb interaction. Therefore, for non-ideal plasmas the simple classical picture can not be applied and the Coulomb logarithm is a poor approximation. The collision time for electron-electron collisions follows from eq. 2.24

$$\tau_{ei} = \frac{4\pi\varepsilon_0^2}{Z^2 e^4}\frac{m_e^2 v_e^3}{n_i \ln\Lambda}\,. \tag{2.29}$$

Doing proper integrations over the velocity distributions of the species involved by using the Fokker-Planck equation (see later) one gets that the collision times behave like

$$\tau_{ee} : \tau_{ei} : \tau_{ie} : \tau_i = 1 : \frac{2}{Z^2} : \frac{2}{Z^2}\frac{n_e}{n_i} : \frac{1}{Z^4}\left(\frac{m_i}{m_e}\right)^{1/2}\frac{n_e}{n_i}\left(\frac{T_i}{T_e}\right)^{3/2}. \tag{2.30}$$

From the collision time the mean free path can be calculated as $\lambda_{mfp} = \tau_{ei} v_e$. Fusion plasmas possess a mean free path of about 15 km. This is much larger than the typical laboratory plasma dimensions, leading to the term *collision-less* plasma. The mean free path for fusion reactions is still four orders of magnitude larger at this temperature. When the plasma is heated, often either the electrons or the ions are heated preferentially

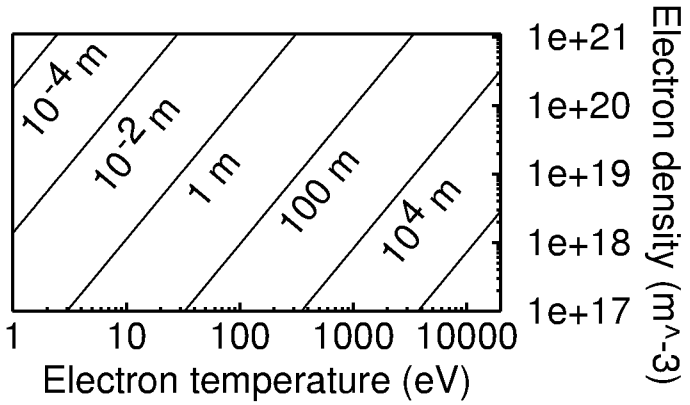

Figure 2.5: *Values of the mean free path of electrons λ_e plotted against electron temperature and electron density.*

(see also Chapter 6). In such a case the characteristic time for heat exchange between the ion and electron components needs to be known. The frequency of the collisions involved is determined by the faster component, the electrons. Due to the mass differences the energy transfer is inefficient, only of the order m_e/m_i of the energy being transferred. Precisely, it is $\tau_{ie}^E = m_i/(2m_e)\tau_{ee}$. Expressions for various characteristic collision times and related relaxation times can be found in [14]. Since $\tau_{ee} \approx 0.1$ ms and $\tau_{ii} \approx 10$ ms in a fusion plasma, the electrons as well as the ions take their Maxwell distributions corresponding to characteristic temperatures T_e and T_i, respectively. Nevertheless, T_e and T_i may be different.

2.6 Electric resistance

If an electric field is applied to the plasma, the electrons and ions are accelerated in opposite directions. The electrons speed up much faster due to their lighter mass. They deliver the gained energy to the ions by Coulomb collisions, yielding a *resistance* η which, according to Ohm's law, connects the electric field $\boldsymbol{E}$ with the current density $\boldsymbol{j}$,

$$\boldsymbol{E} = \eta \boldsymbol{j} \,. \tag{2.31}$$

The net change of electron momentum is supplied by the electric field and by the momentum loss due to collisions:

$$\frac{d}{dt} \langle \Delta p_\parallel \rangle = -eE - \nu_{ei} p_\parallel \tag{2.32}$$

Assuming an equilibrium between driving and dissipative forces, the term on the left hand side should vanish. If we further assume that the current is proportional to the relative velocity of electrons and ions $j = -en_e v$ (remember the last section), we get

$$\begin{aligned} -eE &= \nu_{ei} p_\parallel \\ \eta e^2 n_e v &= \nu_{ei} m_e v \,. \end{aligned} \tag{2.33}$$

Therefore the resistivity is

$$\eta = \frac{m_e}{n_e e^2 \tau_{ei}^E} \propto T_e^{3/2} . \tag{2.34}$$

The exact value of the specific resistance was derived in [15] with the help of kinetic theory and the resulting *Spitzer resistivity* is a factor of about 2 smaller than our first approximation. For $T_e = 1.4\,\mathrm{keV}$, the plasma resistance is comparable to copper ($1.8 \times 10^{-8}\,\Omega\mathrm{m}$). Since η is proportional to $T_e^{-3/2}$, fusion plasmas with $T \approx 10\,\mathrm{keV}$ have resistance values which are an order of magnitude smaller than that of copper. The measurement of the resistance can be used to determine plasma temperatures since it depends only very weakly on the density via $\ln\Lambda$ (see Chapter 9). In laboratory plasmas, the effects of different ion species (impurities) on the resistivity often has to be taken into account. For plasmas in strong magnetic fields, additional corrections have to be made to the electrical resistance. The specific resistance $\eta_\perp$ is approximately twice the value of $\eta_\parallel$.

2.7 Motion of charged particles in electromagnetic fields

The motion of a particle with electric charge q and mass m in electric and magnetic fields can be determined from the combined electrostatic and Lorentz force,

$$\boldsymbol{F} = q\,(\boldsymbol{E} + \boldsymbol{v} \times \boldsymbol{B}).$$

2.7.1 Homogeneous magnetic field

For $E = 0$ and a homogeneous magnetic field, the kinetic particle energy remains constant because the Lorentz force is always perpendicular to the velocity and can thus change only its direction, but not its magnitude. The motion of charged particles is then described in terms of the velocity components parallel and perpendicular to the magnetic field, $\boldsymbol{v}_\parallel$ and $\boldsymbol{v}_\perp$. Only $\boldsymbol{v}_\perp$ interacts with $\boldsymbol{B}$, leading to a circular motion perpendicular to $\boldsymbol{B}$. The centrifugal force $mv_\perp^2/r$ balances the Lorentz force $qv_\perp B$ for a gyration radius r equal to the *Larmor radius*

$$\rho_L = \frac{mv_\perp}{|q|B} .$$

If $\frac{1}{2}mv_\perp^2 = k_B T$ is taken for the two-dimensional thermal motion perpendicular to $\boldsymbol{B}$, it is

$$\rho_L = \frac{(2mk_BT)^{1/2}}{|q|B} .$$

In a typical fusion plasma ($T = 10\,\mathrm{keV}$, $B = 5\,\mathrm{T}$), the electrons have a Larmor radius $\rho_{L,e} = 67\mu\,\mathrm{m}$ and deuterons have $\rho_{L,i} = 4.1\,\mathrm{mm}$. The frequency of the gyration, called *cyclotron frequency* $\omega_{c,q}$, follows from $v_\perp = \omega_c\,\rho_L$ to be

$$\omega_{c,q} = \frac{|q|B}{m_q} .$$

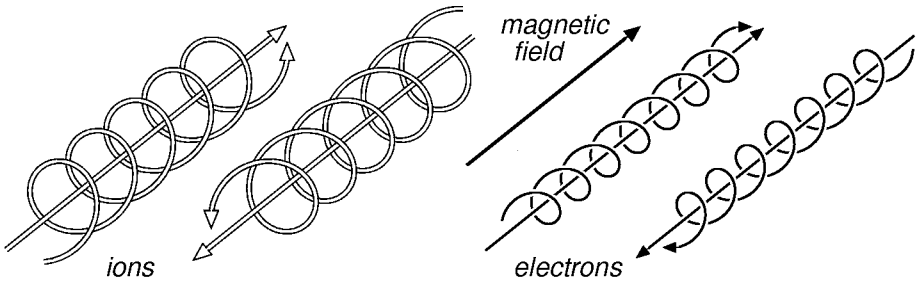

Figure 2.6: Orientation of the gyration orbits of electrons and ions in a magnetic field.

In fusion experiments, the electron cyclotron frequency $\omega_{c,e}$ is of the same order of magnitude as the plasma frequency $\omega_{p,e}$.

The Hall *parameter*

$$x_q = \omega_{c,q}\tau_{qq} \tag{2.35}$$

counts the number of cyclotron revolutions between succeeding collisions. A magnetized plasma is characterized by $x_e \gg x_i \gg 1$.

The *magnetic moment* μ is defined as the product of the current I times the area A which is surrounded by the current. Thus, the magnetic moment of a single gyrating particle is

$$\mu = I \cdot A = \frac{q\omega_c}{2\pi} \cdot \pi\rho_L^2 = \frac{mv_\perp^2}{2B} = \frac{\epsilon_\perp}{B}\,, \tag{2.36}$$

where $\epsilon_\perp$ is the perpendicular fraction of the kinetic energy. The magnetic field produced by the gyrating particles counteracts the externally imposed magnetic field $\boldsymbol{B}$, i.e. the *plasma is diamagnetic.*

2.7.2 Motion in a constant magnetic field due to an additional force

If in addition to the Lorentz force, a force $\boldsymbol{F}$ acts on the charged particle, the equation of motion is

$$m\frac{d\boldsymbol{v}}{dt} = q\,(\boldsymbol{v} \times \boldsymbol{B}) + \boldsymbol{F}\,.$$

The motion of the particle under the influence of $\boldsymbol{F}$ can be separated from the gyration due to $\boldsymbol{B}$ by considering the *guiding centre* of the particle, as shown in Figure 2.7. The guiding centre 'c' is the centre of the gyration cycle. Its position $\boldsymbol{r}_c$ can be written as

$$\boldsymbol{r}_c = \boldsymbol{r} + \boldsymbol{r}_g\,. \tag{2.37}$$

where $\boldsymbol{r}$ is the position of the particle and $\boldsymbol{r}_g$ the gyration radius vector

$$\boldsymbol{r}_g = \frac{m}{qB^2}\,\boldsymbol{v} \times \boldsymbol{B}\,.$$

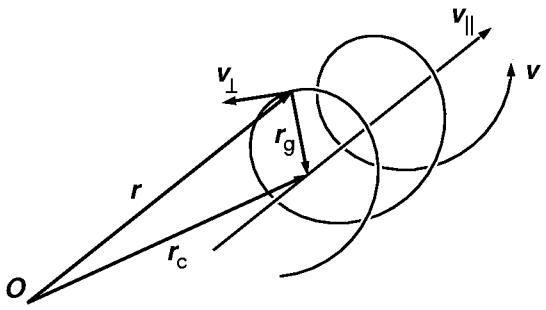

Figure 2.7: *Definition of the guiding centre motion.*

In *strongly magnetized* plasmas such as in fusion experiments, the Lorentz force dominates other forces $\boldsymbol{F}$. Then, ρ_L is often much smaller than other length scales, and ω_c much higher than other frequencies. Consequently, the particle orbit is well described by the motion of the guiding centre. With the assumption of a constant B, the velocity of the guiding centre can be obtained by differentiating equation (2.37):

$$\begin{aligned}\boldsymbol{v}_c = \dot{\boldsymbol{r}}_c &= \boldsymbol{v} + \frac{m}{qB^2}\frac{d\boldsymbol{v}}{dt} \times \boldsymbol{B} \\ &= \boldsymbol{v} + \frac{1}{qB^2}\left(q(\boldsymbol{v} \times \boldsymbol{B}) + \boldsymbol{F}\right) \times \boldsymbol{B}\,.\end{aligned}$$

Using the vector relation

$$(\boldsymbol{v} \times \boldsymbol{B}) \times \boldsymbol{B} = (\boldsymbol{v}_\perp \times \boldsymbol{B}) \times \boldsymbol{B} = \boldsymbol{B}(\boldsymbol{v}_\perp \cdot \boldsymbol{B}) - \boldsymbol{v}_\perp(\boldsymbol{B} \cdot \boldsymbol{B}) = -\boldsymbol{v}_\perp B^2\,,$$

the guiding centre motion follows to be

$$\boldsymbol{v}_c = \boldsymbol{v}_\parallel + \frac{\boldsymbol{F} \times \boldsymbol{B}}{qB^2}\,.$$

The velocity of the guiding centre can be split into components perpendicular and parallel to the magnetic field,

$$\boldsymbol{v}_{c,\perp} = \frac{\boldsymbol{F}_\perp \times \boldsymbol{B}}{qB^2}, \qquad \frac{dv_{c,\parallel}}{dt} = \frac{F_\parallel}{m}\,. \tag{2.38}$$

Any force with perpendicular components to the magnetic field leads to a motion perpendicular to $\boldsymbol{B}$ and $\boldsymbol{F}$ with the velocity $\boldsymbol{v}_{c,\perp}$. If $\boldsymbol{F}_\perp$ is constant, $\boldsymbol{v}_{c,\perp}$ is also constant, which explains the term *drift* for this motion.

2.7.3 E × B drift, gravitational drift

The most important additional force is a constant electric force $\boldsymbol{F} = q\boldsymbol{E}$, which leads to a drift

$$\boldsymbol{v}_E = \frac{\boldsymbol{E} \times \boldsymbol{B}}{B^2}\,. \tag{2.39}$$

This drift velocity does not depend on the sign of the charge or the mass of the particles. Thus, the $\boldsymbol{E} \times \boldsymbol{B}$ drift leads to a macroscopic movement of a plasma. More insight into

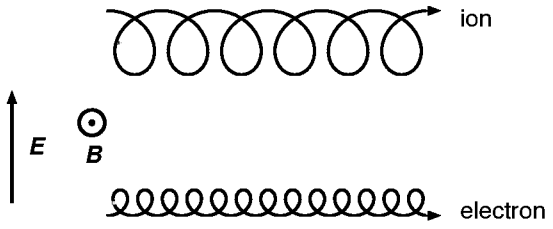

Figure 2.8: $\boldsymbol{E} \times \boldsymbol{B}$ *drift of ion and electron,* $v_E = E/B$.

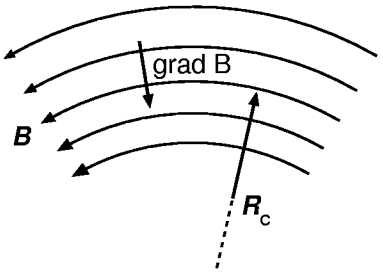

Figure 2.9: *Inhomogeneous magnetic field. Curvature radius and its relation to the field gradient in the absence of a plasma current* ($\nabla \times \boldsymbol{B} = 0$).

the $\boldsymbol{E} \times \boldsymbol{B}$ drift can be gained from Figure 2.8. If the particle accelerates in the electric field, the Larmor radius increases. On the other hand, if it slows down its Larmor radius decreases, leading to the non-closed trajectories shown in Figure 2.8. The net effect is a drift velocity perpendicular to the electric and magnetic fields.

Another drift is due to the gravitation field. If $F_g = mg$ is perpendicular to B, the drift velocity is $v_g = mg/(qB)$. Contrary to $\boldsymbol{E} \times \boldsymbol{B}$ drift, v_g leads to (slow) charge separation because the drift direction is of opposite sign for electrons and ions. This charge separation causes electric fields and subsequent $\boldsymbol{E} \times \boldsymbol{B}$ drifts and thereby points to the fundamental nature of the $\boldsymbol{E} \times \boldsymbol{B}$ drift. In laboratory plasmas, however, v_g is far to small to be of importance.

2.7.4 Particle drift in inhomogeneous magnetic fields

For spatially slowly varying magnetic fields, equation (2.38) can still be applied if the relative variation of B is small along one gyration of the particle. One important example is the particle drift in a magnetic field with a transverse gradient. The particle orbit has a smaller radius of curvature on that part of its orbit located in the stronger magnetic field. This leads to a drift perpendicular to both the magnetic field and its gradient. Quantitatively, the force on a particle with magnetic moment μ (see equation (2.36)) can be written as

$$\boldsymbol{F}_{\nabla B} = -\mu \nabla B \,,$$

leading to

$$\boldsymbol{v}_{\nabla B} = -\frac{m v_\perp^2}{2qB^3} (\nabla_\perp B) \times \boldsymbol{B} \,. \tag{2.40}$$

Let us consider a curved magnetic field in the case that the plasma current does not play a role, $\nabla \times \boldsymbol{B} = 0$ or, more generally, $\nabla \times \boldsymbol{B} \parallel \boldsymbol{B}$. As sketched in Figure 2.9, there is a correlation between the field gradient and the curvature radius R_c:

$$\frac{\boldsymbol{R}_c}{R_c^2} = -\frac{\nabla_\perp B}{B} \,. \tag{2.41}$$

Since the particles follow the curved magnetic field lines, a centrifugal force $\boldsymbol{F}_c = mv_\parallel^2 \boldsymbol{R}_c/R_c^2$ is exerted, which is responsible for the drift velocity

$$\boldsymbol{v}_R = \frac{mv_\parallel^2}{qB^2} \frac{\boldsymbol{R}_c \times \boldsymbol{B}}{R_c^2} . \tag{2.42}$$

Combination of equations (2.40), (2.41), and (2.42), yields

$$\boldsymbol{v}_R + \boldsymbol{v}_{\nabla B} = \frac{m}{q} \frac{\boldsymbol{R}_c \times \boldsymbol{B}}{R_c^2} (v_\parallel^2 + \tfrac{1}{2} v_\perp^2) .$$

In a very rough approximation $v_\parallel^2 + \frac{1}{2}v_\perp^2 \approx v^2$, i.e. the resulting drift is proportional to the particle energies.

As a first application of these drifts, consider the electrons and protons captured in the earth's magnetic field (trapping in a magnetic field will be discussed in the next section). Due to the gradient and curvature of the earth's magnetic field, these electrons and protons drift around the equator, the electrons from west to east and the protons in the opposite direction, producing the so-called electron current, shown in Figure 2.10.

2.7.5 The guiding centre equations in general geometry

In fusion plasmas the geometry of the magnetic field is usually very complex. Therefore, it is mandatory to derive the guiding centre equations rigorously for arbitrary geometry.

Most elegantly this was done by Littlejohn [16]. He showed, that the guiding centre equations can be derived from a generalized Lagrangian. We will outline the general idea and the results only. Littlejohn has shown that there is a non-canonical transformation such, that the particle motion can be expressed independently from the gyroangle α to arbitrary order in a small parameter $\epsilon_B = |\rho/L_B|$ (ρ is the gyro radius and $L_B = B/|\nabla B|$ is the scale length of the magnetic field). This set of phase space coordinates ($\boldsymbol{R}, V_\parallel, V_\perp$, or $\boldsymbol{R}, V_\parallel, \mu$) is called guiding centre coordinates. In this coordinates the magnetic moment constructed as

$$\mu = \frac{mV_\perp^2}{2ZeB(\boldsymbol{R})}$$

is conserved. Note, however, that the "true" $\mu = mv_\perp^2/(2ZeB)$ resulting from the velocity $v_\perp$ in the real space is not conserved in general.

To first order in ϵ_B and for $\frac{d}{\Omega dt} \ll 1$ the following results have been obtained assuming the set of independent variables to be $\vec{R}, V_\parallel, \mu$:

The time derivatives of $\boldsymbol{R}$, μ and $V_\parallel$ can be obtained from the well known Lagrangian formalism [16] with the single particle Lagrangian

$$L = Ze\boldsymbol{A}^* \cdot \dot{\boldsymbol{R}} + \frac{1}{Ze}\mu\dot{\alpha} - \frac{1}{2}mV_\parallel^2 - \mu B - Ze\phi \tag{2.43}$$

which gives the Euler-Lagrange equations

$$
\begin{aligned}
Ze(\boldsymbol{E}^* + \dot{\boldsymbol{R}} \times \boldsymbol{B}^*) &= m\dot{V}_\parallel \boldsymbol{b} + \mu \boldsymbol{\nabla} B && (2.44)\\
\dot{\mu} &= 0 && (2.45)\\
\dot{\alpha} &= \frac{ZeB}{m} && (2.46)\\
\dot{\boldsymbol{R}} \cdot \boldsymbol{b} &= V_\parallel. && (2.47)
\end{aligned}
$$

The modified field quantities are defined as in Littlejohns work [16]:

$$
\begin{aligned}
\boldsymbol{A}^* &= \boldsymbol{A} + \frac{m}{Ze} V_\parallel \boldsymbol{b} && (2.48)\\
\boldsymbol{B}^* &= \boldsymbol{B} + \frac{m}{Ze} V_\parallel \boldsymbol{\nabla} \times \boldsymbol{b} && (2.49)\\
\boldsymbol{E}^* &= -\boldsymbol{A}_t^* - \boldsymbol{\nabla}\phi && (2.50)\\
\boldsymbol{b} &= \frac{\boldsymbol{B}}{B}. && (2.51)
\end{aligned}
$$

Finally we are left with the following equations of motion

$$
\begin{aligned}
\dot{\boldsymbol{R}} &= \frac{1}{B_\parallel^*}\left[V_\parallel \boldsymbol{B}^* + \frac{1}{Ze}\boldsymbol{b} \times (\mu \boldsymbol{\nabla} B - Ze\boldsymbol{E}^*)\right] && (2.52)\\
\dot{V}_\parallel &= -\frac{1}{B_\parallel^*}\boldsymbol{B}^* \cdot (\mu \boldsymbol{\nabla} B - Ze\boldsymbol{E}^*) && (2.53)\\
\dot{\mu} &= 0 && (2.54)\\
\dot{\alpha} &= \Omega = \frac{ZeB}{m}. && (2.55)\\
& && (2.56)
\end{aligned}
$$

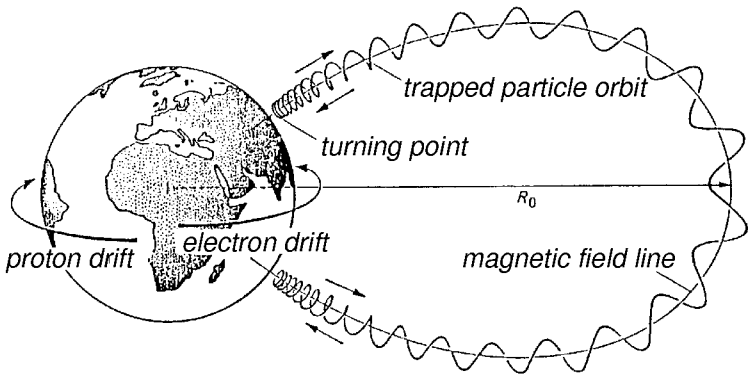

Figure 2.10: *Drifts of electrons and protons in the earth's magnetic field.*

2.8 Adiabatic invariants

It is well known from classical mechanics, that whenever a system has a periodic motion, the action integral $\oint p\,dq$ taken over a period is a constant of motion. Here p and

q are the generalized momentum and coordinate. If the fields in the system change slowly compared with the characteristic period and on a scale large compared with the characteristic length of the motion, then the quantity $\oint p\,dq$ remains constant, too, and is called an *adiabatic invariant.*

Adiabatic invariants play an important role in plasma physics. There are three adiabatic invariants, each corresponding to a different type of motion.

Indeed, the magnetic moment $\mu = mv_\perp^2/2B$ defined earlier is the first adiabatic invariant with respect to the motion of charged particles in an electromagnetic field. The periodic motion is the Larmor gyration, p is the angular momentum $m\,v_\perp\,r_g$, and the coordinate q is the angle θ. Considering the action integral yields

$$\oint p\,dq = \oint mv_\perp r_g\,d\theta = 2\pi\,r_g mv_\perp = 4\pi\,\frac{m}{q}\,\mu\,.$$

We see, that μ can change even for slowly varying fields if q/m changes due to ionization. For fusion plasmas this occurs preferentially at the plasma edge.

We have met this adiabatic invariance in the section before and take the opportunity to recall: For a constant and homogeneous magnetic field guiding centre coordinates and real space coordinates agree what implies that μ is strictly conserved. For inhomogeneous and time dependent magnetic fields we observe that μ is conserved to a certain order in the ordering parameters ϵ_B and $\frac{d}{\Omega dt}$ only. Littlejohn's result that a phase space transform exists which finds a redefined μ as a conserved quantity can be regarded as formal expression of the term "adiabatic invariance".

The invariance of μ is the basis for magnetic mirrors, which is schematically shown in Figure 2.11. The parallel velocity of a particle in a (spatially or temporally) varying magnetic field is determined by μ =constant and energy conservation $\frac{1}{2}mv^2$ =constant. The combination of these conditions, $\frac{1}{2}mv_\parallel^2 + \mu B$ =constant, reveals that $v_\perp$ increases with increasing B and hence $v_\parallel$ decreases. The criterion for particle reflection ($v_\parallel = 0$) at the high field ends of the mirror machine is

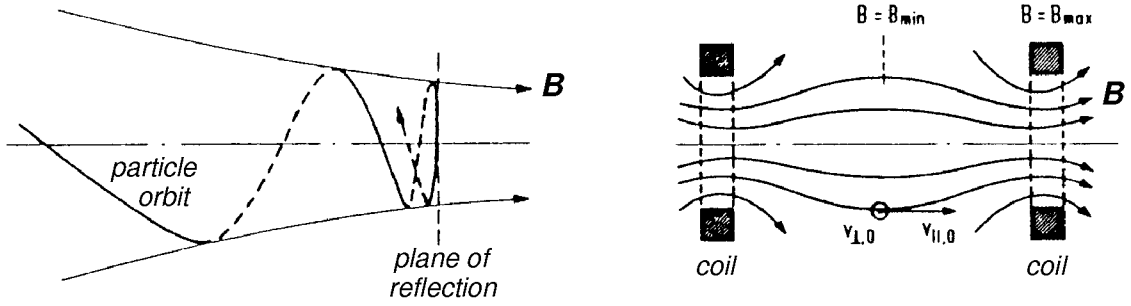

Figure 2.11: *Magnetic field lines of a simple axisymmetric magnetic mirror.*

$$\tfrac{1}{2}mv^2 = \tfrac{1}{2}mv_{\parallel,0}^2 + \mu B_{\min} \;\leq\; \mu B_{\max}\,, \tag{2.57}$$

where $v_{\parallel,0}$ is the parallel velocity in the low field region. If the mirror ratio is defined as $R = B_{\max}/B_{\min}$ and equation (2.57) is divided by $\mu B_{\min} = \frac{1}{2}mv_{\perp,0}^2$, the velocity ratio

$$\frac{v_{\parallel,0}}{v_{\perp,0}} \leq \sqrt{R-1} \tag{2.58}$$

describes the criterion for particle confinement. The earth's magnetic field is an example of a magnetic mirror. It forms two belts of confined charged particles originating from the solar wind (see Figure 2.10). Obviously, particles which do not meet the condition (2.58) are lost from magnetic mirrors. This so called "loss cone" in velocity space is refilled by collisions and therefore pure mirror configurations have a very poor plasma confinement.

The second or *longitudinal invariant* is

$$J = m \oint v_{\parallel}\, d\ell\,.$$

Consider a particle between two magnetic mirrors: It bounces between them and therefore has a periodic motion at the bounce frequency. A constant of this motion is $\oint m v_{\parallel}\, d\ell$ with ℓ being the length between two mirrors and $v_{\parallel}$ the longitudinal velocity. However, the motion is not exactly periodic, because the guiding centre drifts across field lines, and thus the constant of the motion becomes in general an adiabatic invariant. From this we can conclude that the particles will drift on $J = const.$ contours.

If this contours are closed the drift motion is also periodic and we observe another constant of motion – the so called third adiabatic invariant. Note, however, that to guarantee invariance the perturbations have to be even slower (see table) than the drift period. The third adiabatic invariant turns out to be the total magnetic flux Φ enclosed

Table 2.1: *characteristical times of motion for typical fusion parameters in a a stellarator reactor similar to W7-X: ($B = 5\,\mathrm{T}$, large radius: $20\,\mathrm{m}$, small radius $2\,\mathrm{m}$, $T = 15\,\mathrm{keV}$, $n = 3 \cdot 10^{20}\,\mathrm{m}^{-3}$)*

	gyration time τ_g	bounce time τ_{bounce}	drift time τ_{drift}
electrons	$\approx 7 \cdot 10^{-12}\,\mathrm{s}$	$\approx 10^{-6}\,\mathrm{s}$	$\approx 6 \cdot 10^{-2}\,\mathrm{s}$
deuterons	$\approx 3 \cdot 10^{-8}\,\mathrm{s}$	$\approx 10^{-4}\,\mathrm{s}$	$\approx 6 \cdot 10^{-2}\,\mathrm{s}$
α-particles	$\approx 3 \cdot 10^{-8}\,\mathrm{s}$	$\approx 3 \cdot 10^{-5}\,\mathrm{s}$	$\approx 10^{-4}\,\mathrm{s}$

by the drift surface. Obviously, the particles will stay on a surface such that the total number of lines of force enclosed remains constant as $\boldsymbol{B}$ varies. This invariant has few applications because most fluctuations of $\boldsymbol{B}$ occur on a time scale short compared with the drift period.

Appendix A

The following table provides you with characteristic plasma parameters and their numerical value for typical fusion plasmas, namely $T_e = T_i = 10^4\,\mathrm{eV}$, $Z = 1$, and $n_e = n_i = 10^{20}\,\mathrm{m}^{-3}$, $B = 5\,\mathrm{T}$ for magnetically-confined experiments and $n_e = n_i = 10^{31}\,\mathrm{m}^{-3}$ for inertially-confined experiments (see also Chapter 15). It is $a = e^4 \ln\Lambda/(6\pi\varepsilon_0^2)$.

Name	Formula	Magnetic fusion	Inertial fusion
Average distance	$\overline{r} \approx (\frac{4}{3}\pi n)^{-1/3}$	$0.2\ \mu\mathrm{m}$	$3 \times 10^{-11}\,\mathrm{m}$
Debye length	$\lambda_D = \sqrt{\varepsilon_0\, k_B T/(n_e e^2)}$	$75\ \mu\mathrm{m}$	$2.4 \times 10^{-10}\,\mathrm{m}$
Landau length	$\lambda_L = e^2/(\pi\varepsilon_0\, k_B T)$	$10^{-13}\,\mathrm{m}$	$10^{-13}\,\mathrm{m}$
de Broglie length	$\lambda_{\mathrm{dB}} = \hbar/(\sqrt{m_e k_B T})$	$3 \times 10^{-12}\,\mathrm{m}$	$3 \times 10^{-12}\,\mathrm{m}$
Mean free path	$\lambda_{qk} = v_{th,q}\tau_{qk}$	$15\,\mathrm{km}$	$150\,\mathrm{nm}$
Larmor radius	$\rho_{L,q} = m_q v_\perp/(\lvert q\rvert B)$	$67\ \mu\mathrm{m}$ (e), $4.1\,\mathrm{mm}$ (i)	
Thermal velocity	$v_{th,q} = \sqrt{3k_B T_q/m_q}$	$7.3 \times 10^7\,\mathrm{m/s}$ (e), $1.7 \times 10^6\,\mathrm{m/s}$ (i)	$7.3 \times 10^7\,\mathrm{m/s}$ (e), $1.7 \times 10^6\,\mathrm{m/s}$ (i)
Plasma frequency	$\omega_{p,e} = \sqrt{n_e e^2/\varepsilon_0\, m_e}$	$600\,\mathrm{GHz}$	$2 \times 10^{17}\,\mathrm{Hz}$
Cyclotron frequency	$\omega_{c,q} = \lvert q\rvert B/m_q$	$900\,\mathrm{GHz}$ (e), $0.5\,\mathrm{GHz}$ (i)	
Electron collision time	$\tau_{ee} = \frac{\sqrt{3}}{a}\sqrt{m_e} n_e^{-1} (k_B T_e)^{3/2}$	$140\ \mu\mathrm{s}$	$5.4 \times 10^{-15}\,\mathrm{s}$
Ion collision time	$\tau_{ii} = \frac{\sqrt{3}}{aZ^4}\sqrt{m_i} n_i^{-1} (k_B T_i)^{3/2}$	$6\,\mathrm{ms}$	$2.3 \times 10^{-13}\,\mathrm{s}$
Electrical resistance	$\eta = m_e/(n_e e^2 \tau_{ei}^E)$	$1 \times 10^{-9}\,\Omega\,\mathrm{m}$	$3 \times 10^{-10}\,\Omega\,\mathrm{m}$
Plasma parameter	$N_D = \frac{4}{3}\pi\, n\, \lambda_D^3$	2×10^8	500
Coulomb logarithm	$\ln\Lambda = \ln\left(\frac{9}{\sqrt{2}} N_D\right)$	17	4.4
Hall parameter	$x_q = \omega_{c,q}\tau_{qq}$	1×10^8 (e), 3×10^6 (i)	

Bibliography

[1] Y. Eliezer and S. Eliezer: *The Fourth State of Matter*, Bristol: Hilger (1989).

[2] N.A. Krall and A.W. Trivelpiece: *Principles of Plasma Physics*, New York: McGraw-Hill (1973).

[3] F.F. Chen: *Introduction to Plasma Physics*, New York: Plenum Press (1974).

[4] G. Schmidt: *Physics of High Temperature Plasmas*, New York: Academic Press (1979).

[5] R.B. White: *Theory of Tokamak Plasmas*, Amsterdam: North-Holland (1989).

[6] R.D. Hazeltine and J.D. Meiss: *Plasma Confinement*, Redwood: Addison-Wesley (1992).

[7] B. B. Kadomtsev: *Tokamak Plasma: A Complex Physical System*, Bristol: IOP Publ. (1992).

[8] P.A. Sturrock: *Plasma Physics*, Cambridge: Cambridge University Press (1994).

[9] R.J. Goldston and P.H. Rutherford: *Introduction to Plasma Physics*, Bristol: IOP Publ. (1995).

[10] J.A. Bittencourt: *Fundamentals of Plasma Physics*, Oxford: Pergamon Press (2nd ed, 1995).

[11] J.A. Wesson: *Tokamaks*, Oxford: Oxford University Press (2nd ed, 1997).

[12] K. Miyamoto: *Fundamentals of Plasma Physics and Controlled Fusion*, Tokyo: Iwanami Press (1997).

[13] M.N. Saha: *On a Physical Theory of Stellar Spectra*, Proc. Roy. Soc. **A99** (1921) 135.

[14] D.L. Book: *NRL Plasma Formulary*, Washington: Naval Research Laboratory (1990).

[15] L. Spitzer, Jr., and R. Härm: *Transport Phenomena in a Completely Ionized Gas*, Phys. Rev. **89** (1953) 977.

[16] R. G. Littlejohn, J. Plasma Phys. **29**, 302 (1983).

[17] L. D. Landau, E. M. Lifshitz, Course in Theoretical Physics Vol 1: Mechanics, Butterworth-Heinemann (1982)

Chapter 3

An Introduction to MHD

Bruce D. Scott

3.1 What MHD is

Magneto-hydro-dynamics (MHD) means magnetic fluid dynamics. It is a model system designed to treat macroscopic dynamics of an electrically neutral fluid which is nevertheless made up of moving charged particles, and hence reacts to magnetic fields. Because the magnetic field is in turn produced by electric currents — here, a relative drift between the two fluids of opposite charge density which permeate each other — the resulting dynamical system is rich in nonlinear character.

This is a heuristic introduction to the ideas of fluid dynamics and MHD. Each fluid — they may be termed electrons and ions — is separately treated as a perfect fluid which reacts in a dissipation-free way to the electric and magnetic fields. By perfect fluid, the concept of thermodynamic equilibrium is implied: the effects of dissipation in all forms are taken to be negligible. These include resistivity, thermal conductivity, and viscosity. The two fluids interact only through the electric and magnetic fields they induce. These fields in turn react to changes in the distribution of sources, which are the charge densities and currents represented by the two fluids. Externally imposed fields may also be present. An infinitesimal element of each fluid is assumed to contain an arbitrarily large number of charged particles of the corresponding species, but to be small compared to the spatial scale over which macroscopic thermodynamic or field quantity varies. The picture is a meaningful one if this scale is large compared to the mean-free path between particle collisions, and the radius of gyration of each particle about magnetic field lines is negligibly small. This is the "ideal two-fluid model" of plasma dynamics.

Then, because the mass of an individual electron is so much smaller than that of an individual ion, the contribution of the electrons to fluid inertia may be neglected. With a few additional assumptions which in effect define a parameter regime, the system is treated as a single fluid which responds to a magnetic force of the Lorentz type, except that the plasma current enters instead of the fluid velocity. The magnetic field,

responding to the electric field as usual, is actually advected by the velocity field, since the latter is related in a constitutive way to the electric field. This is the "ideal MHD model" of plasma dynamics, a subset of the two-fluid model.

3.2 The Ideas of Fluid Dynamics

A fluid is in essence a continuous medium. Rather than an ensemble of particles, each individually treated, *populations* of particles are treated. The system is described in terms of a velocity flow field, a density field, and a few thermodynamic state variables. In the simplest picture, the fluid is an ideal gas, in which all state variables are simple relations of the density and temperature.

3.2.1 The density in a changing flow field — conservation of particles

We are first interested in how the density of the fluid evolves, when the flow field is known. This involves the deformation of volumes by the flow. Consider first a volume, V, which is fixed in space. The conservation of particles follows simply from counting: the change of the number of particles, N, in V is given by the number of particles entering V, less those that leave V. Consider that V is bounded by a surface, S, an element of which is ΔS with unit normal $\hat{\mathbf{e}}_\mathbf{S}$. For each area element, the number of particles which cross it in a time interval, Δt, is given by

$$\delta N = n\,\Delta x\,\Delta S\,\Delta t, \qquad \Delta x = v\cos\theta\,\Delta t = \mathbf{v}\cdot\hat{\mathbf{e}}_\mathbf{S}\,\Delta t,$$

where $n = N/V$ is the density of particles per unit volume, θ is the angle between the velocity vector and the unit normal, and Δx gives the thickness of the region containing particles which cross ΔS during Δt (a note on signs: the unit normal points outward, so a positive δN, indicating particles leaving V, contributes negatively to the change in the total number of particles, ΔN).

Since S is a closed surface, we may add up all the contributions from the ΔS's by performing a surface integral:

$$\Delta N = -\oint_S \Delta S\, n\mathbf{v}\cdot\hat{\mathbf{e}}_\mathbf{S}\,\Delta t.$$

Since V is fixed, a change in N affects the density:

$$\Delta N = \oint_V dV\,\Delta n,$$

so upon setting these two expressions equal, we have

$$\oint_V dV\,\Delta n = -\oint_S \mathbf{dS}\cdot(n\mathbf{v})\,\Delta t,$$

where ΔS and $\hat{\mathbf{e_S}}$ have been combined into $\mathbf{dS}$. Note now that since S is the surface which encloses V, we may apply the Gaussian divergence theorem:

> For any volume V enclosed by surface S, with directional element $\mathbf{dS}$, any continuously differentiable vector $\mathbf{F}$ satisfies
>
> $$\oint_V dV\, \nabla \cdot \mathbf{F} = \oint_S \mathbf{dS} \cdot \mathbf{F}.$$

Therefore, we may write:

$$\oint_V dV\, \Delta n = -\Delta t \oint_V dV\, \nabla \cdot n\mathbf{v}.$$

This is valid for arbitrary V; specifically, it is valid for an infinitesimal volume about any point. This means the integrands must themselves be equal, since in general they do not vanish. Further taking $\Delta t \to 0$, we obtain

$$\frac{\partial n}{\partial t} = -\nabla \cdot n\mathbf{v}$$

as a statement of conservation of particles of number density n, advected by velocity $\mathbf{v}$. It holds for a *fixed* reference frame. The partial time derivative refers to the fact that V is fixed in space.

So what is meant by divergence?

Suppose now that we take the same flow and particle distribution, but now let the boundary surface elements of the volume move with the fluid. Note now that no particles enter or leave V:

$$\Delta N = 0.$$

The volume does, however, change with time: since the density is given by $n = N/V$, its change is inverse to that in V:

$$\frac{\Delta n}{n} = -\frac{\Delta V}{V}.$$

At each point, the boundary element moves with the velocity:

$$\Delta \mathbf{x} = \mathbf{v}\Delta t.$$

The separation of points changes according to spatial variations in the velocity:

$$\Delta \mathbf{x}_2 - \Delta \mathbf{x}_1 = (\mathbf{v}_2 - \mathbf{v}_1)\Delta t.$$

A volume may be expanded in a combination of two ways: spreading or stretching. If the direction of a surface element $\mathbf{dS}$ is taken as the z-direction at some point, spreading is due to the expansion perpendicular to the element: $\partial v_x/\partial x + \partial v_y/\partial y$. Stretching is due

to longitudinal variation: $\partial v_z/\partial z$. The sum of these is called the "divergence", and the divergence of a velocity means the same thing as the expansion of the advected volume:

$$\Delta V = V\nabla \cdot (\Delta \mathbf{x}),$$

or, including Δt, which commutes with spatial derivatives,

$$\frac{\Delta V}{\Delta t} = V\nabla \cdot \frac{\Delta \mathbf{x}}{\Delta t} = V\nabla \cdot \mathbf{v}.$$

With this for the volume change, the density change is given by

$$\frac{\Delta n}{\Delta t} = -\frac{n}{V}\frac{\Delta V}{\Delta t} = -n\nabla \cdot \mathbf{v},$$

or

$$\frac{dn}{dt} = -n\nabla \cdot \mathbf{v},$$

as a statement of conservation of particles of number density n, advected by velocity $\mathbf{v}$. It holds for the "co-moving" reference frame. Note that the total time derivative, d/dt, gives changes in the frame moving with the fluid at each point, hence the name co-moving.

One final note: a common name for the equation for the conservation of particles is often called the "continuity equation", since the fact that n and $\mathbf{v}$ are continuously differentiable field quantities has been implicitly used to get it.

3.2.2 The advective derivative and the co-moving reference frame

We now have two statements of the general conservation of particles in terms of the density, n, and the velocity with which they are advected, $\mathbf{v}$. One is in the fixed reference frame:

$$\frac{\partial n}{\partial t} = -\nabla \cdot n\mathbf{v}.$$

The other is in the co-moving reference frame:

$$\frac{dn}{dt} = -n\nabla \cdot \mathbf{v}.$$

These are actually the same statement in two different coordinate systems. Let the fixed system be denoted as (t, x, y, z) and the co-moving frame as (t', x', y', z'). The transformation between them, which is a *local* transformation, may be written:

$$dx' = dx - v_x dt, \qquad dy' = dy - v_y dt, \qquad dz' = dz - v_z dt.$$

The time derivative transforms as

$$\frac{d}{dt} = \frac{\partial}{\partial t} + \frac{dx}{dt}\frac{\partial}{\partial x} + \frac{dy}{dt}\frac{\partial}{\partial y} + \frac{dz}{dt}\frac{\partial}{\partial z}$$

$$= \frac{\partial}{\partial t} + v_x \frac{\partial}{\partial x} + v_y \frac{\partial}{\partial y} + v_z \frac{\partial}{\partial z}$$

where the velocity components are not differentiated because the transformation is local. In general form,

$$\frac{d}{dt} = \frac{\partial}{\partial t} + \mathbf{v} \cdot \nabla.$$

This is the time derivative in the co-moving frame, written in terms of the time derivative in the fixed frame and the local, instantaneous velocity. It is also known as the "advective derivative", or in some texts the substantiative derivative. Its usefulness is that the laws governing the motion or constitutive change of fluid elements are often most easily formulated in the co-moving frame (or the fluid element's rest frame) and then transformed into the fixed frame. One can readily see that the two equations for the fluid density are equivalent.

3.2.3 Forces on the fluid — how the velocity changes

We now allow the velocity to change, and see how it is caused to change. We examine the forces on the fluid element in the co-moving frame, and then transform to the fixed frame. We consider only fluid pressure and electromagnetic (Lorentz) forces, neglecting such others as gravitation or the effects of moving boundaries.

Consider first the fluid pressure, p. Each of the fluid particles is moving with a velocity, $\mathbf{w}$, in the co-moving frame, and the average of $\mathbf{w}$ over all the particles in a fluid element is zero. Nevertheless, the fluid exerts pressure on any surface, according to the rate at which momentum is transferred by the random particle motion. If p is prescribed, we may compute the net force, $\mathbf{F}$, on any fluid element by adding up the forces, $\Delta\mathbf{F}$, on each surface element, $\mathbf{dS}$:

$$\Delta\mathbf{F} = p\,\mathbf{dS}.$$

Summing all the force elements over a closed surface gives an area integral:

$$\mathbf{F} = \oint_S \mathbf{dS}\, p.$$

Since the force is exerted on the enclosed volume, V, we may apply another vector theorem:

> For any volume V enclosed by surface S, with directional element $\mathbf{dS}$, any continuously differentiable scalar ζ satisfies
>
> $$\oint_V dV\, \nabla\zeta = \oint_S \mathbf{dS}\, \zeta.$$

It is important to get the correct sign: the force is exerted against the surface from the surrounding fluid; hence the signs in the above should all be negative (except for the theorem). Considering a cubical fluid element, oriented such that the pressure on the

right is higher than that on the left: the forces on the top and bottom are equal and opposite, the forces on the front and back are equal and opposite, but the force from the right towards the left is greater that the force from the left toward the right. There is a net force from right to left, given by the pressure difference, $\Delta p = p_{\rm right} - p_{\rm left}$, times the surface area, ΔS. If the coordinates are set up such that z increases towards the right, we can see that the force from right to left is *opposite* to the directional gradient in the pressure. Since the size of the element is Δz, then the force is given by

$$\mathbf{F} = -\Delta p\,\Delta S\,\hat{\mathbf{e}_z} = -\Delta z\,\Delta S\,(\Delta p/\Delta z)\hat{\mathbf{e}_z} = -\Delta V\,\nabla p \rightarrow -\oint_V dV\,\nabla p$$

This force acts to accelerate the fluid element. The mass in the element is given by the mass of each particle, m, times the number of particles, N, in the volume V. The element accelerates according to

$$Nm\frac{d\mathbf{v}}{dt} = \mathbf{F},$$

or taking the volume to zero about a given point, the velocity change can be taken inside the integral:

$$\oint_V dV\,nm\frac{d\mathbf{v}}{dt} = -\oint_V dV\,\nabla p.$$

Dispensing with the volumes as before, we obtain

$$nm\frac{d\mathbf{v}}{dt} = -\nabla p,$$

in the co-moving frame, and

$$nm\left(\frac{\partial}{\partial t} + \mathbf{v}\cdot\nabla\right)\mathbf{v} = -\nabla p,$$

in the fixed frame.

This is the force law which determines how the fluid velocity field changes in reaction to gradients in its pressure. Standing alone, it is the force law for a neutral fluid.

Adding the Lorentz force is straightforward, since the force is a body force, one which acts on the element as a whole and not through the surface. The force on N particles of charge q in the fixed frame is

$$\mathbf{F} = Nq\left(\mathbf{E} + \frac{\mathbf{v}}{c}\times\mathbf{B}\right) = \oint_V dV\,nq\left(\mathbf{E} + \frac{\mathbf{v}}{c}\times\mathbf{B}\right),$$

so that the integrand is added to the neutral fluid force law to obtain the force law for a charged fluid:

$$nm\left(\frac{\partial}{\partial t} + \mathbf{v}\cdot\nabla\right)\mathbf{v} = -\nabla p + nq\left(\mathbf{E} + \frac{\mathbf{v}}{c}\times\mathbf{B}\right).$$

Note that one could just as easily derive the Lorentz force term in the co-moving frame as well, with $\mathbf{v}$ zero, and then transform to the fixed frame via the Lorentz transformation (the low-velocity form of which is the transformation used in Section 1B).

We now have equations describing the evolution of the density and velocity of a fluid in general, so we could build up the two-fluid system consisting of one set of these for each species, and then close the system with Maxwell's equations for the electric and magnetic fields. This would only be complete for an isothermal system, though, so we do need to discuss how the pressure changes.

3.2.4 Thermodynamics of an ideal fluid — how the temperature changes

The simplest system is the ideal fluid: one which evolves quasi-statically through successive states of local thermodynamic equilibrium. Changes are expected to be slow enough such that equilibrium is maintained, but fast enough so that fluid elements do not exchange entropy.

In thermodynamic equilibrium with only isentropic changes considered, the first law reads:

$$\Delta E + p\,\Delta V = \Delta Q \to 0.$$

E is the internal energy of a given fluid element of N particles. For the ideal gas law,

$$E = \frac{3}{2}NkT.$$

V is the volume occupied by the N particles. Over infinitesimal time intervals,

$$\frac{dE}{dt} + p\frac{dV}{dt} = 0,$$

in the co-moving frame.

We already know how the volume changes:

$$\frac{dV}{dt} = V\nabla \cdot \mathbf{v}.$$

Given that the number of particles is kept fixed,

$$\frac{3}{2}Nk\frac{dT}{dt} + pV\nabla \cdot \mathbf{v} = 0,$$

and since the density is $n = N/V$,

$$\frac{3}{2}nk\frac{dT}{dt} + p\nabla \cdot \mathbf{v} = 0.$$

Now, transforming to the fixed frame, we have the relation governing the change of the fluid's temperature given the flow field and all the thermodynamic state variables:

$$\frac{3}{2}nk\left(\frac{\partial T}{\partial t} + \mathbf{v} \cdot \nabla T\right) + p\nabla \cdot \mathbf{v} = 0.$$

3.2.5 The composite fluid plasma system

Under the preceding conditions: perfect fluid with an ideal gas law, no reactions that create or destroy particles of any species, maintenance of local thermodynamic equilibrium...

The system of several fluids each made up of charged particles of species α evolves according to

$$\begin{aligned}
\frac{\partial n_\alpha}{\partial t} + \nabla \cdot n_\alpha \mathbf{v}_\alpha &= 0, \\
n_\alpha m_\alpha \left(\frac{\partial}{\partial t} + \mathbf{v}_\alpha \cdot \nabla \right) \mathbf{v}_\alpha &= -\nabla p_\alpha + n_\alpha q_\alpha \left(\mathbf{E} + \tfrac{\mathbf{v}_\alpha}{c} \times \mathbf{B} \right), \\
\frac{3}{2} n_\alpha k \left(\frac{\partial T_\alpha}{\partial t} + \mathbf{v}_\alpha \cdot \nabla T_\alpha \right) &\quad + p_\alpha \nabla \cdot \mathbf{v}_\alpha = 0,
\end{aligned}$$

while the electric and magnetic fields evolve according to Maxwell's equations:

$$\begin{aligned}
\nabla \cdot \mathbf{E} &= 4\pi \textstyle\sum_\alpha n_\alpha q_\alpha, \\
\frac{1}{c} \frac{\partial \mathbf{E}}{\partial t} &= \nabla \times \mathbf{B} - \tfrac{4\pi}{c} \textstyle\sum_\alpha n_\alpha q_\alpha \mathbf{v}_\alpha,
\end{aligned}$$

$$\begin{aligned}
\nabla \cdot \mathbf{B} &= 0, \\
\frac{1}{c} \frac{\partial \mathbf{B}}{\partial t} &= -\nabla \times \mathbf{E}.
\end{aligned}$$

Note that the charge density and the current have been specified in terms of the fluid variables:

$$\rho_{ch} = \sum_\alpha n_\alpha q_\alpha, \qquad \mathbf{J} = \sum_\alpha n_\alpha q_\alpha \mathbf{v}_\alpha,$$

The above constitutes a closed system governing the evolution of several charged ideal fluids and the electric and magnetic fields they induce. Note that external fields may also be imposed.

3.3 From Many to One — the MHD System

In many cases, the regime of parameters in which the plasma finds itself allows considerable simplification of the multi-fluid system. The fact that the electron mass is so much smaller than that of any ion allows one to neglect the electron inertia in comparison to that of the ions, with the result that the electron force equation becomes a relation for the electric field in terms of the velocity and magnetic field.

For purposes of illustration it is useful to consider that there is only one ion species.

The following assumptions are made: (1) The "displacement current", which is the term involving the time derivative of $\mathbf{E}$, is negligible because the time for a light wave to cross the system is much shorter than any relevant dynamical scale. (2) The electron mass is sufficiently small that parallel force balance on the electrons is maintained at all times. This allows the neglect of electron inertia. For the ideal MHD system we assume that the parallel electron dynamics are generally negligible; this means the components of both ∇p_e and $\mathbf{E}$ parallel to the magnetic field. (3) The drift velocity of the electrons relative

to the ions due to the current is small compared to the ion velocity. This allows one to assume that all species move with the same velocity, when specifying velocities. (4) Pressure forces are negligible compared to Lorentz forces on all the fluids. (5) The system is approximately neutral, such that the total charge density is negligible compared to that of any constituent. Note that this does not mean that $\mathbf{E} \to 0$, but that the spatial scale of any variation is large compared to the Debye length of the plasma, and that the plasma frequency is faster than any rate of change. This means, however, that we can use the relation of zero charge density as a good approximation for the electron density in terms of the ions. For one ion species with charge Ze, this means

$$n_e \approx Z n_i.$$

These assumptions will be checked once we explore the dynamical scales of the MHD system.

3.3.1 The MHD force equation

The electron and ion force equations appear as

$$\begin{aligned} n_i M_i \left(\frac{\partial}{\partial t} + \mathbf{v}_i \cdot \nabla\right) \mathbf{v}_i &= -\nabla p_i + n_i Z e \left(\mathbf{E} + \tfrac{\mathbf{v}_i}{c} \times \mathbf{B}\right), \\ 0 &= -\nabla p_e - n_e e \left(\mathbf{E} + \tfrac{\mathbf{v}_e}{c} \times \mathbf{B}\right), \end{aligned}$$

Adding these and using the charge neutrality relation, we obtain

$$\rho \left(\frac{\partial}{\partial t} + \mathbf{v} \cdot \nabla\right) \mathbf{v} = -\nabla p + \frac{1}{c} \mathbf{J} \times \mathbf{B}.$$

This is the MHD force equation. To get it, we have written p for the total pressure, $p = p_e + p_i$, and $\rho = n_i M_i$ for the mass density. We have further dropped the subscript on the ion velocity, using this as the bulk fluid velocity. The electron velocity is obtainable from $\mathbf{v}$ and $\mathbf{J}$. Note that the current is

$$\mathbf{J} = n_i Z e v_i - n_e e v_e.$$

The electrons have two roles: (1) They provide pressure, and can be dominant in doing so (but only if the temperatures are allowed to be unequal). (2) They keep the system quasi-neutral through their ability to move arbitrarily fast along the magnetic field lines.

3.3.2 Treating several ion species

One can easily generalise the MHD force equation to a system of several ion species by defining the total velocity as the velocity of the "center of mass":

$$\rho \mathbf{v} = \sum_i n_i M_i \mathbf{v}_i,$$

where the sum is over all the ion species. The mass density evolves according to the continuity equations for all ion species:

$$\frac{\partial \rho}{\partial t} + \nabla \cdot \rho \mathbf{v} = 0.$$

Provided all the temperatures are equal, this can be done for the energy equation as well:

$$C_v \left(\frac{\partial}{\partial t} + \mathbf{v} \cdot \nabla \right) T + p \nabla \cdot \mathbf{v} = 0,$$

where the specific heat at constant volume is

$$C_v = \frac{3}{2} k \sum_\alpha n_\alpha,$$

and the sum is over all species, including the electrons. Alternatively, this may be combined with the continuity equation to reflect the fact that p/ρ^γ, with $\gamma = 5/3$, is conserved in the dynamics, even for several species (see below).

One very important note: the system can be treated as ideal either if the heat exchange among the particle populations is (1) negligible or (2) so fast that the temperatures are all kept equal. In laboratory plasmas the first of these limits is usually well-satisfied for dynamics, and the second is usually valid for quasi-static equilibria.

3.3.3 The MHD kinematic equation

We need now only determine how the magnetic field evolves, and since the current is given by

$$\mathbf{J} = \frac{c}{4\pi} \nabla \times \mathbf{B},$$

that will be enough to close the system.

The magnetic field evolves according to

$$\frac{1}{c} \frac{\partial \mathbf{B}}{\partial t} = -\nabla \times \mathbf{E},$$

and from the electron force equation we have

$$\mathbf{E} + \frac{\mathbf{v}_e}{c} \times \mathbf{B} = -\frac{1}{n_e e} \nabla p_e.$$

For the dynamical scales of interest, it will become clear that the pressure gradient is negligibly small in this equation (recall we are neglecting parallel electron dynamics). This is assumption (4) above. We have already assumed that $\mathbf{J}$ is small enough that the electron and ion velocities are equal to high accuracy (assumption 3). This implies that the component of the fluid velocity across the magnetic field is given by the "E-cross-B velocity":

$$\mathbf{v} = \frac{c}{B^2} \mathbf{E} \times \mathbf{B},$$

which means that all the particles E-cross-B drift together across the magnetic field lines, preventing any significant charge build-up. Substituting for **E** in the equation for **B**, we obtain

$$\frac{\partial \mathbf{B}}{\partial t} = \nabla \times (\mathbf{v} \times \mathbf{B}).$$

This is the MHD kinematic equation. Whether or not the magnetic field has important effect on the dynamics, it describes how the magnetic field is advected by the flow velocity. Much of the character of MHD springs from this equation, especially its most important consequence: flux conservation. We will see what this is and what it means in a moment.

3.3.4 MHD at a glance

The complete ideal MHD system is collected here for clarity.

The continuity equation:

$$\frac{\partial \rho}{\partial t} + \nabla \cdot \rho \mathbf{v} = 0.$$

The MHD force equation:

$$\rho \left(\frac{\partial}{\partial t} + \mathbf{v} \cdot \nabla \right) \mathbf{v} = -\nabla p + \frac{1}{c} \mathbf{J} \times \mathbf{B}.$$

The adiabatic pressure equation:

$$\left(\frac{\partial}{\partial t} + \mathbf{v} \cdot \nabla \right) p + \frac{5}{3} p \nabla \cdot \mathbf{v} = 0.$$

The MHD kinematic equation:

$$\frac{\partial \mathbf{B}}{\partial t} = \nabla \times (\mathbf{v} \times \mathbf{B}).$$

Ampere's law:

$$\mathbf{J} = \frac{c}{4\pi} \nabla \times \mathbf{B}.$$

3.3.5 The Flux Conservation Theorem of Ideal MHD

There is an important result that arises immediately from the MHD kinematic equation. This is that the magnetic flux through any surface element advected by the fluid remains constant no matter what the flow field. Closely related is that the flux through the surface defined by any closed curve within the fluid is also conserved. The result gives rise to the concept of the magnetic flux tube.

3.3.6 Proving flux conservation

Consider an arbitrary, infinitesimal surface defined by a triangle of infinitesimal sides. Three points, $\mathbf{x}_0$, $\mathbf{x}_1$, $\mathbf{x}_2$, are given, and the surface element is

$$\mathbf{dS} = \frac{1}{2}(\mathbf{x}_1 - \mathbf{x}_0)\times(\mathbf{x}_2 - \mathbf{x}_1).$$

The magnetic flux through the surface is given by $\mathbf{B}\cdot\mathbf{dS}$, and it changes according to

$$\frac{d}{dt}\mathbf{B}\cdot\mathbf{dS} = \frac{d\mathbf{B}}{dt}\cdot\mathbf{dS} + \mathbf{B}\cdot\frac{d}{dt}\mathbf{dS}.$$

Remembering that the surface and magnetic field are advected by the fluid,

$$\frac{d\mathbf{B}}{dt} = \frac{\partial\mathbf{B}}{\partial t} + \mathbf{v}\cdot\nabla\mathbf{B}.$$

Now find how the surface element changes:

$$\frac{d}{dt}\mathbf{dS} = (\mathbf{x}_1 - \mathbf{x}_0)\times\frac{1}{2}(\mathbf{v}_2 - \mathbf{v}_1) + \frac{1}{2}(\mathbf{v}_1 - \mathbf{v}_0)\times(\mathbf{x}_2 - \mathbf{x}_1),$$

noting that $d\mathbf{x}/dt = \mathbf{v}$. Reform this in terms of contributions to $\Delta\mathbf{x}\times\mathbf{v}$:

$$\begin{aligned}\frac{d}{dt}\mathbf{dS} &= -(\mathbf{x}_1 - \mathbf{x}_0)\times\tfrac{1}{2}(\mathbf{v}_1 + \mathbf{v}_0) - (\mathbf{x}_2 - \mathbf{x}_1)\times\tfrac{1}{2}(\mathbf{v}_2 + \mathbf{v}_1)\\ &\quad - (\mathbf{x}_0 - \mathbf{x}_2)\times\tfrac{1}{2}(\mathbf{v}_0 + \mathbf{v}_2)\\ &= -\textstyle\sum_j \Delta\mathbf{x}_j\times\mathbf{v}_j,\end{aligned}$$

where j tracks the midpoint of each line segment. Employ a vector identity to replace this expression by

$$\frac{d}{dt}\mathbf{dS} = -(\mathbf{dS}\times\nabla)\times\mathbf{v}.$$

We require to further re-form this; using the component-index representation of the right side, we have

$$\begin{aligned}[(\mathbf{dS}\times\nabla)\times\mathbf{v}]_i &= \epsilon_{ipq}(\epsilon_{plm}\,\Delta S_l\,\partial_m)\,v_q\\ &= \epsilon_{pqi}(\epsilon_{plm}\,\Delta S_l\,\partial_m)\,v_q\\ &= \Delta S_q\,\partial_i\,v_q - \Delta S_i\,\partial_q\,v_q,\end{aligned}$$

which may be written in vector form as

$$\frac{d}{dt}\mathbf{dS} = \mathbf{dS}(\nabla\cdot\mathbf{v}) - (\nabla\mathbf{v})\cdot\mathbf{dS}.$$

Inserting this back into the original expression for the flux evolution, obtain

$$\begin{aligned}\frac{d}{dt}\mathbf{B}\cdot\mathbf{dS} &= \left(\tfrac{\partial\mathbf{B}}{\partial t} + \mathbf{v}\cdot\nabla\mathbf{B}\right)\cdot\mathbf{dS} + \mathbf{B}\cdot\left[\mathbf{dS}(\nabla\cdot\mathbf{v}) - (\nabla\mathbf{v})\cdot\mathbf{dS}\right]\\ &= \mathbf{dS}\cdot\left(\tfrac{\partial\mathbf{B}}{\partial t} + \mathbf{v}\cdot\nabla\mathbf{B} - \mathbf{B}\cdot\nabla\mathbf{v} + \mathbf{B}\nabla\cdot\mathbf{v}\right)\\ &= \mathbf{dS}\cdot\left(\tfrac{\partial\mathbf{B}}{\partial t} - \nabla\times\mathbf{v}\times\mathbf{B}\right) = 0,\end{aligned}$$

since the expression in parentheses vanishes according to the MHD kinematic equation.

This proves the flux conservation theorem for an infinitesimal surface element advected by the fluid. It follows that the flux through any *surface* advected by the fluid is also conserved; simply add up all the surface elements.

3.3.7 Magnetic flux tubes

As a result of the fact that the magnetic flux through any surface advected by the fluid is conserved, we may find a group of field lines which serve as the boundary for a definite volume. Define a closed curve which is the boundary for a small but finite surface, the magnetic flux through which is not zero. Follow each field line an arbitrary distance away from the original curve, and define another curve which intersects the same field lines. This is a "magnetic flux tube". Note that the magnetic flux through the sides of the tube is zero, and because the flux is conserved it stays zero.

Under advection of a flow which deforms the flux tube, the identity of the flux tube is maintained, even though the flux tube may be very greatly twisted and tangled with several other flux tubes. The consequence of this is that the field line topology is not allowed to change.

Consider two flux tubes which may be defined in a sheared magnetic field. Shear in the magnetic field may be thought of as follows: Consider a horizontal plane in which parallel lines are drawn. Now consider a plane immediately above or below the first one, in which parallel lines are also drawn. If the orientation of each set of parallel lines changes from plane to plane, then the field represented by the drawn lines is said to be "sheared", and the shear can be quantified by giving the rate of change of this angle of orientation with perpendicular distance. Label two very narrow flux tubes, one lying in one such plane and another lying initially in a plane immediately below the first one, "a" and "b", respectively. Due to the shear, when the flux tubes are brought together by a flow field, they cross. Propose that they might pass through each other as they are forced together. Before the interaction, the magnetic flux through the sides of both tubes is zero. If they are allowed to pass through each other, the field lines due to tube "a" would intersect the sides of tube "b", and vice versa. The magnetic flux through the sides of the tubes would no longer be zero. This is in obvious contradiction to the flux conservation theorem, so the conclusion is that the flux tubes are never allowed to cross. Note that this conclusion holds as well for flux tubes of infinitesimal cross-section, and hence for individual field lines.

> In ideal MHD, magnetic flux tubes and field lines cannot be advected through each other, because of the magnetic flux conservation theorem.

Below, we will explore how this constraint is relaxed by a finite plasma resistivity.

3.4 Dynamics, or the Wires-in-Molasses Picture of MHD

Note that the magnetic force term in the MHD force equation can be split into two pieces using an elementary vector identity:

$$\frac{1}{c}\mathbf{J}\times\mathbf{B} = \frac{1}{c}\left(\frac{c}{4\pi}\nabla\times\mathbf{B}\right)\times\mathbf{B} = -\nabla\frac{B^2}{8\pi} + \frac{\mathbf{B}\cdot\nabla\mathbf{B}}{4\pi}.$$

These two contributions denote "magnetic pressure" and "magnetic tension", respectively. Magnetic pressure may be combined with gas pressure:

$$\rho\left(\frac{\partial}{\partial t}+\mathbf{v}\cdot\nabla\right)\mathbf{v}=-\nabla\left(p+\frac{B^2}{8\pi}\right)+\frac{\mathbf{B}\cdot\nabla\mathbf{B}}{4\pi},$$

where one notes that it behaves like an energy density with two degrees of freedom (for which the pressure and energy density are equal).

The other contribution is magnetic tension. It is part of what gives MHD its unique character (flux conservation, or the advection of magnetic field lines is the other part). To see why it is called tension, consider the magnetic field due to a wire carrying current, surrounded by a vacuum. The field lines are described by loops centered upon the wire, and the forces are obviously zero because it is a vacuum. A cylindrical coordinate system may be defined, with z in the direction of the wire and r perpendicular to it. The only nonzero component of $\mathbf{B}\cdot\nabla\mathbf{B}$ is

$$\mathbf{B}\cdot\nabla\mathbf{B}=-\frac{B^2}{r}\hat{\mathbf{e}}_\mathbf{r}.$$

This shows that magnetic tension is a force which acts in the direction of the curvature vector (towards the loop's center), a general result for a curved field line. Since the current outside the wire vanishes, the tension and pressure forces must be in balance: since $B\sim I/r$,

$$-\nabla\frac{B^2}{8\pi}=2\frac{B^2}{8\pi}\frac{1}{r}\hat{\mathbf{e}}_\mathbf{r}=\frac{B^2}{4\pi r}\hat{\mathbf{e}}_\mathbf{r}=-\mathbf{B}\cdot\nabla\mathbf{B}.$$

In such a situation, which can also exist in a plasma where the current is not zero, magnetic pressure and tension are in balance, and the configuration is termed "force-free".

3.4.1 Magnetic pressure waves

Consider a compression in a magnetised plasma in equilibrium, perpendicular to the magnetic field. The velocity depends only on the direction perpendicular to the field, and it is itself directed perpendicular to the field. In this situation,

$$\mathbf{B}\cdot\nabla\mathbf{B}=0,$$

since $\mathbf{B}$ is compressed perpendicular to its direction. The field lines are compressed together with the fluid, according to the MHD kinematic equation:

$$\frac{\partial\mathbf{B}}{\partial t}=-\mathbf{v}\cdot\nabla\mathbf{B}-\mathbf{B}\nabla\cdot\mathbf{v},$$

where the third piece, $\mathbf{B}\cdot\nabla v$, vanishes due to the geometry. This equation states that $\mathbf{B}$ reacts exactly as would a density:

$$\frac{\partial\mathbf{B}}{\partial t}+\nabla\cdot\mathbf{v}\mathbf{B}=0.$$

With the vanishing magnetic tension, the force equation reads

$$\rho\left(\frac{\partial}{\partial t}+\mathbf{v}\cdot\nabla\right)\mathbf{v}=-\nabla\left(p+\frac{B^2}{8\pi}\right).$$

The result is exactly analogous to sound waves, since both the pressure and magnetic field are perturbed in the same way. Consider small perturbations of short wavelength, on which scale the equilibrium pressure and magnetic field is homogeneous. We "linearise" the equations by retaining terms only to first order in the perturbations, which are denoted by a tilde symbol. For example, B^2 becomes $B^2+2\mathbf{B}\cdot\widetilde{\mathbf{B}}$, with the term quadratic in $\widetilde{\mathbf{B}}$ neglected. The velocity requires no symbol, since it is understood to belong to the perturbations. Both pressure and magnetic perturbations are induced by compression in the velocity:

$$\frac{1}{\gamma p}\frac{\partial\widetilde{p}}{\partial t}=\frac{1}{B}\frac{\partial\widetilde{B}}{\partial t}=-\nabla\cdot\mathbf{v},$$

with $\gamma=5/3$. The perturbed force equation reads

$$\rho\frac{\partial\mathbf{v}}{\partial t}=-\nabla\left(\widetilde{p}+\frac{B\widetilde{B}}{4\pi}\right),$$

and note the factor of two arising from perturbing B^2. These may be combined into a wave equation:

$$\frac{\partial^2\widetilde{B}}{\partial t^2}-\left(\frac{B^2}{4\pi\rho}+\frac{\gamma p}{\rho}\right)\nabla_\perp^2\widetilde{B}=0,$$

where it is noted that the derivatives are all perpendicular to $\mathbf{B}$.

The second term in the parentheses will be recognised as the square of the adiabatic sound velocity v_s. The first term introduces the characteristic velocity of MHD in general, and the velocity of propagation of small magnetic disturbances in particular. It is the square of the "Alfvén velocity":

$$v_A^2=\frac{B^2}{4\pi\rho},$$

after Hannes Alfvén, who is recognised as the founder of the MHD description of plasma fluid dynamics. Magnetic pressure waves, like sound waves, are longitudinal waves, but unlike sound waves they are in their pure form only when the disturbance propagates perpendicular to the magnetic field. In general, when both gas pressure and magnetic pressure are present, they both contribute to the actual wave speed: $v^2=v_s^2+v_A^2$. More on the ratio of gas to plasma pressure shortly.

3.4.2 Alfvén waves: magnetic tension waves

Because the magnetic field also exhibits tension, transverse waves similar to waves on a taut string also occur in MHD. Assume now that there is a divergence-free perturbation of a magnetised plasma in equilibrium, still perpendicular to the magnetic field. The

velocity now depends only on the direction parallel to the field, although it is itself directed perpendicular to the field. In this situation,

$$\nabla \cdot \mathbf{v} = \widetilde{p} = \mathbf{B} \cdot \widetilde{\mathbf{B}} = 0,$$

since the disturbance is a transverse-shear perturbation. The field lines are not compressed, but are bent, according to the MHD kinematic equation:

$$\frac{\partial \mathbf{B}}{\partial t} = -\mathbf{v} \cdot \nabla \mathbf{B} + \mathbf{B} \cdot \nabla \mathbf{v},$$

where the divergence piece, $\mathbf{B}\nabla \cdot \mathbf{v}$, vanishes due to the geometry. Field line bending becomes clearer when this expression is re-cast in the co-moving frame:

$$\frac{d\mathbf{B}}{dt} = \mathbf{B} \cdot \nabla \mathbf{v}.$$

The single contribution arises due to the fact that the field line is moved in alternate directions according to position along it.

This is a new situation, in which the pressure is unperturbed, and the magnetic field is perturbed only through the component perpendicular to the equilibrium field. For homogeneous perturbations:

$$\begin{aligned} \frac{\partial \widetilde{B}_\perp}{\partial t} &= \mathbf{B} \cdot \nabla \widetilde{v}_\perp, \\ \rho \frac{\partial \widetilde{v}_\perp}{\partial t} &= \tfrac{\mathbf{B} \cdot \nabla \widetilde{B}_\perp}{4\pi}, \end{aligned}$$

where there is no factor of two since the perturbed field component is perpendicular. These may be combined into a wave equation:

$$\frac{\partial^2 \widetilde{B}_\perp}{\partial t^2} - \frac{B^2}{4\pi\rho} \frac{(\mathbf{B} \cdot \nabla)^2}{B^2} \widetilde{B}_\perp = 0,$$

where note now that the derivatives are all parallel to $\mathbf{B}$.

This type of disturbance propagates parallel to $\mathbf{B}$, and it is a transverse wave. It is called an "Alfvén wave", since it is the type of propagating wave which exists in MHD but not in neutral fluid dynamics. Its propagation speed is purely the Alfvén velocity. The detection of Alfvén waves in the solar wind by spacecraft in the 1960s gave evidence that MHD phenomena do occur in nature and are not a theoretical artifice.

The concept of field line tension is now clear, since the behavior of the field line in MHD is the same as that of a taut string: "pluck it, and transverse waves run down the line". The concept of "field line bending" is closely related: curvature of a field line gives rise to the magnetic tension force. However, field line bending should not be considered as a force in itself, but a cause of one.

> A general description of MHD can be that of "molasses threaded by wires". The wires are magnetic field lines, which exert force on the fluid and which are advected by the fluid as it moves. Additions to this are that the wires exert pressure as well as tension, tending to repel each other, and that in the ideal limit the fluid is not viscous.

One final note: the attractive force between two wires is due to magnetic tension overcoming magnetic pressure.

3.5 The Validity of MHD

The Alfvén velocity as just introduced determines the natural time scale of any MHD phenomena of a confined system. With this in hand, we are in a position to judge the validity of MHD by providing *a posteriori* checks on its fundamental assumptions. The Alfvén times are discussed first, and then the checks are made.

3.5.1 Characteristic time scales of MHD

Although they were derived for small disturbances on a homogeneous background, the wave velocities for propagation perpendicular and parallel to the magnetic field indicate the characteristic time scales for adjustment to equilibrium for general perturbations of any confined MHD system. This is much the same as the way the time it takes for a sound wave to cross a neutral fluid in hydrostatic equilibrium under gravity gives the characteristic adjustment time for that fluid. The reason is that a global free oscillation is nothing more than the longest-wavelength limit of the appropriate wave. Examples of the neutral fluid case would be an ocean layer, the Earth's atmosphere, or the Sun. In that case, for a scale length a, the sound-wave transit time is

$$\tau_s = a/c_s,$$

which is also the inverse of the frequency of the fundamental global mode of oscillation (cf. the five-minute oscillation observed on the Sun).

For a confined plasma in equilibrium the sound speed is replaced by the Alfvén velocity, v_A. It must be noted, though, that the geometry of the confined system is important, since different types of waves propagate parallel to and perpendicular to the magnetic field. With characteristic scale lengths $L_\perp$ perpendicular to the field and $L_\parallel$ parallel to the field, two time scales are of interest. Due to the propagation of magnetic pressure waves, we have the

$$\text{"fast Alfvén", or compressional Alfvén time:} \qquad \tau_A = L_\perp/v_A.$$

From the propagation of magnetic tension waves (Alfvén waves) we have the

$$\text{"slow Alfvén", or shear Alfvén time:} \qquad \tau_A = L_\parallel/v_A.$$

Both of these are usually written as "τ_A" in the literature, and one has to extract the meaning from the context. The name "shear Alfvén time" originates from the fact that parallel length scales for many laboratory plasma instabilities arise from the existence of magnetic shear in the equilibrium configuration.

These time scales and characteristic velocities can be deduced directly from the MHD force and kinematic equations by "scaling" them. Assuming that the spatial scale is a, the kinematic equation yields:

$$\frac{\partial \mathbf{B}}{\partial t} = \nabla \times (\mathbf{v} \times \mathbf{B}) \qquad \rightarrow \qquad \frac{B}{\tau} \sim \frac{Bv}{a},$$

and the force equation yields:

$$\rho \frac{d\mathbf{v}}{dt} = -\nabla p + \frac{1}{c}\mathbf{J} \times \mathbf{B} \qquad \rightarrow \qquad \rho \frac{v}{\tau} \sim \frac{B^2}{4\pi a},$$

if the gas pressure is negligible. These similarity relations may be solved for v and τ, given B and a, and the result is $v \sim v_A$ with $\tau \sim a/v_A$.

3.5.2 Checking the assumptions

With a as a representative spatial scale and τ_A as the corresponding time scale, we may now examine the MHD assumptions listed in Section III, a little out of order.

(1) The displacement current is neglected because $v_A << c$. This is easily satisfied for laboratory and space plasmas.

(5) Quasineutrality depends on both $\tau_A \omega_{pe} >> 1$ and $r_i >> \lambda_D$. The latter three parameters in this list are the electron plasma frequency ($\omega_{pe}^2 = 4\pi n e^2/m_e$), the ion Larmor gyroradius ($r_i^2 = c^2 M_i T_i / e^2 B^2$), and the Debye screening length ($\lambda_D^2 = T/4\pi n e^2$). The former inequality is needed to neglect the parallel electric field, as the time scale for the electrons to equilibrate charge is ω_{pe}. The latter is needed in order to use the Lorentz force in the fluid description, since the Lorentz force has the gyroradius as its implicit length scale and the particles are not supposed to individually interact.

(3) Fluid elements of all species move with velocity $\mathbf{v}$, with the relative drift implied by $\mathbf{J}$ negligible. This requires $J \ll n e v_A$, or using Ampere's law to express J in terms of B (as magnitudes), we find

$$\frac{r_i^2}{a^2} \equiv (\text{"drift parameter"})^2 \ll \text{"plasma beta"} = \beta \equiv \frac{8\pi p}{B^2}.$$

(The plasma beta is discussed below.) Neglecting ion inertia as a correction to the E-cross-B velocity for ions depends on the same limit, since $\tau_A \Omega_i >> 1$ is an equivalent statement ($\Omega_i = eB/M_i c$ is the ion gyrofrequency). The statement that the drift parameter be smaller than some limit is a requirement on how strongly the plasma is magnetised, and that it must be smaller than $\beta^{1/2}$ is usually well-satisfied in any fusion or space plasma application.

(2) Electron inertia is negligible because $m_e \ll M_i$ in general. It is negligible compared to the pressure gradient if $n m_e v_A / \tau << p/a$, which implies $\beta >> m_e/M_i$. This has no

impact on the MHD kinematic equation, since ∇p is negligible to that anyway. But this serves as a check that electron inertia is negligible even when ion inertia is very strong compared to pressure corrections, which is why a limit on β makes sense (see below).

(4) That ∇p is negligible compared to the Lorentz force term is implied as well by (3), since $\mathbf{J}\times\mathbf{B}/c$ is comparable to ∇p and $J \ll nev_A$. If $\beta \ll 1$, then this is even more so.

3.5.3 A comment on the plasma beta

The "plasma beta", defined by

$$\frac{\text{gas pressure}}{\text{plasma pressure}} = \frac{8\pi p}{B^2} \equiv \beta,$$

is very important in plasma fluid dynamics. It gives the relative importance of the gas pressure to the magnetic field as the restoring force to any disturbance. If $\beta \gg 1$, then the magnetic force has a negligible effect on the dynamics, but the magnetic field is still advected by the flow. This is called "MHD kinematics". It is important in studies of the generation of a magnetic field by a conducting fluid undergoing motion forced by other means, such as convection in a gravitational field. The generation of a large-scale magnetic field by convective turbulence is called the "dynamo effect", and it is thought to be the most likely scenario for the origin of planetary and stellar magnetic fields. (A note: some treatments define β with 4π instead of 8π.)

In the opposite limit, $\beta \ll 1$, the gas pressure drops out of the MHD force equation to lowest order in β, but it remains as a slight correction to the geometry of any equilibrium. For such a "low-beta" plasma, the gas pressure is still important because it can break the tendency of magnetic pressure and tension to cancel. A consequence is that a finite gas pressure prevents the establishment of a force-free equilibrium, to which the plasma tends to relax in many important configurations, even in a situation with a nonzero current density. In addition, the gas pressure can cause instability in an equilibrium which would otherwise be stable to MHD perturbations ("MHD-stable"). In the tokamak configuration for a fusion plasma, for example, this fact is responsible for limiting the plasma beta to quite low values.

The tendency of magnetic pressure and tension to cancel is ultimately the reason that assumptions (3) and (5) have to be separately checked.

3.6 Parallel Dynamics and Resistivity

One limit which was not examined above is the role of parallel dynamics: the general case of flows parallel to the magnetic field. If we compare the drift velocity implied by $\mathbf{J}$ not to v_A but to v_s, we get a different limit: $\beta \gg r_i/a$ (the reader is invited to check this). The drop of one power of the drift parameter places a rather strict limit on how low the beta can be allowed to go. In solar plasmas the drift parameter is really very small, so this point can be ignored. In fusion plasmas, especially tokamak and stellarator plasmas in which β is quite limited by effects arising from the gas pressure, the limit

can be violated, and it is nearly always violated in the boundary regions of the plasma. It is important to realise that a perturbation compressing the gas purely parallel to the magnetic field involves no disturbance of the field. A small disturbance of this type merely leads to longitudinal sound waves propagating parallel to the field lines. Such parallel effects may be neglected for any disturbance of the general equilibrium or violent instability, since these evolve on Alfvén time scales. However, transport phenomena may give rise to force imbalances along the field lines, and these would relax on the parallel sound transit time scale. If phenomena on this scale are of global importance, then the kinematic MHD equation will be affected since although these effects are parallel, the forces they cause may have a nonzero perpendicular curl. When this is the case, studies of the consequences must treat the electron and ion fluids separately, on an equal footing. Further inquiry along these lines is beyond the scope of this introduction to MHD.

A simpler effect which breaks the ideal MHD constraints but still allows treatment of the system as MHD and as a single fluid is electrical resistivity. Resistivity means an exchange of momentum between electrons and ions as their respective fluids drift past each other. The details of the electron-ion collision process are complex, due to the fact that the angle through which an electron is scattered upon close approach to an ion depends strongly on the relative velocity. Nevertheless, by the inclusion of a simple momentum exchange term loosely based on a collision frequency, a qualitative picture of the most important consequence can be given: magnetic field line diffusion, or how those flux tubes tangled together at arbitrarily small scale eventually relax. MHD with electrical resistivity is called "resistive MHD".

Consider a plasma with a single ion species of charge e, and allow the ions and electrons to exchange momentum. The continuity and energy equations are unaffected, but the electrons lose momentum to the ions on a time scale given by a collision frequency, ν_{ei}:

$$0 = -\nabla p_e - n_e e\left(\mathbf{E} + \frac{\mathbf{v}_e}{c}\times\mathbf{B}\right) - n_e m_e \nu_{ei}(\mathbf{v}_e - \mathbf{v}_i),$$

in which inertia is still neglected. To conserve momentum, the same term appears with opposite sign in the ion momentum equation:

$$n_i M_i \frac{d\mathbf{v}_i}{dt} = -\nabla p_i + n_i e\left(\mathbf{E} + \frac{\mathbf{v}_i}{c}\times\mathbf{B}\right) + n_e m_e \nu_{ei}(\mathbf{v}_e - \mathbf{v}_i).$$

We now add these two to obtain the resistive MHD force equation:

$$\rho\left(\frac{\partial}{\partial t} + \mathbf{v}\cdot\nabla\right)\mathbf{v} = -\nabla p + \frac{1}{c}\mathbf{J}\times\mathbf{B}.$$

Note that since the MHD force equation is one for *total* momentum, the addition of resistivity does not alter its form.

Now consider the MHD kinematics. Solving the electron momentum equation for $\mathbf{E}$, obtain

$$\mathbf{E} + \frac{\mathbf{v}_e}{c}\times\mathbf{B} = -\frac{\nabla p_e}{n_e e} - \frac{m_e \nu_{ei}}{n_e e^2} n_e e(\mathbf{v}_e - \mathbf{v}_i).$$

As before, we neglect the pressure force and assume that $\mathbf{v}_e$ is $\mathbf{v}$. Note as well that $n_e e(\mathbf{v}_e - \mathbf{v}_i) = \mathbf{J}$. (The astute reader will note the slight complications that arise when the charge state of the ions differs from $+1$; let this be left as an exercise.)

The electron force balance, modified by resistivity, now reads

$$\mathbf{E} + \frac{\mathbf{v}}{c} \times \mathbf{B} = \eta \mathbf{J},$$

where $\eta = m_e \nu_{ei} / n_e e^2$ is the resistivity. Inserting this relation into the MHD kinematic equation, we find

$$\frac{\partial \mathbf{B}}{\partial t} = \nabla \times (\mathbf{v} \times \mathbf{B}) - \nabla \times \frac{\eta c^2}{4\pi} \nabla \times \mathbf{B}.$$

Assuming for the moment that η is homogeneous, the double-curl operation may be reduced, re-casting the kinematic equation as

$$\frac{\partial \mathbf{B}}{\partial t} = \nabla \times (\mathbf{v} \times \mathbf{B}) + \frac{\eta c^2}{4\pi} \nabla^2 \mathbf{B}.$$

This has the form of a diffusion, which is the role that resistivity plays. The eventual fate of tangled magnetic flux tubes is now apparent. Supposing that

$$\frac{v_A}{a} \gg \frac{\eta c^2}{4\pi} \frac{1}{a^2},$$

or in terms of the "Lundquist number", S, and "resistive decay time", τ_R,

$$S \equiv \frac{\tau_A}{\tau_R} \gg 1, \qquad \tau_R = \frac{a^2}{\eta c^2 / 4\pi},$$

the system evolves according to ideal MHD on large scales. When flux tubes are tangled on ever-smaller scales, however, some scale, λ, is reached at which $S(a \to \lambda) \sim 1$. At that scale the magnetic field lines lose their identity through diffusion and "re-connection", and the tangles are smoothed out.

3.7 Towards Multi-Fluid MHD

Further relaxing the assumptions of MHD brings one eventually to the necessity of treating all the constituent fluids on an equal footing, especially when further "collisional" phenomena become important. This is in any case beyond the goal of this study, which is to introduce the ideas of MHD. Interested readers will no doubt find it stimulating both to explore MHD phenomena further, and to consider in more depth the different effects one finds in two- or more-fluid dynamics. For this purpose a set of references is provided.

References

A good MHD text, both for an introduction to MHD and for further study of the basic phenomena (it is the very best book containing reconnection and MHD turbulence): *Nonlinear Magnetohydrodynamics*, by D. Biskamp (Cambridge, 1993). It cites all of the references below.

A perhaps more introductory text which is less like a review is *Ideal Magnetohydrodynamics*, by J. P. Freidberg (Plenum Press, New York, 1987).

The standard text for astrophysical MHD applications is *Cosmical Magnetic Fields*, by E. N. Parker (Clarendon Press, Oxford, 1979). Convection of magnetic flux tubes and dynamo theory form the centerpiece of this book.

A tokamak-oriented text which includes the basic MHD problems as well as the more complicated phenomena one encounters is *Theory of Tokamak Plasmas*, by R. B. White (North Holland, Amsterdam, 1989).

The best source on two-fluid dynamics is still the review article by S. I. Braginskii, in *Reviews of Plasma Physics*, M. A. Leontovich, ed. (Consultants Bureau, New York, 1965), Vol. 1, p. 205. It contains a systematic derivation of the equations from kinetic theory as well as a clear introduction to the effects represented by the individual terms (and why they appear). One obtains a good understanding of the dependence of both the two-fluid and MHD models on the kinetic theory of plasmas, and their range of validity.

Chapter 4

Tokamaks: Equilibrium, Stability and Transport

Hartmut Zohm

4.1 Introduction

The goal of confining a plasma in a magnetic field can be achieved in various geometries. The quality of the magnetic confinement is characterized by different criteria. For nuclear fusion, the following points are of special interest:

- The ratio of kinetic plasma pressure, averaged over the plasma volume, to magnetic pressure $\beta =< p > /(B^2/(2\mu_0))$. This number is a measure of the economic efficiency of the confinement since the fusion power output roughly scales as p^2 and B is the magnetic field which has to be provided externally. Usually, β is limited by the occurrence of MHD instabilities.
- The energy confinement time $\tau_E = W_{pl}/P_{heat}$ which is one of the quantities appearing in the Lawson criterion $n_i \tau_E T_i \geq f(T_i)$ and characterizes the quality of the heat insulation, i.e. the transport properties of the configuration.

The simplest approach is a linear configuration (mirror, pinch) which suffers from losses appearing at the ends. Today, these points are optimized in devices with toroidal geometry. Today, the TOKAMAK configuration is the best developed; the STELLARATOR is expected to show confinement properties of similar quality.

4.2 Plasma Equilibrium

4.2.1 The Steady State MHD-Equations

The equilibrium of a plasma in a magnetic field can be described by the MHD equations. Equilibrium is described by neglecting the temporal derivatives. If, in addition, no flow

is considered ($\mathbf{v} = 0$), the equations reduce to

$$\nabla p = \mathbf{j} \times \mathbf{B} \tag{4.1}$$

$$\nabla \times \mathbf{B} = \mu_0 \mathbf{j} \tag{4.2}$$

$$\nabla \cdot \mathbf{B} = 0 \tag{4.3}$$

The first equation is the force balance which states that a current flowing perpendicular to the magnetic field exerts a force on the fluid element. In equilibrium, this force balances the plasma kinetic pressure, i.e. everywhere in the plasma, the local pressure gradient is balanced by the Lorentz force. In particular, for $\nabla p = 0$, the fields $\mathbf{j}$ and $\mathbf{B}$ are collinear (*force free region*). Eq. (4.2) and (4.3) are Maxwell's equations for a static magnetic field.

4.2.2 Equilibrium in the Linear Pinch

A simple analytic solution of eqns. (4.1) - (4.3) can be given in the case of a linear cylindrical configuration, the so-called pinch. The simplest case is a z-pinch, i.e. a cylinder carrying a current in the z-direction (see Fig. 4.1).

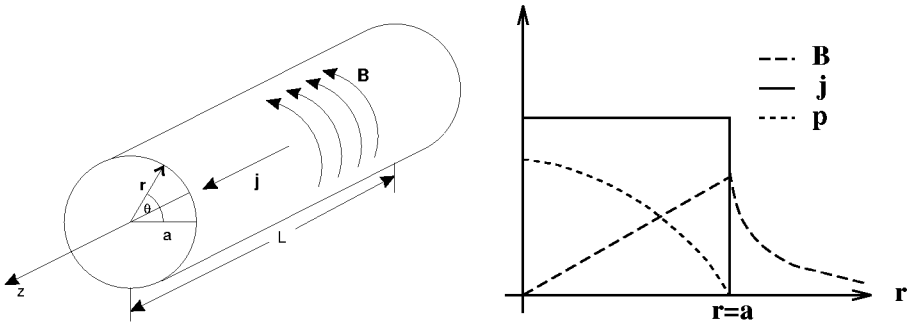

Figure 4.1: The linear z-pinch: geometry and radial profiles of j_z, B_θ and p for the example shown in the text.

Here, the magnetic field is purely azimuthal and the force balance reads

$$\frac{dp}{dr} = -j_z \cdot B_\theta \tag{4.4}$$

To explicitly calculate the radial profile $p(r)$, we have to specify a current density profile $j_z(r)$. For simplicity, we chose $j_z = const. = j_0$ inside the plasma of radius a and $j_z = 0$ outside. Then we can solve eq. (4.2) in cylindrical geometry to obtain

$$B_\theta = \frac{\mu_0 I_p}{2\pi a^2} r \quad \text{for} \quad r \leq a \tag{4.5}$$

$$B_\theta = \frac{\mu_0 I_p}{2\pi r} \quad \text{for} \quad r > a \tag{4.6}$$

where $I_p = j_0 \pi a^2$ is the total current flowing in the plasma. Using this result, we can integrate eq. (4.4) to yield

$$p(r) = \frac{\mu_0 I_p^2}{4\pi^2 a^2} \left(1 - \left(\frac{r}{a}\right)^2\right) \tag{4.7}$$

Fig. 4.1 shows a plot of the profiles. Calculating β_p, i.e. the ratio of average kinetic pressure and magnetic pressure associated with the poloidal field

$$\beta_p = \frac{2\mu_0 < p >}{B_\theta^2} \tag{4.8}$$

we find $\beta_p = 1$ for this particular example. It can be shown that this is a general result for the z-pinch, independent of the profiles specified.

This simple equilibrium calculation does not include a stability analysis, i.e. we have shown that a state with $\partial t \rightarrow 0$ exists, but we do not know whether this is a stable solution. This will be done in the next section. For the z-pinch, one can show that it is unstable unless we add a magnetic field in the z-direction. Fig. 4.2 shows this magnetic configuration (*screw pinch*).

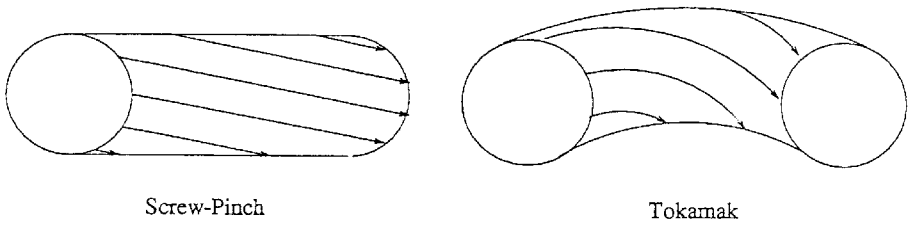

Figure 4.2: Magnetic configuration of the screw-pinch and analogous tokamak.

As can be seen, the magnetic field lines helically wind around the magnetic axis. If we bend the cylindrical screw-pinch to form a torus, we obtain a tokamak geometry. For large aspect ratio (i.e. ratio of major and minor radius $A = R/a$), a tokamak can be approximated by a screw-pinch periodic in z with period $2\pi R$. The properties of the field lines are characterized by the safety factor q defined by

$$q = \frac{number\,of\,toroidal\,windings}{number\,of\,poloidal\,windings} \tag{4.9}$$

of a field line on the torus. In the limit of the screw-pinch, the relation $q = (r/R)(B_t/B_\theta)$ holds. From stability considerations it follows that $q \geq 1$ (see below), so that $B_t \approx r/(Rq)B_\theta$. Inserting typical tokamak values (e.g. ASDEX-Upgrade $a = 0.5$ m, $R = 1.65$ m and $q = 3$), we arrive at $B_t \approx 10 B_\theta$, i.e. for this screw pinch $\beta_t = 2\mu_0 < p > /B_t^2 \approx 1$ %. Thus stability requirements have a severe impact on the economic properties of the device.

In a screw pinch or tokamak, there is the possibility of poloidal currents that exert a force on the plasma. For $\mathbf{j}_p \times \mathbf{B}_t \uparrow\uparrow \mathbf{j}_t \times \mathbf{B}_p$, the plasma pressure balanced by the magnetic field is higher than in the pure z-pinch; in this case $\beta_p > 1$ and the poloidal current weakens the original $\mathbf{B}_t$, therefore the plasma is said to be *diamagnetic*. In the opposite case, $\mathbf{j}_p \times \mathbf{B}_t \uparrow\downarrow \mathbf{j}_t \times \mathbf{B}_p$, we can sustain less pressure, and $\beta_p < 1$ (*paramagnetic* plasma).

4.2.3 The Grad-Shafranov Equation

For an axisymmetric system like the tokamak, it is convenient to re-write the force balance eqn. (4.1). For this purpose, we need the following ideas:

- As $\nabla p = \mathbf{j} \times \mathbf{B}$, $\nabla p \cdot \mathbf{j} = \nabla p \cdot \mathbf{B} = 0$. Therefore the field lines of $\mathbf{j}$ and $\mathbf{B}$ lie in the surfaces of constant pressure.
- The flux integrals $\int \mathbf{B}\, d\mathbf{A}$, $\int \mathbf{j}\, d\mathbf{A}$ have a constant value on the $p = const.$ surfaces for an arbitrary curve C on this surface, since $\mathbf{j}$ and $\mathbf{B}$ lie in this surface and thus any part of the integrals on the surface vanishes. These surfaces are therefore called *flux surfaces* and can be labelled by the (scalar) fluxes. Also, p is only a function of the fluxes.
- As $\nabla \cdot \mathbf{B} = \nabla \cdot \mathbf{j} = 0$, any flux integral $\int \mathbf{B}\, d\mathbf{A}$, $\int \mathbf{j}\, d\mathbf{A}$ has a constant value if the arbitrary surface A is surrounded by the same curve C and thus we are free to chose the surface A. This means that each flux surface can be assigned a unique value of the flux, independent of the geometry in which the flux was calculated.

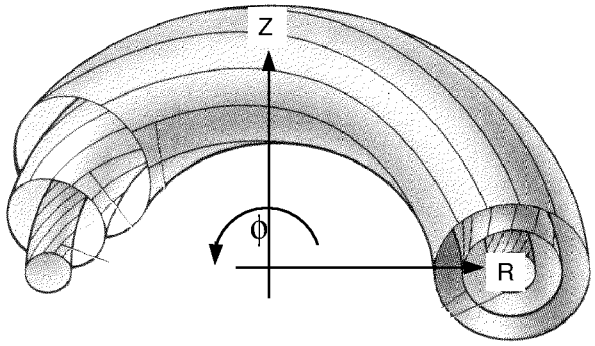

Figure 4.3: Co-ordinates used for the Grad-Shafranov equation.

On a torus, there are two topologically different types of curves: Those winding around the torus in the toroidal direction and those winding around the torus in the poloidal direction. If we chose a curve winding around in the toroidal direction, integration over the domain enclosed by this surface yields the poloidal magnetic flux function Ψ and the total poloidal current I_{pol}. Both functions are constant on the flux surface and the magnetic field can be calculated as

$$B_\phi = \frac{\mu_0 I_{pol}}{2\pi R} \tag{4.10}$$

$$B_R = -\frac{1}{2\pi R}\frac{\partial \Psi}{\partial Z} \tag{4.11}$$

$$B_Z = \frac{1}{2\pi R}\frac{\partial \Psi}{\partial R} \tag{4.12}$$

where the co-ordinates from Fig. 4.3 have been used. Note that with this definition, Ψ denotes the poloidal flux per unit length in toroidal direction ($[\Psi] = Vs/m$). Using these quantities, the force balance can be re-written as

$$-\Delta^* \Psi = -R\frac{\partial}{\partial R}\left(\frac{1}{R}\frac{\partial \Psi}{\partial R}\right) + \frac{\partial^2 \Psi}{\partial z^2} = \mu_0 (2\pi R)^2 p(\Psi)' + \mu_0^2 I_{pol}(\Psi) I'_{pol}(\Psi) \tag{4.13}$$

known as the Grad-Shafranov equation. The prime denotes the derivative of a flux surface quantity with respect to Ψ. Eq. (4.13) is usually nonlinear in Ψ. To solve it, we

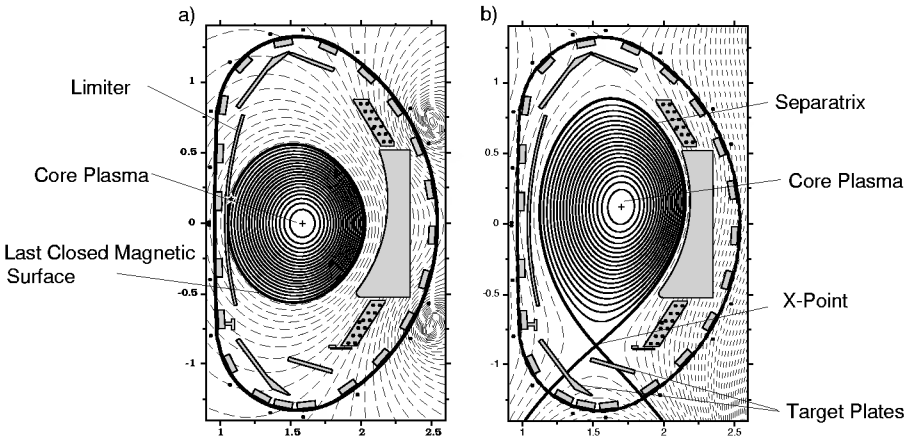

Figure 4.4: Typical poloidal cross-sections of a tokamak.

can e.g. specify $p(\Psi)$ and $I_{pol}(\Psi)$ and then solve for $\Psi(R, Z)$. Usually, one will specify boundary conditions. If the plasma is surrounded by a perfectly conducting vacuum vessel, the vessel is a flux surface and therefore $\Psi = const.$ at the vessel determines shape and position of the plasma boundary. To satisfy these conditions, we have to add a solution of the homogeneous equation, i.e. a function Ψ_{ext} with $\Delta^*\Psi_{ext} = 0$. Such a field is produced by external coils, i.e. the solution of the Grad-Shafranov equation with fixed boundary and profile functions tells us how to arrange external control currents to maintain the plasma in equilibrium.

4.2.4 The Tokamak

The tokamak principle was already introduced in chapter 2. The plasma acts as a secondary winding of a transformer. Ramping down the current in the primary coil induces a loop voltage in the discharge vessel; after breakdown, a toroidal current flows in the plasma. This current heats the plasma via its resistance (**O**hmic **H**eating, the primary coil is also called the OH coil). The current itself creates the poloidal magnetic field, the toroidal field is produced by external coils (contrary, a stellarator produces all its field components by external coils). The poloidal field coils maintain the plasma in force equilibrium as described by eq. (4.13). A sketch of the tokamak principle is shown in Fig. 1.11.

Fig. 4.4 shows typical examples for poloidal cross-sections calculated with eq. (4.13). One can see that the flux surfaces are not centered to one axis, but are slightly shifted. This *Shafranov shift* is due to the forces trying to expand the torus radially outward:

- The kinetic pressure of the plasma.
- The expansion force of a current loop due to the $\mathbf{j} \times \mathbf{B}$ force.

The sum of these two forces is called *hoop force*. In Fig. 4.4 b), one can see that the plasma cross-section does not necessarily have to be circular; in fact, elongation and triangularity produced with additional poloidal field coils enhance plasma performance

(see next section). One also sees the different ways to limit a plasma: Fig. 4.4 a) shows a so called *limiter* case, where a material limiter defines the last closed flux surface, in Fig. 4.4 b), this last closed flux surface is defined magnetically by a so-called *separatrix*; plasma crossing the separatrix flows along field lines to the material plates at the bottom of the vessel. This configuration is called a magnetic *divertor*.

4.3 Stability of an Equilibrium State

As has been mentioned before, the Grad-Shafranov eqn. (4.13) describes a force equilibrium, but it does not tell us if the equilibrium is stable, i.e. if a small variation of the plasma parameters or the external control currents will lead to another equilibrium or to an unstable situation. Therefore, we have to analyze the stability properties of a configuration by a separate treatment.

MHD instabilities lead to various deleterious effects of plasma performance: Large-scale instabilities can lead to a loss of plasma control (e.g. during a *disruption*, the plasma current collapses in an uncontrollable way) whereas small scale perturbations and MHD turbulence can significantly enhance radial transport of particles and energy. Nevertheless, in some cases instabilities may help to control parameters; e.g. ELMs (Edge Localized Modes) periodically expel impurities from the plasma edge and help keep the plasma clean.

4.3.1 Methods of Stability Analysis

From MHD theory, there are different ways to analyze the stability of a given equilibrium. Often, the analysis is done by introducing a perturbation of the equilibrium configuration as a displacement ξ of a fluid element. Two methods are especially useful to analyze stability against such displacements:

- The energy principle: This approach calculates the energy W_{MHD} of the configuration as a functional of the displacement vector. Stability is obtained if the second order change in energy $\delta^2 W_{MHD}\{\xi\}$ is positive for an arbitrary ξ (the linear variation is zero due to the equilibrium condition). This method is useful to prove that a configuration is *not* stable, because it is sufficient to find one unstable ξ; on the other hand, stability is hard to prove.

- Eigenmode analysis: Here, the time-dependent MHD equations are solved with an eigenmode ansatz for the displacement ξ. An ansatz often used is the Fourier decomposition in time and space. For the screw pinch, the spatial Fourier ansatz means periodicity in poloidal and toroidal co-ordinate θ and ϕ. Note that in a real torus, symmetry in the θ direction is only an approximation and coupling of poloidal harmonics will occur. For linearized MHD equations, this leads to an eigenvalue problem for each single Fourier mode

$$\xi = \xi_{mn}(r) e^{i(m\theta - n\phi)} e^{\gamma t} \tag{4.14}$$

The indices m and n are called poloidal and toroidal modenumbers, for real γ, stability means $\gamma < 0$. If γ has an imaginary part, the eigenmode is called overstable and will exhibit a temporal oscillation. If γ is real and positive, it can be interpreted as a linear growth rate. The saturated amplitude of an instability can only be found by introducing nonlinear effects such as changes in the equilibrium introduced by the perturbation.

Perturbations are easily excited if the field lines do not ergodically cover a flux surface but close upon themselves after few surroundings of the torus. These flux surfaces are the ones with rational safety factor q; they are called *resonant surfaces* and a standing wave with mode numbers $q = m/n$ can occur.

4.3.2 Classification of Instabilities

In a confined plasma, an instability is driven by the free energy contained in the equilibrium configuration. In a tokamak, there are two main sources of free energy: the kinetic energy of the plasma and the energy of the magnetic field generated by the plasma. Instabilities can therefore be driven by the radial gradient of either the pressure or the current profile. At low β, the magnetic energy is much higher than the kinetic energy and the instabilities will mainly be current-driven; at high β, we expect the pressure driven instabilities to become significant.

In cylindrical approximation, the perturbed magnetic field has a radial component. The growth of this field is governed by Faraday's law. Inserting Ohm's law for the plasma yields, in the linearized case

$$\frac{\partial B_{1r}}{\partial t} = -\frac{1}{r}\frac{\partial E_{1z}}{\partial \theta} = \frac{1}{r}\frac{\partial}{\partial \theta}\Big(\eta j_{1z} + (\mathbf{v}_1 \times \mathbf{B}_0)_z\Big) \tag{4.15}$$

where the subscript 1 refers to the perturbed quantities and the subscript 0 to the equilibrium quantities. From this we deduce that there are two ways for a perturbation to grow:

- Ideal case (no resistivity, i.e. $\eta \to 0$): Flow of plasma perpendicular to the field lines; in this case, $\mathbf{v} \times \mathbf{B}$ balances the E-field and in the fluid frame ($\mathbf{v} = 0$), magnetic flux is conserved, i.e. $\mathbf{B}$ moves with the fluid. This means that there is no change in the *topology*.
- Resistive case ($\eta \neq 0$): A current flows along the equilibrium field lines and generates the B-field; in this case, the topology is changed (*tearing* and *reconnection* of field lines).

Fig. 4.5 shows two examples: the so-called *kink* as a typical ideal instability, the *tearing mode* as a resistive one. In the case of the tearing mode, so-called *magnetic islands* form. Note that the magnetic island is a nonlinear solution of the MHD equations.

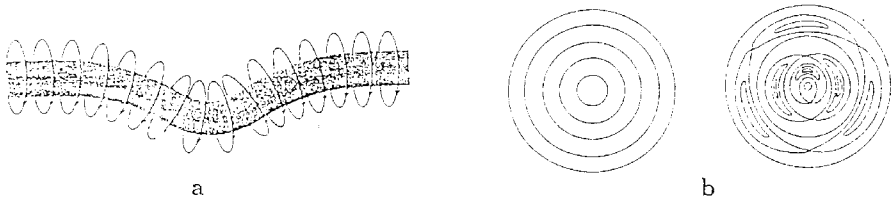

Figure 4.5: Ideal kink (a) and resistive tearing (b) instability. In (b), magnetic islands are formed.

4.3.3 Examples

A simple example of an unstable situation is the case of an elongated plasma. In order to vertically elongate a plasma cross-section, we have to run coil currents of the same sign and order of magnitude than the plasma current. For a perfectly centered plasma, the net force is zero. However, any shift δz of the plasma current center increases the attractive force of the coil towards which the plasma moves, so that further acceleration results. The plasma experiences a vertical displacement event (VDE). As the plasma has negligible mass, this is a very fast event (on the order of the Alfven time scale, i.e. $\approx \mu$s). In order to feedback control this instability, one therefore has to provide conducting structures that, via induction, slow down the motion to a ms timescale.

Other MHD phenomena have been shown to influence the achievable β of a configuration. An example is the *external kink* driven by current gradients near the edge imposing restrictions on the possible current profiles. Restrictions on the pressure profile come from the so-called interchange instability. Here, neighbouring flux tubes can change place, analogous to the Rayleigh-Taylor instability of a normal fluid, if the field line can shorten and thus lose magnetic energy due to this process. As can be seen in Fig. 4.6, this is the case when the radius of curvature is parallel to the pressure gradient (so-called 'bad curvature'). Conversely, if the radius of curvature is anti-parallel to the pressure gradient, an interchange of plasma and magnetic field will increase the magnetic energy and thus be stabilising ('good curvature'). In a screw pinch, only the poloidal field is curved and its curvature is 'bad', i.e. potentially destabilising. Stability is then achieved by sufficient shear dq/dr so that adjacent field lines have a different pitch angle and are not easily interchanged. In a torus, the toroidal field is also curved, exhibiting an area of good curvature on the inside and bad curvature on the outside of the torus. Thus, sability has to be determined by integrating along a field line and summing up the various stabilising and destabilising contributions. This leads to the Mercier criterion

$$\left(\frac{q'}{q}\right) > -\frac{8\mu_0 p'}{(rB_0)^2}(1-q^2) \tag{4.16}$$

As $p' < 0$, this means stability for all pressure profiles with $q > 1$; for $q \leq 1$, the shear has to be nonzero to provide stability. At high β, however, a new type of mode, the so-called *ballooning instability*, can develop. This mode has a small perturbation component along the magnetic filed, which allows a variation of the amplitude such that it concentrates on the outside of the torus, i.e. in the bad curvature region. Above a (shear dependent) critical pressure gradient, the energy gained by concentrating there is higher than the energy needed to bend the equilibrium field lines, and the mode becomes unstable.

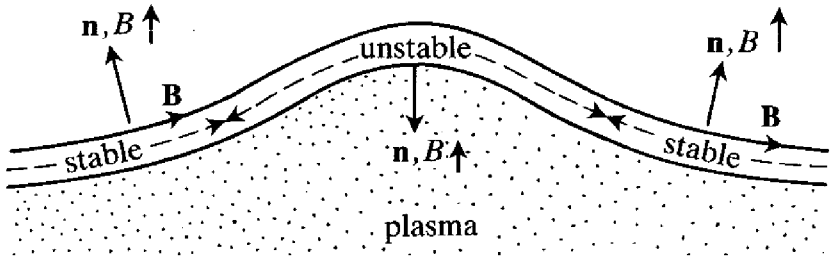

Figure 4.6: Interchange instability in a curved magnetic field.

A simultaneous optimization of pressure and current profiles yields a limit for the achievable β for given safety factor q_a and with $q_0 > 1$:

$$\beta_{max}[\%] = c\frac{I[\mathrm{MA}]}{a[\mathrm{m}]B_t[\mathrm{T}]} \tag{4.17}$$

This limit is known as the *Troyon limit*, the constant c depends only on the plasma shape and varies between ≈ 3 and 5. Theory predicts an increase in c with elongation and triangularity; this is confirmed by various experiments.

Other examples for MHD instabilities are sawteeth and disruptions, each of them linked to a special rational surface ($q = 1, q = 2$). This is treated in chapter the section on experimental results of the tokamak.

4.4 Transport in a Fusion Plasma

4.4.1 Transport equations

For one single particle in a toroidal device, the confinement is perfect. In reality, collisions, drifts and MHD turbulence lead to a radial transport of particles and energy (i.e. perpendicular to the magnetic flux surfaces). It is this transport which determines the global energy and particle confinement times τ_E and τ_p.

To analyse the nature of transport, we define the particle flux $\mathbf{\Gamma}$ as the number of particles passing through a magnetic surface per unit area and time. For $\mathbf{\Gamma}$ we make the following ansatz:

$$\mathbf{\Gamma} = -D\nabla n + n\mathbf{v} \tag{4.18}$$

stating that there is a diffusive part driven by the density gradient (characterized by the diffusion coefficient D) due to the statistical random walk of particles and a convective part due to a directed motion $\mathbf{v}$. The equation of continuity links $\mathbf{\Gamma}$ to the temporal change in density via

$$\frac{\partial n}{\partial t} = -\nabla\mathbf{\Gamma} + S \tag{4.19}$$

where $S(r,t)$ is a source term describing the change in plasma density due to ionisation or recombination (i.e. processes which cannot be described as a flux into or out of the volume element). Finally, in equilibrium, n does not change in time and we obtain

$$\nabla(D\nabla n) + \nabla\cdot(n\mathbf{v}) = S \tag{4.20}$$

For a known source function and with given D and $\mathbf{v}$, we can therefore determine the plasma density profile. On the other hand, measured density profiles are used to determine D and, with some additional assumptions, v. Transport of other quantities as e.g. energy can be treated analogously.

4.4.2 Transport Coefficients

In a magnetized plasma, we distinguish between transport coefficients parallel and perpendicular to the magnetic field, e.g. $D_\parallel$ and $D_\perp$. In general, the condition $D_\parallel \gg D_\perp$ holds. The confinement properties of a magnetic configuration are governed by the perpendicular coefficients, we will therefore focus on those.

The simplest approach to calculate diffusion coefficients comes from the random-walk ansatz. Here, we assume that, due to collisions with other particles, a particle makes a step Δx perpendicular to the magnetic field after a time Δt. If the step can be done in either direction $\pm\Delta x$ with equal probability, the process is purely diffusive and the diffusion coefficient D is given by

$$D \approx \frac{\Delta x^2}{2\Delta t} \tag{4.21}$$

In order to estimate D, we have to evaluate Δx and Δt. The latter is given by the inverse of the collision frequency ν_c. With appropriate averaging we obtain the following relations for a 90^o scattering (made up of many small angle scatterings) for electron-electron (ee), electron-ion (ei) and ion-ion (ii) collisions (we assume a pure hydrogen plasma, i.e. $Z = 1$):

$$\nu_{ee} \approx \nu_{ei} \propto \frac{ne^4}{\sqrt{m_e} T_e^{3/2}} \tag{4.22}$$

$$\nu_{ie} = \left(\frac{m_e}{m_i}\right)\nu_{ee} \tag{4.23}$$

$$\nu_{ii} = \left(\frac{m_e}{m_i}\right)^{1/2}\left(\frac{T_e}{T_i}\right)^{3/2}\nu_{ee} \tag{4.24}$$

In the so-called classical approach to transport, we take Δx to be the Larmor radius r_L

$$\Delta x = r_L = \frac{\sqrt{2mkT}}{eB} \tag{4.25}$$

However, the location $\mathbf{R}$ of the guiding centre of the gyro-orbit is given by

$$\mathbf{R} = \frac{\mathbf{p} \times \mathbf{B}}{qB^2} \tag{4.26}$$

In a collision, momentum balance requires $\Delta\mathbf{p}_a = -\Delta\mathbf{p}_b$, and thus, for like-particle collisions, $\Delta\mathbf{R}_a = -\Delta\mathbf{R}_b$. Therefore, at each collision, the particles just change place so that like-particle collisions do not contribute to particle transport (note that heat can be transferred that way, because a hot particle may change place with a cold one).

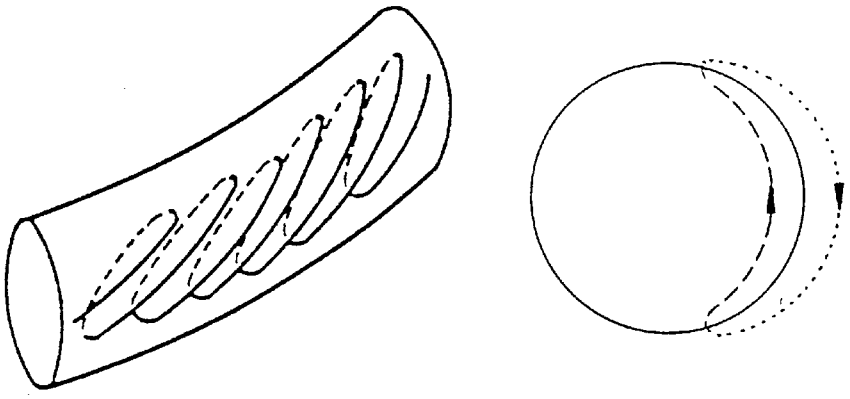

Figure 4.7: Banana Orbits in a toroidal configuration

The situation changes for electron-ion collisions. Here, $q_a = -q_b$ and therefore $\Delta\mathbf{p}_a = -\Delta\mathbf{p}_b$ leads to $\Delta\mathbf{R}_a = \Delta\mathbf{R}_b$. Thus diffusion is ambipolar, electrons and ions make a step of equal magnitude and direction per collision. The diffusion coefficient is then given by

$$D_{e,class} = \nu_{ei}\, r_{L,e}^2 = \nu_{ie}\, r_{L,i}^2 = D_{i,class} \tag{4.27}$$

For the thermal conductivities, similar arguments can be applied to show that the relation $\chi_i \approx (m_i/m_e)^{1/2}\chi_e \approx 40\chi_e$ should hold. However, experimentally determined diffusion coefficients are larger by a factor of $\approx 10^5$! Also, the electron heat conductivity is found to be comparable to that of the ions. Therefore, classical transport cannot be the dominating transport process in a fusion plasma.

So far, we did not consider the effects of the toroidal geometry. This is the subject of the so-called *neoclassical* transport theory. The main differences to classical transport theory arise from two facts:

- Along a magnetic field line, $|B|$ is not constant; a particle moving along a field line sees a higher field on the inside of the torus and, for sufficient $v_\perp/v_\parallel$, may be reflected in this magnetic mirror (see chapter 2). Therefore we have to distinguish between *trapped* and *passing* particles. It can be shown that the number of trapped particles is given by $n_t/n = \sqrt{2\epsilon}$ where $\epsilon = r/R$ is the inverse aspect ratio of the flux surface. A simple result of this effect is that the electrical conductivity is lowered in neoclassical theory as trapped particles cannot contribute to the toroidal current.

- Due to ∇B and curvature drifts, the path of a trapped particle deviates from the magnetic surface. Therefore, the projection of the trapped particle orbit in a poloidal plane is not a sector of a circle, but rather has a banana-like shape (see Fig. 4.7). These orbits are known as *banana orbits*. One can show that the banana width is given by

$$r_B = \frac{r_L q}{\sqrt{\epsilon}} \tag{4.28}$$

For trapped particles, an *effective* collision frequency $\nu_{eff} \approx \nu_c/(2\epsilon)$, where ν_c can be any of the collisionalities discussed above, is defined. This takes into account, that a trapped

particle becomes a passing one when its pitch angle has changed by $\sqrt{2\epsilon}$. Finally the ratio $\nu_* = \nu_{eff}/\nu_t$, where ν_t is the inverse of the time a particle needs to transit the banana, determines wheter the particle can complete a banana orbit between two collisions.

There are three different regimes of neoclassical transport:

- Collisional or Pfirsch-Schlüter regime: Here, $\nu_* > 1$, particles do not complete their banana orbits but are scattered before. In this case, D is evaluated to be

$$D_{PS} = q^2 \, r_L^2 \, \nu_c = q^2 \, D_{class} \tag{4.29}$$

  As we have seen, q typically ranges between 2 and 5, so transport is strongly increased.

- Banana regime: Here, $\nu_* < \epsilon^{3/2}$, particles follow the banana orbit several times before they are scattered. We can apply the random walk argument for the $\sqrt{2\epsilon}$ trapped particles with step size r_B and typical time interval $1/\nu_{eff}$:

$$D_B \propto \sqrt{2\epsilon} \, r_B^2 \, \nu_{eff} = \frac{r_L^2 q^2}{\epsilon^{3/2}} \nu_c = \frac{q^2}{\epsilon^{3/2}} D_{class} \tag{4.30}$$

  For typical values, e.g. $\epsilon = 1/3$ and $q = 5$, this yields $D_B = 130 \, D_{class}$.

- Plateau regime: Here, $1 > \nu_* > \epsilon^{3/2}$ and one can derive $D_{Pl} \approx v_{th} \, r_L^2 \, q/R$. This result is independent of ν_c (hence the name). Numerical values for D_{Pl} are in between the Pfirsch-Schlüter and the Banana regimes, so that, with rising collisionality, a smooth transition occurs between the regimes.

These neoclassical terms have to be added to the classical terms, however, they completely dominate the latter. We have seen that, due to neoclassical effects, transport coefficients can be increased by two orders of magnitude, nevertheless, they still cannot explain the experimental observations, especially for the electron channel. Today, theory tries to explain this so-called *anomalous* transport by nonlinear MHD turbulence models. It is found both theoretically and experimentally that the plasma exhibits turbulent eddies of a radial extension Δx of a few cm and a lifetime Δt of several 100 μs. If we calculate the diffusion coefficient according to (4.21), we arrive indeed at typical values of 1 m^2/s which could explain the experimental observations. However, the precise identification of the responsible small-scale MHD instabilities is a subject of ongoing research in the field of fusion plasma physics. In particular, it has become clear that a simple description in terms of one dominant mode does not exist and several contribution must be taken into account, for the different species and the large variation of plasma parameters from the edge to the core.

Chapter 5

Kinetic Theory

A.G. Peeters

5.1 Introduction

As many of my colleagues I have the difficulty in deciding what to write in roughly 15 pages about a field as developed as kinetic theory of plasmas. I have made the decision between a formal derivation of the very basic equations, and a more handwaving discussion that gives insight in the basic mechanisms and their consequences for plasma physics, in favor of the latter possibility. This because most students will never deal with the formal part of the theory but will frequently use a simple picture or a derived result that explains some of the basic properties. In this chapter I want to explain the following mechanisms

1. Landau damping
2. The physics and some properties of the Fokker-Planck collision term

5.2 Markoff process

First the Markoff process will be discussed. This describes, for instance, the Brownian motion of particles. We will encounter such processes when discussing the collisions as well as the physical mechanism of Landau damping.

Below we will, for simplicity, discuss only changes in the position of the particle. Suppose there is a random process that leads to small changes ($\Delta\mathbf{x}$) in the position ($\mathbf{x}$) of a particle. Different particles at the same position can have different displacements, and we define a function $\psi(\mathbf{x}, \Delta\mathbf{x})$ that gives the probability of a change in position $\Delta\mathbf{x}$ of a particle at $\mathbf{x}$ in a time Δt. If no particles leave the system then this probability function satisfies

$$\int \mathrm{d}(\Delta\mathbf{x})\psi(\mathbf{x}, \Delta\mathbf{x}) = 1. \tag{5.1}$$

We will assume that ψ does not explicitly depend on time, i.e. the time derivative of the distribution of particles over space is determined entirely by giving the distribution at that instant of time. There are no 'history' effects. Such a process is called a Markoff process.

To describe the distribution of particles over space we introduce a distribution function F, which gives the number of particles (N) in a certain volume $\mathrm{d}^3\mathbf{x}$ as a function of position

$$\mathrm{d}^3N = F(\mathbf{x})\mathrm{d}^3\mathbf{x} \tag{5.2}$$

Alternatively, with just one particle one can interpretate the normalized distribution, i.e. $\int \mathrm{d}^3\mathbf{x}\, F(\mathbf{x}) = 1$, as the probability density. The probability P of finding a particle in a region $\mathrm{d}^3\mathbf{x}$ around the position $\mathbf{x}$ would then be

$$\mathrm{d}^3P = F(\mathbf{x})\mathrm{d}^3\mathbf{x} \tag{5.3}$$

The Markoff process will change the distribution function. The distribution a time point t can be found from the distribution at time $t - \Delta t$ by integrating over all possible changes $\Delta\mathbf{x}$

$$F(\mathbf{x},t) = \int \mathrm{d}(\Delta\mathbf{x}) F(\mathbf{x}-\Delta\mathbf{x}, t-\Delta t)\psi(\mathbf{x}-\Delta\mathbf{x}, \Delta\mathbf{x}) \tag{5.4}$$

We assume the changes in $\mathbf{x}$ are small and make a Taylor expansion of the distribution and probability function

$$\begin{aligned} F(\mathbf{x}) \;=\; & \int \mathrm{d}(\Delta\mathbf{x}) \Bigg[\psi F - \Delta\mathbf{x} \cdot \left(\psi \frac{\partial F}{\partial \mathbf{x}} + F \frac{\partial \psi}{\partial \mathbf{x}} \right) - \Delta t \frac{\partial F}{\partial t} \\ & + \frac{1}{2} \Delta\mathbf{x}\Delta\mathbf{x} : \left(\psi \frac{\partial^2 F}{\partial \mathbf{x}\partial \mathbf{x}} + 2 \frac{\partial \psi}{\partial \mathbf{x}} \frac{\partial F}{\partial \mathbf{x}} + \frac{\partial^2 \psi}{\partial \mathbf{x}\partial \mathbf{x}} F \right) \Bigg] \end{aligned} \tag{5.5}$$

where all quantities are evaluated at the position $\mathbf{x}$. Taking the limit $\Delta t \to 0$, and defining the averages

$$\langle \Delta\mathbf{x} \rangle = \lim_{\Delta t \to 0} \frac{1}{\Delta t} \int \mathrm{d}(\Delta\mathbf{x})\, \Delta\mathbf{x}\, \psi(\mathbf{x}, \Delta\mathbf{x}) \tag{5.6}$$

$$\langle \Delta\mathbf{x}\Delta\mathbf{x} \rangle = \lim_{\Delta t \to 0} \frac{1}{\Delta t} \int \mathrm{d}(\Delta\mathbf{x})\, \Delta\mathbf{x}\Delta\mathbf{x}\, \psi(\mathbf{x}, \Delta\mathbf{x}) \tag{5.7}$$

yields the equation

$$\frac{\partial F}{\partial t} = -\frac{\partial}{\partial \mathbf{x}} \cdot \Big[\langle \Delta\mathbf{x} \rangle F \Big] + \frac{1}{2} \frac{\partial}{\partial \mathbf{x}} \cdot \frac{\partial}{\partial \mathbf{x}} \cdot \Big[\langle \Delta\mathbf{x}\Delta\mathbf{x} \rangle F \Big] \tag{5.8}$$

This equation gives the evolution of the distribution function F. The first term gives a convective contribution, while the second term is a dispersive term.

5.3 The Vlasov/Fokker-Planck equation

It is not difficult to write down the equations which we think describe the plasma well. For the plasmas that will be discussed here the parameters are such that we do not

expect quantum effects to be important. The equations then consist of the equation of motion of the particles

$$\frac{\mathrm{d}\mathbf{x}}{\mathrm{d}t} = \mathbf{v}, \tag{5.9}$$

$$\frac{\mathrm{d}\mathbf{p}_i}{\mathrm{d}t} = e_i\left[\mathbf{E} + \frac{\mathbf{v}\times\mathbf{B}}{c}\right], \tag{5.10}$$

where $\mathbf{p}$ is the particle momentum, t is the time, e_i the particles charge, $\mathbf{E}$ and $\mathbf{B}$ are the electric and magnetic field, and $\mathbf{v}$ is the particle velocity. And the Maxwell equations for the fields

$$\nabla\cdot\mathbf{E} = 4\pi\rho, \tag{5.11}$$

$$\nabla\cdot\mathbf{B} = 0, \tag{5.12}$$

$$\nabla\times\mathbf{E} = -\frac{1}{c}\frac{\partial\mathbf{B}}{\partial t}, \tag{5.13}$$

$$\nabla\times\mathbf{B} = \frac{1}{c}\mathbf{J} + \frac{1}{c}\frac{\partial\mathbf{E}}{\partial t}, \tag{5.14}$$

where c is the speed of light and ρ and $\mathbf{J}$ are the charge density and current density, which are determined by the charged particles

$$\rho = \sum_i e_i\delta(\mathbf{x}-\mathbf{x}'), \tag{5.15}$$

$$\mathbf{J} = \sum_i e_i\mathbf{v}_i\delta(\mathbf{x}-\mathbf{x}'). \tag{5.16}$$

Here the sum is over all particles.

Solving this set of equations is the real problem since the equations of motion are $6N$ equations with N being the total number of particles. Although particles codes exist they can never solve the equations for all particles (usually one particle in these codes represents many particles in reality). Therefore, one has to make a number of approximations to derive a simpler description of the plasma which is tractable for analytic or numeric treatment. Below we will construct a kinetic equation, the Fokker-Planck equation, using hand waving arguments.

To simplify the description we introduce a distribution function $f(\mathbf{x},\mathbf{v},t)$, that gives the number of particles (d^6n) in the phase space element $\mathrm{d}^3\mathbf{x}\mathrm{d}^3\mathbf{v}$ at time t

$$\mathrm{d}^6n = f(\mathbf{x},\mathbf{v},t)\mathrm{d}^3\mathbf{x}\mathrm{d}^3\mathbf{v}$$

The particles at position $\mathbf{x}$ and with velocity $\mathbf{v}$ move through phase space according to the equations of motion (5.9) and (5.10) with no particles being lost. The distribution function must therefore satisfy a continuity equation

$$\frac{\partial f}{\partial t} + \mathrm{div}_{\mathbf{x},\mathbf{v}}\left[(\dot{\mathbf{x}},\dot{\mathbf{v}})f\right] = 0, \tag{5.17}$$

where 'div' is the divergence operator in six dimensional space. The change in velocity is determined by the force that contains the exact electric and magnetic fields [see Eq. (5.10)]. These fields consist of the fluctuating fields that are due to discrete charged

particles within the Debye sphere as well as the more smeared out fields in accordance with the smoothed distribution function

$$\rho = \sum_i e_i \int f_i \mathrm{d}^3\mathbf{v}, \quad \mathbf{J} = \sum_i e_i \int \mathbf{v} f_i \mathrm{d}^3\mathbf{v}, \tag{5.18}$$

and the externally imposed fields. The influence of the discrete particles are called collisions and are modeled by a term $\partial f/\partial t|_{\mathrm{col}}$, for which an explicit expression is derived in section 1.5. Our kinetic equation thus can be written in the form

$$\frac{\partial f}{\partial t} + \mathrm{div}_{\mathbf{x},\mathbf{v}}\left[(\mathbf{v}, \frac{e}{m}(\mathbf{E} + \frac{\mathbf{v}\times\mathbf{B}}{c}))f\right] = \left.\frac{\partial f}{\partial t}\right|_{\mathrm{col}} \tag{5.19}$$

, where the fields in the left hand side are calculated from the sources given in Eq. (5.18). Because $\mathbf{x}$ and $\mathbf{v}$ are independent in this equation, and because

$$\frac{\partial}{\partial \mathbf{v}} \cdot \mathbf{v} \times \mathbf{B} = 0, \tag{5.20}$$

this equation can be written in the form

$$\frac{\partial f}{\partial t} + \mathbf{v} \cdot \frac{\partial f}{\partial \mathbf{x}} + \frac{e}{m}\left[\mathbf{E} + \frac{\mathbf{v}\times\mathbf{B}}{c}\right] \cdot \frac{\partial f}{\partial \mathbf{v}} = \left.\frac{\partial f}{\partial t}\right|_{\mathrm{col}}. \tag{5.21}$$

Which is the mentioned Fokker-Planck equation if one uses the collisional model discussed in section 1.5.

When collisions are neglected, i.e. when the right hand side of the equation above is set to zero, the equation is known as the Vlasov equation. This equation describes the collisionless limit, and is already rich in its structure since it is nonlinear in the velocity distribution through the electric and magnetic field which depend on the velocity distribution itself.

5.4 Landau damping

Landau damping is one of the most important kinetic effects. This damping can be obtained from the Vlasov equation and, therefore, it is a collisionless damping mechanism. We will assume a electro static wave for which the magnetic field is zero. From the Maxwell equations one finds

$$\mathbf{k} \times \mathbf{E} = 0 \quad \text{or} \quad \mathbf{E} \parallel \mathbf{k}, \tag{5.22}$$

the electric field is parallel to the wave vector. We will assume an electric field of the form

$$\mathbf{E} = \tilde{E} \cos[kx - \omega t]\mathbf{e}_x \tag{5.23}$$

where the wave vector has been chosen to lie in the x-direction. We will assume this electric field is sufficient small, such that it leads to a small perturbation only.

We will discuss the Landau damping on the basis of a Markoff process. This is a very unusual way of introducing the damping mechanism. In all text books it is introduced through the Vlasov equation. However, the mathematics is more complicated, and the interpretation as well as the limits of validity are not immediately clear. Below we will study the individual particle motion.

Since we will assume the electric field to be relatively small we can integrate the relevant equation of motion

$$m\frac{\mathrm{d}v}{\mathrm{d}t} = e\tilde{E}\cos[kx - \omega t] \tag{5.24}$$

along an unperturbed orbit

$$x = x_0 + v_0 t \tag{5.25}$$

The result is

$$\begin{aligned}
\Delta v &= \frac{e\tilde{E}}{m}\int_0^t \mathrm{d}t' \cos[kx_0 + (kv_0{-}\omega)t'] \\
&= \frac{e\tilde{E}}{m}\frac{1}{kv_0{-}\omega}\Big[\sin[kx_0 + (kv_0{-}\omega)t] - \sin[kx_0]\Big] \\
&= \frac{e\tilde{E}}{m}\frac{2}{kv_0{-}\omega}\sin\left[\frac{(kv_0{-}\omega)t}{2}\right]\cos\left[kx_0 + \frac{(kv_0{-}\omega)t}{2}\right]
\end{aligned} \tag{5.26}$$

It is clear from this expression that Δv will be large when $kv_0 - \omega = 0$, or

$$v_0 = \frac{\omega}{k}. \tag{5.27}$$

This is the resonance condition. When the particles have a velocity equal to the phase velocity of the wave they will 'see' a constant electric field in there frame of motion, and can therefore be accelerated or decelerated. If the velocity of the particle and the phase velocity are very different the particle will see a rapidly oscillating field from which it can not extract energy efficiently. Whether the change in velocity is positive of negative depends on the initial phase of the particle with respect to the wave (kx_0). We will assume that there is some random process that destroys the phase relation between the particles and the wave on a typical time-scale τ. This allows us to see the interaction with the wave as a Markoff process. We can directly derive that

$$\langle \Delta v \rangle = \frac{1}{2\pi\tau}\int_0^{2\pi} \mathrm{d}(kx_0)\Delta v\Big|_{t\to\tau} = 0 \tag{5.28}$$

$$\langle \Delta v \Delta v \rangle = \frac{1}{2\pi\tau}\int_0^{2\pi} \mathrm{d}(kx_0)\Delta v \Delta v\Big|_{t\to\tau} = \frac{e^2\tilde{E}^2}{m^2}\frac{2}{(kv_0{-}\omega)^2\tau}\sin^2\left[\frac{(kv_0{-}\omega)\tau}{2}\right] \tag{5.29}$$

The function $\langle \Delta v \Delta v \rangle$ is shown in Fig. 5.1. The following properties can be seen.

1. The function is peaked around the resonance condition. Only particles that have a velocity approximately equal to the phase velocity can change their energy efficiently.

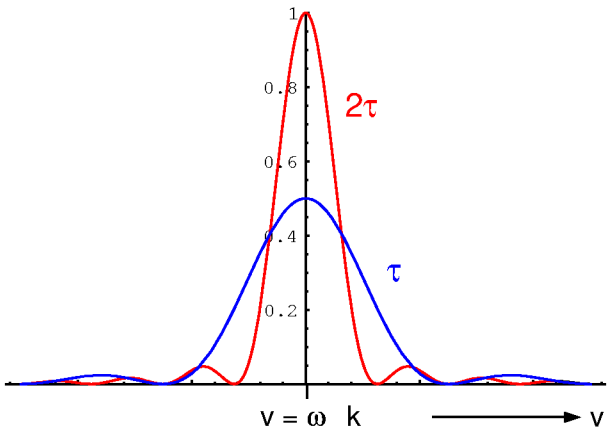

Figure 5.1: *The quantity* $\langle \Delta v \Delta v \rangle$ *as a function of* v.

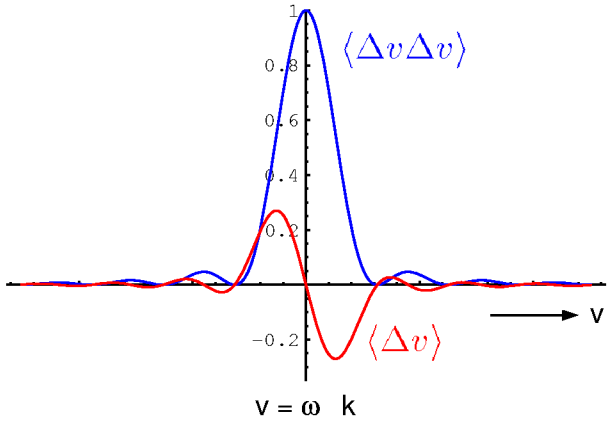

Figure 5.2: *The quantities* $\langle \Delta v \rangle$ *and* $\langle \Delta v \Delta v \rangle$ *as a function of* v.

2. There is a finite width of the resonance due to the finite coherence time τ. This width is roughly

$$\left(v - \frac{\omega}{k} \right) \tau \approx \pi \tag{5.30}$$

If the difference of the particle and the phase velocity is small, such that the particle does not appreciably changes its phase during the coherence time τ, it can still efficiently exchange energy with the wave. This effect is already beyond the usual derivation of the Landau damping from the Vlasov equation since in that case one obtains a delta function.

3. If one increases τ the maximum at $v = \omega/k$ increases, but also the width of the function decreases. The net exchange of energy between the particles and the wave turns out to be independent of τ.

For the linear perturbation we found that $\langle \Delta v \rangle = 0$, and $\langle \Delta v \Delta v \rangle \neq 0$. However, $\langle \Delta v \Delta v \rangle \propto \tilde{E}^2$, and therefore it is of second order in the small electric field. To be consistent we would also have to calculate $\langle \Delta v \rangle$ up to second order. This can be done

by again integrating the force due to the electric field along the perturbed orbit

$$\Delta x(t) = \int_0^t \Delta v(t')\mathrm{d}t' \tag{5.31}$$

where in this equation Δv is the lowest order change in the velocity v. If one assumes that τ is sufficient small such that $k\Delta x(\tau) < 1$ is satisfied, one can show that

$$\langle \Delta v \rangle = \frac{1}{2}\frac{\partial}{\partial v}\Big[\langle \Delta v \Delta v \rangle\Big], \tag{5.32}$$

where $\langle \Delta v \Delta v \rangle$ is given by the expression derived above. The dependence of Δv on v is shown in Fig. 5.2. This contribution can be understood as follows. If a particle is slightly slower than the wave and its phase relation is such that it looses energy it will become even slower and will then be out of resonance with the wave. However, if its phase relation is such that the energy is increased it will be brought into resonance with the wave and it can absorb energy for a longer time. Therefore, on average, the particles with velocities slightly smaller than the wave will be accelerated. Similar arguments apply to particles that are faster than the wave but they will have a net decrease in velocity.

Using the equation for the evolution of the distribution function one can calculate the change in energy of the particles, which is of course the energy absorption from the wave

$$\frac{\partial E}{\partial t} = \int \mathrm{d}^3\mathbf{v}\,\frac{1}{2}mv^2\frac{\partial f}{\partial t} = \int \mathrm{d}^3\mathbf{v}\left[mv\langle \Delta v \rangle + \frac{1}{2}m\langle \Delta v \Delta v \rangle\right] f \tag{5.33}$$

This expression is understandable since the change in energy of a single particle is

$$\frac{1}{2}m(v+\Delta v)^2 - \frac{1}{2}mv^2 = mv\Delta v + \frac{1}{2}m\Delta v \Delta v \tag{5.34}$$

We can now discuss the different mechanisms that contribute to the change in energy

1. The energy is quadratic in the velocity. Random changes in v lead to a non-vanishing change in the energy $m\langle \Delta v \Delta v \rangle/2$.

2. The average $\langle \Delta v \rangle$ is asymmetric in v, however, $\int v\langle \Delta v \rangle < 0$. If f is not a function of v then this term will give a negative contribution. It turns out that in this case the negative contribution exactly cancels the positive contribution of $m\langle \Delta v \Delta v \rangle/2$.

3. However if f is a function of velocity such that there are more particles for which $v < \omega/k$ than for $v > \omega/k$ $\int \langle \Delta v \rangle f > 0$, and there is a net increase in particle energy, i.e. an absorption of wave energy.

There will be a net absorption of wave energy if the gradient of the distribution function at $v = \omega/k$ is negative. That the absorption is proportional to the gradient in the distribution can also be seen if one writes the equation for the evolution of the distribution function in the form

$$\frac{\partial f}{\partial t} = \frac{1}{2}\frac{\partial}{\partial v}\left[\langle \Delta v \Delta v \rangle \frac{\partial f}{\partial v}\right] \tag{5.35}$$

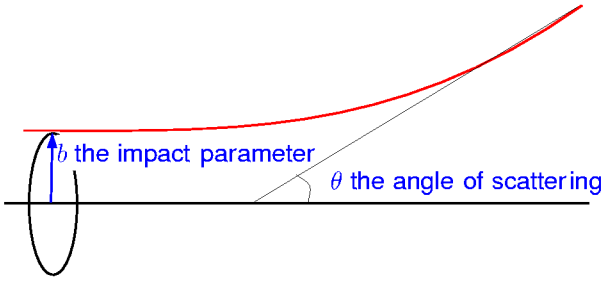

Figure 5.3: *Scattering of the particle in the center of mass frame*

i.e. the evolution is a diffusion equation in velocity space. If the gradient of the distribution is zero, the time derivative is also zero. If the gradient of the distribution is positive than the particles give energy to the wave. This will lead to an instability in which the wave amplitude is exponentially increasing. Such a process could be seen as a laser where the positive gradient means an population inversion.

Finally let us briefly discuss the limits of landau damping. If the coherence time becomes to long our linear calculations are no longer valid. Particles then make multiple bounces in the potential of the wave, i.e. they are trapped in this potential. Such a process in neglected in our calculations since we have assumed that $k\Delta x(\tau) < 1$, so no multiple bounces are allowed. The absorption in the case of multiple bounces goes down. The mechanism of Landau damping does not rely explicitly on collisions. However, there has to be some random process which destroys the coherence between the particles and the wave on a short enough time scale. In a plasma these are usually collisions. Since the amount of energy absorption is independent of the coherence time (if it is not too long) the collision frequency which could determine the coherence time without appearing explicitly in the expression for the amount of damping of the wave.

5.5 The Fokker-Planck collision term

As mentioned the discreteness of the particles leads to collisions. A two body coulomb interaction leads to a scattering over an angle θ in the center of mass frame as sketched in Fig. 5.3. This angle is determined by the impact parameter b through the equation

$$\sin(\theta/2) = \frac{b_0}{\sqrt{b^2 + b_0^2}} \tag{5.36}$$

where b_0 is the impact parameter for 90° angle scattering

$$b_0 = \left| \frac{e_i e_j (m_i + m_j)}{m_i m_j |\mathbf{v}_i - \mathbf{v}_j|^2} \right| \tag{5.37}$$

Three length scales can be introduced.

1. The impact parameter $b = b_0$ for ninety degree angle scattering.

2. The mean inter-particle distance $d = n^{-1/3}$

3. The Debye length λ_D which is the typical length scale over which the charge of a particle is screened by the other particles.

For $b < b_0$ large angle scattering collisions occur. For $b_0 < b < d$ the collisions are small angle scattering two body collisions. For $d < b < \lambda_D$ the collisions consist of many relatively weak interactions occurring at the same time. In this latter regime, however, we will treat the cumulative effect of the many interactions as the sum of independent two body processes.

The collisions lead to random changes in the velocities of the particles. Since particles which are separated by more than a Debye length do not interact due to the screening of the charge, only particles that are relatively close have to be considered in the collision processes. Since the Debye length is, for the plasmas of interest to us, much smaller than the plasma size, the plasma can be treated as approximately homogeneous on this scale and the collisions can be treated locally. The collision operator we hope to find depends on the local velocity distribution and does not require an integration over position.

We can now address the question: Is a change in velocity more likely to occur due to one large angle scattering collision or many small angle scattering collisions. Given a particle with velocity $\mathbf{v}$, then the number of large angle scattering collisions this particle undergoes per second is roughly given by

$$\pi b_0^2 \int |\mathbf{v}-\mathbf{v}'| f(\mathbf{v}') \mathrm{d}^3\mathbf{v}' \tag{5.38}$$

If we want to compare this rate with the small angle scattering processes we have to calculate how long it takes for many small angle scattering processes to generate a ninety degree angle scattering. The scatter angle for $b > b_0$ is roughly

$$\theta \approx 2\frac{b_0}{b} \tag{5.39}$$

This small angle scattering processes lead to a diffusion in θ with the diffusion coefficient being proportial to

$$D_{\theta\theta} = \int_{b_0}^{b_{\max}} \int |\mathbf{v}-\mathbf{v}'| 4\frac{b_0^2}{b^2} f(\mathbf{v}\prime) \mathrm{d}^3\mathbf{v} 2\pi b \mathrm{d}b = 8\pi b_0^2 \ln\left(\frac{\lambda_d}{b_0}\right) \int |\mathbf{v}-\mathbf{v}_1| f(\mathbf{v}_1) \mathrm{d}^3\mathbf{v}' \tag{5.40}$$

The typical time-scale for ninety degree angle scattering is

$$\delta t = \frac{\pi^2}{4 D_{\theta\theta}} \tag{5.41}$$

and therefore the quotient of this time and the time of one single ninety degree angle scattering is

$$\frac{32}{\pi^2} \ln\left(\frac{\lambda_d}{b_0}\right) \approx 3 \ln\left(\frac{\lambda_d}{b_0}\right) \tag{5.42}$$

Using the expressions for λ_d and b_0, assuming a plasma that consists of electrons and Hydrogen ions only, and using the estimate

$$\frac{e_1 e_2 (m_1 + m_2)}{m_1 m_2 |\mathbf{v}\text{-}\mathbf{v}_1|^2} \approx \frac{e^2}{3T} = \frac{1}{24\pi n \lambda_d^2} \tag{5.43}$$

one finds

$$\frac{\lambda_d}{b_0} = 24\pi\lambda_d^3 \propto \text{ the number of particles in the Debye sphere} \gg 1 \tag{5.44}$$

The logarithm appearing in the equation above is called the Coulomb logarithm. For fusion plasmas the logarithm has a typical value of 15 and the effect of small angle scattering collisions is clearly much larger than that of one single angle scattering collision. We will therefore, neglect the latter collisions.

Let us not derive the explicit form of the collision operator. We choose a coordinate system $(\mathbf{e}_1, \mathbf{e}_2, \mathbf{e}_3)$, with $\mathbf{e}_3$ aligned with the relative velocity $\mathbf{g} = \mathbf{v}\text{-}\mathbf{v}'$. The scattering over the angle θ leads to a change in the relative velocity

$$\delta\mathbf{g} = g(\cos\phi \sin\theta, \sin\phi \sin\theta, 1 - \cos\theta) \tag{5.45}$$

as sketched in Fig. 5.3. In the equation above the angle ϕ must be seen as a random angle. It then follows that there is no contribution that is first order in $\theta \ll 1$. We therefore, must go to second order. Since we consider small angle scattering the terms of increasing order are decreasing in magnitude. We therefore keep terms of second order only. The change in the $\mathbf{e}_3$ direction of a particle 1 colliding with particle 2 is

$$\delta\mathbf{v}_1 = \frac{m_2}{m_1 + m_2}\delta\mathbf{g} \approx -\frac{m_2}{m_1 + m_2}\mathbf{g}\frac{\theta^2}{2} = -\frac{2e_1^2 e_2^2 (m_1 + m_2)}{m_1^2 m_2}\frac{\mathbf{g}}{g^4}\frac{1}{b^2} \tag{5.46}$$

The change in the velocity $\mathbf{v}$ per second is

$$\begin{aligned} \langle\Delta\mathbf{v}\rangle &= -\frac{2e_1^2 e_2^2 (m_1 + m_2)}{m_1^2 m_2}\int \mathrm{d}^3\mathbf{v}' \int_{b_0}^{\lambda_d} 2\pi b \mathrm{d}b \frac{\mathbf{g}}{g^3}\frac{1}{b^2} f_2(\mathbf{v}') \\ &= -\frac{4\pi e_1^2 e_2^2 (m_1 + m_2)\ln\Lambda}{m_1^2 m_2}\int \frac{\mathbf{g}}{g^3} f_2(\mathbf{v}')\mathrm{d}^3\mathbf{v}' \end{aligned} \tag{5.47}$$

The change $\Delta\mathbf{v}$ in the direction perpendicular to $\mathbf{g}$ is zero to all orders because of the random angle ϕ. However, the average of $\Delta\mathbf{v}\Delta\mathbf{v}$ has a nonzero average. In this direction there is, therefore, a diffusion but no convection.

$$\begin{aligned} \Delta\mathbf{v}\Delta\mathbf{v} &\approx g^2\frac{\theta^2}{2}(\mathbf{e}_2\mathbf{e}_2 + \mathbf{e}_3\mathbf{e}_3) = \frac{\theta^2}{2}g^2\left(\frac{g^2\overline{\mathbf{I}}\text{-}\mathbf{gg}}{g^2}\right) \\ &= \frac{2e_1^2 e_2^2}{m_1^2}\left(\frac{g^2\overline{\mathbf{I}}\text{-}\mathbf{gg}}{g^4}\right)\frac{1}{b^2} \end{aligned} \tag{5.48}$$

The average over all particles that collide with particle 1 per second is

$$\langle\Delta\mathbf{v}\Delta\mathbf{v}\rangle = \frac{4\pi e_1^2 e_2^2 \ln\Lambda}{m_1^2}\int\left(\frac{g^2\overline{\mathbf{I}}\text{-}\mathbf{gg}}{g^3}\right) f_2(\mathbf{v}')\mathrm{d}^2\mathbf{v}' \tag{5.49}$$

If we now apply the equation we derived for the Markov process

$$\frac{\partial f_1}{\partial t} = -\frac{\partial}{\partial \mathbf{v}} \cdot \left[\langle \Delta \mathbf{v} \rangle f_1 \right] + \frac{1}{2} \frac{\partial}{\partial \mathbf{v}} \frac{\partial}{\partial \mathbf{v}} \left[\langle \Delta \mathbf{v} \Delta \mathbf{v} \rangle f_1 \right] \tag{5.50}$$

substitute our results for $\langle \Delta \mathbf{v} \rangle$ and $\langle \Delta \mathbf{v} \Delta \mathbf{v} \rangle$ and use the relation

$$\frac{\partial}{\partial \mathbf{v}'} \left(\frac{g^2 \bar{\mathbf{I}} - \mathbf{gg}}{g^3} \right) = -\frac{2\mathbf{g}}{g^3} \tag{5.51}$$

we can write the collision operator in the form

$$\frac{\partial f_1(\mathbf{v})}{\partial t} = \frac{2\pi e_1^2 e_2^2 \ln \Lambda}{m_1} \frac{\partial}{\partial \mathbf{v}} \cdot \int \mathrm{d}^3 \mathbf{v}' \left(\frac{g^2 \bar{\mathbf{I}} - \mathbf{gg}}{g^3} \right) \cdot \left[\frac{f_2(\mathbf{v}')}{m_1} \frac{\partial f_1(\mathbf{v})}{\partial \mathbf{v}} - \frac{f_1(\mathbf{v})}{m_2} \frac{\partial f_2(\mathbf{v}')}{\partial \mathbf{v}'} \right] \tag{5.52}$$

Note that the collision operator is a local operator, i.e. all quantities are evaluated in the same position. Also the operator is nonlinear in the distribution function.

The collision operator conserves particles

$$\int \mathrm{d}^3 \mathbf{v}\, C_{ab} = 0, \tag{5.53}$$

momentum

$$\int \mathrm{d}^3 \mathbf{v}\, [m_a \mathbf{v} C_{ab} + m_b \mathbf{v} C_{ba}] = 0, \tag{5.54}$$

and energy

$$\int \mathrm{d}^3 \mathbf{v}\, [m_a v^2 C_{ab} + m_b v^2 C_{ba}] = 0. \tag{5.55}$$

Furthermore it satisfies the H-theorem The change in the entropy density s due to collisions can be shown to be larger than zero

$$\frac{\partial s}{\partial t} = -\sum_a \sum_b \int \mathrm{d}^3 \mathbf{v}\, \ln f_a C_{ab} \geq 0. \tag{5.56}$$

The entropy production is zero if and only if the distribution function of all species is Maxwellian with a common temperature and mean velocity.

5.6 Relaxation times

In this section we first look at the typical time scales for slowing down and deflection of a test particle and then discuss the macroscopic relaxation times due to collisions.

Using a test particle and a Maxwellian background it is possible to derive relaxation times for a particle with a certain velocity. Because the momentum and energy of the test particle are small compared to the total momentum and energy, the integral part of the collision operator will be neglected. A test particle, initially described by a delta function $\delta(\mathbf{u}-\mathbf{u}_t)$, then experiences a drag and a spreading in velocity space. The spreading must be interpretated in a statistical manner. The value of the test particle

distribution for velocity $\mathbf{v}$ after some time t gives the probability that the test particle has velocity $\mathbf{v}$ at time t.

Below we briefly discuss the dependence of the diffusion (in velocity space) and slowing down on the particles energy The slowing down frequency ν_s is defined as

$$\frac{\mathrm{d}\mathbf{u}_t}{\mathrm{d}t} = -\nu_s \mathbf{u}_t, \tag{5.57}$$

where $\mathbf{u}_t$ is the test particle velocity.

In Fig. 5.4 the normalized slowing down frequency

$$\overline{\nu}_{s,tb} = \frac{m_e^2 v_{the}^3}{8\pi e^4 n \ln\Lambda}\nu_{s,tb} = \frac{m_e m_b}{m_t^2}\left[1+\frac{m_t}{m_b}\right]\frac{G[x\sqrt{m_b/m_e}]}{x}, \tag{5.58}$$

and the normalized diffusion coefficient parallel and perpendicular to the test particle velocity

$$\overline{D}_{\parallel} = \frac{m_e^2 v_{the}}{4\pi e^4 n \ln\Lambda} D_{\parallel} = \frac{m_e^2}{m_t^2}\frac{2G[x\sqrt{m_b/m_e}]}{x} \tag{5.59}$$

$$\overline{D}_{\perp} = \frac{m_e^2 v_{the}}{4\pi e^4 n \ln\Lambda} D_{\perp} = \frac{m_e^2}{m_t^2}\frac{\mathrm{Erf}[x\sqrt{m_b/m_e}]\text{-}G[x\sqrt{m_b/m_e}]}{x}, \tag{5.60}$$

are shown as a function of the normalized velocity $x = v/v_{the}$. In the equations the test particle (index t) and the background particles (index b) are assumed to have unit charge, and equal temperature. Erf is the error function and G

$$G(x) = \frac{\mathrm{Erf}[x]\text{-}x\mathrm{Erf}'[x]}{2x^2} \tag{5.61}$$

is the Chandrasekhar function. Three regimes can be identified

$u_t \ll v_{thi} \ll v_{the}$ The slowing down time and the diffusion coefficient are independent of energy.

$v_{thi} \ll u_t \ll v_{the}$ The effect of electron collisions is the same as the previous case. The effect of ion collisions however is different. The diffusion due to collisions with ions is mainly perpendicular to the test particles velocity. And both the diffusion coefficient and the slowing down frequency due to collisions with ions decrease as the test particle velocity increases.

$v_{thi} \ll v_{the} \ll u_t$ Diffusion is mainly perpendicular to the test particle velocity. Collisions with electrons and ions give roughly the same contribution. For ions the slowing down is mainly due to collisions with electrons, whereas for electrons the contribution of ion and electron collisions are approximately equal.

The relaxation times discussed so far are the "microscopic" relaxation times of a test particle. One can also define macroscopic relaxation times by calculating the typical time scale for momentum and energy transfer between different species, assuming that

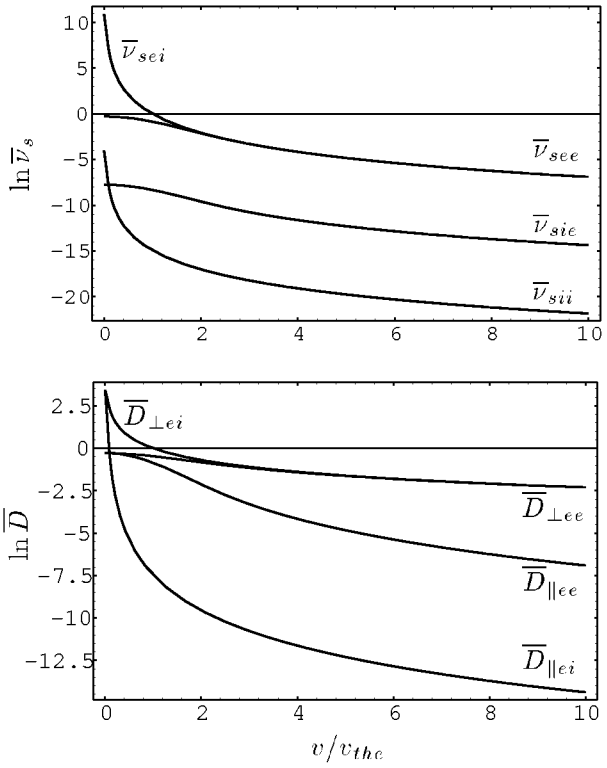

Figure 5.4: *Slowing down frequency and parallel and perpendicular diffusion coefficient.*

the distribution of every species is given by a Maxwellian, however, with different mean velocity and temperature. The momentum transfer time between species a and b is calculated by assuming equal temperature but different mean velocity $\mathbf{u}_a$ and $\mathbf{u}_b$. One can derive that

$$\mathbf{F}_{ab} = m_a n_a (\mathbf{u}_b - \mathbf{u}_a)/\tau_{ab}, \tag{5.62}$$

with the momentum transfer time τ_{ab} being

$$\tau_{ab}^{-1} = \frac{16\sqrt{\pi} n_b e_a^2 e_b^2}{3 m_a} \ln \Lambda_{ab} \left[\frac{1}{m_a} + \frac{1}{m_b} \right] \frac{1}{(v_{tha}^2 + v_{thb}^2)^{3/2}} = \nu_{ab}, \tag{5.63}$$

with ν_{ab} being the collision frequency. From Eqs. (5.62) and (5.63) one can derive that $\mathbf{F}_{ab} = -\mathbf{F}_{ba}$. For like particle collisions a collision time τ_{aa} can be defined by taking $a = b$

$$\tau_{aa}^{-1} = \frac{4\sqrt{\pi} n_a e_a^4 \ln \Lambda_{aa}}{3 m_a^{1/2} T_a^{3/2}}. \tag{5.64}$$

In this time a distribution function that consists of two Maxwellians which are shifted with respect to each other relaxes to one Maxwellian with the mean velocity determined by momentum conservation. In the case of a small mass ratio $m_a/m_b \ll 1$ one finds

$$\tau_{ab}^{-1} = \frac{4\sqrt{2\pi} n_b e_b^2 e_a^2 \ln \Lambda_{ab}}{3 m_a^{1/2} T_a^{3/2}}. \tag{5.65}$$

The energy exchange time is calculated assuming the species have a different temperature. The energy exchange rate is

$$Q_{ab} = \int \mathrm{d}^3\mathbf{v} \, \frac{1}{2} m_a v^2 C_{ab} - \mathbf{u}_a \cdot \mathbf{F}_{ab}. \tag{5.66}$$

One can derive that

$$Q_{ab} = \frac{3n_a m_a (T_b\text{-}T_a)}{\tau_{ab}(m_b + m_a)}, \tag{5.67}$$

from which it follows that the energy exchange time is

$$\tau_{ab}^E = \frac{m_a + m_b}{2m_a}\tau_{ab}. \tag{5.68}$$

Again it can easily be verified that $Q_{ab} = \text{-}Q_{ba}$.

It follows from the expressions above that

$$\begin{aligned} &\tau_{ee} : \tau_{ee}^E : \quad \tau_{ii} \quad : \quad \tau_{ii}^E \quad : \tau_{ei} : \quad \tau_{ie} \quad : \quad \tau_{ei}^E \quad : \quad \tau_{ie}^E \quad \approx \\ &1 \ : 1 \ : \sqrt{m_i/m_e}\ \sqrt{m_i/m_e}\ 1 \ : \ m_i/m_e \ : \ m_i/m_e \ : \ m_i/m_e. \end{aligned} \tag{5.69}$$

The slowest processes are the energy exchange between electron and ions and the momentum transfer from electrons to ions. It is therefore possible to have a two temperature plasma with both species having approximately the Maxwell distribution due to like particle collisions. The electrons will reach this Maxwell faster than the ions. Due to the efficient pitch angle scattering of electrons by ions the electron-ion collision frequency is of the same order as the electron-electron collision frequency. Because of the high ion mass the scattering of ions by electrons is small and the ion-electron collision frequency is $\sqrt{m_e/m_i}$ smaller than the ion-ion collision frequency.

Chapter 6

Plasma Heating

Dirk Hartmann

6.1 Introduction

In chapter 2 it was shown that the reaction D+T $\rightarrow$^{4}He +n +17.6 MeV will most likely be used in a fusion reactor because it has the highest cross-section at the lowest energies. Even so, the required plasma temperature to ignite the fusion plasma is still about 10 keV and thus much higher than what occurs during plasma start-up in tokamaks and stellarators. Therefore some additional heating is required to raise the plasma temperature until the fusion reaction commences to a sufficient extent and supplies the necessary heating. After the plasma has ignited the α-particles, i.e. ^{4}He, continue to heat the plasma and balance the energy loss of the plasma due to radiation and particle leakage.

Over the past 40 years of fusion research different means have been proposed and investigated to heat a plasma. Of those, some heating methods have been found to be particularly suitable to heat a fusion plasma to sufficiently high temperature. They have been used to used to study plasmas under situations similar to those that will be encountered in a fusion reactor. An overview over these heating methods is given in this chapter. The reader interested in more detailed information is referred to the literature [1-4]. The heating schemes to be discussed include the following:

Ohmic heating (OH) assumes a singular role. It is the Joule dissipation of the toroidal plasma current that is driven in a tokamak. By itself this heating does not suffice to drive the plasma to reactor relevant temperatures. It is not usable for stellarators since it would unduly modify the magnetic field structure.

Neutral beam injection heating (NBI) consists of injecting a beam of neutral fuel atoms at high energy into the plasma. These neutral atoms can cross the magnetic field lines but are confined by the very same magnetic field once they have become ionized in the plasma. Beam energy and plasma density determine the location where most of the beam becomes ionized. Through collisions the beam ions transfer their energy to the bulk plasma.

Electromagnetic wave heating consists of launching high power electromagnetic waves into the plasma. Depending on the choice of frequency, plasma density and composition different constituents of the plasma can be heated. Wave heating is predominantly applied in the range of the ion cyclotron frequencies (30-100 MHz), lower hybrid frequencies (1-10 GHz) and electron cyclotron frequencies (50-150 GHz).

α-particle heating, finally, sustains the plasma temperature in a fusion reactor. Only few fusion experiments operate with the same gas mixture of deuterium and tritium as a reactor; thus α-particle heating usually does not take place in fusion experiments. Initially the α-particles carry 20% of the fusion energy, i.e. 3.5 MeV. But they need to be confined sufficiently long so that they can impart their energy onto the other plasma constituents while thermalizing. Control of the current profile, then solely determined by the bootstrap current, might still require additional ohmic or non-inductive current.

Heating of the plasma means that the kinetic energy of the electrons and ions is increased. The heating schemes employed usually do not heat the different plasma species by the same amount. Rather only a fraction of the plasma particles is given kicks in velocity. Furthermore, this velocity increase is not isotropic. Thus, in most cases, applying a heating method to the plasma causes a deviation of the Maxwellian velocity distribution. Subsequent collisions between the heated fraction and the bulk plasma, however, lead to randomization and equipartition of the additional energy. This additional energy, in turn, causes enhanced radiation losses and particle losses to the walls. Eventually, the plasma reaches a new steady-state where the energy input per time balances the energy losses and where the velocity distribution of the plasma constituents has some deviation from a Maxwellian. This power flow is schematically shown in Fig. 6.1. There the conversion efficiency of the electric power into heating power (up to 50% in some cases) and the loss in the process of coupling the heating power to the plasma have been included.

If a neutral beam is injected at an oblique angle or if waves are launched predominantly in one direction with respect to the main magnetic field then not only the temperature profile but also the current profile is changed due to the heating, i.e. the velocity distribution of the electrons is no longer symmetric with respect to the direction of the magnetic field. This so called **non-inductive current drive** is desirable for tokamaks in order to extend the pulse duration and to access operation regimes of superior confinement which often depend on the current profile. Current drive might also be necessary for stellarators in order to compensate for the bootstrap current.

6.2 Ohmic heating

A current flows in the plasma if an electric field is applied in the direction of the magnetic field. This current is predominantly carried by electrons since the ions are basically immobile. Due to the finite resistivity of the plasma the current is dissipated by Joule heating.

In the electric field, E, the electrons are accelerated up to a drift velocity at which the driving force of the field is balanced by the frictional force due to collisions with the

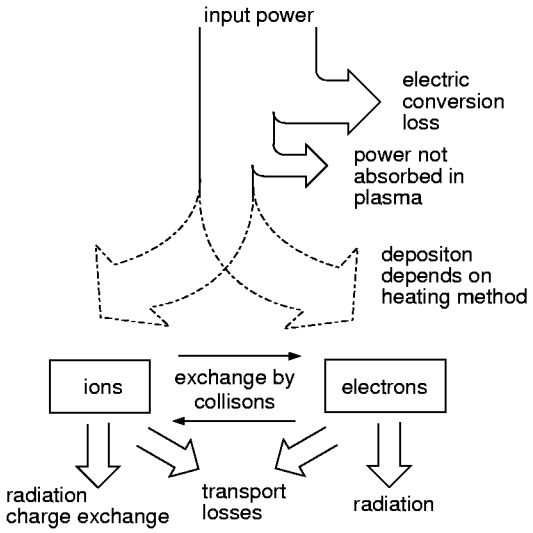

Figure 6.1: Principle of power flow for plasma heating.

ions and other electrons. Ohm's law applies and the plasma resistivity, η, is defined by $E = \eta j$, where j is the parallel current density. The plasma resistivity was calculated in chapter 1. It decreases with plasma temperature as $T_e^{-3/2}$. The local ohmic power density, p, is given by $p(r) = \eta(r)j^2(r)$. Usually the current profile is peaked in the center where the electron temperature is highest. The total heating power is calculated by integration to be

$$P = 2\pi R \cdot 2\pi \int_0^a \eta(r) j^2(r) r dr,$$

where R is the major and a is the minor radius of the plasma. Even though the resistivity decreases with temperature, this in itself does not rule out the use of ohmic heating to raise the plasma temperature till ignition. The plasma current, however, cannot be arbitrarily increased since it has been found, that magnetohydrodynamic stability requires the q-value at the plasma edge, q_a, to be greater than 2 (see chapter 6.2). Thus with $q_a = aB_\phi/RB_\theta > 2$ and $B_\theta = \langle j \rangle \pi a^2 \mu_0 / 2\pi a$ one obtains for the average current density

$$\langle j \rangle < \frac{1}{\mu_0} \frac{B_\theta}{R}.$$

In ASDEX Upgrade this limits the plasma current to 1.6 MA. The central current could be higher, but this would also increase the sawtooth-activity (see chapter 7.3).

The maximum achievable temperature can be estimated from power balance: $\eta j^2 = 3nT/\tau_E$, where τ_E is the energy confinement time which is dependent on plasma parameters (chapter 7.5). The empirical knowledge of many experiments and of different operating regimes has been condensed into statistical scaling laws for τ_E. For ohmic tokamak discharges it has been found that τ_E does not depend on plasma current, but depends on central plasma density and minor radius. For typical densities and magnetic fields one predicts temperatures of about 3 - 4 keV which are much too low for ignition, leading to the requirement of additional heating. Unfortunately the situation is even aggravated by the finding that for these additional heating methods the energy confinement time depends on the total input power P_{tot} according to $\tau_E \propto P_{tot}^{-0.5}$. Thus in order

to double the energy content of the plasma the heating power has to be quadrupled. The proportionality factor and the details of the scaling depend on the confinement regimes of stellarators and tokamaks. In recent years plasma research has focussed on confinement regimes where this proportionality factor is higher (chapter 7.6).

Technically the toroidal electric field is induced in the tokamak by changing the magnetic flux ϕ through the center of the torus (chpater 2.6). The plasma in the torus constitutes the single secondary winding of a transformer. The flux through the center of the torus is changed by ramping the current in the primary windings.

6.2.1 Neutral beam injection heating

A beam of plasma fuel atoms (H, D, T) at high velocities ($\geq$ 50 keV) is injected into the plasma since only neutrals can cross the magnetic field lines. In the plasma the beam atoms are ionized through ionization by electrons (important only at low electron temperatures of 1 keV), charge exchange (dominant process below 90 keV for deuterium beam), and ionization by ions (dominant process above 90 keV for deuterium beam). In total these different processes lead to an approximately exponential decay of the beam neutral density along its path. In a reactorgrade plasma a 100 keV deuterium beam has a decay length of about 0.3m. Since the diameter of a reactor plasma will be much larger this would entail edge heating. Therefore it is desirable to go to higher injection velocities in order to penetrate deeper into the plasma.

Once the beam atoms have become ionized the ions follow drift orbits according to the magnetic field structure of the plasma. Efficient heating with neutral beam injection requires that the ions are well confined in the plasma during the time it takes them to slow down and impart their energy on the bulk of the plasma. Neutral beam injectors are usually set up such so to inject the beams at an acute angle to the magnetic field lines as to limit trapping of the ions in local magnetic mirrors and possible concurrent ion loss to a small portion of the beam, even though it is technologically demanding to fit the beam duct between the field coils. Other loss mechanisms include reverse charge exchange processes with the remaining neutrals in the plasma and - in small devices -insufficient ionisation in the plasma, so called shine-through.

The beam ions are slowed down by collisions with plasma ions and electrons. For typical values of $T_i = T_e = 5$ keV and 100 keV deuterium beam the velocities are ordered as : $v_i^{th} \ll v_i^b \ll v_e^{th}$. At high beam energies collisions with electrons are the most frequent. They cause the beam to be slowed down without much change of the direction of propagation and cause the electrons to be dragged along. After the beam energy has become smaller than a critical energy, E_c, given by

$$E_c = 14.8 \frac{A_b}{{A_i}^{2/3}} T_e,$$

where A_b, A_i are the charge states of the beam ions and plasma ions respectively, collisions with plasma ions become dominant. These lead to a scatter in the direction of the original beam velocity in addition to the slowing down. Together, the decrease of the beam energy, E_b, is given by:

$$\frac{dE_b}{dt} = -2\frac{E_b}{\tau_s}[1 + \left(\frac{E_c}{E_b}\right)^{3/2}]$$

where τ_s is the slowing down time of an ion by an electron with faster velocity (see chapter 3). The first term describes the slowing down on electrons and the second term describes the slowing down on ions. The total energy imparted on ions during the slowing down process of a beam with initial energy, E_{b0}, can be calculated by integrating the second part of the equation. The result is shown in Fig. 6.2. Nowadays many experiments have beam energies comparable to the critical energy, thus NBI equally heats ions and electrons. At ASDEX Upgrade the injection energy is 55 keV for deuterium and the critical energy of a 3 keV deuterium plasma is $E_c = 57$ keV.

The basic elements of a neutral beam injection system are shown in Fig. 6.3. Efficient acceleration of the beam particles is only possible with electric fields and requires them to be charged. These particles, say D^+, are generated in an RF or hot tungsten wire plasma discharge. This plasma is kept in a "bucket" with permanent magnets aligned on the outside walls to limit the interaction between the plasma and the walls. One side of the bucket consists of a grid. The ions are extracted through this grid and accelerated in a positive electric field of up to several hundred keV. The hole structure of the extraction and acceleration grids allow some steering of the beamlets. By passing the beam through a gas target at low density the beam is partially neutralized through charge exchange processes. A magnet after the neutralizer separates out the unwanted fraction of still unneutralized ions and electrons and steers them onto a water-cooled dump. The neutrals are unaffected by the magnetic field and propagate through the beam duct into the plasma. Strong vacuum pumps are required to keep the pressure low in the beam duct and at the appropriate levels in the neutralization chamber. Usually the ion source also creates D_2^+ and D_3^+. These molecules gain the same energy during the acceleration process, but have a lower velocity corresponding to their higher mass and they get ionized closer to the plasma edge. Therefore initial beam ion energies in the plasma then are distributed over energies at E_{b0}, $E_{b0}/2$ and $E_{b0}/3$.

Beams with energies higher than 100 keV are necessary to penetrate deeper into the plasma. The neutralization efficiency of the gas target decreases rapidly with beam energy. It has its maximum of 60 % at 19 keV. The neutralization efficiency of negative ions, D^-, depends less on the beam energy because the affinity of the additional electron to the deuterium is weak. However, extracting large beam currents of negative ions out of an ion source is difficult, even though it can be improved by adding cesium to the source plasma. A large fraction of electrons leaves the ion source together with the ions which need to be separated out by additional small magnetic fields in the extraction region. The goal of the present research endeavors is to extract 40 A of ion current and accelerate it to 1 MeV as to be useful for ITER [5].

Neutral beam injection has proven very reliable on a number of fusion experiments. Some of its advantages are that the injectors can be tested separately on test-beds, the power deposition can be calculated to good accuracy and injecting neutrals into the center of the plasma is a means of particle refueling. Disadvantages are that the injectors have to be in the immediate vicinity of the torus thus they are being subject to high neutron fluxes and tritium contamination. Present research on NBI focuses on the further development of

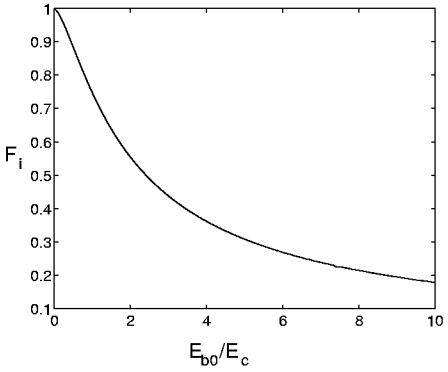

Figure 6.2: Fraction F_i of the initial beam energy E_{b0} going to ions during the slow down process.

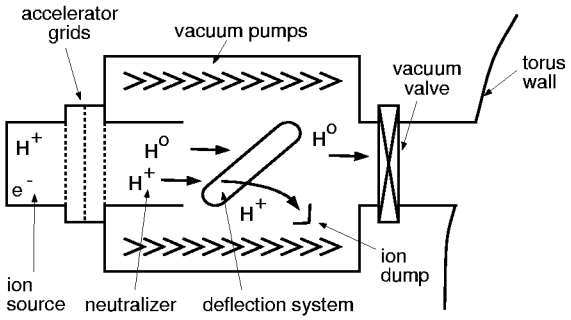

Figure 6.3: Principle of neutral beam injection line.

injectors based on negative ion acceleration, new neutralizers based on plasma discharges or lasers, with the goal of reaching high efficiency and continuous operation.

6.3 Electromagnetic wave heating

Heating the plasma with electromagnetic waves has been proposed early on and has since then been used successfully on many fusion devices. Good heating efficiency requires sufficiently strong absorption wave mechanisms in the plasma. They exist for frequencies in the range of the ion cyclotron frequency (30-80 MHz), in the range of the lower hybrid frequency (several GHz) and in the range of the electron cyclotron frequency (several tens of GHz). For electromagnetic waves outside these frequency ranges absorption generally is weak due to the small collision frequencies in a fusion grade plasma.

The ideal wave heating system consists of a generator that is capable of delivering high power electromagnetic waves at the desired frequency and that is preferably able to operate steady state. The electromagnetic wave power is transported using low loss transmission lines to a structure inside of the plasma vessel that acts like an antenna. The antenna couples to a wave that can propagate in the plasma such that all the incoming wave power is launched into the plasma. The wave then transports the power to a desired location in the plasma where the wave is completely absorbed, i.e. where the wave imparts all its power onto a group of plasma particles. During the time that these particles take to slow down by collisions and spread their additional energy to the rest of the plasma they are not lost from the plasma confinement region. Eventually a new steady-state situation arises between the driving force by the wave and the collisional drag of the plasma that leads to a deviation of the particle velocity distribution from a Maxwellian.

For most of the interesting frequency ranges the size of the fusion plasma is much larger than the wavelengths of the excited plasma waves. In addition, the plasma pressure is much smaller than the magnetic pressure so the propagation of the waves in the plasma can be described to good approximation with the cold plasma dispersion relation of chapter 10.3.2. derived for an infinite homogeneous plasma where the dispersion

relation is solved at each location with the local values of plasma density, magnetic field, etc.. In the local cartesian coordinate system the z-axis points into the direction of the static magnetic field B_0 which points into the toroidal direction. The antenna imposes boundary conditions and fixes the values of k_z of the launched waves for a given frequency, ω, of the wave generator. From the local dispersion relation one can then find the solutions $N_x \equiv ck_\perp/\omega$ of the plasma waves. It gets interesting where N_x=0 (cutoff) or $N_x = \infty$ (perpendicular wave resonance). Cutoffs mark regions of the plasma where the wave cannot propagate and resonances mark regions where the phase and group velocity go to zero, thus where the wave energy is bound to pile up unless "something happens". Near former regions the waves are being reflected and regions beyond the cutoff are not accessible save by some generally weak wave tunneling through the cutoff-region where $N_x < 0$. In the latter region the phase velocity becomes smaller than the thermal velocity of the plasma particles and the cold plasma dispersion relation is no longer sufficient to describe the plasma properly. Rather thermal effects need to be included. This can be done in an orderly fashion by including the particle velocity distribution in the derivation of the dispersion relation as was done for some special cases in chapter 10.4.. This tremendously increases the complexity of the dispersion relation but also resolves the unphysical resonances since they are replaced by additional solutions of the dispersion relation. At the former resonances coupling to new waves occurs. The dispersion relation also predicts damping of the waves. This does not come as a surprise since the Kramers-Kronig relations state (based on causality) that resonances in the real part of the dispersion relation are connected with a non-vanishing imaginary part (usually predicting damping).

The damping processes of the wave can be understood on a kinematic level. If a charged particle moves in the same direction and with about the same speed as the phase velocity of a wave and a component of the wave electric field points into the direction of propagation, the wave electric field in the moving frame of the particle stays constant and the particle is accelerated or decelerated depending on its position with respect to the wave. If there are more particles that are decelerated than there are particles that are accelerated then there is net energy transfer from the wave to these resonant particles. The wave is damped and the average velocity of the particles is increased. For a Maxwellian velocity distribution wave damping can become significant for waves with phase velocities between one and three times the thermal velocity. Since collisions only partially restore the distribution function such an absorption process leads to a local deviation in velocity space. This damping mechanism is called Landau damping (chapter 3.4). With the addition of a static magnetic field the situation becomes slightly more complicated. The motion along the magnetic field still separates out and a wave-particle resonance is possible if the wave has an electric field component along the magnetic field and its phase velocity component, $\omega/k_\parallel$, and the particle velocity component, $v_\parallel$, fulfill the requirement: $v_\parallel - \omega/k_\parallel \approx 0$. This is called Landau damping. Electromagnetic waves in the plasma with frequencies of several GHz (waves in the range of the lower hybrid resonance frequency) have phase velocities on the order of the thermal velocities in the plasma and are absorbed by this damping mechanism.

If the wave has a circularly polarized component it can also couple to the gyro-motion of the particles. Resonant interaction requires $v_\parallel - \omega/k_\parallel - l\Omega/k_\parallel \approx 0$ where l is the number of the harmonic. This process is called Landau cyclotron damping. The resonance condition

says that energy transfer between the wave and the resonant particles is possible not only if the Doppler-shifted wave frequency matches the gyro-frequency of the particle, Ω, but also if it is a multiple, l, of this frequency. If $l \neq 1$ it is necessary that the wave field has a gradient perpendicular to the magnetic field. Consider heating at the first harmonic, i.e. $l = 2$. Let's say that at one point particle velocity and electric field point in the same direction and the particle is being accelerated. After the particle has rotated half a gyro-orbit, the electric field has already completed a full revolution. Thus the electric field points again in the same direction, yet the velocity direction of the particle is reversed and the particle is decelerated during the second half of its gyro-motion. On average no net energy transfer takes place. If, however, the electric field changed magnitude over the plane of the gyro-orbit of the particle, i.e. if the electric field has a gradient, then net energy transfer does become possible.

A similar damping process exists involving the interaction between the magnetic moment of the gyrating particle and the axial magnetic field of the wave, where the magnetic moment replaces the charge and the magnetic field replaces the wave electric field in above discussion. It is called transit time magnetic pumping (TTMP).

Concludingly, an electromagnetic wave that can propagate into a plasma and is not hindered by cutoffs from accessing a perpendicular wave resonance, can be absorbed there. The absorption coefficient depends on (1) the amount of the wave power that is converted into a wave that has the (2) proper polarization and phase velocity to be resonant with particles of the plasma and (3) the slope of the velocity distribution function of the resonant particles. In addition, large field amplitudes can lead to a nonlinear enhancement of the wave absorption process.

The changes in the distribution function, in particular if a tail of fast, confined particles with decreased collision frequencies is created, can be useful for current drive if the toroidal symmetry is broken and the waves are preferentially launched into one direction.

In the cold plasma dispersion relation resonances do occur if N_x^2 goes to infinity which is the case when

$$K_{xx} \equiv 1 - \sum_s \frac{\omega_{ps}^2}{\omega^2 - \omega_{cs}^2} = 0,$$

where ω_{ps} is the plasma frequency and ω_{cs} is the signed cyclotron frequency of species s. This yields resonances at the lower hybrid frequency $\omega_{lh}^2 \equiv \omega_{ps}^2/(1 + \omega_{pe}^2/\omega_{pe}^2)$, the upper hybrid frequency $\omega_{uh} \equiv \omega_{ce}^2 + \omega_{pe}^2$ and at the ion-ion-hybrid frequency (close to the ion cyclotron frequencies). The latter occurs only in a multi species plasma. Surprisingly no resonances occur at the ion cyclotron or the electron cyclotron frequencies, ω_{ci} and ω_{ce}, respectively. At these frequencies the cyclotron motion of the ions and electrons short-circuits the circularly polarized wave component that rotates in the same direction as the considered species, thus completely quelling a possible resonance. As mentioned earlier, thermal and relativistic corrections in the case of electrons need to be included to obtain the cyclotron resonances.

These resonances define the predominant frequency ranges used for RF plasma heating in today's large magnetic confinement experiments. They will be discussed in detail in the following. For completeness also Alfvén waves will be discussed briefly even though none of the large experiments employ them in a heating scheme.

6.3.1 Alfvén wave heating

Near the plasma edge an arrangement of current carrying poloidal conductors, called current straps, excites a fast wave in the plasma. The wave propagates perpendicularly across the magnetic surfaces until it hits the Alfvén resonance, which is the confluence of the slow and the fast wave.

In the considered frequency region, $\omega \ll \omega_{ci}, \omega_{ci}$, the cold plasma dielectric tensor elements are given by, $K_{xx} \approx \omega_{pi}^2/\omega_{ci}^2$, $K_{xy} \approx 0$, $K_{zz} \approx -\omega_{pe}^2/\omega^2$, and with $\omega_{pe}^2/\omega^2 \gg 1$ the dispersion relation becomes:

$$(N_z^2 - K_{xx})(N_x^2 + N_z^2 - K_{xx}) = 0.$$

This dispersion relation has two solutions:

slow (shear Alfvén) wave: $\omega = k_\parallel v_A$,

fast (compressional Alfvén) wave: $\omega = k v_A$,

where $v_A \equiv \omega_{ci}/\omega_{pi} \cdot c$ is the Alfvén velocity encountered earlier.

In an inhomogeneous plasma for given frequency, ω, and parallel wavenumber, $k_\parallel$, the shear Alfvén wave exists only on one magnetic surface where the density and magnetic field are such that $\omega = k_\parallel v_A$. Group and phase velocity are tangential to that surface. The compressional Alfvén wave, however, can propagate across the magnetic surfaces until it approaches the shear wave surface. There the compressional wave couples its energy to the shear wave which is subsequently damped on electrons. This location is the Alfvén resonance and the whole process is schematically shown in Fig. 6.4.

The wavelength of the compressional wave is about one meter. This requires wide antennas because the high $k_\parallel$-components of the antenna are evanescent as seen from $k_x^2 = \omega^2/v_A^2 - k_\parallel^2 < 0$.

Up to now not much encouraging experimental data exists. Usually there was no unique sign of heating. However, since the theoretically predicted current drive efficiency is high, interest in this form of heating has not waned.

Heating in the ion cyclotron range of frequencies

Again, the fast wave is launched in the plasma by a set of poloidal current-carrying conductors. They travel almost perpendicular to the magnetic field lines into the plasma center where they can be absorbed at an ion cyclotron resonance or an ion-ion-hybrid resonance. The location of these resonances depends predominantly on the magnetic field strength. In a tokamak, for example, the toroidal magnetic field decreases radially proportional to 1/R, thus the resonant zones are vertical layers where $\omega_{ci}(R) = \omega$.

In this frequency range, $\omega \approx \omega_{ci}$, except at very low density the slow wave is evanescent. Then $|K_\parallel| \gg |K_{xx}|, |K_{xy}|$ and the fast wave dispersion relation is given by:

$$N_x^2 = K_{xx} - N_z^2 - \frac{{K_{xy}}^2}{K_{xx} - N_z^2}$$

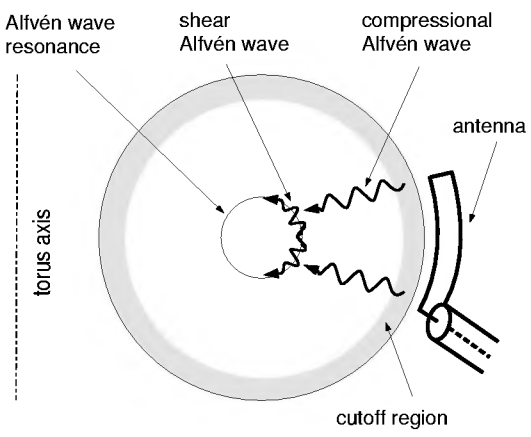

Figure 6.4: Principle of Alfvén wave heating.

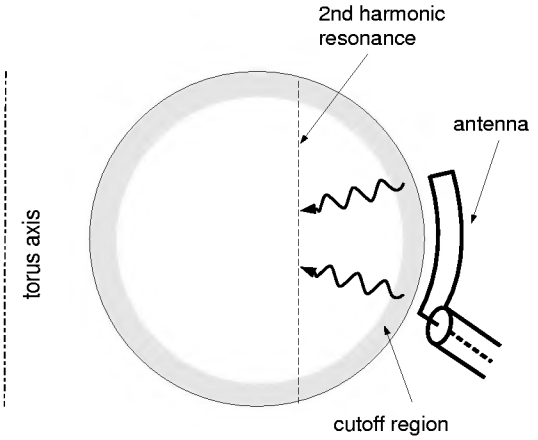

Figure 6.5: Principle of 2nd harmonic ion cyclotron heating.

This wave is elliptically polarized with a small component of the electric field in the direction of the magnetic field. There is a cutoff at the plasma edge for densities $< 2 \times 10^{18} m^{-3}$. Note that, as said before, for a single species plasma this dispersion relation does not have a resonance even though K_{xx} goes to infinity at the ion cyclotron resonance. The situation changes if finite Larmor radius effects (FLR) are taken into account or the plasma is allowed to have more than one ion species.

After FLR contributions have been added to the fast wave dispersion relation one finds that due to the parallel electric field component and for higher electron temperatures there is weak Landau and TTMP damping of the electrons even if no ion resonance is in the plasma. Using this process is called "fast wave heating" and is often used to drive a current in the plasma by phasing the current straps such that the radiated $k_{\|}$-spectrum is skewed. The current is not only an effect of the local changes in the velocity distribution function but also due to the decreasing collision frequency at higher velocities that alleviates sustaining the changes in the distribution function. More about current drive at the end of this chapter.

With the addition of the FLR contribution to the dielectric tensor elements absorption zones appear in the vicinity of the harmonics of the ion cyclotron layers and Landau cyclotron damping can occur. The resonance width is usually small compared to the minor radius of the plasma. Using this process is called "cyclotron harmonic damping". To determine the strength of the damping also the polarization of the wave in the vicinity of the resonance has to be included. Even with FLR effects the damping at the fundamental resonance is small due to the unfavorable polarization. It has its maximum at the second harmonic and decreases to higher harmonics. Fig. 6.5 shows the evanescent zone near the plasma edge where $N_x^2 < 0$ and the resonance layer for 2nd harmonic heating in a tokamak-like cross-section.

At the fundamental the change in the distribution is uniform over all velocities, at the higher harmonics a tail of fast particles is created that becomes more anisotropic with velocity since the particles predominantly gain perpendicular energy.

If the plasma consists of another species of low concentration, say the omnipresent hydrogen in a deuterium plasma, absorption at the hydrogen resonance becomes very strong

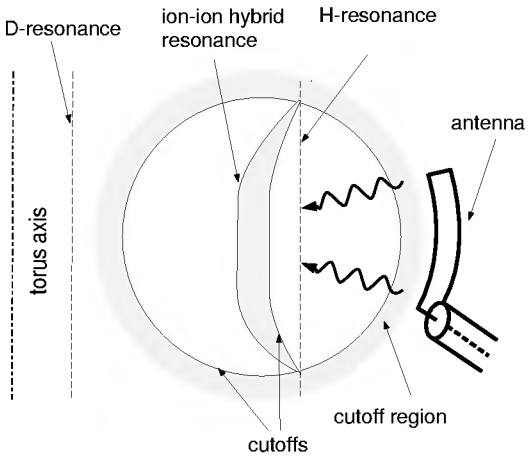

Figure 6.6: Principle of mode-conversion heating.

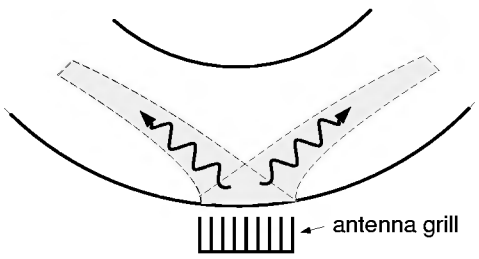

Figure 6.7: Wave propagation for lower hybrid heating.

due to Landau cyclotron damping on the hydrogen. This is possible because in the vicinity of the hydrogen resonance a considerable fraction of the wave power is left circularly polarized because the polarization is determined by the majority deuterium. This scheme is called minority heating. Because all the power is absorbed by the minority ions, a strong tail in the distribution function is created. The energies are often higher than the critical energy, E_c, and the tail relaxes mostly due to collisions with electrons.

For a higher concentration of the second species the beneficial effect on the polarization in the vicinity of the resonance of the second species decreases and so does the damping. However, above a critical concentration of a few per cent a new resonance and an associated cutoff occur: the ion-ion-hybrid resonance. The location of cutoffs and resonances are shown schematically in Fig. 6.6 for the case of hydrogen in deuterium. The resonance calls again for a more detailed analysis using the FLR expansion. It is found that near this resonance a mode-conversion of the fast wave to an ion-Bernstein wave occurs. The ion-Bernstein wave has an electric field component in the direction of the magnetic field and is strong Landau damped on electrons. Now the location of the antenna becomes important. If it is located on the low field side the wave is only weakly damped at the cyclotron resonance. At the cutoff it is partly reflected and it partly tunnels to the resonance layer where it then couples to an IBW. There is an upper limit of about 25% of the power of the fast wave that can mode convert to an IBW on a single pass. If the antenna is located on the high field side direct coupling to the IBW is possible. Except for some stellarator-like experiments RF antennas are usually installed on the low field side for practical reasons.

The direct heating of the electrons through this mode-conversion scheme makes it again possible to use it for current drive. However, the location of the mode-conversion layer is critically dependent on the concentration of the minority species thus the repeatability of the experiments very much depends on the gas inventory of the apparatus walls.

Low loss coaxial transmission lines and generators (that were developed for radio communications etc.) are readily available. Usually in antennas the radiated power is only a small fraction of the reactive power. Therefore they are coupled with other reactive

elements to form a resonant circuit that is matched to the impedance of the transmission lines.

Good absorption efficiencies, in particular in dense and hot plasmas, have been obtained. The large electric fields in the antenna and the dependence of the plasma coupling on the plasma properties intrinsically link the RF system to the plasma such that separate testing and conditioning are of limited use only.

Present research focuses on a better understanding of the antenna plasma coupling, more detailed investigation of the absorption mechanisms and the development of higher power cw generators.

6.3.2 Lower hybrid heating

A slow wave is launched with a wave guide. In the plasma it travels at a small angle with respect to the magnetic field lines, this causes the wave to circle the torus several times until the center of the plasma is reached. Landau damping along the path often becomes more important than ion damping near the lower hybrid resonance.

In the lower hybrid frequency domain the ordering is $\omega_{ci} \ll \omega_{lh} \ll \omega_{ce}$. The dispersion relation of the slow mode is approximately given by

$$N_x^2 = K_{zz}(1 - N_z^2/K_{xx}).$$

As in the preceding RF heating schemes the wave has to tunnel through an evanescent region in front of the antenna until a minimal density given by the perpendicular Alfven resonance is reached. A typical cutoff density is $10^{18} m^{-3}$.

Depending on the $k_\parallel$ of the launched spectrum the slow wave can couple to the fast wave and since the group velocity of the fast wave is such as to transport the power back to the plasma edge the wave energy then becomes trapped in the plasma periphery. This occurs for n_c smaller than a critical density, n_c, given by:

$$n_c^2 = \frac{1}{1 - \omega^2/|\omega_{ce}\omega_{ci}|}$$

For typical parameters this means that the parallel wavelength needs to be shorter than 0.2 m. For slow waves that well fulfill this requirement the ratio of group velocity perpendicular and parallel to the magnetic field is independent of $k_\parallel$, thus the wave energy travels into the plasma along well collimated beams mainly along the toroidal direction. With approach of the resonance the angle to the magnetic field lines decreases further. This behavior is schematically shown in Fig. 6.7.

Even though the wave might not yet have reached the resonance its electric field component parallel to the toroidal magnetic field causes Landau damping on the electrons. Since the $k_\parallel$-spectrum of the launched waves is often quite wide (limited by the accessibility condition and the upper end of the antenna spectrum) the resonant velocities extend from the electron thermal velocities up to a substantial fraction of the speed of

light. Thus an electron tail is created extending to very high energies. Near the lower hybrid resonance strong ion damping occurs, predominantly through nonlinear stochastic damping on the ion cyclotron motion.

The antenna arrays consist of a phased array of open rectangular waveguides arranged such that the RF electric field is aligned with the magnetic field. The shape of the antenna face resembles the plasma shape to be able to move the antenna as close as possible to the plasma surface. However, experiments have shown that the antenna creates its own plasma, thus coupling is usually not at problem. The RF generators used are klystrons.

The creation of the long tail in the electron distribution function and the natural occurance near the plasma edge have sparked interest in lower hybrid current drive. Today's technologies of antenna grill launchers allow the necessary tailoring of the $k_{\|}$-spectrum. Experimentally the current drive efficiencies are the best achieved, particularly at low densities and high magnetic fields.

6.3.3 Electron cyclotron resonance heating

In contrast to the two preceding RF heating methods, at electron cyclotron frequencies no evanescent region between the antenna and the plasma exists. Thus the proper polarization can be chosen at the antenna and the desired plasma wave can be excited with good conversion ratio. Only since the mid 70s generators, called gyrotrons, have become available that operate in the frequency range of the electron cyclotron resonance. In this range only electrons respond to the waves since $\omega \approx \omega_{ce} \approx \omega_{pe} >> \omega_{ci}, \omega_{pi}$.

Two plasma modes exist: the O-mode and the X-mode. The O-Mode is linearly polarized with $E||B$ and the X-mode is elliptically polarized with $E \perp B$. For perpendicular propagation ($N_z = 0$), the dispersion relations are given by:

O-mode: $N_x^2 = 1 - \omega_{pe}^2/\omega^2$

X-mode: $N_x^2 = \left(1 - \frac{\omega_{pe}^2}{\omega^2} - \frac{\omega_{ce}}{\omega}\right)\left(1 - \frac{\omega_{pe}^2}{\omega^2} + \frac{\omega_{ce}}{\omega}\right)\left(1 - \frac{\omega_{pe}^2}{\omega^2} + \frac{\omega_{ce}^2}{\omega^2}\right)^{-1}$

The O-mode has a cutoff at the electron plasma frequency. The X-mode has a cutoff below the electron plasma frequency and above the upper hybrid frequency. Fig. 6.8 and Fig. 6.9 schematically show the location of resonances and cutoffs for O- and X-mode. For O-mode heating the electron cyclotron resonance is only accessible for densities below the cutoff given by $\omega_{pe}^2 = \omega^2$. For X-mode heating, because of the additional cutoff, the electron cyclotron resonance is only accessible from the high field side. However, similar to the ion cyclotron resonance, for perpendicular propagation the polarization of the X-mode is almost circular left-handed, thus coupling to the electrons and damping is weak. Efficient absorption requires oblique propagation, whereby the X-mode attains an increasingly right-handed polarization. Again stronger absorption is obtained at the second harmonic. The absorption process is dependent on thermal and relativistic corrections, yet the absorption region is usually very narrow and much smaller than the plasma radius, thus making ECRH useful for localized heating in order to suppress MHD activity.

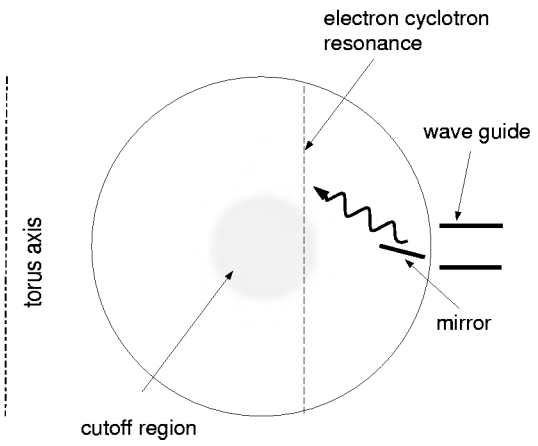

Figure 6.8: Principle of fundamental O-mode heating.

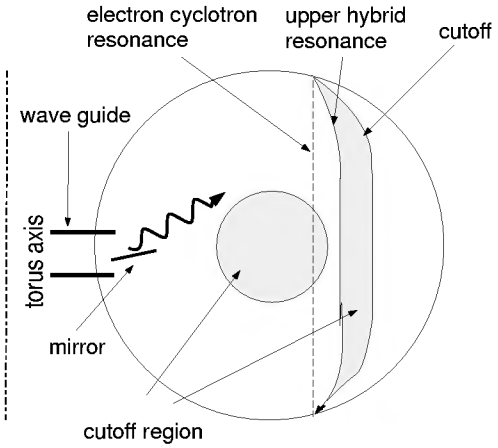

Figure 6.9: Principle of fundamental X-mode heating from high field side.

The limitation to use ECR heating at densities higher than cutoff has recently been overcome by coupling from an O-mode to an X-mode that finally mode-converted to an electron-Bernstein-wave. This tricky scheme is possible at a particular angle of incidence. The experimental proof is a fine example of the predictive power of the warm plasma dispersion relation as well as how sophisticated ECRH experiments have become.

The RF power in the electron cyclotron range of frequencies is generated using gyrotrons. In these devices an electromagnetic wave is coupled to spiraling electrons in a steady magnetic field. The bunching of the electrons in phase space amplifies the wave. Care is taken to amplify only one waveguide mode, e.g. the TE_{02}. Output powers of up to 600 kW for several seconds have been obtained and research is aiming at 1 MW cw gyrotrons. The RF power is coupled out of the gyrotrons using ceramic and lately diamond windows. Latter have very low absorption and high thermal conduction coefficients allowing edge cooling.

Transmission lines consist of waveguides with different mode converters to change the gyrotron output mode into an TE_{11}-mode for O-mode heating or an HE_{11} for X-mode heating. Transmission of Gaussian beams using quasi-optical lines have recently also become available. Finally inside of the torus the direction of the beam can be changed using movable mirrors, allowing off-axis heating without changing the frequency or magnetic field.

The pinpoint accuracy of ECRH due to its narrow deposition profile and the possibility of ray-tracing calculations in an inhomogeneous plasma have made ECRH a valuable and reliable tool. Technical development and testing can be done independently of the plasma. Thus the "power horse" of W7-X will be ECRH with the ambitious goal of 10 $\times$ 1 MW cw gyrotrons.

6.4 α-particle heating

The collisional energy transfer between the 3.5 MeV α-particles to the bulk plasma is the process that will sustain the plasma temperature in a fusion reactor, since the neu-

trons leave the plasma without interaction. However, even the α-particles might not be confined sufficiently long by the magnetic field to thermalize completely. Possible loss mechanisms involve the toroidal field ripple and interaction with coherent MHD activity (toroidal Alfvén eigenmodes). In tokamaks the α-particle confinement improves with plasma current and in stellarators the magnetic field configuration can be optimized. First experimental studies of α-particles were done during D,T shots in fusion experiments TFTR and JET basically confirming the understandings of the loss mechanisms.

6.5 Non-inductive current drive

The discussed heating schemes usually heat only a small fraction of the plasma particles. This can be taken advantage of by asymmetric wave launching or by tangential neutral particle injection to drive a current in the plasma. This is useful in order to reduce or eliminate the necessity of ohmic current in a tokamak or to compensate for the pressure-driven bootstrap current in a stellarator.

A current drive efficiency, γ_{th}, can unambiguously be defined as the ratio of local parallel current density, j, and the local absorbed power density, p: $\gamma_{th} = j/p$. Different experiments are often compared using a scaled figure of merit, γ_{ex}, defined as:

$$\gamma_{ex} = \frac{\bar{n}_e[10^{20}m^{-3}]R[m]I[A]}{P[W]},$$

where $\bar{n}_e$ is the line-averaged density, R is the major radius of the plasma, i.e. the distance between the torus axis and the center of the plasma column, I is the driven plasma current and P is the total absorbed power. With $I \approx \pi a^2 j$ and $P = \pi a^2 \cdot 2\pi R \cdot p$ and $j/p \propto 1/\bar{n}_e$ it is easy to confirm that $\gamma_{th} \propto \gamma_{ex}$.

A number of physical concepts can be used to drive a current in a plasma. The following will be mentioned briefly: pushing of electrons, asymmetric electron collisionality and difference in electron and ion drift.

Electrons are being pushed along the magnetic field lines using Landau damping of waves that are launched in the plasma. This changes the velocity distribution of the resonant electrons until the collisional relaxation balances the driving force. If the antenna current straps are phased properly the waves are launched predominantly in one direction inside the torus, thus a net electron current results. For $\omega/k_{\|} \ll v_e^{th}$ the absolute change in electron momentum for a given loss of energy of the wave is large, but a large fraction of the electrons are trapped in the toroidal field ripple and the collision frequency is large. For $\omega/k_{\|} \gg v_e^{th}$ the collision frequencies are small but there are also few electrons in the distribution function. The compilation of these two effects leads to a theoretical curve shown in Fig. 6.10 identifying the regions of 'bulk" and 'tail" current drive. Lower hybrid, fast wave and ion-Bernstein wave mode-conversion change the tail of the electron distribution function. Alfvén wave current drive is expected to change the bulk with good efficiency. the expected current drive efficiency is $\gamma_{th} \approx 1$. whereas the other RF heating methods have efficiens of $\gamma_{ex} \approx \gamma_{th} \approx 0.1$ at $T_e = 10$ keV with a linear increase with electron temperature.

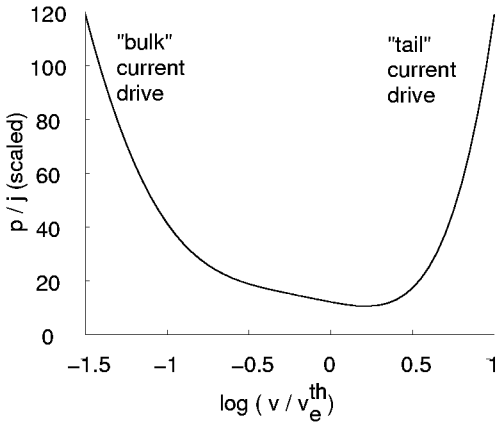

Figure 6.10: Normalized current drive efficiency for Landau damping.

Electron cyclotron heating predominantly changes the perpendicular temperature of the electrons and does not impart much parallel momentum. Still current drive is possible since the electrons that fulfill the resonance condition $v_{\|} = (\omega - \omega_{ce})/k_{\|}$ (relativistic effects are neglected) and are heated will attain a lower collision frequency due to their higher velocity. Therefore their collisional relaxation will be reduced. Actually, this effect is also of great importance for current drive based on Landau damping. Yet there is a small caveat. Because of the radial dependence on the magnetic field, this resonance occurs only a small region next to the location where $\omega = \Omega(r)$. Electrons on the high field side of this resonance will also meet the requirement $v_{\|} = (\omega - \omega_{ce})/k_{\|}$, albeit for reversed velocity. Therefore it is necessary that the wave is strongly damped. Otherwise one creates a shear layer in the current profile without any change in the total current.

If a neutral beam is injected at an angle, the slowing down of the beam ions on the electrons drags the electrons along. This electron current only partially cancels the ion current for two reasons. Firstly, if the plasma consists of two species of different charge states the different ion-electron collision times cause the electron drift to match more closely the ions of the highest charge state. Secondly, electron trapping in the toroidal magnetic field ripple reduces the electron drift. Current drive efficiencies of $\gamma_{ex} \approx 0.03$ have been obtained.

Bibliography

[1] J. Wesson, *Tokamaks*, Sec. Edition, Clarendon Press, Oxford 1997.

[2] K. Miyamoto, *Plasma Physics for Nuclear Fusion*, Rev. Edition, MIT Press, Cambridge, 1989.

[3] M. Wakatani, *Stellarator and Heliotron Devices*, Oxford University Press, New York, 1998.

[4] R.I. Pinsker, Phys. Plasmas, **8**, 1219 (2001).

[5] W. Kraus, Rev. Sci. Inst., **69**, 956 (1998).

Chapter 7

Introduction to Stellarator Theory

Ralf Kleiber

7.1 Introduction

7.1.1 Some history

The stellarator concept was introduced in 1951 by the astrophysicist Lyman Spitzer. In order to introduce rotational transform (see sec. 7.1.2) in a toroidal configuration he proposed to twist a torus into a shape resembling the shape of the number 8 (figure-eight stellarator).

Some years later the first stellarator confinement experiment was built in Princeton (Princeton C stellarator) but was not successful: The plasma was lost very quickly. As was understood later this was mainly due to an incomplete knowledge about the behaviour of resonances in magnetic surfaces. While the Princeton stellarator experiment was still plagued by a low confinement time (a few Bohm times[1] at $T_e \approx 100$ eV) Russian scientists at the 1968 IAEA Novosibirsk conference showed that, with a confinement concept called tokamak, it was possible to achieve an electron temperature of about 1 keV for 30 Bohm times.

This historical situation resulted in the fact that tokamaks became the main line of fusion research in the world while the stellarator concept was pursued only in some places, mainly at the IPP Garching and at the University in Kyoto. Today there is a renewed interest in the stellarator concept as an alternative to the tokamak: A large stellarator of the torsatron[2] type (Large Helical Device (LHD)) started its operation 1998 in Japan at the NIFS; also the German-EU Wendelstein 7-X experiment is being constructed in Greifswald and scheduled to start operation in 2010. Also a new experiment (National Compact Stellarator Experiment (NCSX)) is planned in the USA. Other (smaller) stellarators are in use in the USA (HSX), Spain (TJ-II) and Australia (H-1).

[1] The Bohm time $\tau_B = \frac{a^2}{D_B}$ (a: minor radius) is defined via the Bohm diffusion coefficient $D_B = \frac{1}{16}\frac{k_B T_e}{eB}$.

[2] The stellarator concept appears under different names, e.g. heliotron, torsatron, heliac, which mainly distinguish the way the coil systems were historically constructed. In this text we will not elaborate on this, instead we will use just the collective notion "stellarator".

7.1.2 Some basic notions

Figure 7.1 shows the basic torus geometry of a fusion device with the poloidal and toroidal angles ϑ and φ. The ratio $A = \frac{R}{a}$ of major to minor radius is called the aspect ratio.
If for a given magnetic field $\mathbf{B}(\mathbf{r})$ a function $\Psi(\mathbf{r})$ exists in a region of space such that $\mathbf{B}\cdot\nabla\Psi = 0$ then the surfaces $\Psi(\mathbf{r}) = const$ are called flux surfaces (i.e. the magnetic field is tangent to these surfaces). The existence of nested[3] flux surfaces (fig. 7.1 shows three such surfaces), at least in the main volume of the device, is an essential prerequisite for plasma confinement by a magnetic field. The innermost flux surface that is degenerated into a line is called the magnetic axis. If the equilibrium consists only of nested flux surfaces they are distinguished by a flux surface label $s \in \mathbb{R}$.
A field line on a given flux surface can be specified by a (non-periodic) function $\vartheta = f(\varphi)$. If φ increases by $2\pi n$ ($n \in \mathbb{N}$) the angle ϑ changes by an amount ϑ_n. The quantity ι defined by $\iota := \lim_{n\to\infty} \frac{\vartheta_n}{2\pi n}$ is called the rotational transform[4] and has the same value for each field line on a given flux surface; in general ι is a function of the flux surface label. The s-derivative of the rotational transform is called shear ι'. A flux surface s_0 where the rotational transform is rational $\iota(s_0) = \frac{n}{m}$ ($m, n \in \mathbb{Z}$) is called a rational surface[5]. On a rational surface all field lines are closed lines while on a non-rational surface one field line fills the surface ergodically.
Even if magnetic surfaces do not exist one can obtain a good impression of the field structure by following a field line for many turns and marking with a point the positions where it intersects an arbitrarily chosen poloidal plane. The collection of these points is called a Poincaré plot (an example of this can be seen in fig. 7.7). In such a plot a flux surface shows up by points forming a closed curve.

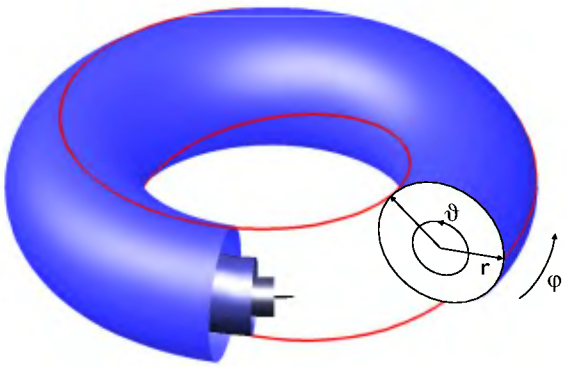

Figure 7.1: Toroidal geometry with nested flux surfaces, magnetic axis and a field line (red) with $\iota = 0.38$.

[3] Be M_S the set of points enclosed by a flux surface S. Then nested means that for all pairs (S_1, S_2) $M_{S_1} \subseteq M_{S_2}$ or $M_{S_2} \subseteq M_{S_1}$.
[4] In the simplest approximation ι can be regarded as the pitch of the field line on the flux surface.
[5] Since the set of rational numbers $\mathbb{Q}$ is dense in $\mathbb{R}$ the same is true for the set of rational surfaces with respect to all flux surfaces.

7.1.3 Tokamak, Stellarator

The way in which the rotational transform ι is generated can be used to distinguish two classes of fusion devices: tokamaks and stellarators. In a tokamak the plasma current, which is e.g. driven by the externally induced electric field, causes the poloidal field that in combination with the toroidal field from the (toroidal) field coils leads to a twisting of the magnetic field lines and thus to a rotational transform. Since usually the current density is highest at the center of the torus ι decreases with increasing radius.

In a stellarator the rotational transform is caused solely by a coil system externally to the plasma without any total plasma current J, i.e.

$$J := \int_{A_\mathrm{P}} \mathbf{j} \cdot d\mathbf{A} = 0, \tag{7.1}$$

where $\mathbf{j}$ is the current density and A_P is a poloidal plasma cross section. Since the influence of the coils is strongest at larger radii the rotational transform increases with increasing radius.

So one main difference between tokamak and stellarator is the existence or absence of a total toroidal plasma current.

The beneficial role of a total plasma current for confinement in a tokamak has two main accompanying disadvantages: Firstly it can lead to violent instabilities called disruptions which destroy the plasma confinement and secondly – in a standard[6] tokamak – the operation time is limited by the necessity of inducing an electric field. An advantage of the tokamak concept is that a tokamak possesses rotational symmetry and thus is a two-dimensional configuration.
The main advantages of a stellarator are that because of $J = 0$ it is inherently disruption free and can be used to achieve steady state operation. It is easy to show that the condition $J = 0$ cannot be satisfied for an axisymmetric configuration and thus a stellarator must have three-dimensional geometry. This makes stellarators geometrically and computationally more complex than tokamaks but, as we will see in the following sections, offers much more flexibility in their design which can be used for their optimisation.

Although in principle the three-dimensional geometry of a stellarator need not have any symmetries one usually imposes two symmetry requirements (see fig. 7.2):

- Periodicity: Invariance against a rotation by $\frac{2\pi}{P}$ in the toroidal direction, where P is the number of – so called – field periods.
- Stellarator symmetry: Invariance against flapping around certain lines.

In a tokamak the rotational transform is of first order in the poloidal field component B_P: $\iota \sim \frac{B_\mathrm{P}}{B_0}$, ($B_0$ is the total field). For a stellarator the first order effect of the helical field component B_h causes the field line to wiggle while the rotational transform, i.e. the poloidal shift that remains after averaging, is only of second order: $\iota \sim \left(\frac{B_\mathrm{h}}{B_0}\right)^2$. This

[6] This is not the case for the so called advanced tokamak where bootstrap current (driven by density and temperature gradients) and current drive are responsible for ι.

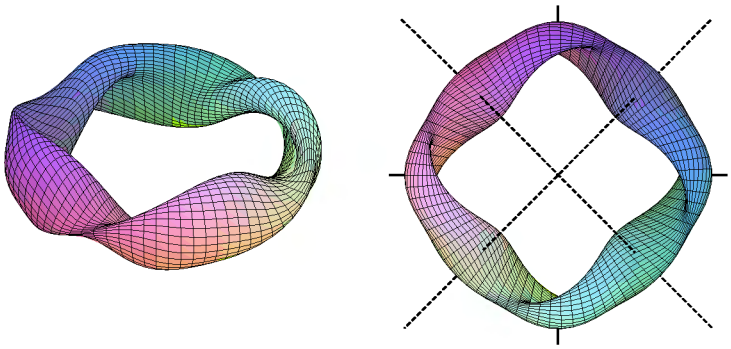

Figure 7.2: Side (left) and top (right) view of a stellarator with $P = 4$. The field periods and the lines for the stellarator symmetry are denoted by short and dashed lines, respectively (here both types of lines do have the respective complementary feature).

behavior of the field line can be understood if one rewrites eq. (7.1) (using $\mathbf{j} = \nabla \times \mathbf{B}$) as a line integral around a poloidally closed curve ∂A_p giving $J = \int_{\partial A_\mathrm{p}} B_\mathrm{p}\, dl = 0$. For this integral to be zero the poloidal field component B_p has to change sign which implies an oscillating behavior of the field line.
Both effects are illustrated for a straight $\ell = 2$ stellarator in fig. 7.3; the wiggling is conspicuous while the rotation of the field line reflects the rotational transform.

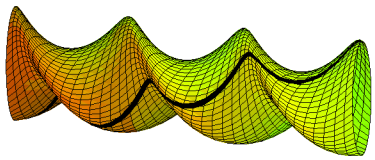

Figure 7.3: Three-dimensional view of one flux surface of a straight ℓ=2 stellarator (three field periods). The thick black line shows one field line.

7.1.4 Coil system

An important part in the engineering design of a stellarator is the question how a coil system must look like in order to produce the desired magnetic field. The classical coil system for e.g. an ℓ=2 stellarator consists of groups of interlinked coils (fig. 7.4 left): A set of planar coils generating the toroidal field component and four helical coils carrying currents running in alternating directions in neighboring coils[7] responsible for the helical field components. The drawback of this kind of coil system is that strong forces can arise between the interlinked coils thus making it difficult to build. Also it can only be used for relatively simple configurations due to its low flexibility with regard to design.

Another possibility for finding a suitable coil system comes from the following observation: If in a toroidal volume V a magnetic field is given that on the boundary surface ∂V is tangential it is possible to calculate a surface current distribution on a second surface outside of ∂V that generates this field; discretizing this current distribution then leads

[7] A configuration with currents flowing always in the same direction is called a torsatron; it does not have toroidal field coils, but instead needs two coils generating a vertical field component.

to a coil system[8]. This way of obtaining a coil system is crucial for the design of modern optimised stellarators since it allows to start from a given plasma shape, which e.g. is obtained by stellarator optimisation (see sec. 7.6), and then calculate the corresponding – so called – modular coil system, which consists of a set of non-planar coils.

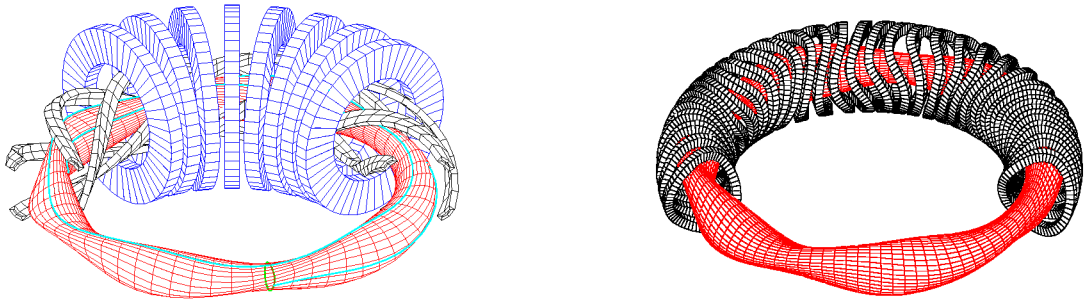

Figure 7.4: Classical (left) and modular (right) coil system for an ℓ=2 stellarator.

7.2 Equilibrium

7.2.1 Equilibrium equations

The system of equations to be solved for a macroscopic fluid equilibrium follows from the general magnetohydrodynamic (MHD) equations by assuming $\frac{\partial}{\partial t} = 0$ and $\mathbf{v} = 0$:

$$\mathbf{j} \times \mathbf{B} = \nabla p, \tag{7.2}$$

$$\nabla \times \mathbf{B} = \mu_0 \mathbf{j}, \tag{7.3}$$

$$\nabla \cdot \mathbf{B} = 0. \tag{7.4}$$

Equation (7.2) gives the balance between Lorentz force and pressure force while eqs. (7.3–7.4) are Maxwells equations. One immediate conclusion is $\mathbf{B} \cdot \nabla p = 0$, i.e. the pressure is constant along a field line and consequently – assuming the existence of flux surfaces – it must be constant on each flux surface. From $\mathbf{j} \cdot \nabla p = 0$ it follows that the current can only flow in a flux surface.

7.2.2 Straight stellarator

It was mentioned in the last section that a stellarator cannot be axisymmetric, so the simplest possible stellarator is a helical symmetric configuration, i.e. all the physical quantities (using cylindrical coordinates) depend only on r and $\varphi - kz$, where k is the parameter determining the length of a period.

[8]Since the corresponing mathematical problem is not well posed there are many different coil systems giving nearly the same magnetic field. This allows to take into account engineering constraints in an optimisation procedure which combines aspects of field accuracy and coil flexibility.

For a vacuum field one has to solve the equation $\Delta\Phi = 0$ to obtain the magnetic potential (b_ℓ are free coefficients)

$$\Phi = B_0 z + \frac{1}{k}\sum_{\ell=1}^{\infty} b_\ell \, I_\ell(\ell k r) \, \sin \ell(\varphi - kz).$$

From this follows an expression for the magnetic surfaces for a general straight stellarator:

$$\Psi = B_0 \frac{kr^2}{2} - r\sum_{\ell=1}^{\infty} b_\ell \, I'_\ell(\ell k r) \, \cos \ell(\varphi - kz) = const.$$

Figure 7.2.2 shows the cross section of stellarators each having only one ℓ component; due to the helical symmetry the curves rotate around the origin for increasing z. Note that the ℓ=1 stellarator is the only one with a non-straight magnetic axis.
Since straight configurations are only of theoretical interest we will in the following always assume toroidal topology.

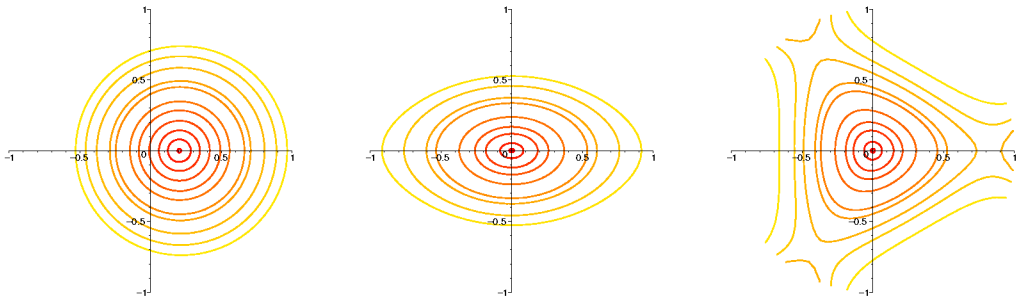

Figure 7.5: Intersection of $\Psi = const$ surfaces with the $z = 0$ plane for an $\ell = 1, 2, 3$ stellarator (from left).

7.2.3 Magnetic coordinates

Typical for a fusion plasma is the extremely high degree of anisotropy introduced by the magnetic field. As an order of magnitude estimate for the perpendicular and parallel length scale one can take the ion gyroradius which is of the order of some 10^{-2} m and the parallel mean free path of a particle which is around some 10^3 m, respectively. Thus it is highly advantageous to have at one's disposal a coordinate system in which the field line can be described by a simple functional form and a separation of the perpendicular and parallel direction is easy.
The so called magnetic coordinates (s, ϑ, φ) are a special curvilinear coordinate system fulfilling these requirements. Here $s \in [0:1]$ is the flux surface label – using magnetic coordinates requires the assumption that nested flux surfaces exist everywhere – and $\vartheta, \varphi \in [0:1]$ are angle-like coordinates. The geometric complexity of the configuration thus becomes hidden in the metric tensor g_{ij}. For calculations in this coordinate system one can use the formalism of tensor calculus.

In magnetic coordinates the magnetic field has the simple form

$$\mathbf{B} = \frac{1}{\sqrt{g}}\left(F'_{\mathrm{T}}\,\mathbf{r}_{,\varphi} + F'_{\mathrm{P}}\,\mathbf{r}_{,\vartheta}\right),$$

where $F'_{\mathrm{T}}, F'_{\mathrm{P}}$ is the s derivative of the toroidal ($F_{\mathrm{T}}(s)$) and poloidal ($F_{\mathrm{P}}(s)$) magnetic flux, $\sqrt{g}$ is the determinant of the metric tensor and $\mathbf{r}_{,\varphi}, \mathbf{r}_{,\vartheta}$ are the covariant basic vectors. This expression shows that in magnetic coordinates the field lines are just straight lines $\vartheta = \iota\,\varphi$ with the rotational transform given by $\iota = F'_{\mathrm{P}}/F'_{\mathrm{T}}$.

7.2.4 Magnetic islands

One vital question for a fusion device is if it possesses nested flux surfaces or not.

Because of axisymmetry this question is simple to answer for a tokamak. Its symmetry allows to reduce the MHD equilibrium equations to one elliptic equation for the flux function $\Psi(r, z)$: the Grad-Shafranov-Equation

$$\left(r\frac{\partial}{\partial r}\frac{1}{r}\frac{\partial}{\partial r} + \frac{\partial^2}{\partial z^2}\right)\Psi + \mu_0 r^2 \frac{\partial p(\Psi)}{\partial \Psi} + \frac{\mu_0}{8\pi^2}\frac{\partial I^2(\Psi)}{\partial \Psi} = 0, \tag{7.5}$$

where $p(\Psi)$ and the current distribution $I(\Psi)$ are arbitrary functions. The fact that p only depends on Ψ ensures a constant pressure on each flux surface. Specifying profiles for p and I and imposing boundary conditions on Ψ (e.g. $\Psi = 0$ at the given plasma boundary) this (in general) nonlinear equation can be solved and directly gives the flux surfaces. Thus there is no problem for axisymmetric equilibria.

For three-dimensional configurations it is generally not possible to show that a flux function exists making it very complicated to obtain information about the existence of flux surfaces.
The complications arising in connection with three-dimensionality can be seen by the following gedanken experiment: Imagine bending a straight stellarator, which always possesses flux surfaces (see eq. (7.2.2)), into a torus. This process can be regarded as adding perturbations with Fourier amplitude $\mathcal{P}_{mn}$ to the original straight equilibrium in order to produce the new toroidal one. It can be shown that the surface which is in resonance with the perturbation $\mathcal{P}_{mn}$ will break up into a chain of islands separated by X-points[9]. The latter are surrounded by ergodic regions where the field lines move chaotically filling out a volume instead of a surface[10]. This is illustrated in fig. 7.6 where the effect of an $m = 5$ perturbation on an equilibrium with flux surfaces is sketched.

How this looks like for a real equilibrium is shown in fig. 7.7. Here a chain with large islands is located around the flux surface where the ι profile crosses $\frac{5}{5}$ (note that the ι profile is constant inside the region occupied by the islands). For a shifted ι profile that does not contain $\frac{5}{5}$ these islands disappear.
The width w of an island can be estimated by

$$w = 4\sqrt{\frac{R}{m\,\iota'}\,\mathcal{P}_{mn}}. \tag{7.6}$$

[9]These islands are called "natural" in order to distinguish them from island caused by effects external to the equilibrium, e.g. small errors in the coils. For natural islands the Fourier number n must be a multiple of the number of field periods.

[10]All this is analogous to nonlinear dynamics where it is shown that perturbations added to an integrable system lead to a destruction of the resonant tori in phase space (see the Poincaré-Birkhoff and Kolmogorov-Arnold-Moser (KAM) theorem). This analogy can be put on rigorous footing by noticing that the field lines in a torus can be described by a Hamiltonian function.

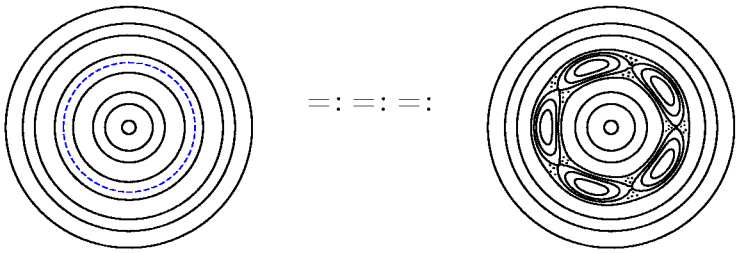

Figure 7.6: Left: Equilibrium with nested flux surfaces (the resonant surface is shown in blue). Right: Equilibrium with perturbation, ergodic regions are indicated with dots.

Using e.g. values typical of Wendelstein 7-X and assuming a perturbation amplitude $\mathcal{P}_{mn} \approx 10^{-4}$ one finds that this perturbation can lead to islands of width $\frac{w}{a} \approx 0.2$ showing that even a small perturbation can create relatively large islands. The danger of islands lies in the fact that they normally lead to a strong deterioration of plasma confinement by allowing particles to quickly cross the region occupied by the island chain. The existence of islands in an equilibrium is an inherent feature of three-dimensional systems, so it is of major interest for stellarator theory to design configurations in such a way that islands are so small that they have nearly no effect on confinement.

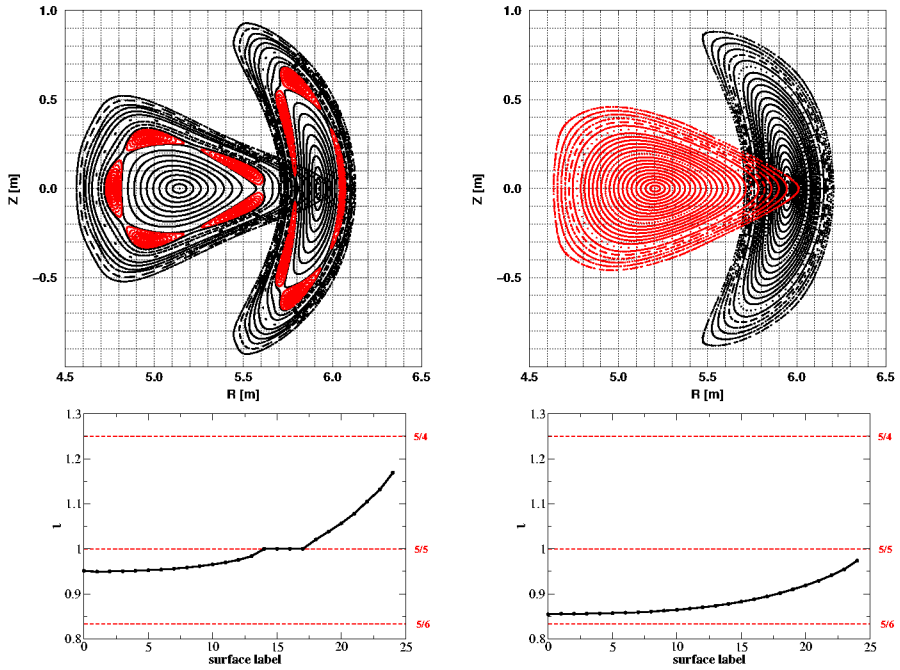

Figure 7.7: Poincaré plots of two Wendelstein 7-X variants with different ι profiles. Left: ι profile including the $\frac{5}{5}$ resonance. Right: The same calculation but with a downward shifted profile avoiding this resonance.

Equation (7.6) shows that rational numbers $\frac{n}{m}$ with low m – so called low order rationals – produce larger islands than rationals with high m and that high shear leads to smaller islands than low shear. Hence there are two strategies to arrive at three-dimensional equilibria with small islands:

- High shear minimises the influence of low order rationals but makes it necessary for the ι profile to cross many rationals. This strategy is followed in e.g. LHD.
- Low shear allows to place the flat ι profile in a region where there are no low order rationals. This line is followed by Wendelstein 7-X.

7.2.5 3D equilibrium codes

In order to describe an equilibrium (without bootstrap current) one has to specify the radial profile of the pressure and the shape of the outer flux surface $\mathcal{S}$ (along with the boundary condition that $\mathbf{B}$ must be tangent to $\mathcal{S}$). For a stellarator the condition $J = 0$ is imposed – the ι-profile then follows – while for a tokamak either the current or the ι-profile must be given. Solution of Eqs. (7.2–7.4) then gives the magnetic field inside $\mathcal{S}$. The shape of $\mathcal{S}$ is usually described using the parametric representation

$$\begin{aligned} R &= \sum_{m,n} R_{m,n} \cos(m\,U - n\,V), \\ Z &= \sum_{m,n} Z_{m,n} \sin(m\,U - n\,V), \\ \phi &= V, \end{aligned}$$

where $U, V \in [0 : 2\pi]$ are parameters and (R, Z, ϕ) are cylindrical coordinates, together with the set of Fourier coefficients $R_{m,n}, Z_{m,n}$.

Since in three dimensions the existence of flux surfaces is not guaranteed the structure of a solution can only be found a posteriori making it non-trivial to obtain pressure profiles which are constant on each flux surface.

The numerical calculation of stellarator equilibria is e.g. carried out with the help of two tools: The Variational Magnetic Equilibrium Code (VMEC) and the Princeton Iterative Equilibrium Solver (PIES).

VMEC

In this approach one *assumes* that the equilibrium has nested flux surfaces, i.e. one ignores the possibility of islands. As we have seen this assumption is generally not true for three-dimensional equilibria. Thus the solution given by the code serves only as an approximation to the exact equilibrium and can be rather bad if this has large islands[11]. Whether the approximation is a good one can only be tested afterwards.

Under this assumption making the energy functional

$$W = \int \left(\frac{B^2}{2\mu_0} + \frac{p}{\gamma - 1} \right) dV$$

[11] Instead of islands the approximative solution shows divergences in the parallel current density $j_\parallel$ at the resonant surfaces. In the exact solution $j_\parallel$ stays finite everywhere.

(γ: adiabatic coefficient) stationary, together with the additional constraint that the mass inside each flux surface does not change by the variation, is equivalent to solving the equilibrium eqs. (7.2–7.4).
The attractiveness of this approach lies in the fact that it is computationally much faster than computing an equilibrium allowing for islands. Thus VMEC has become the standard tool for calculating stellarator equilibria.

PIES

The PIES code permits islands in the equilibrium solution[12]. It solves the MHD equilibrium equations employing a Picard iteration:
i.e. starting with an initial guess $\mathbf{B}^0$ – obtained with e.g. VMEC – it solves the equations

$$\nabla \times \mathbf{B}^{n+1} = \mu_0 \mathbf{j}\left(\mathbf{B}^n\right), \qquad \nabla \cdot \mathbf{B}^{n+1} = 0,$$

where $\mathbf{j}\left(\mathbf{B}^n\right)$ is found from solving

$$\mathbf{j} \times \mathbf{B}^n = \nabla p, \qquad \nabla \cdot \mathbf{j} = 0.$$

The drawback of this approach is its extremely slow convergence making the calculation of an equilibrium very time consuming[13].

7.3 Pfirsch-Schlüter current

One goal of fusion power plant design is to achieve $\beta := \frac{2\mu_0 p}{B^2}$ values of about 5% (averaged in the confinement region). Connected with an increase in the plasma pressure is a shift of the plasma center with respect to the outer plasma surface (Shafranov shift). If this shift is too large the plasma center comes close to the outer plasma surface which may cause problems. So, cautiously one limits β to β_{eq} such that the plasma center keeps a safe distance from its boundary.

For an axisymmetric equilibrium and classical stellarators the Shafranov shift Δ is given approximately by $\frac{\Delta}{R} = \frac{\beta}{\iota^2}$. Usually one defines that β_{eq} is reached if $\Delta = \frac{a}{2}$ resulting in $\beta_{\text{eq}} \approx \frac{\iota^2}{A}$. Typical values are $A \approx 3$, $\iota \lesssim 1$ for a tokamak and $A \approx 10$, $\iota < 1$ for a stellarator. While for a tokamak a useful β-limit results a stellarator with too small ι and large A has a β_{eq} that is too low for fusion applications.

The way out of this difficulty is to use the freedom given by the three-dimensional structure of a stellarator to design $|\mathbf{B}|$ in such a way as to reduce the Shafranov shift.

First we have to understand what causes the Shafranov shift: From the MHD equilibrium relation $\mathbf{j} \times \mathbf{B} = \nabla p$ one obtains the diamagnetic current $\mathbf{j}_\perp = \frac{\mathbf{B} \times \nabla p}{B^2}$. Splitting the quasineutrality relation $\nabla \cdot \mathbf{j} = 0$ into a parallel and perpendicular component gives

[12] A second code allowing for islands is the HINT code which uses the time dependent MHD equations.
[13] An equilibrium calculation for the W7-X configuration using VMEC needs a few minutes computing time on an SX-5 vector computer; the analogous calculation using PIES takes approximately 1 week.

$\nabla\cdot\mathbf{j}_\parallel = -\nabla\cdot\mathbf{j}_\perp$. The diamagnetic current thus gives rise to a parallel current called the Pfirsch-Schlüter (PS) current. As a result one gets

$$\nabla\cdot\mathbf{j}_\parallel = -\frac{2}{B^3}\left(\nabla p\times\mathbf{B}\right)\cdot\nabla\left|\mathbf{B}\right| = -\frac{2|\nabla p|}{B}\kappa_\mathrm{g}$$

with κ_g the geodesic curvature[14] and ∇s the normal vector of the flux surface[15]. The geodesic curvature will also play an important role in the next section and thus will show up as a quantity of main importance for stellarators.

For a simple axisymmetric configuration this equation can easily be solved and gives the PS current as

$$j_\parallel = \frac{\partial p}{\partial r}\frac{2}{\iota B_0}\cos\vartheta.$$

This parallel current density – flowing in different directions at the inside respectively outside of the torus – leads to a vertical magnetic field that in combination with the toroidal and poloidal field results in an outward shift of the plasma: the Shafranov shift.

For a helically symmetric configuration with $\mathbf{B} = \mathbf{B}(r, \vartheta - kz)$ one finds $j_\parallel \sim \frac{1}{\iota - 1}$. It follows for $\iota \ll 1$ that the magnitude of $j_\parallel$ (and consequently the Shafranov shift) in a helically symmetric configuration is much smaller than in an axisymmetric one. Using the VMEC code it is possible to construct quasi-helically symmetric stellarator equilibria[16] for which even a β of 40% leads to nearly no Shafranov shift.

This observation shows the strategy how to reduce the Shafranov shift and increase β_eq for a stellarator: Using the freedom given by the three-dimensional structure one can design $|\mathbf{B}|$ and with it the geodesic curvature in such a way as to minimize the Shafranov shift (more details on this will be given later in sec. 7.6).

Taking the volume averaged ratio of the parallel to the diamagnetic current $\left\langle \frac{j_\parallel^2}{j_\perp^2} \right\rangle$ as a measure for the importance of the PS current one can see the progress of stellarator design with time: While for the classical (non-optimised) stellarator W7-A this ratio is around 12 it could be reduced to 3 for the partly optimised W7-AS and then to 0.5 for the fully optimised W7-X (corresponding to $\beta_\mathrm{eq} \approx 5\%$). This is illustrated in fig. 7.8, where W7-AS for $\beta \approx 2\%$ shows a noticeable Shafranov shift while it is hardly visible in W7-X for $\beta \approx 5\%$.

7.4 Neoclassical transport

7.4.1 Neoclassical transport

The main aim of neoclassical (transport) theory is to calculate the collisional transport of particles and heat – e.g. radial diffusion coefficients for particle and heat fluxes – as

[14] Using a triad $(\mathbf{b}, \mathbf{n}, \mathbf{n}\times\mathbf{b})$ such that $\mathbf{b}$ is the unit B-field vector and $\mathbf{n}$ is the unit normal vector of the flux surface the curvature $\kappa := (\mathbf{b}\cdot\nabla)\,\mathbf{b}$ can be written as $\kappa = \kappa_\mathrm{n}\mathbf{n} + \kappa_\mathrm{g}\mathbf{n}\times\mathbf{b}$ with the geodesic and normal curvature $\kappa_\mathrm{g}, \kappa_\mathrm{n}$. In contrast to the normal curvature the geodesic curvature is an intrinsic property of the surface geometry.

[15] Note that only the derivative of $|\mathbf{B}|$ in the flux surface enters this expression.

[16] In toroidal topology helically symmetric equilibria do not exist; one has to resort to so called quasi-helically symmetric equilibria (see sec. 7.4.2).

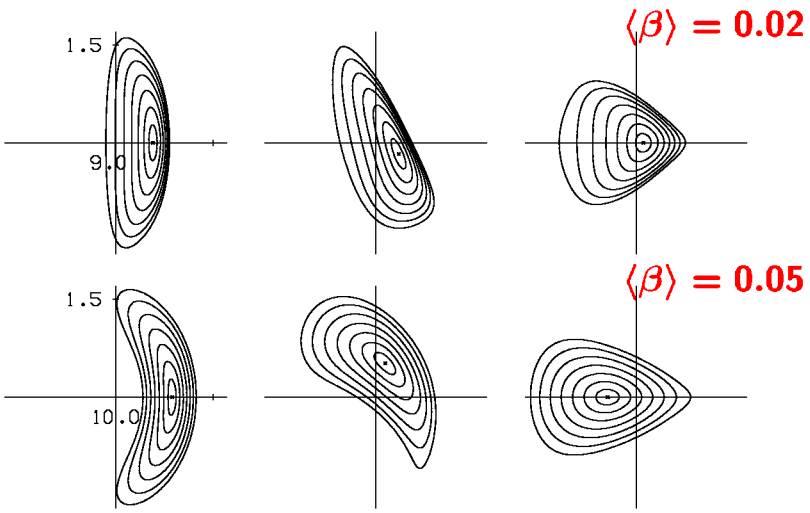

Figure 7.8: Toroidal cuts (at $\varphi = 0, \frac{2\pi}{20}, \frac{2\pi}{10}$) for W7-AS (top) and W7-X (bottom).

functions of the collision rates and the electric field taking into account the toroidal geometry of a fusion device[17]. The theoretical base for neoclassical calculations is collisional kinetic theory especially its drift kinetic simplification.

Figure 7.9 gives an overview on the neoclassical transport for tokamaks and stellarators. Depending on ν_{ei} one finds different regimes: the Pfirsch-Schlüter, plateau and banana regime for high, intermediate and low collisionality, respectively. The three-dimensional geometry of a stellarator can lead to regimes not present in a tokamak. In the long mean free path regime the helical variation of $|B|$ (helical ripple) for a classical stellarator leads to the so called $1/\nu$ regime[18] which is of paramount importance since it can lead to extremely large neoclassical losses potentially dangerous for a stellarator fusion device.

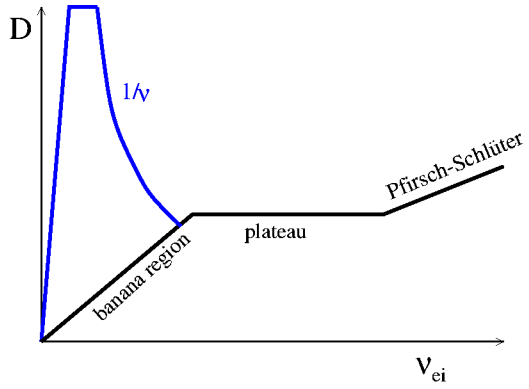

Figure 7.9: Neoclassical diffusion coefficient as a function of collision rate. Black: tokamak. Blue: additional regimes for a stellarator.

For the PS regime a fluid treatment of radial diffusion is possible: For a cylinder the equilibrium equation and Ohm's law ($\eta = \frac{m_e}{ne^2}\nu_{ei}$)

$$\mathbf{j} \times \mathbf{B} = \nabla p, \qquad \mathbf{E} + \mathbf{v} \times \mathbf{B} = \eta \mathbf{j}$$

[17] In cylinder geometry one speaks of classical transport theory.
[18] If an electric field is included a $\sqrt{\nu}$ regime can also be present.

give the perpendicular velocity of the fluid as

$$\mathbf{v}_\perp = \frac{\mathbf{E}\times\mathbf{B}}{B^2} - \frac{1}{B^2}\eta\nabla p$$

consisting of the $\mathbf{E}\times\mathbf{B}$-drift and a radial drift induced by collisions. Using the last term to calculate the radial particle flux $\Gamma = nv_\perp$ and comparing this with Fick's law $\Gamma = -D\nabla n$ leads to the classical diffusion coefficient

$$D_\mathrm{c} = \left(1 + \frac{T_\mathrm{i}}{T_\mathrm{e}}\right)\rho_\mathrm{e}^2\nu_\mathrm{ei}. \tag{7.7}$$

A more complicated calculation in toroidal geometry[19] including the PS current gives an additional factor (PS factor) and leads to the larger neoclassical diffusion coefficient $D_\mathrm{nc} = (1 + \frac{1}{\iota^2})D_\mathrm{c}$.

To understand the origin of the banana and $1/\nu$ regime one has to look at the motion of particles. For this task it is sufficient to use the guiding center equations of motion[20]:

$$\dot{\mathbf{R}} = v_\parallel\mathbf{b} + \mathbf{v}_\mathrm{d}, \tag{7.8}$$
$$\dot{v}_\parallel = -\mu\,\mathbf{b}\cdot\nabla|\mathbf{B}|, \tag{7.9}$$
$$\dot{\mu} = 0 \tag{7.10}$$

with the perpendicular drift velocity ($\mathbf{b} := \mathbf{B}/|\mathbf{B}|$ and $\mu := \frac{v_\perp^2}{2B}$ the magnetic moment per unit mass):

$$\mathbf{v}_\mathrm{d} = \frac{\mu B + v_\parallel^2}{B\Omega}\,\mathbf{b}\times\nabla|\mathbf{B}|. \tag{7.11}$$

From these equations[21] follows the very important fact that particles with low enough energy can be trapped around a minimum of $|\mathbf{B}|$ while for higher energies they can stream (nearly) freely. A particle trapped in a minimum of B shows a fast bouncing motion superposed onto a slow drift. This slow drift motion can be separated by averaging over the fast bouncing motion (bounce average) and gives the motion of the bounce center[22]: $\langle\mathbf{v}\rangle = \frac{1}{\tau_\mathrm{b}}\oint\mathbf{v}\,dt$ (τ_b: bounce time).

In a tokamak trapped particles move on so called banana orbits with radial width Δ_b. The center of a banana orbit slowly drifts toroidally but not radially, i.e. $\langle\mathbf{v}\rangle$ has only a toroidal component. Collisions cause particles to jump from one banana orbit to another thus leading to a random walk with step size Δ_b resulting in a diffusion coefficient (given

[19]This can most easily be seen by using the general relation $\Gamma = n\int\eta j^2\frac{dS}{|\nabla p|}$ (with $\eta_\perp \approx 2\eta_\parallel$) connecting the particle flux Γ with the resistive dissipation integrated over one flux surface. Thus the additional dissipation caused including parallel (PS) currents leads to an increase in the particle flux by the PS factor.

[20]See the lecture "Introduction to fusion plasmas".

[21]Note that eq. (7.9) follows from eqs. (7.8), (7.10) and energy conservation.

[22]To obtain the drift kinetic theory the fast gyrating particle had been replaced via averaging by its slowly drifting guiding center. Now drift kinetic is further reduced to a theory with the bounce center as the slowly moving basic entity obtained by averaging over the comparatively faster bounce motion of the guiding center.

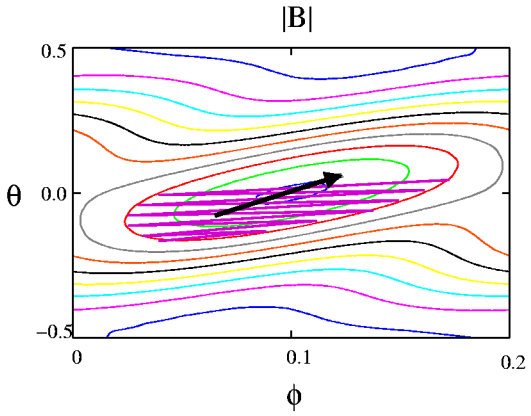

Figure 7.10: Motion of a trapped particle near a minimum of B (contour lines). The red line shows the actual motion of the guiding center while the black arrow shows the motion of the bounce center.

by $D = \frac{l^2}{\tau}$, where l is the diffusion step length and τ the collision time[23]) in the banana regime as $D_\mathrm{b} = \Delta_\mathrm{b}^2 \nu_\mathrm{ei}$.

As a very simple model for $|\mathbf{B}|$ in a stellarator one often uses

$$B = B_0 \left(1 - \epsilon_\mathrm{t} \cos\vartheta - \epsilon_\mathrm{h} \cos\left(\ell\vartheta - P\varphi\right)\right),$$

where $\epsilon_{\mathrm{t,h}}$ measures the strength of the toroidal or helical component, respectively.
For $\epsilon_\mathrm{t} = 0$ the bounce center drifts along the helical minimum (helically trapped particle) and $\langle \mathbf{v} \rangle$ has no component in the radial direction.
Adding a toroidal component ($\epsilon_\mathrm{t} \neq 0$) leads to a net radial component of $\langle \mathbf{v} \rangle$ which can be computed by performing the bounce average of

$$v^r = \mathbf{v}_\mathrm{d} \frac{\nabla r}{|\nabla r|} = \frac{\mu B + v_\parallel^2}{\Omega} \kappa_\mathrm{g}.$$

This result can be used to estimate a diffusion coefficient by noting that the diffusion step length is $l = \frac{\langle v_\mathrm{r} \rangle}{\nu_\mathrm{ei}}$.

$$D_{1/\nu} = f_\mathrm{t} \frac{\langle v^r \rangle^2}{\nu_\mathrm{ei}} \sim f_\mathrm{t} \frac{T^{\frac{7}{2}}}{nB^2} \kappa_\mathrm{g}^2 \tag{7.12}$$

(f_t: fraction of trapped particles).
This equation also shows the crucial role played by the geodesic curvature; its importance for the PS-current we have already seen in sec. 7.3. Thus decreasing the size of the geodesic curvature in the region where particles are trapped is beneficial for minimizing the neoclassical transport.
Summarizing the above picture one can say that caused by the toroidal curvature a helically trapped particle in a stellarator in general acquires a radial drift eventually leading to its loss; these particles are responsible for the $1/\nu$ regime.

[23] One can show that only collisions between unlike particle species lead to particle diffusion, while for heat diffusion collisions between like particle species are important.

One can argue more generally: the axial symmetry of a tokamak gives the toroidal momentum as a conserved quantity and it follows as a consequence that the maximal deviation of a (trapped or untrapped) particle from the flux surface is limited; this results in a relatively low neoclassical transport. The situation is different for a stellarator: Caused by its three-dimensional structure a conserved quantity and the related constraint on the orbit width does in general not exist[24] possibly leading to rapid particle losses showing up as the $1/\nu$ regime.

The strong dependence of $D_{1/\nu}$ on T is the cause why the $1/\nu$ regime is dangerous for a (classical) stellarator: The high temperature necessary for fusion leads to losses which are too high for a fusion power plant to work. So in order to construct a viable stellarator power plant it is of utmost importance to reduce this kind of neoclassical losses. From eq. (7.12) one can see the possible ways how to do this: Designing a stellarator in such a way that the particles get trapped in a region with small geodesic curvature leads to a small neoclassical radial transport. This path is followed in the design of W7-X and as a result neoclassical losses in W7-X are small enough to be compatible with fusion power plant requirements.

7.4.2 Quasi symmetry

Using magnetic coordinates (s, ϑ, φ) (see sec. 7.2.3) the guiding center equation of motion for $\dot{\mathbf{R}}$ (eq. (7.8)) can be written as

$$\dot{s} = \frac{1}{\sqrt{g}D}\frac{e\rho_\parallel}{m}\left(\rho_{\parallel,\vartheta} I - \rho_{\parallel,\varphi} J\right), \tag{7.13}$$

$$\dot{\vartheta} = \frac{1}{\sqrt{g}D}\frac{e\rho_\parallel}{m}\left[-F_P' - \left(I\rho_\parallel\right)_{,s} + \left(\tilde{\beta}\rho_\parallel\right)_{,\varphi}\right], \tag{7.14}$$

$$\dot{\varphi} = \frac{1}{\sqrt{g}D}\frac{e\rho_\parallel}{m}\left[-F_T' + \left(J\rho_\parallel\right)_{,s} - \left(\tilde{\beta}\rho_\parallel\right)_{,\vartheta}\right] \tag{7.15}$$

with $\rho_\parallel := mv_\parallel/(eB)$, $D := 1 + \rho_\parallel \mathbf{B}\cdot\mathbf{j}/B^2$, $\sqrt{g} := -(JF_P' + IF_T')/B^2$ and $\tilde{\beta}$ a function that can be calculated from B.

This formulation shows that the motion of the guiding center formulated in the special coordinate system of magnetic coordinates depends *only* on the function $B(s, \vartheta, \varphi)$ (magnetic topography) but not on the spatial structure of the flux surfaces which would show up as the metric tensor. Formulated sloppily one can say that in magnetic coordinates the particles do not "see" the real geometry of the configuration but only the magnetic topography. This observation leads to the notion of quasi-symmetry[25] as a symmetry of the magnetic topography formulated in magnetic coordinates but not of the configuration in real space.

Configurations with $B = B(s, \vartheta)$ or $B = B(s, k\vartheta - P\varphi)$ (k, P: integer parameters) are called quasi-axisymmetric or quasi-helical symmetric, respectively. They can be realized

[24] Quasi-symmetric configurations (see next section) do have conserved quantities.

[25] The qualifier "quasi" is meant to indicate that this symmetry only exists for B in a specially chosen coordinate system. Additionally it hints that quasi-symmetry is attainable in a three-dimensional configuration only to some approximation but not exactly.

in a torus and examples are known (e.g. see fig. 7.11). On the other hand the quasi-symmetries $B = B(s, \varphi)$ and $B = B(s)$, which would guarantee that a particle stays exactly at a flux surface[26], can not be achieved for toroidal systems.

For a configuration possessing a quasi-symmetry it follows from the guiding center equations of motion that there exists a conserved quantity[27]. This conserved quantity limits the maximal excursion of a particle from the flux surface (as noted in the last section) and thus eliminates the cause for the existence of the $1/\nu$ regime. Detailed calculations indeed show that e.g. a quasi-helical symmetric stellarator shows similar neoclassical transport as a corresponding tokamak.

As an illustration fig. 7.11 shows one flux surface of a quasi-helical symmetric configuration with six field periods. In real space it has a complicated three-dimensional structure and shows no apparent symmetries other than the ones described in sec. 7.1.3. After transformation to magnetic coordinates the helical symmetry of B becomes manifest.

Quasi-helical symmetric configurations have a bootstrap current which endangers their usefulness. Thus one considers another class of configurations, called quasi-isodynamic, where the second adiabatic invariant $J := \int v_\parallel dl$ (l: length along a field line) is nearly constant on the flux surfaces. In these configurations (without symmetry of B) the μ, J substitution particle (discussed in sec. 7.4.1) drifts poloidally. W7-X belongs to the class of quasi-isodynamic stellarators.

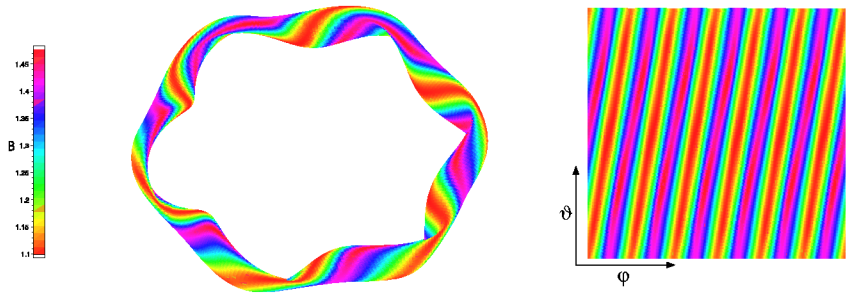

Figure 7.11: Quasi-helical symmetric stellarator in real space (left) and magnetic coordinates (right) (one flux surface is shown, color indicates the magnitude of B).

7.5 MHD stability

Since the vast field of stability quickly becomes very technical we will only give a short overview of the basic concepts of MHD stability.

Having found a plasma equilibrium configuration that meets the requirements described in the former sections it remains to show if a small perturbation applied to the system

[26] A configuration fulfilling $B = B(s)$ exactly would be called isodynamic.
[27] For e.g. quasi-helical symmetry the quantity $F_T - F_P - \rho_\parallel(I + J)$ is conserved.

grows or decays with time. In the first case the equilibrium configuration is unstable and plasma confinement may be destroyed quickly.

Formally one uses time dependent equations, symbolically written as $\frac{\partial}{\partial t} g = \mathcal{M} g$ with g denoting the dynamical variables and $\mathcal{M}$ a nonlinear operator. The solution is split into a time independent part representing the equilibrium under investigation and a time dependent part describing the perturbation: $g(\mathbf{r}, t) = g_0(\mathbf{r}) + g_1(\mathbf{r}, t)$. Assuming small perturbations $g_1 \ll g_0$ the nonlinear operator $\mathcal{M}$ is linearized resulting in the linear operator $\mathcal{L}$. Usually one is interested only in solutions behaving exponentially in time[28] justifying the ansatz $g_1 = \widetilde{g}(\mathbf{r}) e^{-i\omega t}$ (with the complex eigenvalue ω). Specification of boundary conditions on $\widetilde{g}$ then leads to the eigenvalue problem $\mathcal{L}\widetilde{g} = \omega \widetilde{g}$. The equilibrium is unstable if $\mathrm{Im}(\omega) > 0$ showing that the initially infinitesimal perturbation is growing exponentially with time.

Since for MHD the operator $\mathcal{L}$ is self-adjoint its eigenvalue problem only has solutions with $\omega^2 \in \mathbb{R}$ and can be formulated as a variational problem: The system is unstable if a perturbation $\xi(\mathbf{r})$ exists such that $\delta^2 W[\xi] < 0$ where the functional[29] $\delta^2 W$ is given by

$$\delta^2 W[\xi] = -\frac{1}{2} \iiint \left[S^1 + S^2 + S^3 + S^4 + S^5 \right] d^3 r.$$

The expressions for $S^1(\xi) \ldots S^5(\xi)$ are complicated and instead of giving the details here it suffices to note their general properties: S^1, S^2 and S^5 describe the influence of field line bending, field compression and fluid compression, respectively; they act stabilizing on $\delta^2 W$. In contrast to this S^3 and S^4 are indefinite and depend on the pressure gradient p' and the parallel current density $j_\parallel$; these two terms can cause $\delta^2 W$ to become negative. The instabilities caused by these terms are called pressure or current driven.

From the large zoo of MHD instabilities we briefly look at the kink and the ballooning instability: The kink instability is driven by a parallel current and consequently does not exist in a stellarator. Pressure is the energy source for the ballooning instability which bear this name since e.g. in a tokamak it has its maximal amplitude in the region of unfavorable curvature i.e. at the outside of the torus. This instability disappears for fixed pressure gradient if the pressure is low enough and thus provides a stability β-limit. W7-X is designed in such a way that it is stable against the ballooning instability for $\beta \lesssim 5\%$.
For a tokamak large scale kink and ballooning instabilities limit the operation regime while for a stellarator only kink modes have been found experimentally, hitherto.
As an illustration fig. 7.12 shows a ballooning instability in a quasi-axially symmetric stellarator. This picture also demonstrates a very general structural property of modes in a magnetized plasma: the wavelength in the direction perpendicular to the field lines is much smaller than the wavelength along the field line. This high degree of anisotropy of the instability reflects the anisotropy introduced by the magnetic field.

[28] Perturbations growing algebraically in time may exist but because of their slow growth normally are of no interest.

[29] $\delta^2 W$ is the second variation of the functional W from sec. 7.2.5.

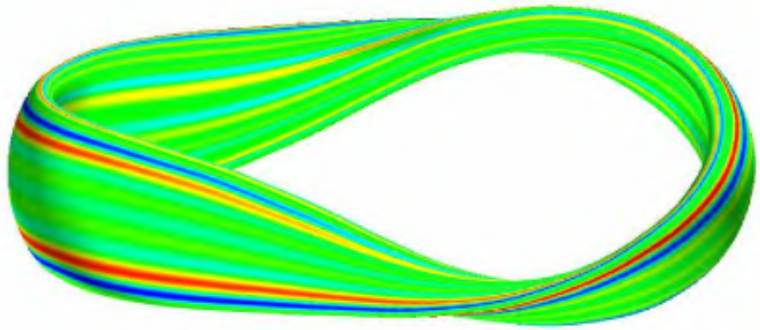

Figure 7.12: Eigenfunction for a ballooning mode. Shown is the pressure perturbation on a flux surface (high/low pressure is colored with red/green).

7.6 Stellarator optimisation

In secs. 7.2–7.5 we have discussed four points which are of vital importance for a stellarator as a fusion device. Stellarator optimisation is the comprehensive framework where these points (and other) are put together in order to arrive at a viable design for a fusion device. Crucial for optimisation is the high degree of freedom provided by the three-dimensional structure of a stellarator.

Since the main goal of stellarator optimisation is to find equilibria that have good confinement properties one first has to quantify what one understands by "good confinement properties". This is done by assigning to each equilibrium configuration from the configuration space Con[30] a real number as a quality measure by providing a function $\mathcal{Q} : \mathrm{Con} \mapsto \mathbb{R}$. The construction of this function requires the consideration of the physics one regards as relevant for confinement and the design targets.

In the design of W7-X one required:

- Nested magnetic surfaces with small islands;
- Small Shafranov shift for $\beta \approx 5\%$;
- Small neoclassical transport;
- MHD stability, especially stability against ballooning modes for $\beta \approx 5\%$;
- Good α-particle confinement:
  α-particles are needed for the heating of the plasma and thus they must not leave the fusion device in a time shorter than their slowing down time;
- Small bootstrap current:
  This is another current driven by the pressure gradient. In contrast to the PS-current it gives rise to a total toroidal current causing a shift in ι with increasing

[30] Since we have seen in sec. 7.2.5 that an equilibrium (except for its profiles) can be uniquely defined by specifying its outer flux surface the space Con can be identified with the set of Fourier coefficients used in the representation of this surface.

β. Since ι control is crucial for the confinement properties (see e.g. sec. (7.2.4)) such a shift was considered to be undesirable[31];

- Feasible modular coils:
  For actually building a device constraints emerge motivated by engineering considerations regarding the design of the modular coils (e.g. a minimal distance between neighboring coils must be kept, the coil curvature cannot be too large). Some of them can be taken into account in the plasma optimisation.

In the optimisation procedure, which is carried out computationally, first an outer flux surface is specified from which (using VMEC) the corresponding equilibrium configuration is computed; based on this equilibrium the function $\mathcal{Q}$ is calculated. This procedure is repeated – employing an optimisation algorithm – with changed outer flux surface until $\mathcal{Q}$ has reached a maximum. When the optimised equilibrium has been found the actual coil system is calculated subsequently.

Depending on the criteria and the design goals many different configurations can be found via optimisation. One possible result from this procedure, the optimised stellarator Wendelstein 7-X, is shown in fig. 7.13.

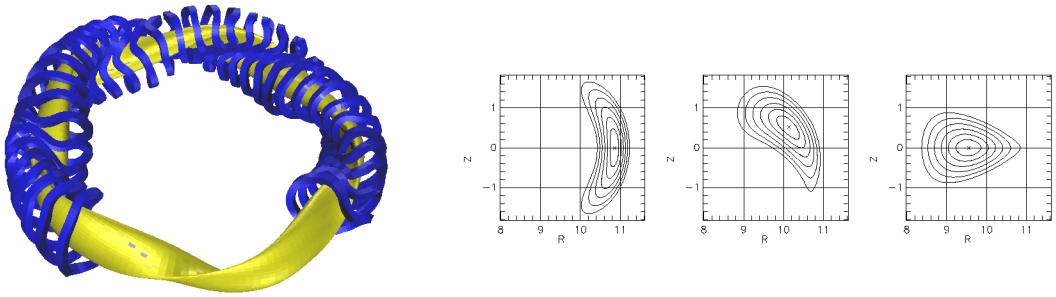

Figure 7.13: Left: Wendelstein 7-X plasma configuration with modular coils. Right: Toroidal cuts through the equilibrium configuration at $\phi = 0, \frac{2\pi}{20}, \frac{2\pi}{10}$.

Literature

There exists no good textbook about stellarator physics (as e.g. the book by Wesson for tokamaks). So everything is scattered in articles which generally are difficult to understand for the beginner. For this reason I here give references to some of the few more basic articles.

- A.H. Boozer, "What is a stellarator", Physics of Plasmas, vol. 1, p. 1647 (1998).
  A more advanced introductory article with an explanation of magnetic coordinates.
- G. Grieger et al., "Physics optimization of stellarators", Physics of Fluids, vol. B4, p. 2081 (1992).
  Overview on the physics design for Wendelstein 7-X; very condensed.

[31] Quasi-axisymmetric configurations are an exception to this consideration.

- W. Lotz et al., "Optimization, MHD mode and α-particle confinement behaviour of Helias equilibria", Proceedings IAEA (1992).
  Describes the optimisation leading to Wendelstein 7-X; advanced reading.

- G. Grieger et al., "Das Fusionsexperiment Wendelstein 7-X", Physikalische Blätter, vol. 49, p. 1001 (1993).
  Very basic article.

- K. Miyamoto, "Plasma Physics for Nuclear Fusion", The MIT Press (1989).
  Some chapters include stellarator specific issues.

- J. Nührenberg, "Quasi-symmetries in toroidal confinement", Europhysics News, p. 216 (Dez. 1998).
  A short introduction into the concept of quasi-symmetries.

- F. Wagner, "Stellarators and optimised stellarators", Transactions of Fusion Technology, vol. 29, p. 407 (1996).
  Very good introduction; recommended.

- F. Wagner, "Topics in toroidal confinement", Plasma Physics and Controlled Fusion, vol. 39, p. A23 (1997).
  Experimental oriented introduction.

- M. Wakatani, "Stellarator and Heliotron Devices", Oxford University Press (1998).
  One of the few books about stellarators but written very technically.

Chapter 8

Experimental Results from Stellarators

Rudolf Brakel

8.1 Introduction

Stellarator, in a general sense, is the generic name for devices which confine a fusion plasma by a magnetic field that is completely generated by external coils, although it is modified to a certain extent by pressure driven currents flowing in the plasma itself. Therefore, stellarators do not need a large toroidal net plasma current for confinement, and with the advent of powerful auxiliary heating sources in the 1970's stellarators did no longer require the plasma current for ohmic heating. One of the milestones in stellarator research was the demonstration of net current free plasma sustainment by neutral beam injection in Wendelstein 7-A in 1981. Present-day stellarators are exclusively heated by electron cyclotron resonance heating (ECRH), ion cyclotron resonance heating (ICRH), neutral beam injection (NBI) and by combinations of these methods.

The absence of a large plasma current in a stellarator constitutes its inherent capability of steady state operation and there are no risks of current driven instabilities, in particular current disruptions. Beyond these obvious advantages stellarators have to prove their reactor potential by demonstrating that they can meet in particular the requirements of high-β operation (required for economy), high confinement (required to reach ignition) and particle and power exhaust (required for density control, ash and heat removal). This chapter highlights, after introducing the various stellarator concepts, the experimental achievements with respect to these key issues.

8.2 The stellarator family

The use of external fields offers a large freedom of how to realize the key to magnetic confinement: the formation of toroidally closed nested magnetic surfaces by a helical twist of the magnetic field lines, the so called rotational transform ι ($\iota = 1/q$ is the inverse of

the tokamak safety factor q. It denotes the angle in terms of 2π at which a magnetic field line is poloidally displaced after one toroidal turn). Accordingly, experimental work on stellarators is rather diversified. Small to medium size experiments are designed to test the feasability of various construction and optimization principles. Superconducting large scale devices are going to close the gap to the large tokamaks with the additional option of steady state operation.

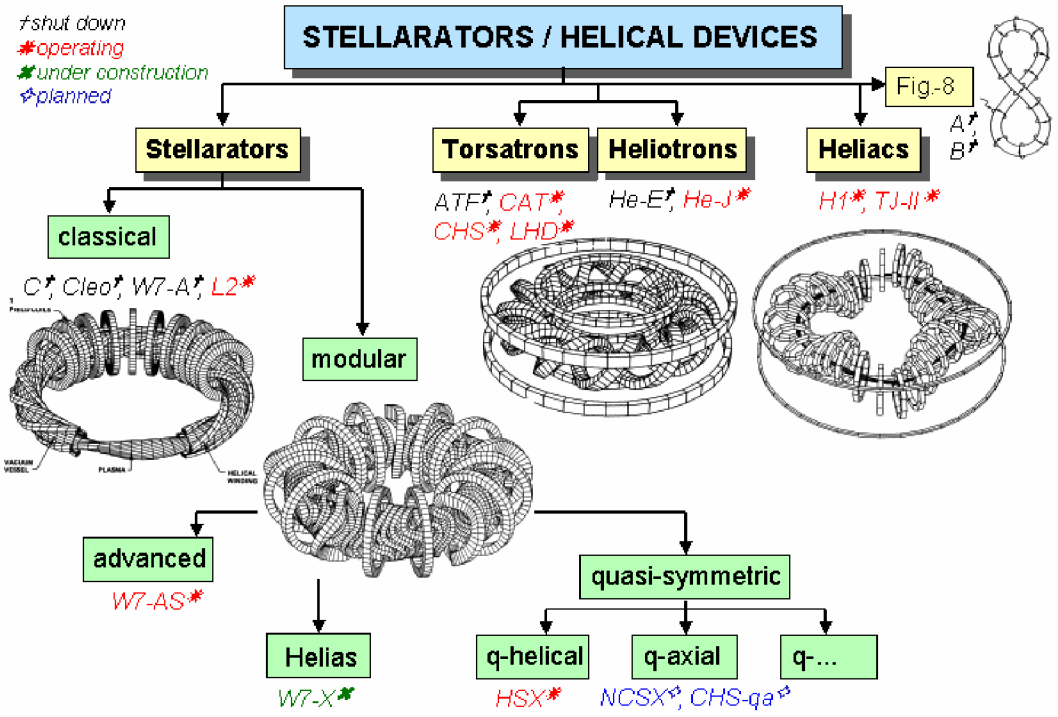

Figure 8.1: *The different stellarator concepts. The coil systems shown are those of W7-A (classical l=2 stellarator), W7-AS (modular advanced stellarator), ATF (l=2 torsatron) and TJ-II (heliac).*

A genealogy of the different types of stellarators or helical devices is sketched in Fig. 8.1, which is intended to feature the basic principles but is far from being complete. In the first stellarators, Model A and B at Princeton University, the rotational transform was generated by bending a toroidal arrangement of coils into a *Figure-8* shape. *Classical stellarators*, in a narrow sense, such as Wendelstein 7-A use $2l$ toroidally closed helical conductors, the current in adjacent conductors running in opposite directions. Additional toroidal field coils are required to produce a net toroidal field. The use of the two coil sets gives experimental flexibility with respect to the magnetic field structure. However, the interlink of the coil sets and large magnetic forces make the *classical stellarator* unattractive for a reactor design. These drawbacks are somewhat alleviated by *torsatrons*, e.g. the Large Helical Device (LHD), and *heliotrons*, e.g. Heliotron-E, but at the expense of experimental flexibility. *Heliotrons/torsatrons* have l helical conductors with parallel currents. They provide a net toroidal field and the vertical field generated by the net toroidal current is balanced by additional poloidal field coils not interlinked with the helical ones. Similar to a *Figure-8* device a *heliac* produces the rotational trans-

form by a three dimensional (3D) helical magnetic axis: the centre of the toroidal field coils follow a helical line around a central conductor. The *heliac* principle is realized for example in TJ-II.

Device	**Location**	**Type**	M	R/m	a/m	B/T
ATF	Oak Ridge	torsatron	12	2.1	0.27	2
CHS	Nagoya/Toki	torsatron	8	1.0	0.2	2
LHD	Toki	torsatron, sc[1]	10	3.9	0.6	3
Heliotron E	Kyoto	heliotron	19	2.2	0.2	1.9
Heliotron J	Kyoto	heliotron	4	1.2	0.2	1.5
TJ-II	Madrid	heliac	4	1.5	0.2	1
W7-AS	Garching	advanced stell.	5	2.0	0.18	3
W7-X	Greifswald	helias, sc	5	5.5	0.53	3
HSX	Madison	quasi helical	4	1.2	0.15	1.4
NCSX	Princeton	quasi axial	3	1.4	0.33	1.7
CHS-qa	Toki	quasi axial	2	1.5	0.47	1.5
QPS	Oak Ridge	quasi poloidal	2	0.9	0.33	1

Device	**shear**	**well**	**Status**
ATF	medium	central	1988–1994
CHS	medium	central	1988–running
LHD	medium	central	1998–running
Heliotron E	high	hill	1980–1997
Heliotron J	low	global	1999–running
TJ-II	low	global	1998–running
W7-AS	low	global	1988–2002
W7-X	low	global	under construction
HSX	low	global	2001–running
NCSX	medium	well	under approval
CHS-qa	low	well	under design
QPS	medium	well	under design

Table 8.1: *Some stellarators and helical devices (M: number of field periods, R: major radius, a: minor radius, B: maximum magnetic field)*

Apart from technical problems which have to be expected for reactor-scale helical windings the magnetic field properties of the traditional stellarator types can be optimized only within the constraints imposed by the particular concept. These restrictions relaxed considerably with the invention of so called *modular stellarator coils* by Rekher and Wobig in 1972 which are 3D in shape and poloidally closed. Modular coils allow to approximate arbitrary current distributions on a toroidal surface which then completely define the magnetic field in the volume enclosed by the surface. Along with a tremendous increase in computing power the modular coil concept gave way to advanced physics optimization of stellarators. In fact, traditional stellarators need to be optimized. They suffer from a rather low β-limit (β is the ratio of plasma pressure p to magnetic pressure

[1] sc=superconducting

$B^2/2\mu_0$) and from very large *neoclassical* plasma losses in the collisionless regime which is required for a reactor. The pressure is limited by a pressure induced outward shift of the magnetic surfaces, the so called Shafranov-shift (equilibrium β-limit; a further limit, the stability β-limit, is due to the onset of pressure driven MHD-instabilities that degrade the confinement). Owing to its 3D-structure, the stellarator magnetic field is strongly modulated along the field lines, causing plasma particles with a small momentum parallel to the field lines to be trapped in the local magnetic mirrors. Such locally trapped particles are rapidly lost by the $B \times \nabla B$-drift which is perpendicular to the field lines.

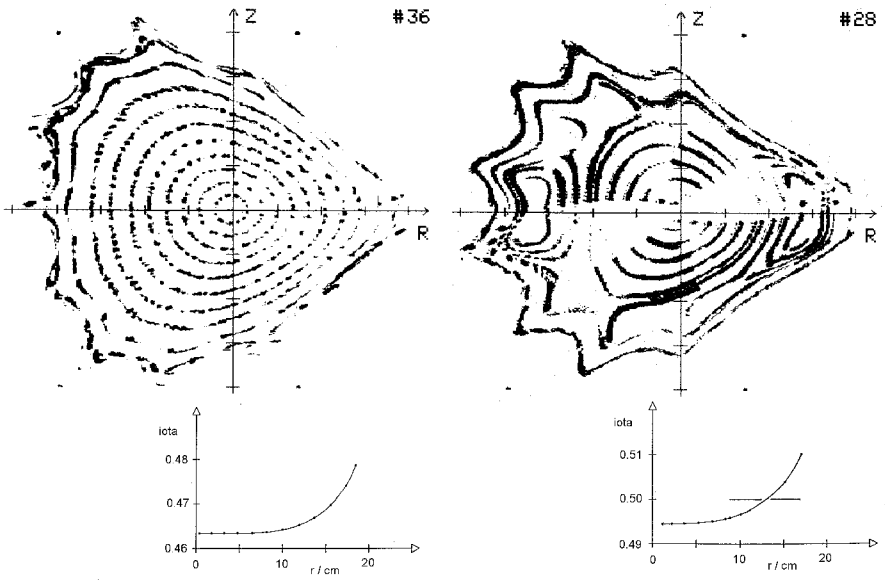

Figure 8.2: *Poloidal cuts through vacuum field flux surfaces in W7-AS and radial profiles of the rotational transform measured by the fluorescing rod technique. In case that the ι --profile contains rational values n/m that "resonate" with field perturbations B_{nm} the unpertubated nested surfaces (left) break up and large magnetic islands appear (right) [1].*

Wendelstein 7-AS, the proof-of-principle experiment for *advanced stellarator* optimization, is optimized with respect to a reduced Shafranov shift. Its successor, Wendelstein 7-X, is a large modular helical axis stellarator (*helias*) presently being under construction. Its design is much further optimized leading for example to a further reduction of the Shafranov shift and of the neoclassical losses [3]. In *quasi-symmetric stellarators*, which are still 3D in Cartesian coordinates but nearly 2D in magnetic coordinates, the effective field ripple and thus the drift losses are significantly reduced. Such configurations are similar to a tokamak, which is axially symmetric. Various kinds of quasi-symmetry are currently under consideration. A quasi-symmetry has first been realized in the *helically symmetric experiment* (HSX). Further devices are being planned, e.g. the National Compact Stellarator Experiment NCSX and the Compact Helical System CHS-qa, both having *quasi axial symmetry*, and QPS with *quasi poloidal symmetry*. The modular design and a low number $M \leq 3$ of field periods allows for a compact design with comparatively small aspect ratio, $A = R/a$. Table 8.1 gives an overview of present stellarator experiments and of those being under construction or being planned.

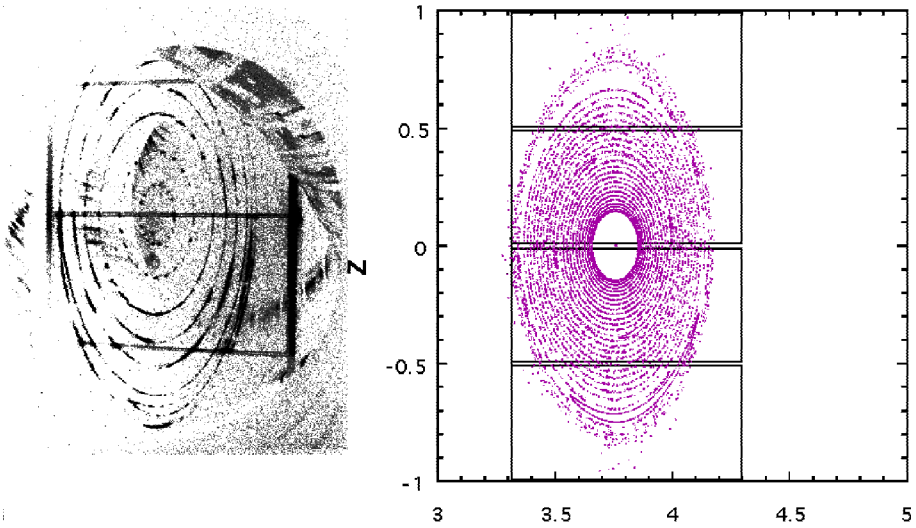

Figure 8.3: *Vacuum field flux surfaces in LHD measured by fluorescing mesh technique at $B = 0.0875$ T (left) and calculated surfaces obtained from a fieldline tracing code including the earth's magnetic field (right, $B_E \approx 5 \times 10^{-5}$ T). The large 1/1 magnetic island at the top is inherent to the particular LHD-configuration and the small island at the bottom is attributed to the earth's magnetic field. The frame supporting the mesh can also be seen [2].*

8.3 Properties of the vacuum field

High quality magnetic flux surfaces are prerequisite for plasma confinement. In contrast to tokamaks flux surfaces in stellarators already exist for the vacuum field and can directly be measured. For this purpose an electron beam is injected parallel to the magnetic field. The beam follows the field line and finally covers the respective flux surface (if it exists). A poloidal cut through the surface is visualized by a fluorescing rod which is swept across a poloidal cross section and imaged, e.g., by a CCD-camera. Alternatively a stationary fluorescent mesh is used. Figure 8.2 shows two examples of vacuum flux surfaces in W7-AS which have been measured at slightly different values of the rotational transform. In the case where ι does not assume low order rational values, such as $\iota = 1/3, 1/2, 2/3$, etc., unperturbed nested surfaces exist. When $\iota = 1/2$ occurs in the confinement volume so called magnetic islands appear. They arise from radial perturbation fields, i.e. being normal to the flux surfaces, with Fourier components $B_{nm} \neq 0$ and $n/m = 1/2$. Such perturbations may be due to external field errors with $n = 1$ and $m = 2$ or they are inherent to the field structure. For example, W7-AS has 5 toroidal field periods leading to inherent $5/m$-components. By closer inspection of the island pattern in Fig. 8.2, right, one realizes that ten small islands (from the 5/10 perturbation) are embedded into two large islands (from the 1/2 perturbation). Furthermore, the corrugated boundary indicates that the outer flux surfaces are already perturbed by the next 5/9 island chain. Generally, magnetic islands appear when the rotational transform assumes a rational value $\iota = n/m$ and is in resonance with a field perturbation $B_{nm} \neq 0$.

External field errors can arise for example from a misalignment of the coil set or from an imperfect compensation of the current lines feeding the coils (the in- and outgoing lines

must be aligned parallel, such that there is no net current producing a stray magnetic field). The susceptibility of flux surfaces to weak external perturbations has instructively been demonstrated at LHD (Fig. 8.3). Measurements at $B = 0.0875$ T show a 1/1-island structure which can be reproduced in a flux surface calculation when the earth's magnetic field of about $B_E \approx 5 \times 10^{-5}$ T is taken into account, i.e. perturbations of the order 5×10^{-4} already produce significant islands. (Actually, this perturbation does not affect the usual LHD-operation at $B > 2$ T where $B/B_E < 3 \times 10^{-5}$).

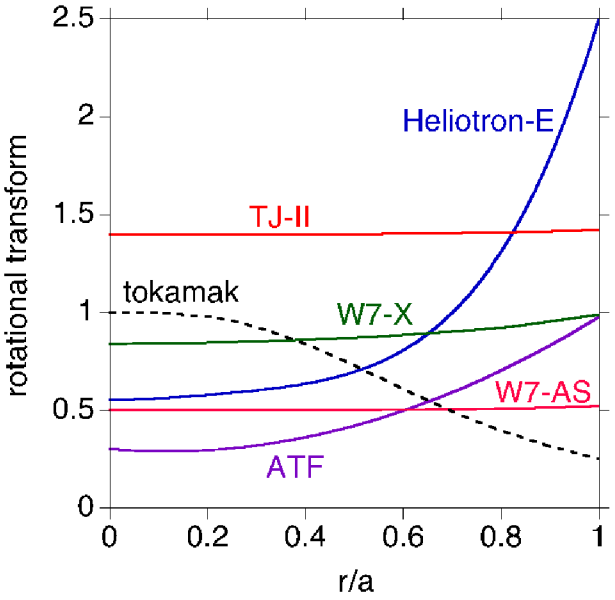

Figure 8.4: *Radial profiles of the rotational transform for different stellarator concepts and a tokamak.*

Magnetic islands short-circuit radial plasma transport. They are therefore detrimental for confinement and have to be avoided or must be made small. Precise machining and alignment of the field coils is therefore prerequisite for high quality flux surfaces in a stellarator. Residual islands can be excluded if the magnetic shear (= radial variation of ι) is very small and the value of the rotational transform is properly adjusted to avoid the major rational numbers (Fig. 8.2, left). This concept is followed by the Wendelstein line. Large magnetic shear reduces the island size. This concept is followed by torsatrons and heliotrons. However, increasing shear allows more islands to enter the confinement volume which for extreme situations may even lead to ergodization of the field lines. Figure 8.4 shows ι-profiles typical for the various stellarator concepts.

The poloidal cross section of a flux surface is far from being circular and may even change with the toroidal position. A convenient label of a flux surface is its *effective radius* r, which is defined as the minor radius of a circular torus having the same major radius R and enclosing the same volume as the flux surface. The parameters of both the field and the plasma are usually expressed by their flux surface average. Such a function of r is referred to as a *radial profile*. Plasma parameters are almost constant on a flux surface since transport parallel to the field lines is usually very fast compared to the perpendicular (radial) transport.

Another key parameter of the magnetic field is related to the average of the magnetic field value on a flux surface. If the average of B increases with r the configuration is said to

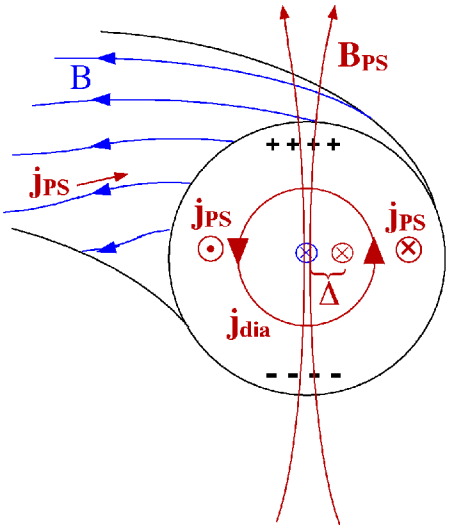

Figure 8.5: *Sketch of the perpendicular (diamagnetic) and parallel (Pfirsch-Schlüter) equilibrium currents. The parallel currents lead to the Shafranov shift* Δ.

have a magnetic well, if it decreases a magnetic hill. Both, magnetic shear and magnetic well are favourable for plasma stability. Wendelstein stellarators and Heliacs have small shear and a global magnetic well; they rely on magnetic well stabilization. In contrast, Torsatrons/Heliotrons have moderate/large shear and a magnetic hill (torsatrons may have a small hill in the centre); they rely on magnetic shear stabilization. The well/hill structure can be changed by shifting the inner flux surfaces radially along R with respect to the outer ones. This can be achieved with a vertical magnetic field which can be externally applied or which arises from the equilibrium currents in a confined plasma (Shafranov shift). The outward shift produces a magnetic well.

8.4 Plasma equilibrium and high-β operation

In the presence of a plasma the vacuum magnetic field is modified by currents flowing in the plasma. The pressure equilibrium requires that the pressure gradient is balanced by the magnetic force, $\nabla p = \mathbf{j} \times \mathbf{B}$ with $\nabla \cdot \mathbf{j} = 0$. It can easily be shown that the current component perpendicular to the magnetic field is $\mathbf{j}_\perp = \mathbf{j}_{dia} = \mathbf{B} \times \nabla p / B^2$. This is the diamagnetic current which decreases the magnetic field inside the plasma. The parallel component can be approximated by $\mathbf{j}_\parallel = \mathbf{j}_{PS} \approx 2 j_\perp / \iota \cos\theta \mathbf{e}_\parallel$ where θ is the poloidal angle. This is the so called Pfirsch-Schlüter (PS) current. In the particle picture the PS-current cancels the separation of electrons and ions arising from the vertical $\mathbf{B} \times \nabla B$ drift in the toroidally curved field. Otherwise the resulting electric field would expel the plasma by the outward directed $\mathbf{E} \times \mathbf{B}$ drift. The currents are sketched in Fig. 8.5. The PS-current produces a vertical dipole field which shifts the plasma outward (Shafranov shift Δ). Approximately, the Shafranov shift is given by

$$\Delta / a = R/a \left(C_{01} / \left(r/R \right) \right)^2 \langle \beta \rangle / \iota^2,$$

where C_{01} is the toroidal curvature term in the Fourier representation of the field and $\langle\beta\rangle$ is the volume average of the normalized pressure $\beta = p/\left(B^2/2\mu_0\right)$. Evidently, the Shafranov shift can be made small by reducing the aspect ratio, R/a, and increasing the rotational transform (the torsatron and heliotron approach) and by decreasing the toroidal curvature (the Wendelstein approach). In the line of W7 stellarators the quantity $C_{01}/(r/R)$ decreases from 1 (W7-A) via 0.7 (W7-AS) to 0.4 (W7-X). The equilibrium β-limit is formally defined as the pressure where the shift of the magnetic axis reaches half the minor plasma radius, $\Delta = a/2$. As a positive effect the Shafranov shift can "dig" a magnetic well, which improves the plasma stability.

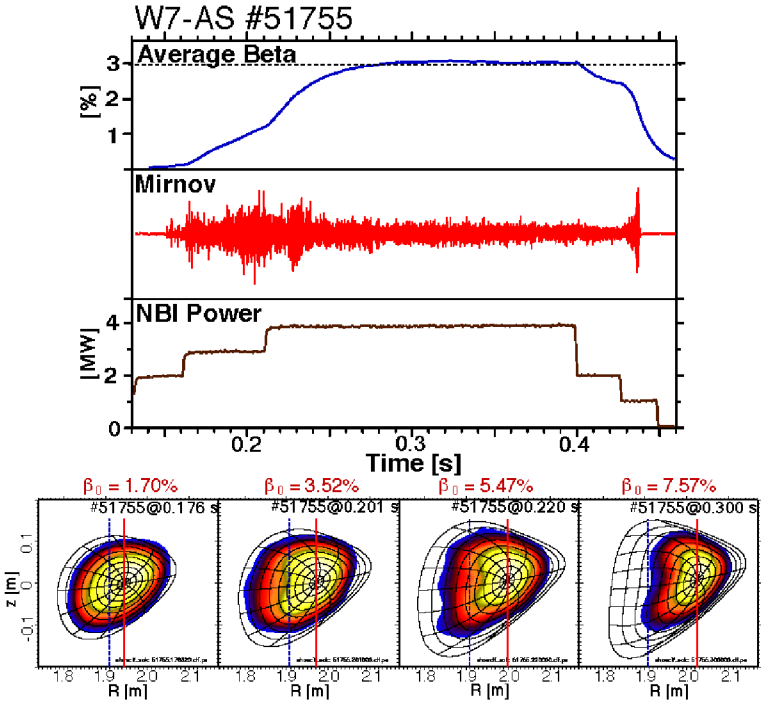

Figure 8.6: *Normalized pressure, magnetic field fluctuations close to the plasma and NBI heating power for a high-β discharge in W7-AS (top). Contours of constant soft X-ray emissivity and flux surfaces calculated by the NEMEC code at selected times of the same discharge. The position of the magnetic axis is $R = 1.91$ m for the vacuum field and moves radially outward with increasing β (bottom) [4].*

Since $\langle\beta\rangle \sim \langle p\rangle/B^2 \sim (W/V_p)/B^2 \sim (\tau_E P)/(V_p B^2)$, where W is the plasma energy, V_p the plasma volume, P the heating power and τ_E the energy confinement time, high-β plasmas are achieved with strong neutral beam heating at reduced magnetic field. Actually, the dependence of β on the experimental control parameters P and B is weaker than indicated by this relations, since the confinement time increases with B and decreases with P (see section 8.5.2). A high-β discharge in W7-AS with $P_{NBI} = 4$ MW at $B = 0.9$ T is shown in Fig. 8.6. The equilibrium magnetic surfaces can be visualized by the contours of constant plasma emissivity which is a function of electron temperature, electron density and the density of plasma impurities, which are constant on flux surfaces. The soft X-ray spectral range is best suited for this purpose. The contours of constant soft-X emissivity are in good agreement with the flux surfaces calculated by the NEMEC equilibrium code. In order to prevent the plasma boundary to be shifted

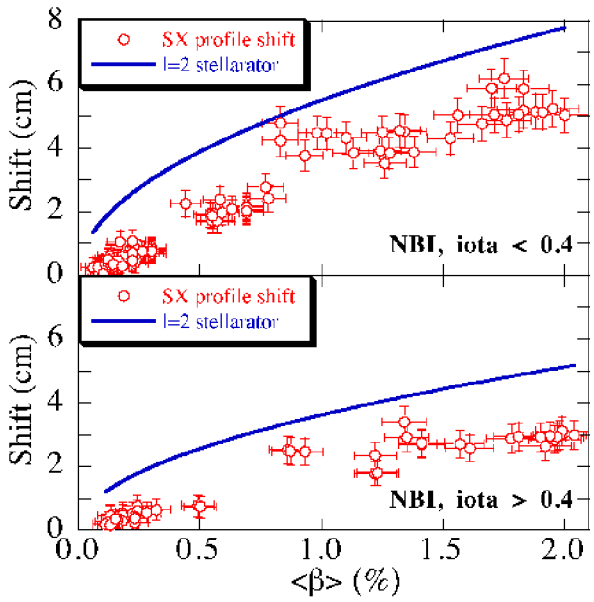

Figure 8.7: *Shift of the magnetic axis as a function of the average plasma pressure in W7-AS. The full lines indicate the shift expected for a classical $l = 2$ stellarator [5].*

onto the vessel wall an external vertical field has to be superposed to the vacuum field which counteracts the dipole field of the equilibrium currents during the high-β phase. Nevertheless, a relative shift of the magnetic axis with respect to the plasma boundary cannot be avoided.

Figure 8.7 shows the increasing displacement with $\langle\beta\rangle$ of the magnetic axis with respect to its vacuum field position as deduced from soft X-ray measurements in various W7-AS discharges. The observed shift is roughly a factor of 2 smaller than that predicted for an equivalent classical $l = 2$ stellarator. This result was an important confirmation of the W7-AS optimization which has predicted a reduction of the PS-current and the associated Shafranov shift by a factor of 2. Additionally, it confirms the expected decrease of the Shafranov shift with increasing rotational transform.

The maximum $\langle\beta\rangle$-values achieved so far in W7-AS (3.4 %) and LHD ($\approx$ 4%) clearly exceed the predicted stability limits ($\langle\beta\rangle = 2\%$ for W7-AS) where Mercier and resistive interchange modes grow unstable. In particular, no hard stability limit with strong MHD events has been observed experimentally up to now. On the contrary, the high-β phase appears to be rather quiescent with respect to magnetic activity, which is indicative for fluctuations and instabilities (see Fig. 8.6, on the top). In both devices high-β discharges are started with an inward shifted vacuum field configuration, providing a magnetic hill, which is unfavourable for stability. The high-β values that can still be achieved may be related to the formation of a stabilizing magnetic well with increasing β. This is in line with observations at CHS and LHD where after an initial increase magnetic fluctuations decrease or saturate at high-β (Fig. 8.8). Up to now the maximum pressure in stellarators seems to be limited by the available heating power rather than by instabilities.

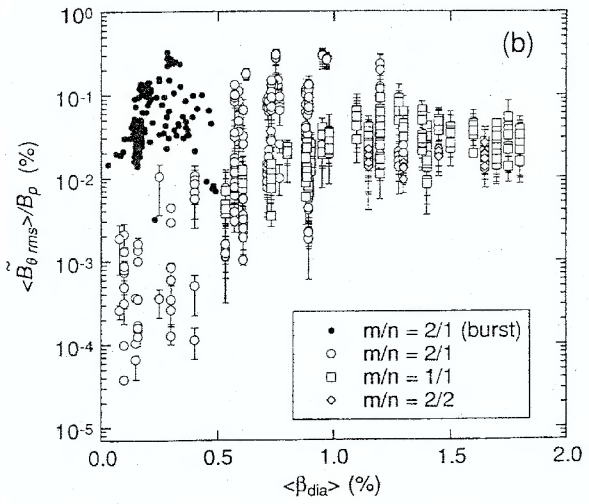

Figure 8.8: *Magnetic fluctuations in CHS measured with pick-up coils at the plasma periphery as a function of the normalized plasma pressure β. The root-mean-square fluctuation level normalized by the equilibrium poloidal field is shown for stationary coherent components with mode numbers $m \leq 2$ (open symbols) [6].*

8.5 Transport and confinement

The outward directed radial transport of particles and energy limits the density and temperature which can be achieved at a given strength of particle and energy sources. Understanding of the transport mechanisms is essential for the extrapolation towards a reactor. As in tokamaks, transport in stellarators cannot be understood only in terms of "neoclassical" diffusion processes. Additional "anomalous" transport even dominates in certain plasma regimes.

8.5.1 Neoclassical transport

Neoclassical transport is a diffusive process which can be described by a random walk model, $D = d^2\nu$, with diffusivity D, collision frequency ν and step size d. In a homogeneous magnetic field d is determined by the Larmor radius (*classical* diffusion). However, a toroidal field is inherently inhomogeneous and the particles undergo drifts in the magnetic field gradient ($\mathbf{B} \times \nabla B$ drift and curvature drift) and additional electric fields ($\mathbf{E} \times \mathbf{B}$ drift, $\mathbf{E}$ arises from space charges). Then d is determined by the distance which a particle can drift away from a flux surface between collisions. If collisions are rare, d becomes much larger than the Larmor radius (*neoclassical* diffusion).

In both tokamaks and stellarators B is higher at the inside (smaller R) than at the outside (larger R) of the torus. This results in a vertically directed $\mathbf{B} \times \nabla B$ drift and a modulation of B along the helical field lines. A particle following a field line thus moves in a magnetic mirror termed toroidal mirror or ripple. The particle can follow a helical trajectory if its parallel momentum is large enough (passing particle). If not, it is trapped in the ripple and bounces between reflection points located at the high field side above and below the equatorial plane. The orbits of toroidally trapped particles

are called "banana orbits" since their poloidal projection resembles a banana. Without collisions both passing and toroidally trapped particles are ideally confined since on the average they spend the same time below and above the surface and there is no net displacement by the drift. With collisions the trapped particles can be displaced by the "banana width" which then determines d (banana- or ν-regime).

In stellarators additional ripple, the helical ripple, arises from the 3D coil structure. These ripples are localized with an extension of the order of the coil spacings (in tokamaks the finite number of coils is only a weak perturbation of axial symmetry). For particles trapped in such a local ripple the vertical drift is not averaged as it is for passing or banana particles and they are rapidly lost unless they are detrapped by collisions. Therefore the diffusivity strongly increases with decreasing collisionality ($1/\nu$-regime). Since a reactor has to operate at high temperature, i.e. low collisionality, the stellarator specific $1/\nu$-regime is detrimental unless transport can be reduced by other means.

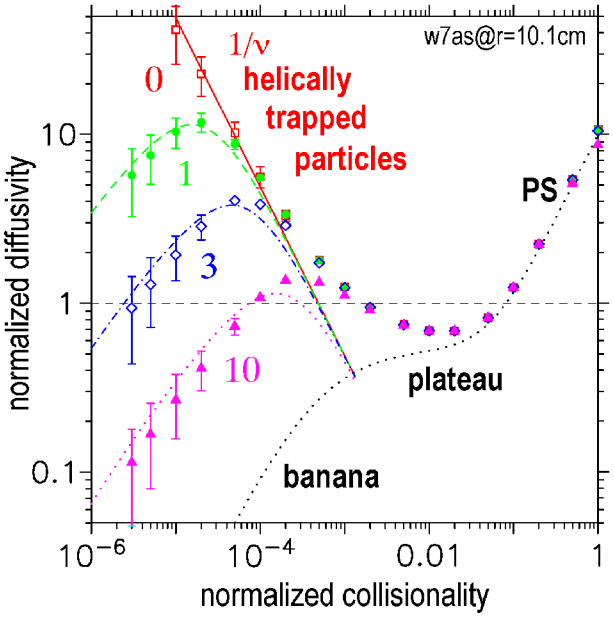

Figure 8.9: *Predicted neoclassical diffusivity of a mono-energetic test particle in W7-AS (normalized to the plateau value of a circular tokamak) as a function of the normalized collisionality ν/v in cm^{-1}. v is the particle velocity. The high diffusivity in the $1/\nu$ regime is strongly reduced with increasing radial electric field, given in terms of E/v in Vs/m^2. The diffusivity in an equivalent elongated tokamak is shown for comparison (dotted line).*

For example, the vertical $\mathbf{B} \times \nabla B$ drift can be averaged out by a superimposed poloidal $\mathbf{E} \times \mathbf{B}$ drift in a radial electric field (see Fig. 8.9). The electric field adjusts itself self-consistently by the ambipolarity of radial ion and electron fluxes, $\Gamma_e = \Gamma_i$, where

$$\Gamma_\alpha = -n_\alpha \left[D_{11}^\alpha \left(\frac{\nabla n_\alpha}{n_\alpha} - q_\alpha \frac{E_r}{T_\alpha} \right) + D_{12}^\alpha \frac{\nabla T_\alpha}{T_\alpha} \right] + \Gamma_{\alpha,ext},$$

n_α is the density of species α, D_{11}^α is the particle diffusivity, and D_{12}^α the transport coefficient for a particle flux driven by the temperature gradient. $\Gamma_{\alpha,ext}$ denotes fluxes which are externally driven, e.g. by the heating method. Since the transport coefficients

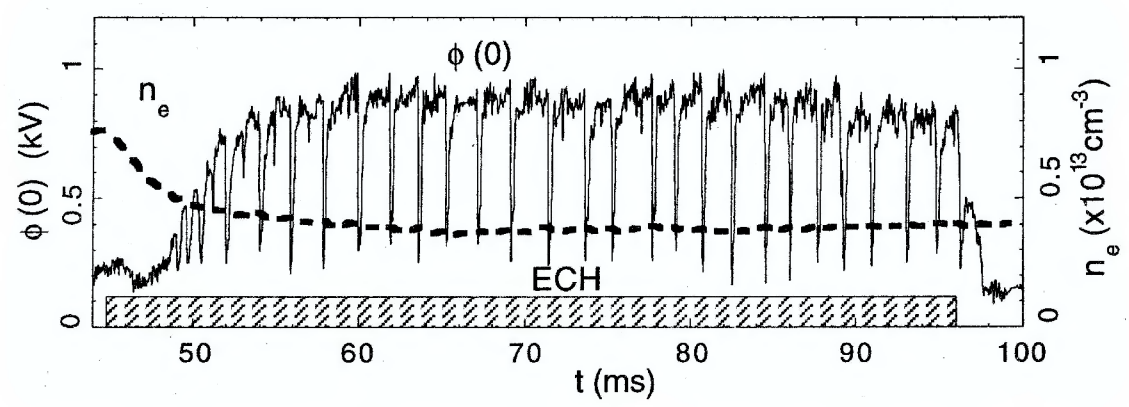

Figure 8.10: *Limit cycle oscilations between bifurcated states of the electric potential in the centre of a low collisionality plasma in CHS [7].*

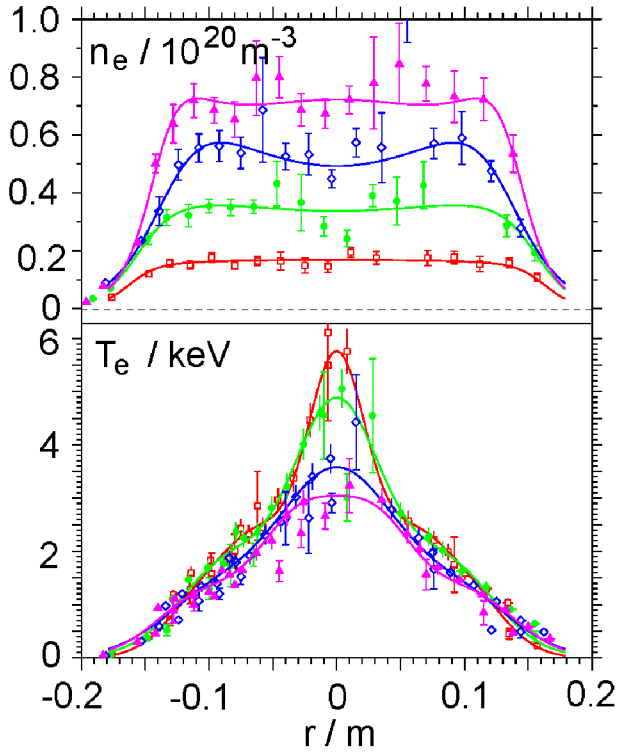

Figure 8.11: *Electron density and temperature profiles in ECRH heated discharges at W7-AS (P_{ECRH} = 1.2 MW). With decreasing density a strong peaking of the central temperature is observed which is attributed to transport reduction by the formation of a radial electric field. Towards the plasma boundary the temperature profile is dependent of the density, indicating a $1/\nu$ scaling of transport [8].*

D have a nonlinear dependence on E_r, multiple solutions of the ambipolarity condition are possible and thus bifurcations may occur. In CHS limit cycle oscillations between bifurcated states of the plasma potential have indeed been observed (Fig. 8.10).

The impact of a radial electric field on transport is evidenced in ECRH heated high electron temperature discharges in W7-AS (Fig. 8.11, P_{ECRH} = 1.2 MW). In the outer

plasma region the electron temperature T_e is independent of the density which is typical for the $1/\nu$-regime ($\mathrm{d}T/dr \sim -P/(n\chi)$ does not depend on n since $\chi \sim \nu^{-1}$, χ is the heat diffusivity and P the heating power). This is different in the centre. Here, with decreasing density a strong peaking of T_e is observed and central values of 6 keV are reached. (With a power of 2 MW the highest temperature in W7-AS, $T_e = 7$ keV, has been achieved). This indicates a reduction of neoclassical transport below the $1/\nu$-level. The high central T_e is accompanied with a strong positive radial electric field (a positive field, the so called electron root, arises if the plasma charges up positive by the loss of electrons). A detailed analysis is given in Fig. 8.12 for a similar discharge at $P_{ECRH} = 0.77$ MW. Close to the centre a radial electric field of up to $E_r = 600$ V/cm is measured by charge exchange recombination spectroscopy. E_r becomes small and even negative (ion root, the plasma charges up negative) towards the boundary. The ion root solution yields good agreement with the experiment at larger radii whereas in the centre the observed electric field is somewhat larger than the electron root solution. Calculating the neoclassical electron heat conductivity χ_e with $E_r = 0$ clearly overestimates the experimental value in the centre by an order of magnitude whereas the electron root solution agrees within a factor of 2. For the central region a full consistence of experimental results and neoclassical predictions could not be achieved with thermal fluxes as the generating mechanism for the electric field. It is therefore assumed that the strong positive electric field is essentially due to an additional electron flux generated by the ECRH, which produces suprathermal electrons trapped in a local magnetic mirror. These electrons are then lost by the $\mathbf{B}\times\nabla B$ drift. (This is similar to a regime with high ion confinement observed earlier in W7-A, where neoclassical ion plateau transport was reduced by a strong negative E_r arising from the orbit losses of perpendicular injected NBI.) At the boundary electron heat transport is clearly anomalous, i.e. it exceeds by far the neoclassical predictions.

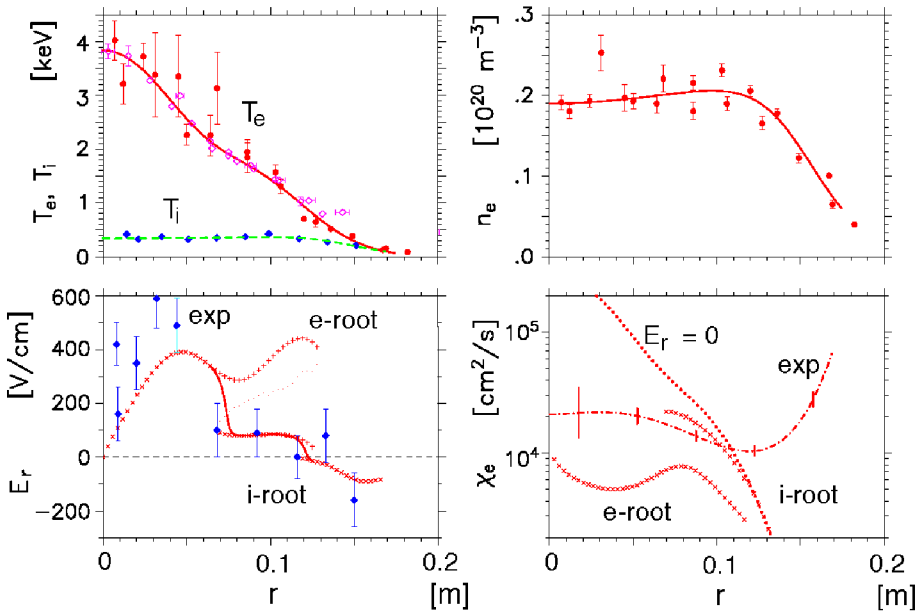

Figure 8.12: *Profiles of T_e, T_i, n_e, E_r and χ_e for a low density ECRH discharge at W7-AS ($P_{ECRH} = 0.77$ MW). For E_r and χ_e the neoclassical predictions from the various roots of the ambipolarity condition are also given. Because of strong electron heating and small collisional energy transfer to the ions T_i is much smaller than T_e [9].*

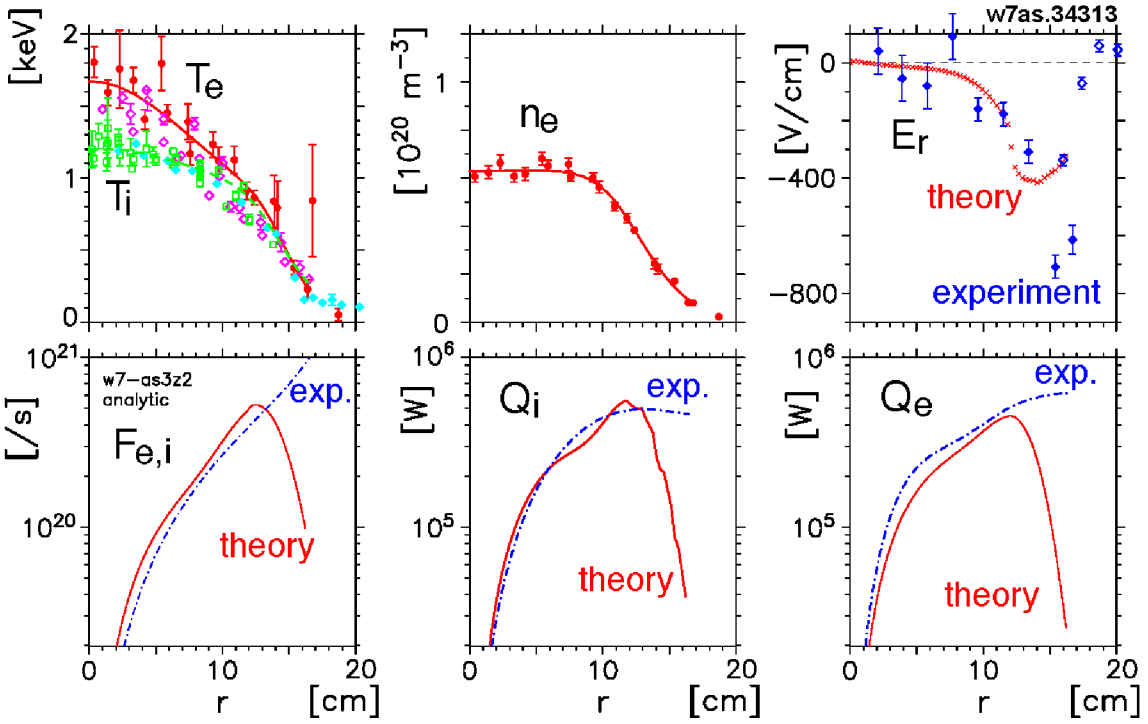

Figure 8.13: *Profiles of temperatures, density and radial electric field and of the particle fluxes $F_e = F_i$ and ion and electron heat flux Q_i and Q_e for a high ion temperature discharge at W7-AS heated by ECRH and NBI ($P_{ECRH} = 0.4$ MW, $P_{NBI} = 0.9$ MW). The experimental fluxes are compared to the neoclassical predictions [10].*

At higher density and with NBI-heating in addition to ECRH a higher ion temperature approaching the electron temperature can be achieved. The analysis of a high ion temperature discharge in W7-AS shows, that in the central plasma region ions and electrons behave neoclassically (Fig. 8.13). For the conditions with $T_e \approx T_i$ a negative electric field (ion root) is neoclassically expected and experimentally found throughout the plasma. The electric field is sufficient to overcome the unfavourable $1/\nu$-scaling for the ion transport coefficients such that the highest ion temperatures in W7-AS up to 1.7 keV have been achieved in this type of discharge. Again, transport is clearly anomalous at the boundary.

Although a radial electric field can considerably reduce neoclassical transport its formation cannot be well controlled experimentally. Therefore, the *a priori* reduction of $1/\nu$-transport already at the design stage of a stellarator is more promising or even mandatory. This can be achieved for example by a quasi-symmetric field structure which is nearly 2D in magnetic coordinates (e.g. HSX) or by minimizing the effective helical ripple (e.g. W7-X). Figure 8.14 shows the calculated electron diffusivity as a function of density for different magnetic configurations that can be realized in HSX. At low density, i.e. low collisionality, D is strongly reduced in the standard QHS (quasi-helically-symmetric) configuration as compared to the so called mirror configuration where a toroidal mirror is introduced by additional coils which spoils the symmetry and leads to $1/\nu$-transport. Already the initial operation of HSX gave the first experimental evidence that in the collisionless regime transport can be strongly reduced by quasi-symmetry. Confinement in ECR-heated discharges is improved by a factor of 6 and, consistent with

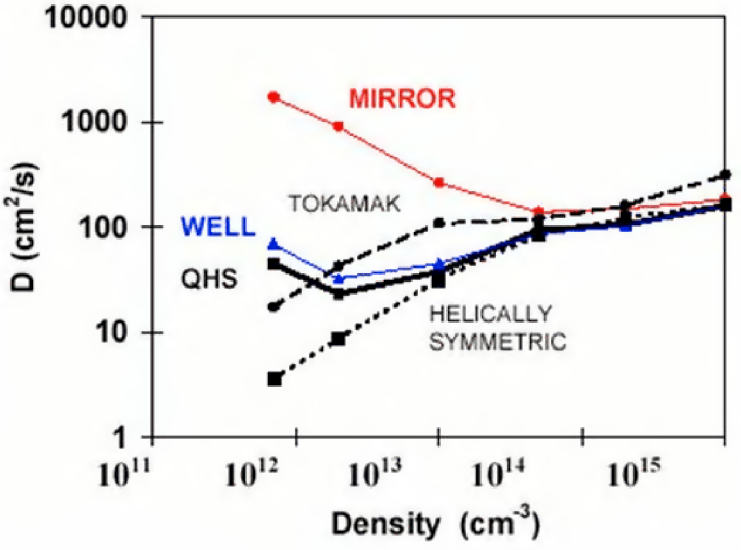

Figure 8.14: *Predicted diffusivity D as a function of density for various magnetic configurations in HSX. For comparison D is also given for an equivalent tokamak and for full helical symmetry [11].*

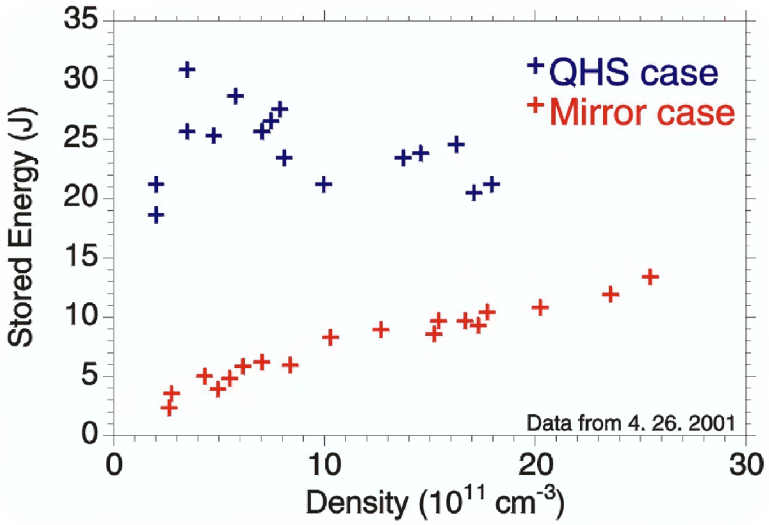

Figure 8.15: *Measured plasma energy as a function of density for the QHS- and the mirror-configurations in HSX [12].*

the predictions, the stored plasma energy decreases with density (collisionality) in the QHS-case and increases in the mirror case (Fig. 8.15). There are further aspects which should improve with quasi-symmetry. For example, viscous damping of plasma rotation is strongly reduced in the quasi-symmetric direction. Since plasma rotation plays a key role in the reduction of anomalous transport and the formation of local transport barriers (see the section 8.5.2), improvements in this area have to be expected for the future.

8.5.2 Anomalous transport

Neoclassical transport in stellarators prevails at low collisionality where the ripple induced losses can become large. At higher collisionality transport is anomalously enhanced compared to the neoclassical predictions, in particular for the electrons. This generally applies close to the boundary (see χ_e in Fig. 8.12 and the fluxes in Fig. 8.13). It is common opinion that anomalous transport originates from plasma turbulence but its nature is not yet resolved. Therefore, empirical scaling laws are used to describe the dependencies of transport on the leading parameters. In case of energy transport the global energy confinement time, $\tau_E = W/(P - dW/dt)$ with plasma energy W and heating power P, is the figure of merit. The International Stellarator Scaling ISS95 has been derived by a statistical analysis of confinement data from W7-AS, W7-A, Heliotron-E, CHS and ATF [13]:

$$\tau_E^{ISS95} = 0.079 a^{2.21} R^{0.65} P^{-0.59} n^{0.51} B^{0.83} \iota^{0.4}.$$

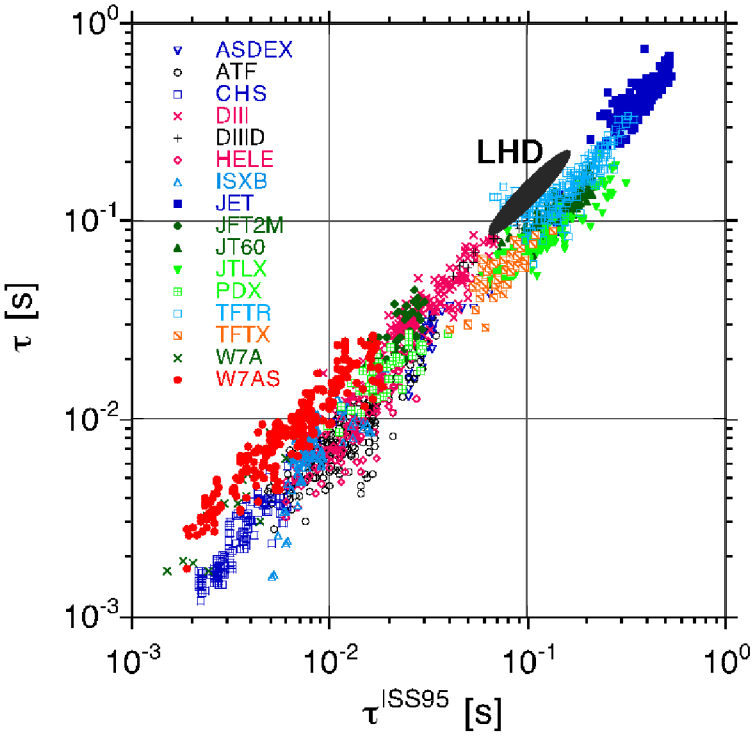

Figure 8.16: *Experimental energy confinement times from stellarator and L-mode tokamak discharges versus the ISS-95 values. The range of recent LHD confinement is indicated [13, 14, 15].*

The expression empirically relates the confinement time τ_E (in s) with the plasma dimensions a and R (in m), the heating power P (in MW), the average value of the plasma density n (in 10^{19} m^{-3}) and magnetic field properties in terms of the magnetic induction B (in T) and the rotational transform ι. Since ι has a radial variation in devices with magnetic shear, it is taken at $r/a = 2/3$ by convention. As in tokamaks confinement in stellarators exhibits a power degradation (τ_E decreases with power). In contrast to tokamaks a significant dependence of confinement on the ion mass (isotope effect) has

not yet been observed. Figure 8.16 shows experimental τ_E-values from various stellarator and (L-mode) tokamak discharges versus the calculated ISS95 values. Meanwhile, the best stellarator confinement has been achieved with $\tau_E = 0.3$ s in LHD, having the largest dimensions, a and R. It is evident that

1. the smaller torsatrons and Heliotrons have a common scaling,
2. confinement in LHD and W7-AS exceeds the torsatrons/Heliotron scaling by a factor of 2,
3. confinement in stellarators scales similar as L-mode confinement in tokamaks.

The better confinement in W7-AS may result from the low magnetic shear but possibly the W7-AS optimization also affects anomalous transport. The improved confinement in LHD is related to an edge transport barrier, i.e. a radially localized region of reduced transport. The barrier leads to a steep temperature gradient and to the formation of a temperature pedestal which is not observed in the smaller devices (Fig. 8.17). The edge barrier is suspected not to be an H-mode due to the lack of key features as ELMs (= edge localized (MHD) modes) and a spontaneous transition but may be related to the existence of the $\iota = 1/1$ surface at the edge.

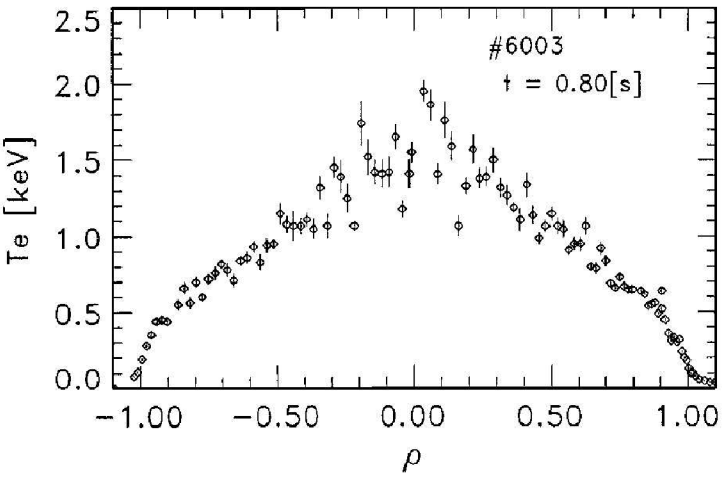

Figure 8.17: *Typical electron temperature profile in a NBI discharge at LHD as a function of normalized effective radius r/a. A steep gradient at the edge forms a temperature pedestal [16].*

The H-mode is a high confinement regime with an edge transport barrier which is caused by a sheared (i.e. radially varying) poloidal $E \times B$ rotation in a radial electric field. It typically improves confinement by a factor of 2. The H-mode was discovered in the ASDEX tokamak and has been observed in W7-AS as the first stellarator. The sheared rotation radially decorrelates turbulent structures which are assumed to be responsible for anomalous transport. Sheared rotation is also an essential ingredient in the formation of internal transport barriers (ITB) not being located at the edge. The rotation can for example be driven by the electric field resulting from the neoclassical particle fluxes.

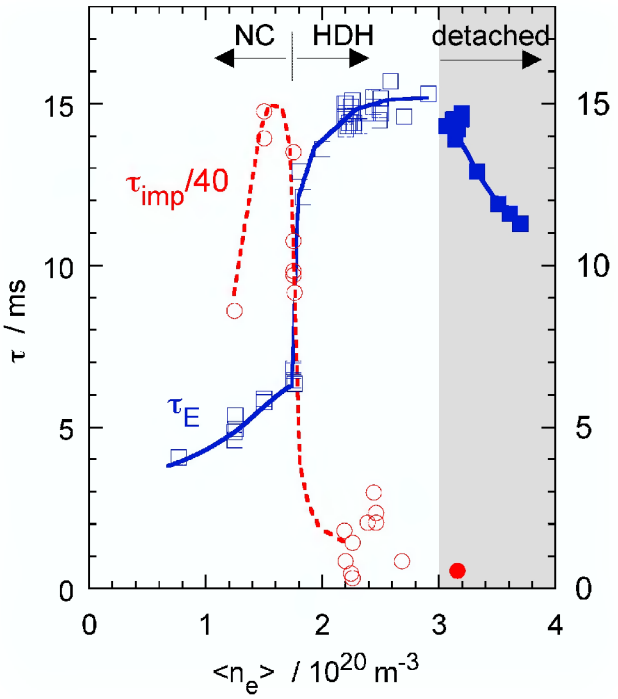

Figure 8.18: *Density dependence of energy and impurity confinement in W7-AS. At a threshold density τ_E doubles whereas τ_{imp} dramatically decreases. At the highest densities the plasma detaches from the targets. ($P_{NBI} = 2$ MW) [17]*

High energy confinement in the H-mode is accompanied with improved particle and impurity confinement, causing a continuous rise of impurity radiation during a discharge. Therefore H-mode discharges are terminated by a radiative collapse (imbalance of heating and radiated power), unless the densities are not kept at a tolerable level by ELMs. In a certain sense, ELMs act like an overpressure valve, decreasing the pressure gradient, if it exceeds a limit. They intermittently enhance transport and remove particles and impurities but also part of the plasma energy. Very recently, a new ELM free high confinement regime has been discovered at W7-AS, which combines the desirable features of simultaneously high energy and low impurity confinement (Fig. 8.18). It occurs above a threshold at very high density ($n_e > 10^{20}$ m^{-3}) and is therefore termed High Density H-mode (HDH). Basic features of the HDH-mode are compared to the normal confinement (NC) in Fig. 8.19. In contrast to transient NC-discharges with increasing impurity radiation and high fluctuation level HDH-mode discharges are quasi-stationary and very quiescent with respect to fluctuations (seen in the H_α-light). Energy confinement exceeds that of NC-discharges by a factor of 2, whereas impurity confinement is lower by a factor of about 10. The analysis of impurity tracer experiments has revealed that in the NC-regime an inward convection of impurities leads to impurity accumulation and a radiation distribution which is peaked at the centre. In contrast, the inward convection is strongly reduced in the HDH-mode and the radiation distribution is hollow and peaked at the edge. Radiation from the plasma core has to be avoided since it decreases the energy confinement, but radiation from the edge is desirable since it reduces the power flux into the divertor and decreases the heat load of the divertor targets. Thus the HDH-mode appears very promising with respect to both confinement and exhaust. The high density in the HDH-mode implies a rather low temperature ($\approx$ 400 eV) and

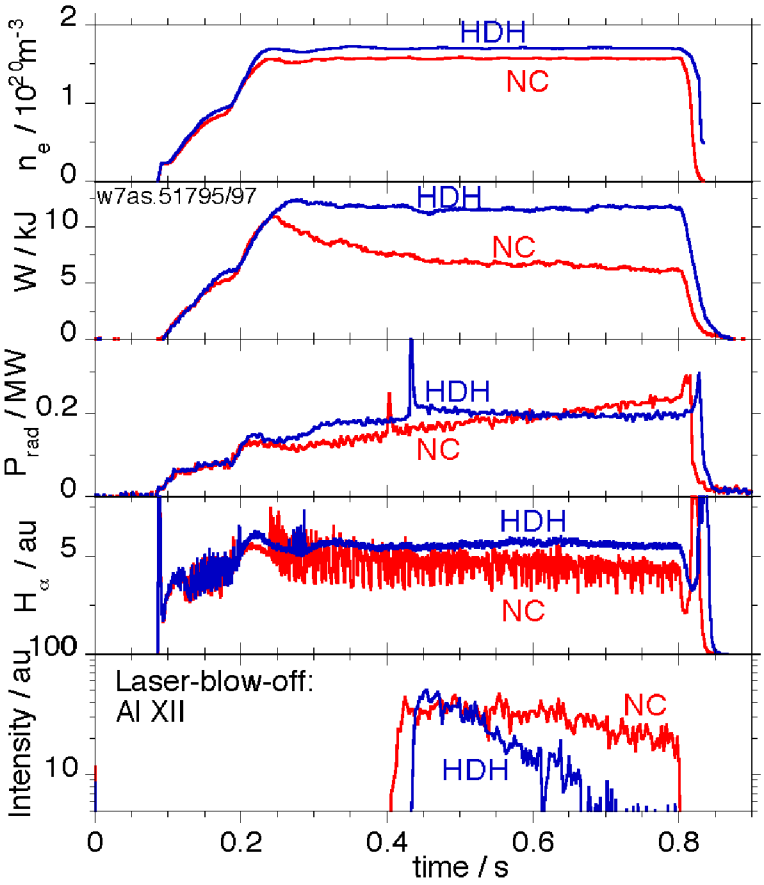

Figure 8.19: *Time traces of plasma density, energy, radiation power and H_α-light for two NBI discharges below (NC = normal confinement) and above (HDH = high density H-mode) the HDH density threshold. The decay curves of aluminium injected as a tracer demonstrate the reduced impurity confinement in the HDH-regime. (P_{NBI} = 1 MW) [18]*

a high collisionality. Up to now it is an open question, if the HDH-mode can also be achieved at lower collisionality (higher temperature) as expected for larger devices.

In low shear stellarators there is strong evidence that the anomalous electron heat conductivity χ_e is increased at rational magnetic surfaces, i.e. at surfaces where $\iota(r) = n/m$ is a rational number. Figure 8.20 shows the sensitive dependence of confinement on the boundary value of ι observed in W7-AS. The best confinement is found right next to low order rational values $\iota = 1/2, 1/3$, etc. (only those have been used in the ISS95 data base). The ι-dependence is reproduced by an empirical model which considers three contributions to the heat conductivity, $\chi_e = \chi_{neo} + \chi_0 + \sum \chi_{nm}$: neoclassical transport, a term describing a basic level of anomalous transport, and an additional term for enhanced turbulence at rational surfaces. The influence of the rational surfaces decreases with magnetic shear. Within this model, the confinement maxima are explained by the circumstance that in the close vicinity of low order rational numbers the density of rational numbers is generally smaller than elsewhere. It is very remarkable that local features in the T_e profile of various tokamaks, e.g. RTP, JET and TEXTOR-94, are also strictly correlated with the occurrence of low order rational $\iota(= 1/q)$ values. Close to these values a strong reduction of heat transport may give rise to local electron transport

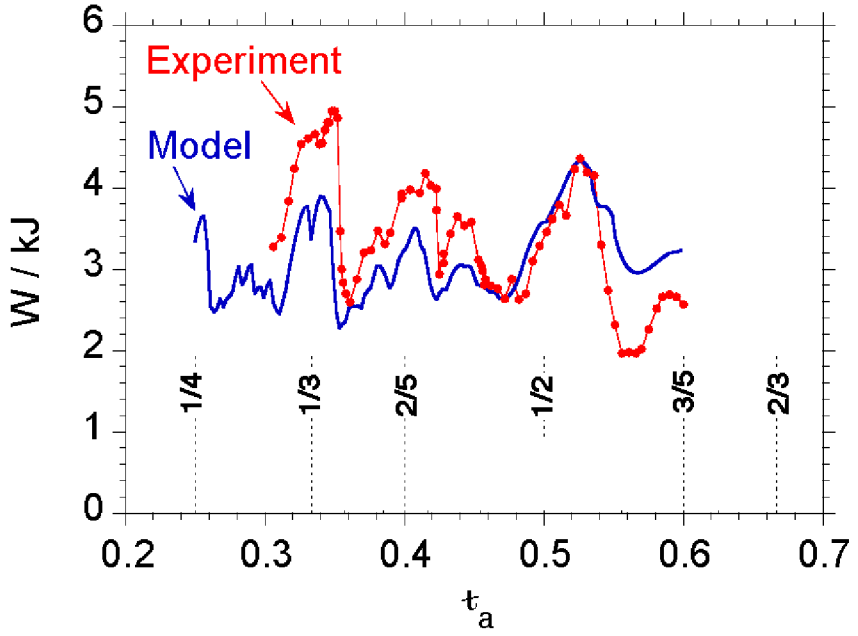

Figure 8.20: *The dependence of confinement on the boundary value of the rotational transform for ECRH discharges in the low shear stellarator W7-AS ($P_{ECRH} = 0.34$ MW). The experimental plasma energy is compared with the kinetic energy of the plasma electrons as calculated from a transport model which assumes enhanced transport at rational magnetic surfaces [19].*

barriers. It may therefore be conjectured that the underlying processes are governed by the same physics in both stellarators and tokamaks.

8.6 Towards steady state

The steady state capability of stellarators has already been demonstrated in the ATF torsatron, although at low performance (Fig. 8.21). A one hour and 17 minutes ECRH discharge has been run at reduced values of magnetic field ($B = 0.51$ T), heating power ($P = 70$ kW) and density ($n \leq 3\ 10^{18}$ m^{-3}). The parameters had to be limited in order to prevent overheating of the copper coils and of the vessel wall, and to avoid the loss of density control. At the low level of heating power, the significant power loss due to atomic processes (ionization, excitation, etc.) kept the electron temperature at a low value of about 30 eV. The discharge was probably terminated by the build-up of impurities from outgassing of the vacuum vessel.

Steady state operation at high performance, i.e. at high field, power and density, requires superconducting coils and a divertor which can handle the power and particle exhaust. The divertor channels the power and particle fluxes emerging from the plasma to target plates where the particles can be pumped after being neutralized and the deposited energy can be removed by active cooling. The first superconducting stellarator, LHD, is not yet equipped with a full divertor and has achieved pulse lengths of 120 s with 400 kW

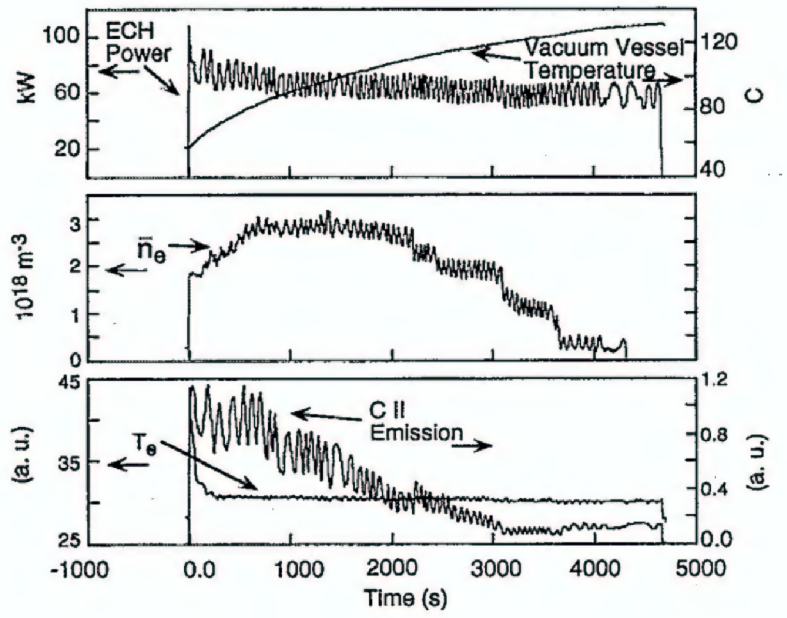

Figure 8.21: *Long pulse discharge in ATF with a pulse length of 4667 s at* $B = 0.51$ *T and 70 kW ECRH power [20].*

ICRH and of 80 s with 500 kW NBI at $B = 2.75$ T and densities around 1.5 10^{19} m^{-3} (Fig. 8.22). With proper divertor it is envisaged to operate LHD for one hour at 3 MW of heating power and W7-X for 30 min at 10 MW.

The different divertor concepts for stellarators are sketched in Fig. 8.23. As a common feature the confinement region with closed flux surfaces is surrounded by a region of open field lines which are "diverted" to target plates. Plasma particles diffuse across the last closed flux surface (LCFS) into the open field line region and follow the field lines to the targets where they are neutralized and deposit their energy.

The *helical divertor* makes use of the intrinsic field line diversion by the helical coils. Just outside the LCFS the field lines are nearly 'confined' for many helical turns in a narrow ergodic layer close to the main plasma. After escaping from this layer they quickly move along the divertor legs to the targets. The divertor structure follows the pitch of the helical coils. The *island divertor* (ID) utilizes the field line diversion within magnetic islands, the islands being intersected by the target plates. The islands are induced either by external perturbation fields generated by additional control coils (e.g. in the *local island divertor*, LID) or they are intrinsic to the configuration (e.g. the island divertor in W7-AS, see also Fig. 8.2). In helical and local island divertors the target region and the main plasma are sufficiently separated, such that the divertor region can be closed except for a slit which allows the plasma flow to enter the divertor chamber. A *closed divertor* geometry allows for efficient pumping of neutrals and prevents their back-streaming into the core plasma. An island divertor of the W7-AS type has a rather small distance between target and core plasma. In this *open island divertor* geometry a high edge density is required to prevent the penetration of recycling neutrals into the core plasma

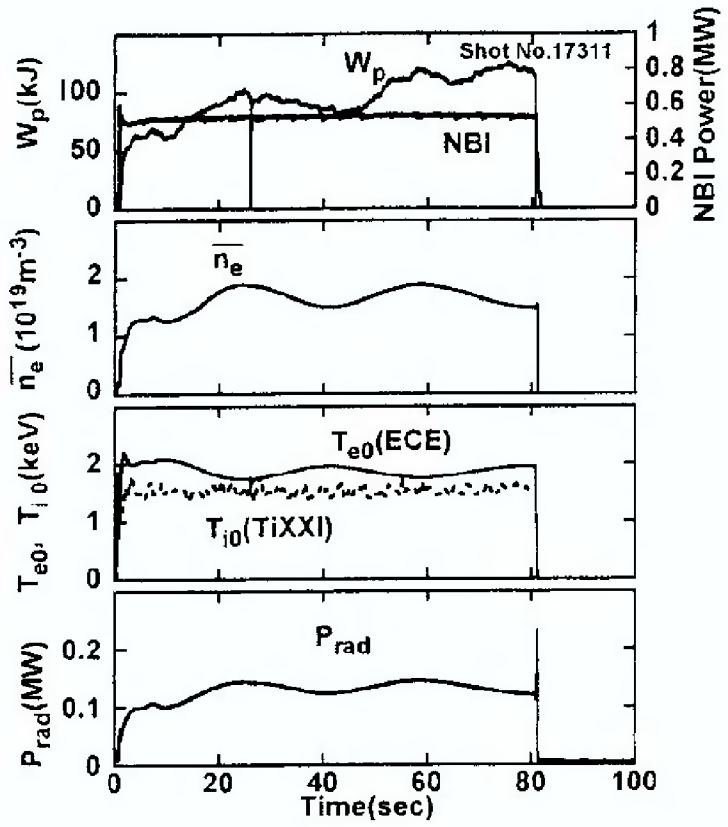

Figure 8.22: *Long pulse discharge in LHD with a pulse length of 80 s at $B = 2.75$ T and 500 kW NBI power [21].*

and the neutrals have to be channelled into the pumping volume behind the targets by so called baffle plates (Fig. 8.24).

The local island divertor concept has successfully been tested in CHS using an externally generated 1/1 magnetic island. Figure 8.25 shows that with LID the plasma density is reduced as compared to a reference discharge without LID when the same gas puff rate is applied. In spite of lower density the LID discharge reaches the same plasma energy, i.e. the temperature increases because of a considerable reduction of impurity radiation, basically from oxygen. The local island divertor is now being implemented as a preliminary pumped divertor in LHD. Although plasma performance is expected to benefit from improved particle and impurity control, the LID is not suited to handle high power fluxes because of its small target area. Therefore, the final concept foreseen for LHD is a closed helical divertor.

The open island divertor has been realized at W7-AS. It uses the $5/m$ natural island chains ($m = 8, 9$, or 10) in combination with ten discrete divertor modules (Fig. 8.24) and serves to explore the general feasibility of the island divertor concept. With the island divertor a new quality of quasi-stationary high-power/high-density NBI discharges could be achieved. The reasons are twofold: improved density and impurity control even at lower density (NC-regime) and, at higher density, the occurrence of the HDH-mode (see

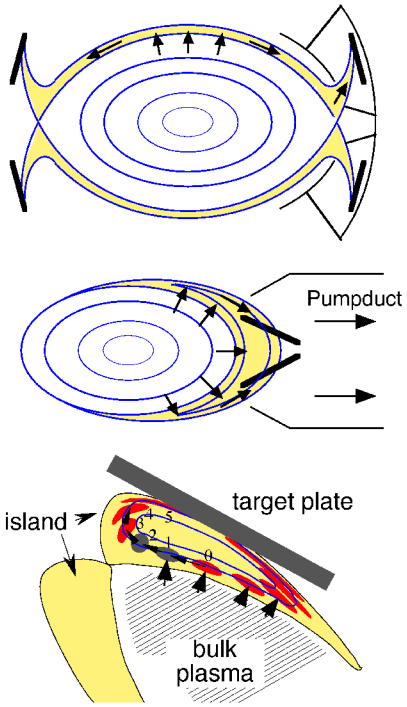

Figure 8.23: *Schematic view of the different divertor concepts for stellarators: the helical divertor with a closed divertor chamber indicated at the right (top), the local island divertor (middle), the target region in an open island divertor (bottom).*

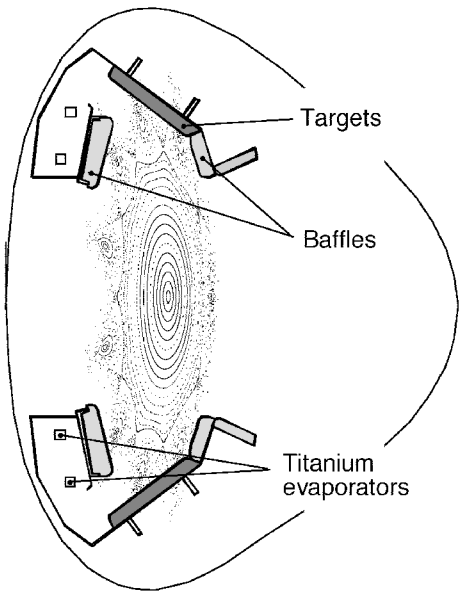

Figure 8.24: *The open island divertor in W7-AS. Poloidal cross section with flux surfaces, islands and divertor modules. Titanium can be evaporated in the sub-divertor chamber for pumping (top). Arrangement of the ten divertor modules (bottom). Targets and baffles are made from graphite [22].*

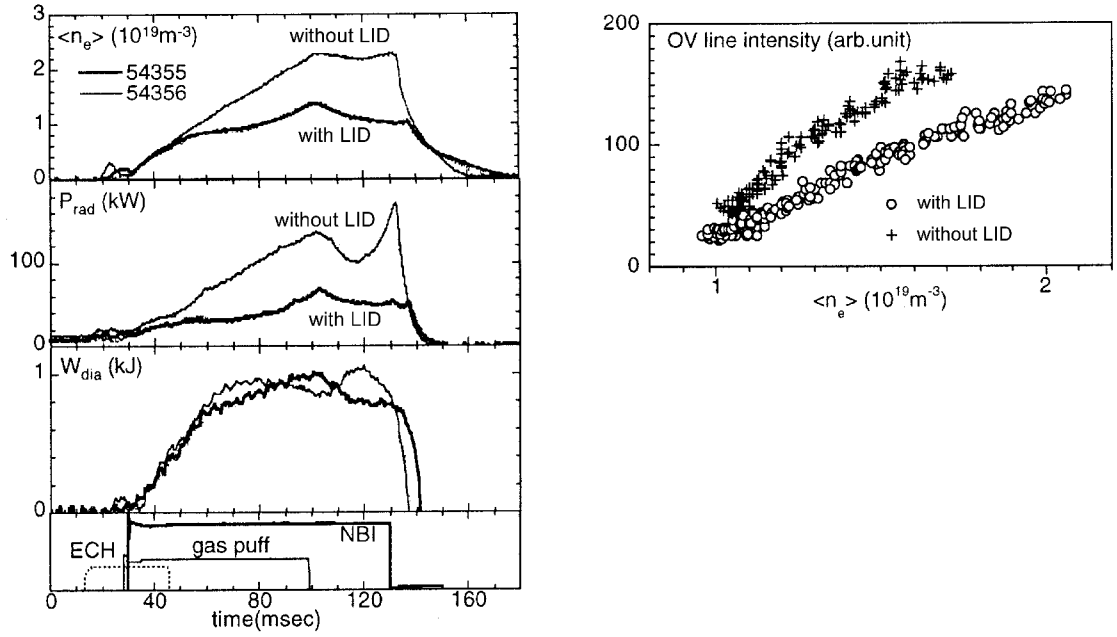

Figure 8.25: *Time evalution of plasma density, radiation power and plasma energy for NBI heated discharges in CHS with and without local island divertor (left). Radiation of O^{4+} impurity ions at 63 nm as a function of plasma density (right) [23].*

above) with simultaneously high energy and low impurity confinement. The edge density, about 5 10^{19} m^{-3}, is sufficiently high for proper divertor action, the impurity radiation – basically from carbon – is concentrated at the plasma edge thus not affecting core confinement, and, at the highest densities stable detachment of the plasma from the targets occurs with a tolerable reduction of plasma energy (see Fig. 8.18). In case of detachment the convective energy and particle fluxes to the target plates nearly vanish since the edge plasma radiates the energy away and the temperature in front of the targets drops to values < 5 eV such that ionization can no longer be sustained. The targets are thus protected by a cold radiating mantle. Figure 8.26 shows the power deposition patterns on a target plate as observed by a thermography camera. In the attached case the dark areas reflect the energy deposition zone where the targets intersect the islands. In the detached case the power deposition vanishes except for a small area which remains attached, but with strongly reduced heat flux.

8.7 Summary

The recent progress in stellarator research has removed the earlier scepticism against the reactor potential of stellarators. The results have shown that the essential drawbacks of traditional stellarators, such as high neoclassical transport losses and low β-limit, can be overcome by optimized magnetic configurations. Plasma confinement is equivalent to that in tokamaks of comparable size and the island divertor has been shown to be a viable exhaust concept. The achievements in terms of the best plasma parameters are summarized in Table 8.2.

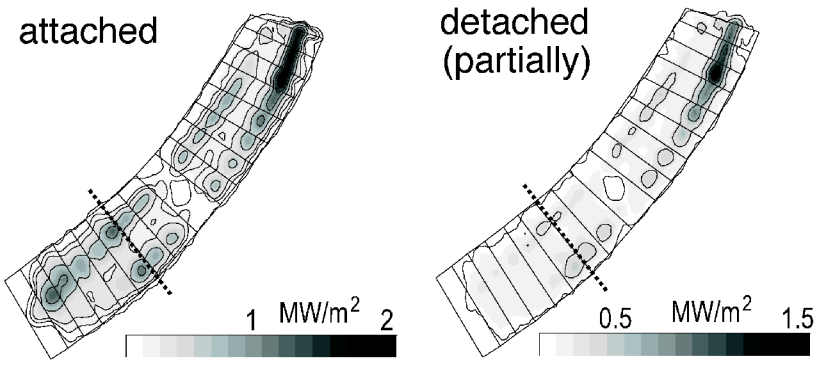

Figure 8.26: *Power deposition pattern on a divertor target plate in W7-AS for attached and detached situations as observed by thermography [24].*

	best	$\langle\beta\rangle$	n	T_e	T_i	τ_E	$n\,T_i\,\tau_E$	**Device**
	values	%	m^{-3}	keV	keV	s	m^{-3} keV s	
$\langle\beta\rangle$	3.4%	3.4	$2.5\ 10^{20}$	0.20	(0.20)	0.004	$2\ 10^{17}$	W7AS[25]
	$\approx 4\%$	≈ 4	$2.8\ 10^{20}$					LHD
n	$4\ 10^{20}$ m^{-3}	≈ 1	$4\ 10^{20}$	0.35	(0.35)			W7-AS[26]
T_e	10.0 keV		$5\ 10^{18}$	10.0	2.0	0.04		LHD[27]
T_i	3.5 keV		$1.3\ 10^{19}$	3.3	3.5	0.09	$2\ 10^{18}$	LHD[28]
τ_E	0.3 s		$6.5\ 10^{19}$	1.1	(1.1)	0.3	$2\ 10^{19}$	LHD[21]
$n\ T_i\ \tau_E$	$2\ 10^{29}$		$6.5\ 10^{19}$	1.1	(1.1)	0.3	$2\ 10^{19}$	LHD[21]
t_{pulse}	120 s		$9\ 10^{18}$	1.3	1.3			LHD[29]

Table 8.2: *The best plasma parameters in stellarators have been achieved in LHD and W7-AS so far. The values in a row have simultaneously been obtained in the same discharge. Ion temperatures in brackets have not been measured, but are assumed to equal the respective electron temperatures.*

The first superconducting large scale device, LHD, has started operation and is continuously being upgraded with respect to heating and exhaust. W7-X is under construction. The mission of these large devices is to test the torsatron and Helias concepts, respectively, under reactor relevant conditions with particular emphasis on steady state operation. In parallel, various strategies of concept optimization are explored in small and medium scale devices, which are already operational (HSX, Heliotron-J) or under design (NCSX, QPS, CHS-qa).

8.8 Recommended literature

- L. Spitzer, *The stellarator concept* [30]
  "The basic concepts of the controlled thermonuclear program at Project Matter-

horn are discussed." (The root of stellarator research. Lyman Spitzer has invented the stellarator and initiated the US fusion program with the Project Matterhorn in 1951)

- A.H. Boozer, *What is a stellarator?* [31]
  "The physics and mathematical concepts that are required to understand stellarators are reviewed."

- T.K. Chu, H.P. Furth, J.L. Johnson, C. Ludesher and K.E. Weimer, *Modular coils - a promising toroidal coil system* [32]
  "The concept of modular coils originated from a need to find reactor-relevant stellarator windings. Considerations of ... basic principles of modular coils... are given"

- H. Wobig, *Magnetic surfaces and localized perturbations in the W VII-A stellarator* [33]
  "In order to study the structure of surfaces under the influence of perturbations, a mapping procedure is used .... '." (The mapping can easily be implemented in a simple computer program. It instructively shows the creation of magnetic islands by perturbations and their dependence on field parameters like rotational transform and magnetic shear).

- G. Grieger et al., *Physics optimization of stellarators* [3]
  "This paper summarizes the status of advanced stellarators both from the conceptual point of view and also from the experimental side."

- R. König, *The divertor program in stellarators* [34]
  "The helical and island divertor concepts .... are introduced and ... the ... experiments performed and planned for different devices are reviewed."

Bibliography

[1] R. Jänicke et al. Detailed investigation of the vacuum magnetic surfaces on the W7-AS stellarator. *Nuclear Fusion*, 33(5):687–704, 1993.

[2] A. Komori. Magnetic flux mapping in LHD. *Stellarator News*, 58:1–2, 1998.

[3] G. Grieger et al. Physics optimization of stellarators. *Physics of Fluids B*, 4(7):2081–2091, 1992.

[4] A. Weller et al. Investigation of the β-limit in the W7-AS stellarator. In *19th IAEA Fusion Energy Conference, 14 - 19 October 2002, Lyon, France*, Vienna, 2003. IAEA. paper IAEA-CN-94/EX/S3-1.

[5] J.V. Hofmann et al. Stellarator optimization studies in W7-AS. *Plasma Physics and Controlled Fusion*, 38:A193–A211, 1996.

[6] S. Okamura et al. High β experiments in CHS. In *Plasma Physics and Controlled Nuclear Fusion Research 1994; Fifteenth Conference proceedings, Seville, Spain, 26 September–1 October 1994*, volume 1, pages 381–388, Vienna, 1995. IAEA. paper IAEA-CN-60/A2-20.

[7] A. Fujisawa et al. Discovery of electric pulsation in a toroidal helical plasma. *Physical Review Letters*, 81(9):2256–2259, 1998.

[8] M. Kick et al. Electric field and transport in W7-AS. *Plasma Physics and Controlled Fusion*, 41(3):A549–A559, 1999.

[9] R. Brakel et al. Confinement in W7-AS and the role of radial electric field and magnetic shear. *Plasma Physics and Controlled Fusion*, 39(12):B273–B286, 1997.

[10] R. Jaenicke et al. High power heating experiments on WENDELSTEIN 7-AS stellarator. *Plasma Physics and Controlled Fusion*, 37(11):A163–A176, 1995.

[11] D.T. Anderson et al. Initial experimental program plan for HSX, 1999. International Stellarator Workshop 27. September - 1 October 1999 Madison, Wisconsin, Usa; paper DE-FG02-93ER54222.

[12] D.T. Anderson and HSX-Team. First plasma results from HSX. *Stellarator News*, 76(July):1–2, 2001.

[13] U. Stroth et al. Energy confinement scaling from the international stellarator database. *Nuclear Fusion*, 36(8):1063–1077, 1996.

[14] H. Yamada and LHD Experimental Group. A first look at the confinement characteristics of NBI plasmas in LHD. *Stellarator News*, 62(march):1–2, 1999.

[15] N. Ohyabu, K. Narihara, LHD G1, and G2 Groups. Temperature pedestal discharges in LHD. *Stellarator News*, 62(march):3–5, 1999.

[16] N. Ohyabu et al. Edge thermal transport barrier in LHD discharges. *Physical Review Letters*, 84(1):103–106, 2000.

[17] K. McCormick et al. New advanced operational regime on the W7-AS stellarator. *Physical Review Letters*, 89, 2002.

[18] R. Brakel et al. Improved performance of the W7-AS stellarator with the new island divertor, 2002. 19th Fusion Energy Conference, 14 - 19 October 2002, Lyon, France; paper EX/C5-4.

[19] R. Brakel and the W7-AS Team. Electron energy transport in the presence of rational surfaces in the wendelstein 7-AS stellarator. *Nuclear Fusion*, 42(7):903–912, 2002.

[20] T.C. Jernigan et al. Long pulse experiments on the advanced toroidal facility. *Physics of Plasmas*, 2(6):2435–2439, 1995.

[21] K. Kawahata et al. Experimental studies on NBI and ICRF heated plasmas in the large helical device. *Plasma Physics and Controlled Fusion*, 42(12):B51–B60, 2000.

[22] P. Grigull et al. First island divertor experiments on the W7-AS stellarator. *Plasma Physics and Controlled Fusion*, 43(12):175–193, 2001.

[23] S. Masuzaki. A study of the plasma properties under a LID configuration in the CHS. *Journal of Plasma and Fusion Research SERIES*, 1:310–313, 1998.

[24] Y. Feng et al. Transport study on the W7-AS island divertor: Physics, modelling and comparison to experiment. In R. Behn and C. Varandas, editors, *Europhysics Conference Abstracts: 29th EPS Conference on Plasma Physics and Controlled Fusion, Montreux, Switzerland, 17–12 June 2002*, volume 26B, pages O–1.06, Vienna, 2002. ECA.

[25] A. Weller et al. Experiments close to the beta-limit in W7-AS. *Plasma Physics and Controlled Fusion*, 45(12):A285–A308, 2003.

[26] F. Wagner et al. Major results from Wendelstein 7-AS stellarator. In *19th IAEA Fusion Energy Conference, 14 – 19 October 2002, Lyon, France*, Vienna, 2003. IAEA. paper IAEA-CN-94/OV/2–4.

[27] Y. Takeiri et al. Formation of electron internal transport barrier and achievement of high ion temperature in Large Helical Device. *Physics of plasmas*, 10(5):1788–1795, 2003.

[28] S. Morita et al. Behaviour of ion temperature in electron and ion heating regimes observed with ECH, NBI and ICRF discharges of LHD. *Nuclear Fusion*, 42(10):1179–1183, 2002.

[29] T. Mutoh et al. ICRF heating and high energy particle production in the Large Helical Device. In *19th IAEA Fusion Energy Conference, 14 – 19 October 2002, Lyon, France*, Vienna, 2003. IAEA. paper IAEA-CN-94/EX/P2–19.

[30] L. Spitzer. The stellarator concept. *Physics of Fluids*, 1(4):253–264, 1958.

[31] A.H. Boozer. What is a stellarator? *Physics of Plasmas*, 5(5):1647–1655, 1998.

[32] T.K. Chu et al. Modular coils – a promising toroidal coil system. *IEEE Transactions on Plasma Science*, 9(4):228–233, 1981.

[33] H. Wobig. Magnetic surfaces and localized perturbations in the W VII-A stellarator. *Zeitschrift für Naturforschung Section A-A Journal of Physical Sciences*, 42(10):1054–1066, 1987.

[34] R. König et al. The divertor program in stellarators. *Plasma Physics and Controlled Fusion*, 44(11):2365–2422, 2002.

Chapter 9

Diagnostics of Fusion Plasmas

Rudolf Neu

9.1 Introduction

To investigate in detail the behaviour of fusion plasmas with their extreme parameters, a large variety of (partially complementary) diagnostic methods have been developed and are being used in present-day experiments. In general, the diagnostic systems of a fusion experiment constitute a major part of it, with regard to hardware as well as capital investment and manpower.

The physics principles of these methods come from all areas of physics, and therefore it is difficult to put them into any order. In the following table we try to do this for the most commonly used diagnostics, with the category name in the first column, the diagnostic name in the second, and the parameter measured in the last column.

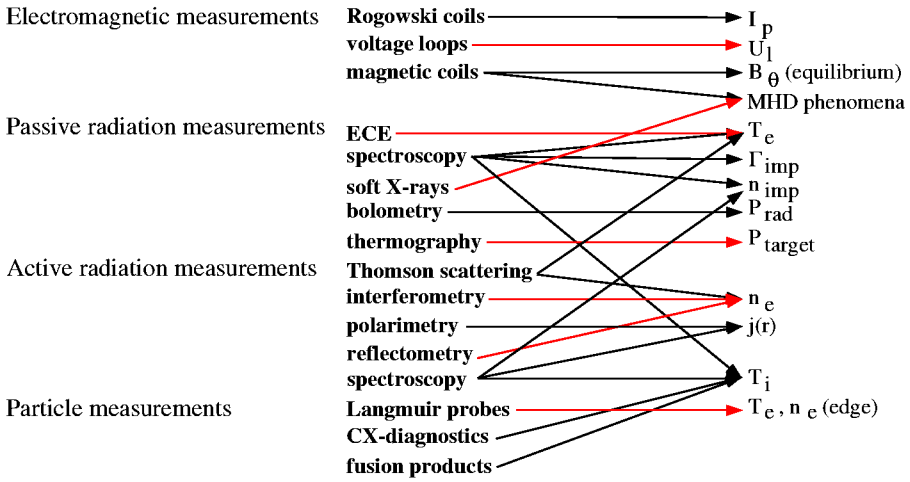

This selection of diagnostics is briefly discussed in the following. The basic physics principles of plasma diagnostics are well described in [1], [2], reviews of diagnostics with emphasis on the experimental aspect are found in [1], [3], and a short overview of basic

diagnostics is given in [4]. These references cover all diagnostics and are commonly available, and in the following text we will cite only additional, specialized papers for the reader interested in further details.

9.2 Electromagnetic measurements

A lot can be learned about gross plasma parameters from relatively simple measurements of magnetic fields and fluxes outside the plasma. Examples are sketched in Figure 9.1.

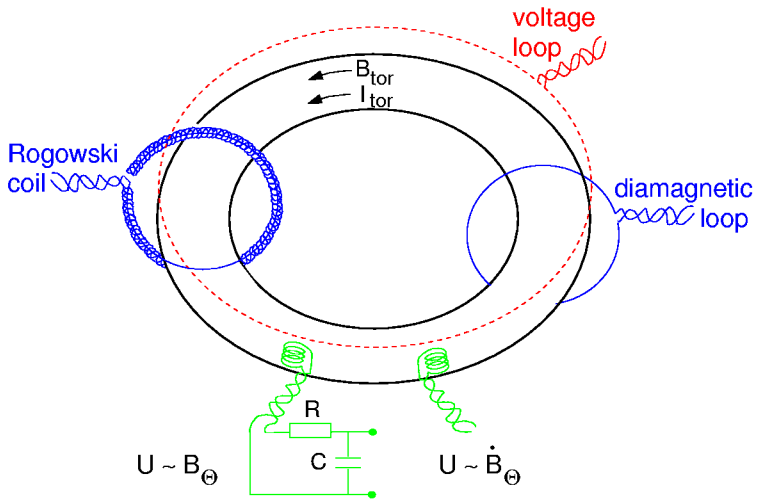

Figure 9.1: Schematic of electromagnetic diagnostics (after [4]).

Magnetic coils: Time-varying magnetic fields can be probed with a small coil of area A with N windings. From Faraday's law $\nabla \times \mathbf{E} = -\partial B/\partial t$ the voltage induced in the coil is

$$U = N \oint_l \mathbf{E} \cdot d\mathbf{l} = N \int_F \nabla \times \mathbf{E} \cdot d\mathbf{F} = -N \int_F \partial \mathbf{B}/\partial t \cdot d\mathbf{F} = -NA\dot{B}$$

if $\mathbf{B}$ is homogeneous over the surface A.

Because the voltage is proportional to the derivative of the total flux enclosed by the wire, its leads are twisted to minimise the area enclosed by them.
In most cases, however, one is interested in the magnetic field B and not in its time derivative. Then an analog integration circuit (as sketched in figure 9.1) with the time constant RC can be used to get an output voltage which is proportional to the magnetic field B, or it can be calculated numerically later from the data.

Such magnetic loops measuring $\dot{B}_\theta$ as indicated in figure 9.1 are used for two purposes.

1) Determination of the plasma equilibrium
A poloidal array of such coils can be used to determine the horizontal and vertical plasma positions, the plasma shape, the stored energy etc. While it is obvious that the difference in B_θ measured by coils directly below and above the plasma is a measure of its vertical position, the relation between the measured signals and the other equilibrium

parameters is more complicated. For circular, large-aspect ratio plasmas these relations can still be deduced analytically, but for elongated plasmas, as are nowadays common, the calculation of the equilibrium from B_θ measurements needs extensive computational effort.

2) Fluctuations
The same poloidal array can also be used to measure fluctuations in the magnetic field (in fact it is even easier, because it needs no time integration). In particular, this array can be used to infer the poloidal periodicity m and the toroidal periodicity n of this MHD instability.

Rogowski coil: A special form of B_θ-coil is the so-called Rogowski coil, a solenoidal coil with constant turn density per unit length n_c (also shown in figure 9.1). The total flux in this coil is

$$\phi = n_c \oint_l \int_F B \; dA \; dl$$

Changing the order of integration and using Ampere's law $\oint_l \mathbf{B} \cdot d\mathbf{l} = \mu_0 \; I$, we get

$$U = \dot{\phi} = \mu_0 \; n_c \; A \; \dot{I}_p$$

and thus integration yields the total plasma current I_p.

It is important that the return wire goes back inside the coil as indicated. Otherwise the coil would also measure the toroidal flux passing through the torus centre.

Voltage loops: In tokamaks the loop voltage U_l induced by the transformer is an important parameter since it drives the plasma current I_p. If I_p does not vary in time, a toroidal loop as shown in figure 9.1 measures U_l directly. Knowing I_p and U_l the electron temperature T_e can be deduced.
The simplified ohmic law for the plasma resistance $\Re$ reads

$$\Re = \frac{U_l}{I_p} = \frac{2\pi R_0 \eta}{\pi a^2} = \frac{2R_0}{a^2 \sigma}$$

where η is the specific resistance and $\sigma = 1/\eta$ the conductivity of the plasma.
The formula for the conductivity of a fully ionized plasma was derived by L. Spitzer:

$$\sigma = 1.9 \times 10^4 \frac{T_e^{3/2}}{Z_{eff} \; ln\Lambda} \quad \Omega^{-1} m^{-1}$$

when $Z_{eff} = \sum_j n_j \cdot Z_j^2 / n_e$ is the so-called effective ion charge which is a good measure of the degree of cleanness of the plasma. The Coulomb logarithm $ln\Lambda$ depends only weakly on T_e and n_e, and by using appropriate values for $ln\Lambda$ and Z_{eff} it is possible to obtain an estimate for T_e, the so-called conductivity temperature T_σ. It is a relatively poor measurement of T_e, but it is useful as a first estimate, as it can be deduced from very simple measurements.

The diamagnetic loop measures the toroidal flux of the plasma, which is related to the normalized plasma pressure.

9.3 Passive radiation measurements

9.3.1 Electron cyclotron emission (ECE)

Electron cyclotron emission is employed to measure radial profiles of the electron temperature, $T_e(r)$. An overview of ECE-diagnostics is found in [5].
Physics principles: The electrons gyrating in the magnetic field act as time-varying dipoles and radiate at the electron cyclotron frequency and its low harmonics, i.e.

$$\omega = n \cdot \omega_{ce} = n \cdot \frac{e\ B}{m_e}$$

For a typical magnetic field of $B = 2T$, the second harmonic($n = 2$) emission frequency is $\nu = 2\pi\omega = 112GHz$. This corresponds to a wave length of $\lambda = 2.8mm$, i.e. the ECE diagnostics uses millimeter waves.
As B is mainly the toroidal field $B = (B_0 \cdot R_0)/R$, with B_0 being the toroidal field at the plasma centre (at R_0), we get a simple relation between frequency and space:

$$\omega_n = n \cdot \frac{e\ B_0\ R_0}{m_e\ R}$$

Because the resonance is very sharp, the emissivity at the fundamental frequency and at low harmonics is so high that the radiation is optically thick. Due to reabsorption the radiation intensity is close to that of a black body, i.e. it follows the Planck curve. As the cyclotron radiation is in the long-wavelength part of the Planck curve (Rayleigh-Jeans law), it is proportional to T_e:

$$I_n(\omega) = \frac{\omega^2\ T_e}{8\ \pi^3\ c^2}$$

with c being the velocity of light. Therefore a measurement of the cyclotron emission at a certain frequency leads directly to $T_e(r)$.

The cyclotron waves can have two different polarizations, $\mathbf{E} \parallel \mathbf{B}$ (the so-called O-mode), or $\mathbf{E} \perp \mathbf{B}$ (X-mode). Most of the emitted power is in the X-mode. Therefore the plasma is usually optically thick to radiation at the 1st and 2nd harmonic in X-mode and at the fundamental frequency in O-mode.

The 1st harmonic in X-mode, however, is reflected at the upper hybrid frequency and does not leave the plasma. Therefore the 2nd harmonics in X-mode and the fundamental frequency in O-mode are used to measure $T_e(r)$.

For optically thin emission lines $I \propto n_e$, and $n_e(r)$ can be deduced in principle, but this is a problematic measurement.

Measurement techniques: Different techniques are used to measure the emission: Fourier transform spectrometry, heterodyne radiometry, Fabry-Perot interferometry, and diffraction grating spectrometry.

The first of these techniques uses a Michelson interferometer. The interference pattern is Fourier transformed, giving the complete ECE spectrum with moderate frequency and time resolution. Especially in plasmas with non-thermal electrons a knowledge of the

complete spectrum is necessary and can be used to determine the energy distribution of the electrons.

All the other techniques measure the emission only at a fixed frequency or in a narrow band, but they have very high time resolution. In the heterodyne technique the emission from the plasma is mixed with radiation from a local oscillator, and the resulting intermediate frequency signal is amplified and detected with a Schottky diode.

In Fabry-Perot spectrometry a parallel-plate etalon is used as a frequency filter, and in diffraction grating spectrometry the radiation from the plasma is conveyed to a diffraction grating. Depending on the frequency, the radiation is diffracted at different angles and is measured with a detector array. This technique allows simultaneous measurement at several different frequencies with good time resolution.

With all these techniques (except the heterodyne technique) the radiation is finally detected with a InSb detector cooled down to about 4 K.

9.3.2 Spectroscopy

Whereas the previous section is concerned with the radiation from free electrons, here we want to discuss radiation involving atoms and ions. Magnetically confined plasmas are always optically thin to this radiation. Its spectrum ranges from the near infrared to the soft X-ray region and contains a lot of information about the plasma composition. Three different mechanisms for the emission of radiation can be distinguished:

1) Radiation from free electrons in the field of ions, so-called bremsstrahlung, or free-free radiation, since it is a transition between two unbound states of the electron. This gives a continuous spectrum as shown in figure 9.2.

2) Recombination radiation from free electrons captured by an ion (free-bound radiation). This spectrum is also continuous, but it contains edges resulting from electrons with negligible energy recombining into a specific energy level of the ion (see figure 9.2).

3) Line radiation from bound electrons in an excited or ionized atom.

Continuum radiation

Because the bremsstrahlung and recombination radiation spectra fall off exponentially with the frequency ν, the slope of this spectrum can be used to deduce T_e, without any need for an absolute calibration. Usually semiconductor detectors (sensitive in the keV range) are used with a pulse height analysis system to measure spectra as sketched in figure 9.2.

The bremsstrahlung intensity depends on the ion species, and if different ion species are present in the plasma, all their contributions have to be added, and the intensity is proportional to Z_{eff}, and therefore an absolutely calibrated measurement can even be used to determine Z_{eff}, which is a good measure of the degree of cleanness of the plasma. To determine Z_{eff} from the level of bremsstrahlung, however, two conditions have to be fulfilled: Firstly, recombination radiation must be negligible, which is the case for very

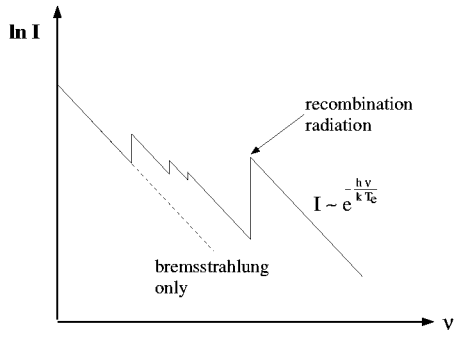

Figure 9.2: Qualitative spectrum of continuum radiation from a plasma.

low photon energies. Therefore this measurement can best be done in the visible and near infrared regions. Secondly, it must be ensured that the range of the spectrum used for this measurement is free of line radiation.

Line radiation

Line radiation from electrons bound in atoms or ions occurs at distinct wavelengths which are specific to this atom (or ion). Therefore line radiation can in principle always be attributed to a certain ion species. This makes it clear that spectroscopy is ideally suited to investigating the behaviour of impurities in a fusion plasma. The main objectives are:

- Identification of the elements present in the plasma.
- Measurement of the impurity influx rates from walls, limiters or divertor target plates from line emission of excited atoms.
- Determination of total impurity concentrations.
- Investigations of transport processes by comparing measured impurity concentration profiles with transport models.

Because T_e is usually peaked in the centre of the plasma and the charge state of atoms strongly increases with T_e, the different charge states of an ion species in the plasma are usually ordered in a shell structure, as shown in figure 9.3 for oxygen. In this case we see that in the inner half of the plasma oxygen is fully ionized and therefore it will not emit line radiation. Lighter species will be fully ionized even further outwards and only heavy species (like the metals) will be partially ionized (and therefore able to radiate) in the inner part of the plasma.

As the excitation energy strongly increases with the charge state ($\sim Z^2$), it becomes clear why plasma spectroscopy has to cover such a wide range of wavelengths. While for the investigation of excited atoms and low ionization stages at and around the plasma edge visible lines can be used, the highly charged ions in the plasma centre emit x-rays, and in a large part of the plasma vacuum ultraviolet lines are emitted.

To cover this whole range different spectrometers involving quite different techniques have to be used.

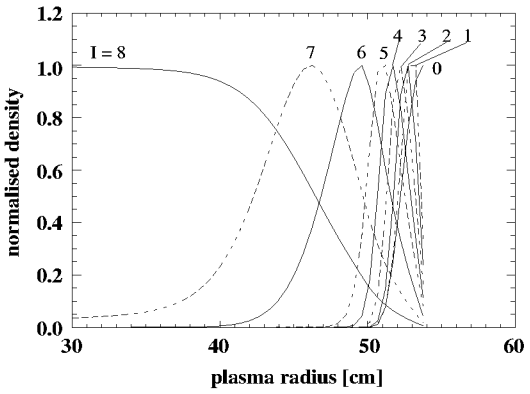

Figure 9.3: Radial distribution of various ionization stages of oxygen for typical plasma parameters and a central electron temperature of $T_e = 1.5\ keV$ in the ASDEX tokamak.

Visible and ultraviolet (700 – 200 nm)
Light can be transferred via glass fibres or normal optical components (for $\lambda \leq 350\ nm$ quartz has to be used), gratings or prisms are used to disperse the spectra and the light is detected with photomultipliers. The spectral resolution can be made very high ($\lambda/\Delta\lambda \approx 10^4$).

Vacuum ultraviolet (VUV, 200 – 30 nm)
In this range light is strongly absorbed even in air and can only be guided in evacuated tubes. Gratings can still be used, and windowless photomultipliers, scintillators, channeltrons or channel plates are used for detection.

Soft X-ray (100 – 1 nm)
The detectors are the same as in the VUV range, but to enhance the reflectivity of the gratings, they are used at grazing angles of incidence (1–20^0). The spectral resolution, however, is relatively low ($\lambda/\Delta\lambda \approx$ 200–2000).

X-rays (2 – 0.1 nm)
In this spectral range Bragg reflection on crystals is used to disperse the spectra. This results in a very good spectral resolution ($\lambda/\Delta\lambda \sim 10^4$). Beryllium windows can be used and air again becomes transparent. Scintillators and proportional chambers are used as detector.

Due to the imense progress in the field of semiconductors, specially adapted diode arrays or CCD-camaras are used more and more in all wavelength regimes.

Doppler measurements

Due to the Doppler effect the radiation emitted by a single atom or ion is shifted in frequency. If ν_0 is the original frequency of the line, the shifted frequency ν in a non-relativistic approach is

$$\nu = \nu_0 \left(1 + \frac{v}{c} \cos\alpha\right)$$

with v being the velocity of the particle and α being the angle between the directions of motion and emission. In a plasma, however, we observe emission from a large ensemble of atoms (ions), and in this case the Doppler effect results in a broadening of the line.

Usually the ions (atoms) are in thermal equilibrium and their energies follow a Maxwellian distribution function, which is isotropic. Then the intensity distribution

of the line is a Gaussian profile:

$$I(\nu) = I_0 \cdot exp(-\frac{mc^2}{2kT_i}\frac{\Delta\nu^2}{\nu_0^2})$$

and the line width (Full Width at Half Maximum, FWHM) is

$$\Delta\nu_{1/2} = 2\nu_0\sqrt{ln2}\sqrt{2kT_i/mc^2}.$$

In general the natural line width has to be folded with the Gaussian profile, but in most practical cases this is a negligible correction.

This technique for the determination of T_i in the plasma centre is widely used with X-ray spectrometers, as mentioned above, because they have a high spectral resolution and can observe ions in the plasma centre.

If the plasma as a whole rotates (toroidally or poloidally), however, the broadened line is also shifted due to the Doppler effect from this motion relative to the observer. This can be measured with spectrometers observing the plasma tangentially.

9.3.3 Bolometry

The energy loss from a plasma due to radiation is often a major contribution to the energy balance and is therefore an important parameter to describe the plasma.

The easiest way to measure the total radiation loss is to use a bolometer. This is a detector specifically designed to have a flat spectral response over a wide frequency range, mainly in the UV region, where the main radiative energy loss occurs.

Usually a bolometer consists of a metal foil that absorbs the energy. The temperature rise of this foil is then equal to the total energy flux divided by the bolometer's thermal capacity. This finite capacity, however, limits the time resolution of this technique to the order of ms.

9.3.4 Soft X-ray diagnostic

A much better time resolution (fraction of μs) can be reached by using semiconductor detectors, which are sensitive in the soft X-ray region $\hbar\omega \sim T_e$). The absolute calibration of these detectors is rather difficult, but they are ideally suited to measuring dynamic processes (such as sawteeth or other MHD instabilities) in the plasma.

Bolometers as well as soft X-ray detectors measure line-integrated signals that do not allow spatial resolution. Because both detector elements can be built very small usually a large number of them are used in a pinhole camera to get at least poor spatial resolution. If several such cameras view the plasma from different directions, as shown in Fig. 9.4, the local emissivity in the plasma can be deduced from the line-integrated signals by an inversion algorithm (tomography).

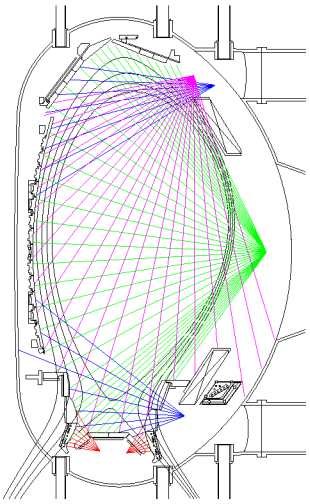

Figure 9.4: Lines of sight of the bolometer camara system in ASDEX Upgrade.

9.3.5 Thermography

For structures which are in contact with the plasma (such as limiters and divertor target plates) it is important to know the power flux hitting them. As these structures heat up, their temperature can be measured with an infrared camera, and from the temperature increase one can deduce the power flux onto the structure.

Alternatively thermocouples can be built into limiters or target plates to measure the temperature increase.

9.4 Active radiation measurements

While in the previous section we discuss diagnostics based on the radiation emitted by the plasma itself, new diagnostic possibilities emerge when we irradiate the plasma with radiation or with particles and observe the scattered or absorbed light or radiation of these particles.

The main advantage of most of the active diagnostics is the good spatial localization, because the measured signal comes from the point where the path of incoming radiation (particles) intersects the observation direction.

9.4.1 Thomson scattering

Principles of light scattering
In a classical description light scattering by charged particles can be thought as follows. An electromagnetic wave impinges on the particle and makes it oscillate. Now it acts like a dipole and radiates. Regarding the masses it is clear that it is mainly the electrons which will get accelerated and will radiate.

The scattered light is frequency-shifted as a consequence of a twofold Doppler effect due to the motion of the electron with regard to the incoming wave and the observer. This frequency shift is given as $\Delta\omega = \mathbf{k} \cdot \mathbf{v}$, where $\mathbf{v}$ is the particle velocity and $\mathbf{k} = \mathbf{k}_{in} - \mathbf{k}_{out}$

is the scattering vector (the difference between the k-vectors of incoming and outgoing waves), as shown in figure 9.5.

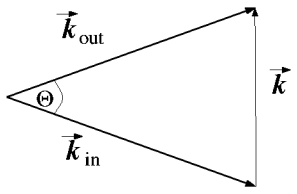

Figure 9.5: Geometry of Thomson scattering.

Again – as in the case of Doppler-shifted line radiation – we observe light not from a single electron but rather from a large ensemble and we have to add up all their contributions. Here, however, we have to consider two different possibilities, depending on the scattering parameter $\alpha = \frac{1}{k\lambda_D}$, with λ_D being the Debye length. Because $k_{in} \approx k_{out}$, one has $k \approx k_{in} \cdot 2sin\frac{\Theta}{2}$ and $\alpha \approx \frac{\lambda_{in}}{4\pi\lambda_D sin(\Theta/2)}$.
If $\alpha \gg 1$, neighbouring particles oscillate in phase and we get coherent scattering determined by collective effects. In this case T_i can be measured from the scattered light, but this technique has not yet been routinely used.
If $\alpha \ll 1$, the wave is scattered at free, uncorrelated electrons and this regime of incoherent scattering is called Thomson scattering. In this case the spectrum of the scattered light (for a fixed scattering angle) is only a function of T_e, as shown in figure 9.6.

A more detailed treatment of light scattering in general and of Thomson scattering is found in [2], [6].

Experimental techniques

The main problem of Thomson scattering is the very small fraction of scattered light, only about 10^{-13} of the incoming power being scattered. Therefore Thomson scattering could only be realized with the development of lasers as powerful and monochromatic sources. But also the detectors have to be optimized to utilize this small amount of scattered light.

The first Thomson scattering systems in the early 60's used ruby lasers ($\lambda = 694.3\ nm$) and optimized photomultipliers. However, one would like to measure T_e at more than one time point in the plasma discharge, and ruby lasers cannot be fired with a repetition rate of more than 1 Hz.

With the invention of silicon avalanche diodes (which are sensitive to infrared light) it was possible to use Nd:YAG lasers with $\lambda = 1.06\ \mu m$ and in 1982 the first Thomson scattering system with a repetition rate of 60 Hz was developed at the ASDEX tokamak. This system with 16 spatial channels is shown in figure 9.7.
To resolve the scattered spectrum, one can use gratings and imaging array detectors or (as on ASDEX) polychromator detectors. In this case the scattered light was observed with three detectors behind different interference filters. Their transmission curves are shown in figure 9.6. As one can show that the ratio of the intensities in different detectors is a monotonic function of T_e, the ratio of two such detector signals allows unique determination of T_e.

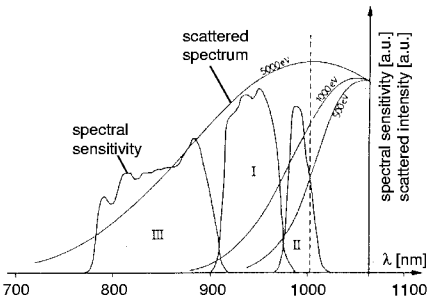

Figure 9.6: Scattering spectra for different electron temperatures and the sensitivity of the three filter/detector combinations.

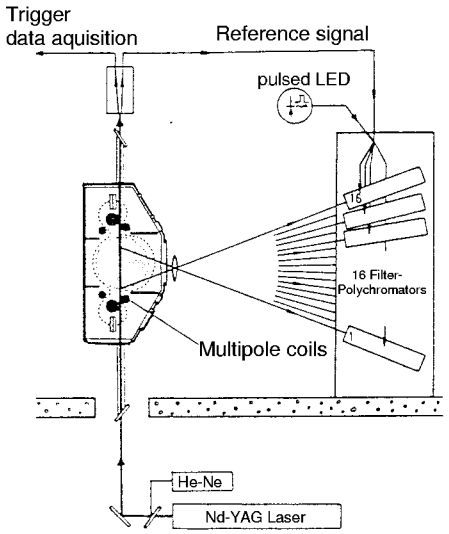

Figure 9.7: Experimental setup of the Thomson scattering experiment on ASDEX.

The absolute value of the scattered signal is proportional to the local electron density. Therefore Thomson scattering can also be used to derive the density profile.

9.4.2 Interferometry

Laser beams interact with the plasma electrons not only by scattering, but also by refraction or reflection. A good overview of plasma interferometry and polarimetry is given in [7].

Physics principles: When the static magnetic field in a plasma can be neglected, the refractive index N for the laser light is $N = (1 - \omega_{pe}^2/\omega^2)^{1/2}$, where ω_0 is the laser frequency and $\omega_{pe} = (n_e e^2/\epsilon_0 m_e)^{1/2}$ is the plasma frequency. For $\omega_0 \gg \omega_{pe}$ this gives an approximately linear relation

$$N \simeq 1 - \frac{\omega_{pe}^2}{2\omega_0^2} = 1 - \frac{e^2}{2\epsilon_0 m_e \omega_0^2} \cdot n_e.$$

This equation is also valid for static magnetic fields as long as the electric field of the laser beam is parallel to the magnetic field. When a laser beam transverses a plasma, it undergoes a phase shift

$$\Delta\Phi \simeq \frac{e^2}{2c\epsilon_0 m_e \omega_0} \int_L n_e \, dl.$$

Therefore interferometry does not give the spatially resolved electron density, but the line integral, which (if the line of sight L goes through the plasma centre) is already a

good parameter to describe a plasma. However, having a number of different lines of sight (and therefore line density measurements), one can deduce the plasma profile by an inversion algorithm.

Experimental techniques : A measurement of the phase shift with interferometry therefore allows determination of n_e. Usually one uses a Mach-Zehnder interferometer as sketched in figure 9.8. The light from the laser is split into three beams, and one of them is frequency modulated. The other two beams travel either through the plasma or along a reference path, but both of them are combined with the modulated beam before they are detected. These detectors now produce an output not at the optical frequency (of the order of $10^{14} Hz$) but at the modulation frequency $\Delta\omega_0$, which is in the convenient range of about 10–100 kHz. The phase shift of the probing beam is determined from the difference Δt in corresponding zero-crossings of the two detector signals. Therefore this method is independent of changes in the laser amplitude.

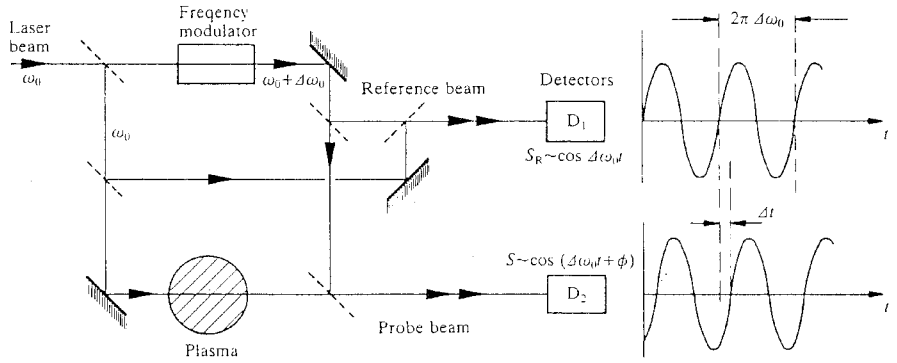

Figure 9.8: Schematic layout of a density interferometer (after [1]).

To be sensitive to small densities, ω_0 should be small (see the equation above), but we also have to consider wave refraction due to density gradients perpendicular to the laser beam, increasing with $1/\omega_0^2$. This would bend the beam and result in misalignment. On the other hand too high values of ω_0 (small wavelengths) make the measurement sensitive to mechanical interference due to vibrations. Therefore the laser frequency has to be chosen as a compromize between both conditions far enough above the plasma frequency ω_{pe}.

Commonly used lasers for fusion type plasmas nowadays are CH_3OH (119 μm), DCN (195 μm) and HCN lasers (337 μm). The frequency modulation is achieved with a rotating grating that Doppler-shifts the laser light.

9.4.3 Polarimetry

The laser light transmitting a plasma is not only shifted in its phase, but it also experiences Faraday rotation. This rotation of the polarization is proportional to the magnetic field component parallel to the laser beam $B_{\|}$ and for a laser transmitted through an inhomogeneous plasma the total rotation α is $\alpha \sim \int_L n_e B_{\|}\, dl$. Knowing $n_e(r)$ from other measurements (for example from interferometry) and with different lines of sight, one can deduce the radial profile of $B_{poloidal}$. This is of great importance because it allows one to determine the current profile inside the plasma.

9.4.4 Reflectometry

When an electromagnetic wave on its way through an inhomogeneous plasma reaches the critical density n_{crit}, where $\omega_0 = \omega_{pe}$, the wave is reflected (as known from metals where the quasi-free electrons act as a mirror). The plasma layer where n_{crit} is reached, is called cut-off layer, and this effect is used in reflectometry. A complete overview on reflectometry is given in reference [8].

In principle a Michelson interferometer is built, where the cut-off layer acts as one of the mirrors. From this the location of the cut-off layer can be determined. Sweeping the frequency of the wave (and therefore utilizing several cut-off layers with different critical densities) the electron density profile can be derived.

9.4.5 Charge exchange spectroscopy

In the section on line radiation it was discussed that light ions (especially the hydrogenic isotopes H and D, but also He) radiate only at the plasma edge because they are fully ionized further inward. This problem can be overcome by injecting a beam of neutral atoms. In collisions of these beam atoms with the plasma ions the latter can take over an electron (charge exchange) and then emit radiation. Energy and angular momentum conservation results in the excitation of high-lying Rydberg-levels, which emit visible radiation even from the heavier ion species. Usually the high-power heating beams are also used for charge exchange spectroscopy.

This technique then allows a measurement of the light ion density in the plasma core. Since the radiation is emitted in the visible range, it can be detected with high spectral resolution, witch allows also Doppler measurements of T_i and of the plasma rotation.

9.5 Particle measurements

Another group of diagnostic techniques relies on the particles leaving the plasma. Although ideally all particles should be confined by the magnetic field, there are a few exceptions that can be used as diagnostic tools.

9.5.1 Langmuir probes

Particle fluxes at the plasma edge can be measured simply by inserting a small electrode into the plasma and applying a variable voltage U_{probe} to it. If the probe current I_{probe} is measured, from the characteristic curve (I_{probe} versus Φ_{probe}) the local values of n_e, T_e and plasma potential can be derived as scetched in Fig. 9.9. These electrostatic probes are called Langmuir probes after I. Langmuir who developed them in the 20's.

However, it is obvious that such probes can only be used in the very edge region of the plasma, and when the plasma becomes dense and hot, the probe disturbs the plasma seriously and this technique can not be applied anymore.

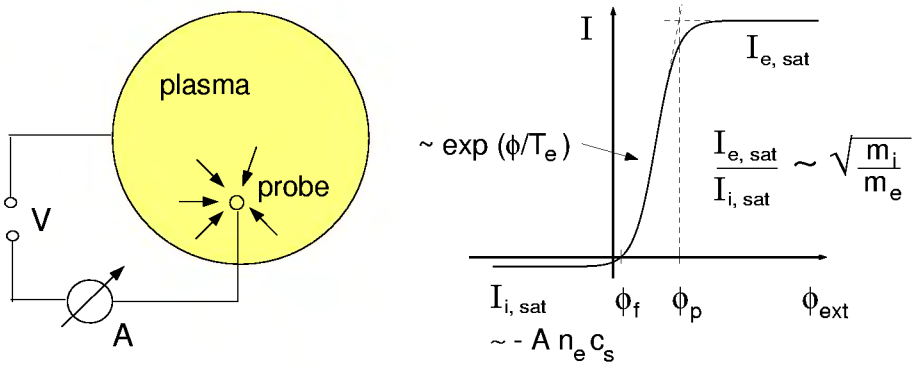

Figure 9.9: Schematic view and signal of a langmuir probe.

9.5.2 Charge exchange diagnostics

The ions in the plasma are in general well confined by the magnetic fields, but in collisions with neutrals also present in the plasma, they can take over an electron and become a neutral atom that can leave the plasma. As in these charge-exchange collisions both particles keep their energy, the neutral atoms leaving the plasma represent the energy distribution of the plasma ions.

Experimental techniques : Neutral particle analyzers consist of two major components, a stripping cell, where in a low-pressure gas the neutral particles are ionized again, and a magnetic and electrostatic energy analyzer to measure their energy spectrum. For plasma ions with a Maxwellian energy distribution this spectrum falls of with energy as $exp(-1/T_i)$ and allows determination of T_i. The diagnostic is especially useful for the detection of deviations from the Maxwell distribution e.g. due to additional heating of the plasma. However, it is a line-integrated measurement and again different lines of sight are necessary to unfold the measurements to get $T_i(r)$.

A second problem is the neutral gas density which decreases towards the plasma centre and in general is very low. Both problems can be overcome by using a beam of neutral atoms injected into the plasma. This increases the neutral atom density in general, and results in a localized source of the charge-exchange neutrals.

Generally CX diagnostics become very problematic with respect to information about the plasma center with increasing size and density of the plasmas since reionization of the atoms becomes large and strongly influences the spectrum of the neutral atoms leaving the plasma. For measurements near the plasma edge it remains very valuable even for high density plasmas.

9.5.3 Fusion products

Usually fusion plasmas nowadays work with hydrogen or deuterium, and therefore fusion reactions between deuterium ions (D) can already occur via two different reaction branches, thereby creating highly energetic protons (p), tritons (tritium nuclei, t), ^3He nuclei and neutrons (n):

$$\begin{array}{lcl} D + D & \longrightarrow & p\ (3.02\ \text{MeV}) + t\ (1.01\ \text{MeV}) \\ D + D & \longrightarrow & n\ (2.45\ \text{MeV}) + {}^3He\ (0.8\ \text{MeV}) \end{array}$$

Neutrons easily escape from any plasma and have been used as a diagnostic tool from the very beginning of fusion research. The charged fusion products are influenced by the magnetic field, but as their Larmor radius in medium-size fusion experiments is of the order of 1/3 of the plasma radius, they can still escape from the plasma. Because neutrons as well as charged particles do not suffer from collisions in the plasma, they carry the full information about the fusion process.

Physics principles: The fusion reaction rate in a pure deuterium plasma is

$$R = \int_V \frac{n_D^2}{2} \cdot <\sigma(v) \cdot v> \ dV$$

where n_D is the deuteron density, $<\sigma(v) \cdot v>$ is the reactivity, the fusion cross-section folded with the velocity distribution of the deuterium ions, and the integral is over the total plasma volume. Because $<\sigma(v) \cdot v>$ is a strong function of T_i, an absolute measurement of the neutron rate is a direct measurement of T_i, provided the deuterium density is known.

As most of the fusion reactions come from the ions in the high-energy tail of the velocity distribution, this method works only for Maxwellian plasmas. Small deviations from the Maxwellian energy distribution (i.e. even a small fraction of suprathermal particles in the tail of the distribution) can significantly alter the fusion reaction rate.

Information on the ion temperature can, however, also be derived from the spectrum of the fusion products. Although their energy is much larger than the ion energy, the spectra are broadened due to the motion of the reacting ions (Doppler effect again), and if the energy spectra can be measured with sufficiently high energy resolution, T_i can be calculated from the spectral width.

Experimental techniques: The neutron emission rate can be measured with BF_3- or with ${}^3He$-filled proportional counters or with ${}^{235}U$ fission chambers. All of these detectors are sensitive only to thermal neutrons (i.e. at $E \approx 0.025eV$), and therefore the neutrons have to be moderated (for example with polyethylene) before they reach the detector. Because neutrons can also transverse the vacuum vessel walls and other structures, this is even a volume-integrated measurement, but because the neutron emission profile is strongly peaked, it can be assumed to be a toroidal line source, and the neutron detectors can be absolutely calibrated for this case.

Neutron spectra can be measured with scintillators, high-pressure ${}^3He$-counters or time-of-flight methods. Collimation of the spectrometers, however, requires strong shielding around the detector to restrict its view into the plasma to a single line of sight. But still absorption and scattering in the tokamak components has to be taken into account by extensive modelling calculations on neutron transport.

Both problems can be overcome by measuring charged fusion products that can easily be collimated and very efficiently be detected in semiconductor detectors. Such detectors have an excellent energy resolution, but have to be installed inside the tokamak, because the charged fusion products cannot leave the vacuum vessel.

9.6 Summary

This short overview of plasma diagnostics has tried to treat the basic plasma diagnostic techniques (i.e. the most commonly used ones), and therefore a lot of specialized techniques have not been mentioned at all.

One should mention, however, that great efforts are still being made to develop new techniques and improve existing ones. Especially the increased radiation level in future DT-experiments establishes the need for new developments because the systems have to withstand the radiation, to be fully remotely controlled or to be installed far away from the fusion experiment/reactor.

Therefore the diagnostics of fusion plasmas is still a very interesting and developing field that involves all areas of physics.

Acknowledgement

Much of this text and many of the figures originate from the script that H.-S Bosch prepared for earlier IPP Summer Universities. He is gratefully acknowledged for making this material available.

Bibliography

[1] Equipe TFR, *Nuclear Fusion* **18** (1978) 647.

[2] Hutchinson, I. H., *Principles of Plasma Diagnostics*, Cambridge University Press, Cambridge, 1987.

[3] Orlinskij, D. V. and Magyar, G., *Nuclear Fusion* **28** (1988) 611.

[4] Wesson, J., *Tokamaks*, Clarendon Press, Oxford, 1987.

[5] Costley, A. E., Recent developments and applications of electron cyclotron emission, in *Basic and Advanced Fusion Plasma Diagnostic Techniques*, volume I, pages 119–138, 1986.

[6] Salzmann, H., Thomson scattering, in *Basic and Advanced Fusion Plasma Diagnostic Techniques*, volume II, pages 477–496, 1986.

[7] Soltwisch, H., Interferometry and Faraday rotation measurements on tokamaks, in *Basic and Advanced Fusion Plasma Diagnostic Techniques*, volume II, pages 343–378, 1986.

[8] Costley, A. E., Diagnosis of fusion plasmas using reflectometry, in *Basic and Advanced Fusion Plasma Diagnostic Techniques*, volume II, pages 379–398, 1986.

Chapter 10

Experimental results from Tokamaks

Wolfgang Suttrop

10.1 Tokamak plasmas

10.1.1 The Tokamak Principle

Nuclear fusion can be achieved in plasmas which are composed of a mixture of deuterium and tritium. At the high temperatures necessary for nuclear fusion, in the vicinity of 10 keV or 100 Million degrees K, the plasma is fully ionised, i.e. consists only of ions and electrons. In order to reach these temperatures, good thermal insulation is necessary, which can be provided by a magnetic field. The Lorentz force makes charged particles spiral (*gyrate*) around magnetic field lines. Electrons and ions can freely move along field lines. If magnetic field lines close themselves inside the plasma volume, the free parallel motion does not result in particle losses from the plasma. Consequently, toroidal field geometry (as sketched in Figure 10.1 a) is most effective for confinement of high temperature plasmas and in fact most magnetic fusion concepts involve this topology.

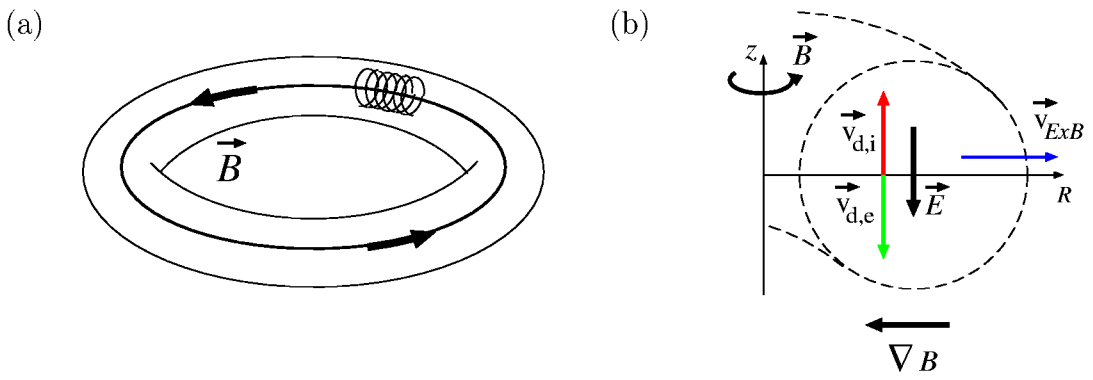

Figure 10.1: *(a) Closed field lines in toroidal geometry (b) outward particle drift in toroidal geometry*

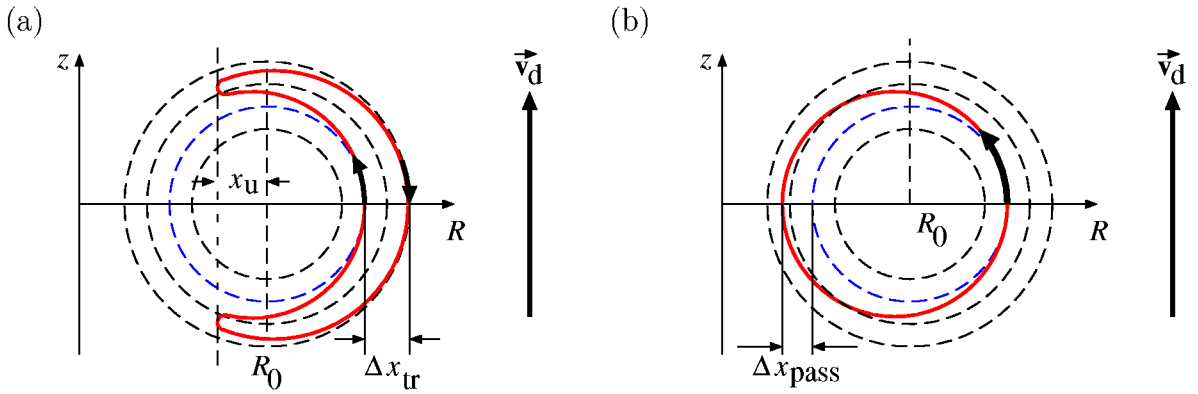

Figure 10.2: *Particle trajectories in toroidal geometry: (a) trapped particles, (b) passing particles*

The toroidal shape of the plasmas implies a non-uniform magnetic field strength. This results in a particle drift (Grad-B and curvature drift) perpendicular to the magnetic field and its gradient. This drift originates from a different gyro-radius at the low and high field sides of the particle orbit. The drift is directed parallel to the torus (vertical) axis in different directions for electrons and ions and hence leads to a separation of charge and a vertical electrical field. The electrical field induces an additional $E \times B$ drift which leads to fast radial losses of electrons and ions (Fig. 10.1 b). Hence, a simple toroidal magnetic field is not sufficient for plasma confinement.

The losses induced by these drifts can be eliminated by introduction of an additional poloidal magnetic field. The resulting helical field directs field lines successively below and above the equator of the device so that vertical drifts result in inward and outward motion, respectively. As a result, the trajectories of the centers of the gyromotion (*gyrocenters*) are displaced from the magnetic field lines but are also closed in themselves. The magnetic moment of the gyromotion is conserved so that with increasing magnetic field strength the velocity parallel to the field reduces. Figure 10.2 shows poloidal sections of two basic types of gyro-center trajectories: *Trapped particles* (Figure 10.2 a) do not have a sufficiently large magnetic moment to reach the location of maximum magnetic field strength and thus are confined to the magnetic low field side. They move in poloidally and toroidally opposite directions on the inner and outer halves of their orbit. The characteristic "banana" shape as viewn in a poloidal section gives rise to the nick-name "banana orbits" for these trajectories. *Passing particles* have a sufficiently large magnetic moment to continue their motion on the high field side (Figure 10.2 b). The associated radial displacement with respect to field lines, Δx, is larger by a factor $\sqrt{R/a} \equiv 1/\sqrt{\epsilon}$ for trapped particles than for passing particles, where R is the *major radius* (distance from torus axis to plasma center) and a the *minor radius* (half of the diameter of the plasma column) of the toroidal plasma.

The effects of toroidicity on particle orbits have several important consequences. Cross-field diffusion by Coulomb collisions is enhanced by the larger radii of the particle orbits compared to their gyroradius (*"neo-classical" diffusion*). In presence of a pressure or density gradient, the average toroidal velocity of trapped particles at a given radial location is not zero. Momentum is transferred by Coulomb collisions to passing particles resulting in a plasma current (*bootstrap current*).

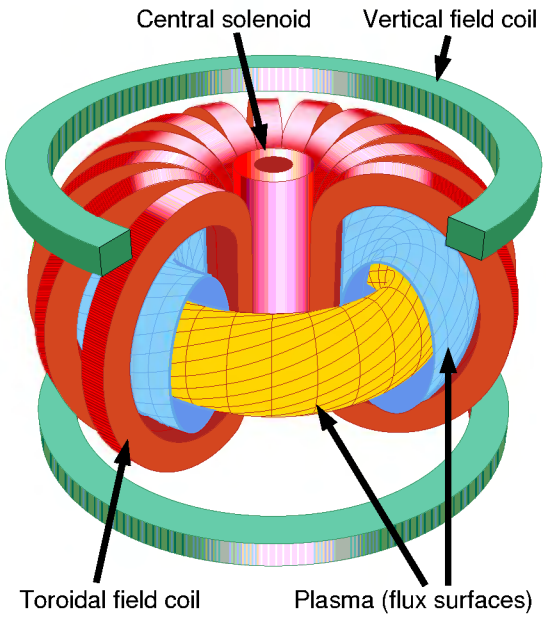

Figure 10.3: Tokamak: Schematic view of main components.

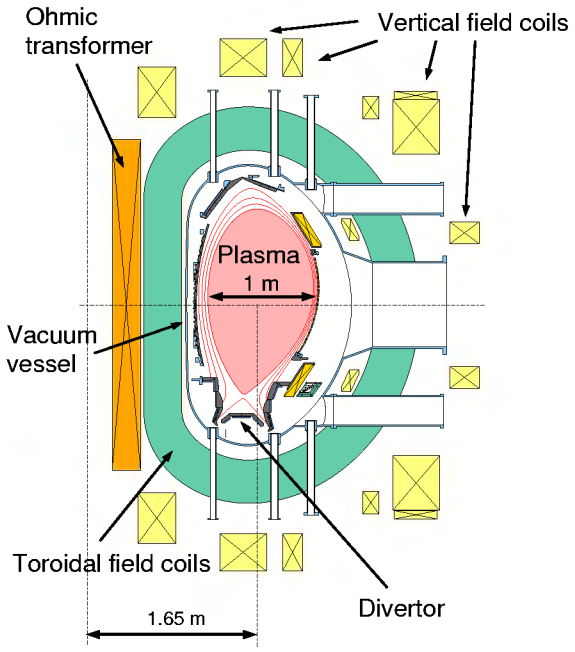

Figure 10.4: Cross section of ASDEX Upgrade (Axi-Symmetric Divertor EXperiment), installed at Max-Planck-Institut für Plasmaphysik, Garching, Germany

The additional poloidal field needed for confinement can be created in different ways. *Stellarators* generate a helical field entirely by external field coils. *Tokamaks* use a plasma current to produce the poloidal field component, while the toroidal field is generated by an axisymmetric arrangement of external coils. The word "tokamak" stems from a Russian acronym for "Toroidal chamber with magnetic coils". In the following, we concentrate on tokamaks.

10.1.2 Components of a tokamak

The main components of a tokamak are illustrated in figure 10.3. Helical magnetic field lines span nested surfaces of constant magnetic flux (*flux surfaces*). The plasma is enclosed in a vacuum chamber (not shown) which is needed to remove air and control the hydrogen pressure outside the plasma. The axisymmetric toroidal field is produced by poloidal currents in a set of magnetic coils surrounding the plasma. A central solenoid is used to produce a time-varying poloidal magnetic flux which induces a toroidal loop voltage, and due to finite plasma resistivity, a plasma current. The plasma is subject to a poloidally and radially outward directed force which results from a finite plasma pressure gradient. This force is balanced by the $j \times B$ force acting on the plasma current due to the helical field and an additional vertical field produced by toroidal currents in external conductors (*vertical field coils*).

As an example, the poloidal cross section of ASDEX Upgrade (Axi-Symmetric Divertor EXperiment) at Max-Planck-Institut für Plasmaphysik, Garching (Germany), is shown in Figure 10.4. This machine can produce plasmas with major radius $R = 1.65$ and

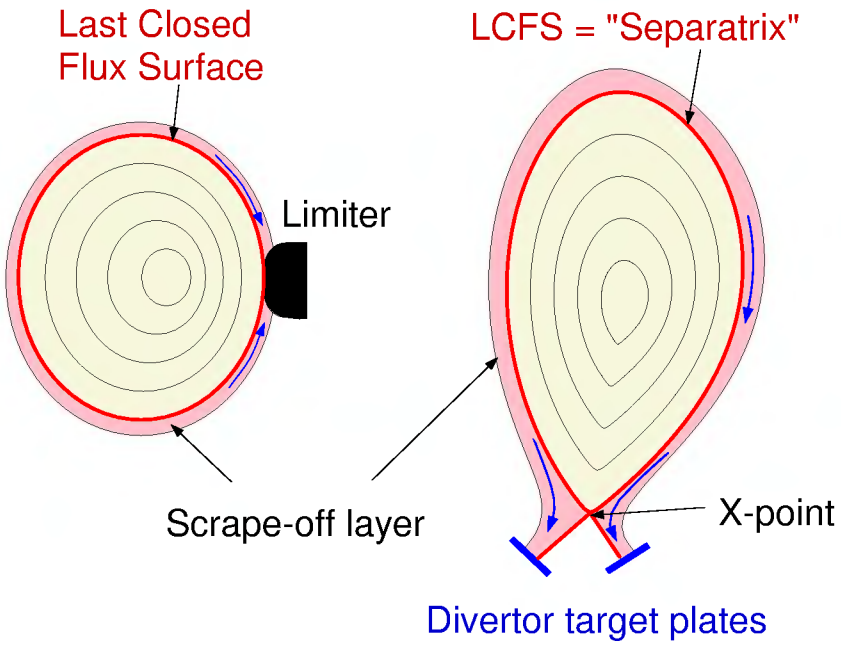

Figure 10.5: Limiter and divertor configurations.

horizontal minor radius $a = 0.5$ m. An array of vertical field coils is installed which do not only produce the vertical field for compensation of the radial outward force but also can create suitable poloidal fields to create a wide range of plasma shapes. Typically, vertically elongated plasmas are produced by toroidal currents in upper and lower shaping coils which have the same direction as the plasma current. This configuration is inherently unstable against vertical displacements. A small upward displacement from the equilibrium position will result in a larger attracting force on the plasma current of the upper coil current than of the lower coil, thereby amplifying the perturbation. This position instability is damped by induced currents in a passive saddle-loop near the plasma ("passive stabilizing loop"). On time scales longer than the L/R time constant of the saddle loop (about 1 ms), the vertical position is actively controlled with an external radial field, i.e. by a differential current in the upper and lower vertical field coils.

10.1.3 Divertor Tokamaks

Quadrupole currents in the poloidal field coils are also used to form a *magnetic divertor* configuration. Figure 10.5 illustrates two basic magnetic configurations of a tokamak plasma. Radial diffusion of particles and heat across the magnetic field will lead to expansion of the plasma until a material wall is intersected. Without a magnetic divertor, this first material contact will be close to the main confined plasma volume, and hence be subjected to strong heat load and particle fluxes. This region, called the *limiter*, must be appropriately designed in order to prevent excessive materials erosion. With a suitable axi-symmetric quadrupole field a magnetic X-point is introduced which defines a magnetic surface (*separatrix*) that intersects the material wall only at a distance from the main plasma. Particles and energy from the main plasma flow along field lines to a separated divertor region where particles are neutralized at the material wall (*target*

plates). A fraction of the neutral particles is reflected towards the separatrix, re-ionised and is streaming back again to the target plates. This recycling flux effectively increases the plasma density in the divertor region. Under normal conditions, the plasma pressure is constant along magnetic field lines, hence the plasma temperature in the divertor is smaller than that at the separatrix near the main plasma. As a result, the erosion damage at the material wall produced by ions can be strongly reduced and cleaner plasmas are obtained compared with a limiter configuration. This favourable property of divertors is exploited in most modern magnetic fusion devices, both tokamaks and stellarators. Figure 10.6 shows cross sections of four tokamaks: ASDEX (Max-Planck-Institut für Plasmaphysik, Garching, Germany), PBX-M (Princeton Plasma Physics Laboratory, Princeton, New Jersey, USA), TCV (Centre de Recherche en Physique des Plasmas, Lausanne, Switzerland) and JET (Joint European Torus, Culham, United Kingdom). These examples illustrate a variety of plasma sizes, cross sections and divertor geometries used in tokamaks.

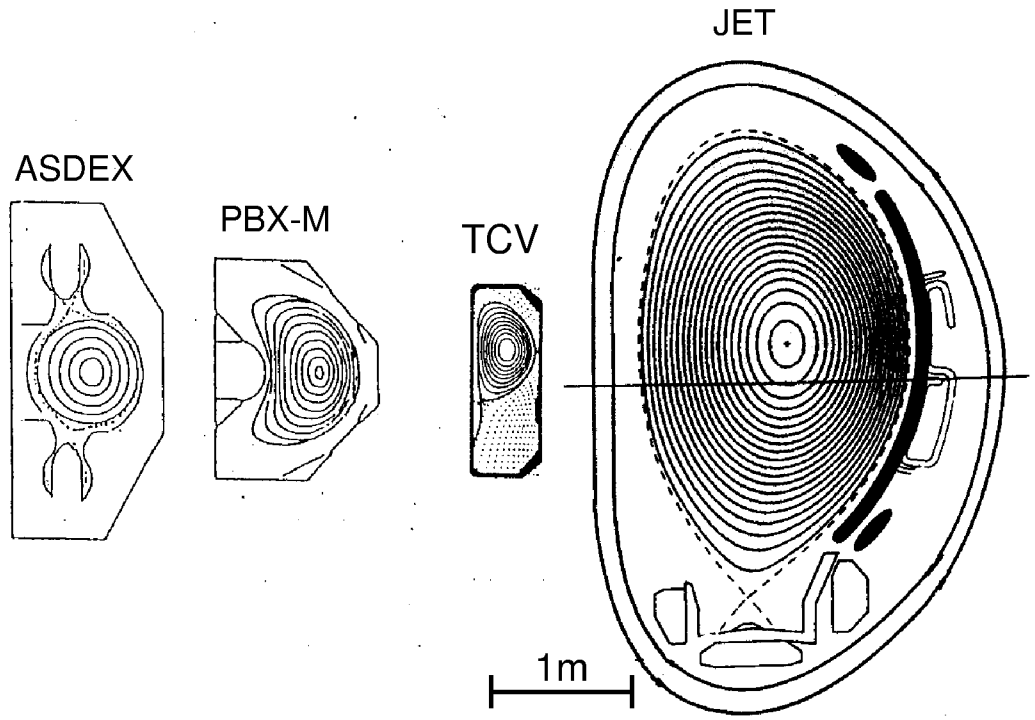

Figure 10.6: Variations of magnetic configurations (poloidal cross sections) in different experiments in shape (ASDEX, PBX-M) and plasma size (TCV, JET).

10.1.4 Magnetic Configuration

At the densities and temperatures reached in fusion plasmas, significant kinetic pressure is obtained in the plasma core and large pressure gradients produce strong forces on the plasma column. The ∇p forces are balanced by $j \times B$ forces arising from the magnetic field interacting with internal (toroidal and poloidal) plasma currents. This force balance is often called the *magnetic equilibrium* of a plasma configuration. (It has

to be stressed that this terminology does not imply the existence of a thermodynamic equilibrium state. In the contrary, because of the presence of strong heat flows into and out of the plasma, fusion plasmas are always open thermodynamic systems, far from thermodynamic equilibrium).

The poloidal magnetic field components B_R, B_z can be expressed by the derivatives of the poloidal magnetic flux ψ through a circle co-axial with the torus axis: $B_R = -(1/2\pi R)\partial\psi/\partial z$, $B_z = (1/2\pi R)\partial\psi/\partial R$. From Ampère's law (toroidal derivatives vanish due to axi-symmetry) the toroidal current density can be expressed as

$$j_{tor} = -\frac{1}{2\pi\mu_0}\left[\frac{1}{R}\frac{\partial^2\psi}{\partial z^2} + \frac{\partial}{\partial R}\left(\frac{1}{R}\frac{\partial\psi}{\partial R}\right)\right] \equiv -\frac{1}{2\pi\mu_0}\frac{1}{R}\Delta^*\psi. \tag{10.1}$$

The magnetic field lines span nested toroidal surfaces of constant plasma pressure which can be labelled with the flux ψ (*flux surfaces*). Expressing the toroidal field B_t by the *poloidal* current I_{pol} within a flux surface, $(\partial(RB_t)/\partial R) = (\mu_0/2\pi)\ (\partial(I_{pol})/\partial R)$, and using Ampère's law again, one obtains the famous Grad-Shafranov-Schlüter equation

$$\Delta^*\psi = \ -4\pi^2\mu_0 R^2 p' - \ \mu_0^2 I_{pol} I'_{pol} \tag{10.2}$$

where the prime ($'$) denotes the derivative with respect to ψ. Solutions of Eq. 10.2 describe the magnetic flux and toroidal current density for an axisymmetric magnetic equilibrium configuration characterized by toroidal current density $j_{tor}(R,z)$ (which contains plasma currents and external shaping coil currents), plasma pressure gradient p' and poloidal current profile I_{pol}.

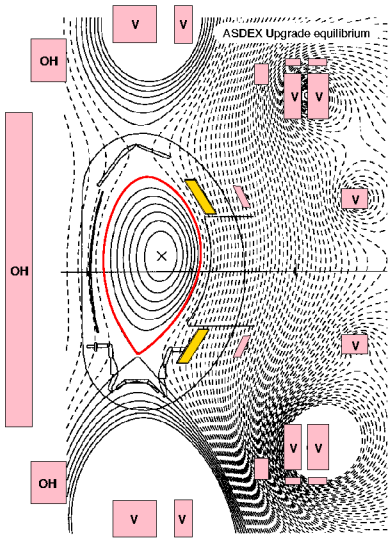

Figure 10.7: Poloidal magnetic flux in and around a shaped tokamak plasma (poloidal section), which is created by toroidal currents - plasma current and a set of external poloidal field coils.

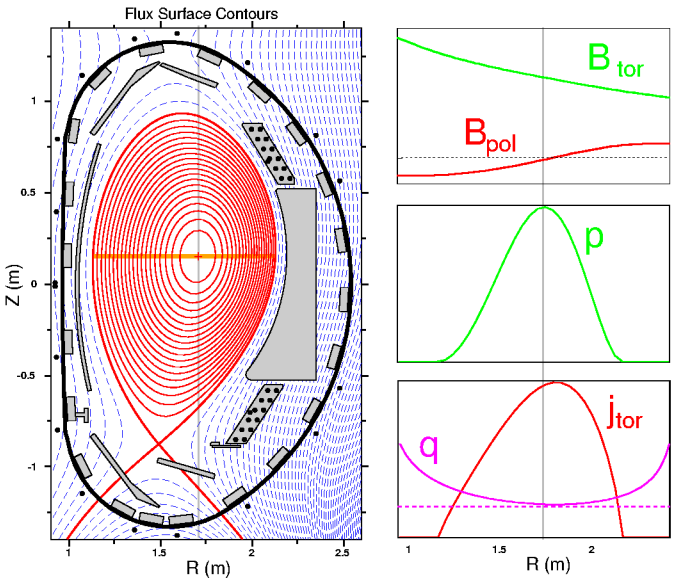

Figure 10.8: Tokamak equilibrium: flux surfaces, radial midplane profiles of B_{tor}, B_{pol}, pressure p, toroidal plasma current j_{tor} and safety factor q.

Figure 10.7 shows (in a poloidal cross-section) contours of constant magnetic flux for an experimental magnetic equilibrium of a plasma in ASDEX Upgrade. The toroidal plasma current generates poloidal magnetic flux which, in superposition with the flux generated by the poloidal field coils, defines a region of magnetic surfaces which are closed in themselves and have no intersection with a material wall. The boundary of this region (*last closed flux surface*, or *separatrix*) is highlighted in Fig. 10.7. Measurements of the magnetic flux are taken at many positions inside the vacuum vessel to reconstruct the experimental magnetic surfaces using Eq. 10.2. The shape of these surfaces can be controlled (feed-forward or feed-back) by the currents in the shaping coils.

Figure 10.8 shows a close-up of the vacuum vessel, the region of closed magnetic surfaces and profiles of the toroidal magnetic field B_{tor}, poloidal magnetic field $B_{pol} = (B_R^2 + B_z^2)^{1/2}$, plasma pressure p and toroidal current density j_{tor} along a horizontal section across the plasma center (indicated in the figure). Magnetic field lines follow a helical path on flux surfaces around the torus. A field line returns to a given poloidal position at a certain increment of the toroidal angle $\Delta\Phi$, which depends on B_t and B_{pol} along the field line. The *safety factor* $q = \Delta\Phi/2\pi$ counts how often a field line passes toroidally around the torus before it returns to the same poloidal position. For cylindrical cross-section and $R/a \gg 1$, $q(r)$ can be approximated as $q = (r/R)(B_t/B_{pol})$. The profile of q is also shown in Fig. 10.8. For a sufficiently peaked j_{tor} profile, q rises monotonically from the plasma center to the edge. This is typically the case if the plasma current is driven entirely by the induced loop voltage so that j_{tor} is determined by the radial resistivity profile. For irrational q, field lines span the entire flux surface. For rational q, field lines join up into themselves after a finite number of passes around the torus, so that helical perturbations can easily occur. Magnetic flux surfaces with integer or low rational q values are important for the stability of tokamak plasmas. In particular, q at the plasma edge has to be above a value of two to avoid a large scale disruptive instability (see section 10.2.3). This defines a minimum toroidal field for any given plasma current. The safety factor in the plasma center is usually clamped to values near or above unity by sawtooth oscillations (section 10.2.3) or other types of magnetohydrodynamic activity.

10.1.5 Plasma Heating

In order to balance heat losses from the plasma, a continuous heat source must exist to maintain the temperatures needed for fusion reactions to occur.

A heat source inherent for tokamaks is the Joule heat ηj^2 which originates from the plasma current and the low but finite resistivity η of a high temperature plasma (*Ohmic heating*). The plasma resistivity is proportional to $T_e^{-3/2}$ so that the Ohmic heating power reduces with increasing plasma temperatures, while the heat loss increases with increasing temperatures and their gradients. In practice Ohmic heating is limited to temperatures up to about 1500 eV, significantly below the temperatures needed to initiate fusion reactions. Neutral particle injection (NBI) or absorption of radio-frequency waves can be used to heat the plasma to temperatures significantly higher than those achieved with Ohmic heating.

For NBI heating, a beam of ionized deuterium is produced and accelerated in an electric field. Typical particle energies are 60 to 140 keV and beam currents range up to 100

A per NBI source. The deuterium beam is guided through a neutralizer chamber filled with neutral deuterium gas. Charge exchange reactions occur for 60% to 90% of the ions (depending on beam energy). Particles not neutralized are deflected by a magnetic field towards the wall of the chamber where they recombine and are pumped out. The fast neutral particles can pass through the tokamak periphery without being affected by the magnetic field. In the plasma, the neutral beam particles undergo charge exchange reactions which produce a population of fast ions. The plasma is heated by collisions of the fast ions with the thermal particles.

Radio frequency heating makes use of resonances in the dispersion relation for waves in plasmas, in particular resonances with the cyclotron motion of ions and electrons (*cyclotron resonance*). Electromagnetic waves are absorbed at the cyclotron resonance (and their harmonics) and the wave energy is converted into increased kinetic energy perpendicular to the magnetic field of the resonant particles. Collisions lead to thermalization of the energy distribution at increased temperature. Due to the different mass of ions and electrons different frequencies must be used. While for ion cyclotron heating (ICRH) frequencies in the range of several ten MHz are used, electron cyclotron resonance heating (ECRH) requires frequencies of the order of 100 GHz. ICRH heating systems typically use vacuum tube amplifiers, coaxial conductors and loop antennas mounted inside the vacuum vessel close to the plasma surface. ECRH power is generated by strong electron beams in a magnetic field with properly tuned magnetic fields (in devices called *gyrotrons*). The microwave power is transmitted in oversized waveguides or by quasi-optical imaging. Antennas are steerable mirrors which launch Gaussian beams that can be directed for variable power deposition positions.

10.1.6 Anatomy of a tokamak plasma

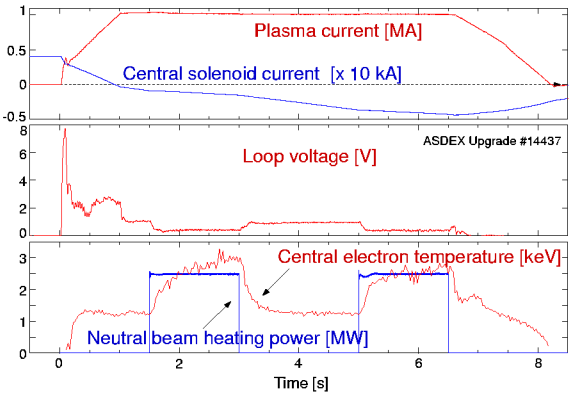

Figure 10.9: Measured time traces for a tokamak plasma during start and plasma current ramp-up phase, flat-top phase, and ramp-down phase.

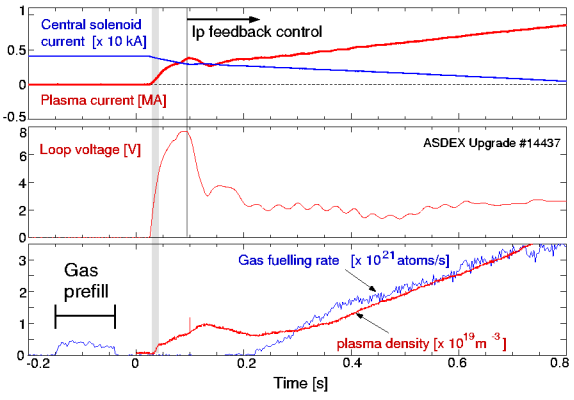

Figure 10.10: Start-up phase of a tokamak plasma: A high loop voltage, generated by a fast central solenoid current ramp, ionises an initial neutral gas prefill.

Figure 10.9 shows for a typical tokamak discharge (example taken from the ASDEX Upgrade tokamak) several measurements as a function of time. After start-up of the discharge, the plasma current I_p is ramped up within one second to its flat-top value of 1

MA. The discharge is terminated after 6.5 s by a ramp down of I_p. The same panel shows I_{OH}, the current in the central solenoid needed to achieve the requested plasma current: Before the start of the pulse, I_{OH} is set to 40 kA. Initially, a large loop voltage (second panel) is needed for break-down. This is achieved with a fast step in I_{OH}. During current ramp up, large flux is consumed due to the inductance of the plasma. During current flat top, flux consumption depends on plasma resistivity. In our example, neutral beams are injected during two time intervals ($1.5 - 3$ s and $5 - 6.5$ s) resulting in an increase of plasma temperature and consequently a decrease of resistivity. This results in the measured reduction of the loop voltage and reduced ramp rate of I_{OH} during the time intervals with auxiliary heating.

Details of the start-up phase of this discharge are shown in Fig. 10.10. A carefully dosed amount of deuterium gas (*gas prefill*) is introduced into the vacuum chamber and then a fast step of I_{OH} is applied to generate a large loop voltage. This results in ionisation of the neutral gas. The resulting free electrons are accelerated and help to further ionize the neutral gas. The plasma density (bottom panel) rises along with the plasma current. After about $t = 100$ ms, the plasma current is feedback-controlled and slowly ramped up. After $t = 200$ ms the plasma density is also feed-back controlled with the gas fuelling rate.

10.2 Experimental results

10.2.1 Confinement and transport

Confinement time

One of the main requirements for a nuclear fusion plasma is a sufficiently large *energy confinement time*, defined as $\tau_E = W_{th}/P_{heat}$, where W_{th} is the thermal stored energy and P_{heat} the heating power required to obtain this energy. The confinement time is a major figure of merit for tokamak performance and is relatively easy to measure. The heating power is the sum of ohmic heating ($V_{loop} \times I_p$) and auxiliary heating power, plus alpha particle power (small in today's tokamaks). The thermal stored energy can be obtained from density and temperature profiles, or approximated by the total stored energy (e.g. from diamagnetic measurements), corrected for the measured or estimated energy of fast (non-thermal) particles, which mainly depends on heating method, heating power and plasma density.

Figure 10.11 shows a scaling of the confinement time (experimental vs. predicted τ_E) for a relatively large number of tokamak experiments with different plasma size. This scaling, termed IPB98(y), is used to predict the performance of the planned International Thermonuclear Experimental Reactor (ITER) from present-day machines and has the form

$$\tau_{E,IPB98(y)} = 0.0365\ I_p^{0.97}\ B_t^{0.08}\ P_{heat}^{-0.63}\ n_e^{0.41}\ M^{0.2}\ R^{1.93}\ \epsilon^{0.23}\ \kappa^{0.67} \qquad (10.3)$$

$\tau_{E,IPB98(y)}$ is the predicted confinement time in seconds, I_p plasma current in MA, B_t toroidal magnetic field in T, P_{heat} auxiliary heating power in MW, n_e line averaged

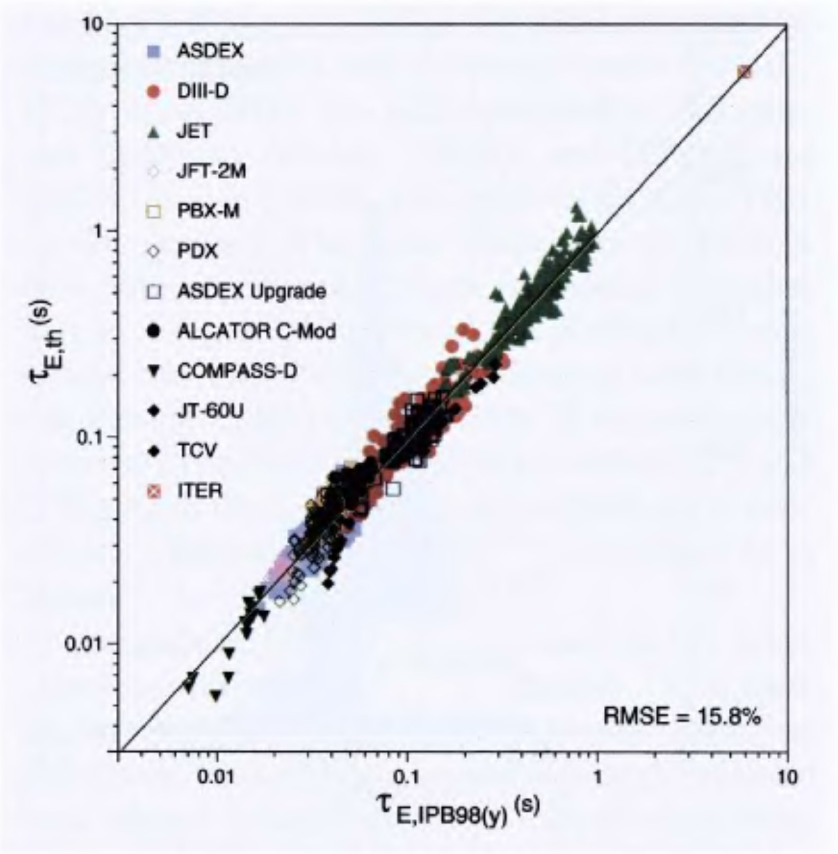

Figure 10.11: Energy confinement time scaling of the International confinement database for a large set of tokamaks

electron density (10^{19} m^{-3}), M ion mass number, R major radius (m), $\epsilon = a/R$, κ is the elongation (ratio of vertical and horizontal minor plasma radius). Energy confinement depends most strongly on plasma current I_p, plasma size (radius R) and elongation κ.

The experimental data base spans more than two orders of magnitude of τ_E in similar plasma types (High confinement mode, see section 10.2.2 below). ITER is designed for $\tau_E \approx 6$ s, which is less than a factor of 10 above the largest confinement times obtained in tokamaks to date. Naturally there are uncertainties with such extrapolations, originating from variance in the data base, and possible physics regime changes from current experimental parameters to a reactor-size plasma. It is therefore interesting to study the physics of heat transport in more detail.

Heat diffusion

Heat transport can be expressed in terms of a local power balance for the electron and ion heat conduction channels

$$q_{\perp e,i} = -n_{e,i}\, \chi_{e,i}\, \mathrm{grad}\, T_{e,i} \pm Q_{e,i} \tag{10.4}$$

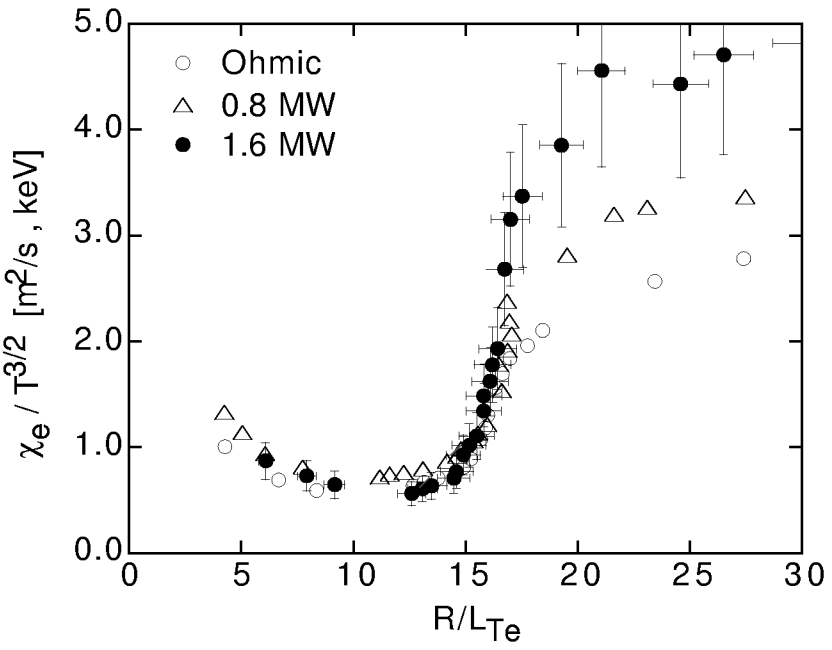

Figure 10.12: Normalized electron heat diffusivity $\chi_e/T^{3/2}$, measured as a function of normalized electron temperature gradient $(\nabla T_e)\, R/T_e = R/L_{T_e}$.

where $\chi_{e,i}$ is the *heat diffusivity*, $n_{e,i}$ the density, grad$T_{e,i}$ the temperature gradient and $q_{\perp e,i}$ the heat flux of the considered species (electrons or ions). $Q_{e,i}$ is the collisional heat transfer between electrons and ions.

For "random walk" radial diffusion dominated by Coulomb collisions, one expects a diffusivity of the order of $\chi_{e,i} \approx \Delta x/\tau_{e,i}$ where Δx is the radial step size (gyroradius for classical diffusion, banana orbit width for neo-classical diffusion in a toroidal plasma) and $\tau_{e,i}$ is the electron-ion collision time. However, is it found that the actual diffusivity in tokamak plasmas is normally significantly larger than the neo-classical value. In addition, heat diffusivity increases with increased heat flux. Historically, this behaviour has been termed "anomalous" transport and it is now known to originate from small-scale turbulence which creates fluctuating poloidal electrical fields. As a result, fluctuating radial $E \times B$ drifts occur which exchange plasma between hot and cold regions.

Various instability mechanisms exist that can drive transport-relevant turbulence. A common feature is that destabilization occurs if the temperature gradient length $L_T = T/\nabla T$ drops below a critical threshold $L_{T,crit}$. The heat diffusivity strongly depends on $L_T/L_{T,crit}$ and scales with $T^{3/2}$ ("gyro-Bohm" dependence). This behaviour is indeed found in experiments, as shown for electron by measurements of χ in ASDEX Upgrade (evaluated using Eq. 10.4). Figure 10.12 is a plot of electron heat diffusivity χ_e (normalised by $T_e^{3/2}$) as a function of inverse gradient length $R/L_{T_e} = R\nabla T_e/T_e$ (R is the major radius at midplane on the low-field side). Three different levels of electron heating power are employed: Ohmic heating and ECRH with 0.8 MW and 1.6 MW RF power. The data points correspond to measurements at different radial locations, central points have low heat flux and low inverse gradient length R/L_T (lower left), plasma edge data appears at high diffusivity (upper right corner of the diagram). The experiment shows

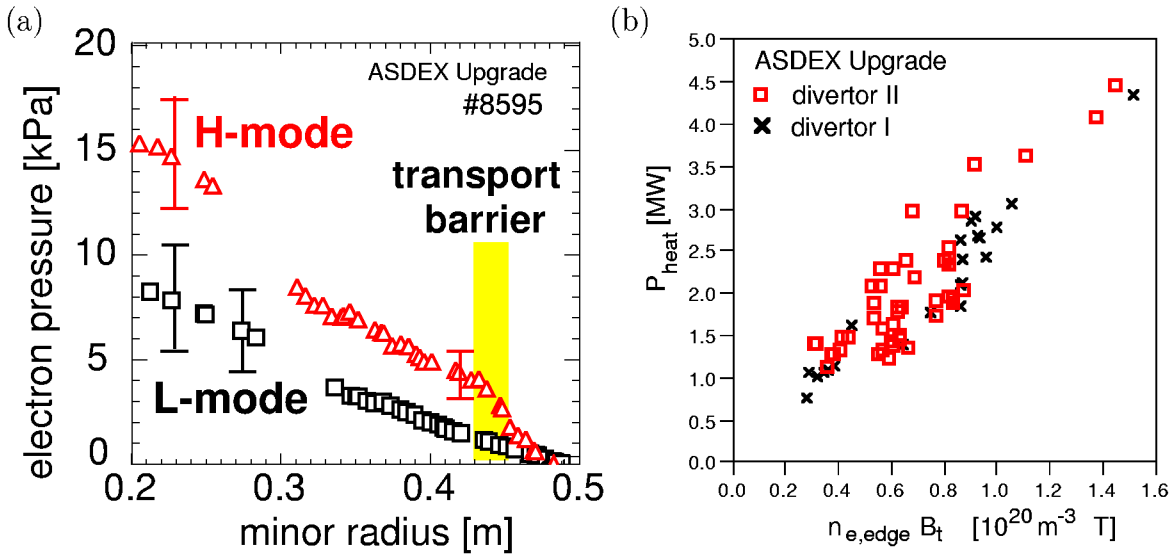

Figure 10.13: *(a) Comparison of electron pressure profiles in L-mode and H-mode, (b) Experimental power threshold for barrier formation*

the predicted increase of χ_e at $R/L_T \approx 15$. Furthermore, data with different heating power (and different temperature) is described by the same normalisation of χ_e by $T_e^{3/2}$.

The existence of a critical threshold for χ_e above which heat transport increases strongly leads to the formation of *canonical* temperature profiles, where L_T is near $L_{T,crit}$, almost independently of the heating power. This is the origin of the strong deterioration of confinement time τ_E with heating power (Eq. 10.3). For fixed gradient length, the central temperature depends strongly on the edge temperature, which is limited by edge instabilities (see sections 10.2.2 and 10.2.3 below). Consequently, high edge pressure and high edge temperature help to achieve high stored energy in the core of a tokamak plasma.

10.2.2 Confinement improvement

High-confinement mode

The level of radial particle and energy transport found in tokamaks is mainly caused by small-scale turbulence. Nevertheless, suppression of this turbulence can be observed in specific cases, leading to a reduction of the particle and heat diffusivity in a restricted plasma volume. This behaviour is often called the formation of a *transport barrier*. With the introduction of a divertor, spontaneous formation of a transport barrier at the plasma edge has been found in the ASDEX tokamak (Garching, 1984). This regime has been termed the *high-confinement* mode ("H-mode"). The effect of the edge transport barrier is demonstrated in Fig. 10.13 (a) for a discharge of the ASDEX Upgrade tokamak before and after transition to H-mode. Since the discovery of H-mode, the plasma state before the transition to H-mode is usually termed "L-mode" (*low confinement* mode). In H-mode, the pressure gradient steepens up at the plasma edge (between $r = 0.43$

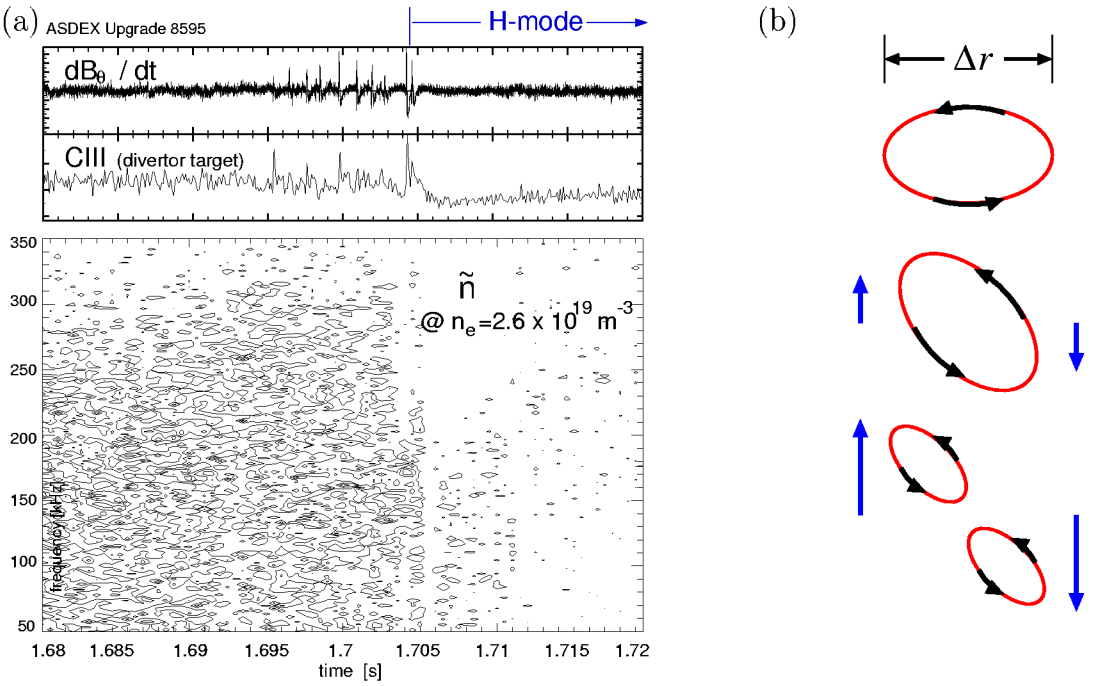

Figure 10.14: *(a) Fluctuations are reduced at the transition from L-mode to H-mode, (b) H-mode model: $E \times B$ shear flow reduces radial size of turbulent eddies*

and 0.45 m for the profile shown), giving rise to a pressure "pedestal", i.e. additional stored energy in the plasma from the pressure offset at the edge. The temperature just inside the transport barrier is significantly higher than in L-mode, allowing (for the same gradient length $L_T = T/\nabla T$) a higher plasma core temperature gradient than in L-mode, resulting in an additional confinement benefit.

The condition to enter High-confinement mode is a minimum heating power across the plasma boundary. Empirically, the threshold power depends on the product of plasma edge density and magnetic field, $P_{heat} \propto n_{e,edge} \times B_t$. Fig. 10.13 (b) illustrates this dependence for the case of two divertor geometries in ASDEX Upgrade. Little influence of the divertor geometry (and other parameters such as heating method) is found.

A typical time history around the transition to H-mode is shown in Fig. 10.14 (a). The heating power is being stepped up to just above the H-mode threshold at $t = 1.65$ s. Large heat flux in L-mode leads to turbulence that can be seen as broad-band density fluctuations in the $\tilde{n}$ spectrogram contour plot. Transport occurs in bursts that appear in the divertor heat flux ($CIII$ spectral line intensity) and main plasma magnetic probes ($\dot{B}$). After the transition to H-mode (at $t = 1.705$ s in the example), the level of density fluctuations is much reduced and the $CIII$ signal in the divertor drops.

While in L-mode additional heating power creates steeper gradients and thus generates more free energy to drive turbulence and enhanced losses, it can also trigger a transition to H-mode, a self-organising process that results in a bifurcation to a state of reduced transport. This transition to H-mode is accompanied with the creation of a radial electrical field gradient, corresponding to sheared rotation of the centers of the particle gyro-motion. It is believed that de-correlation of turbulent $E \times B$ convection

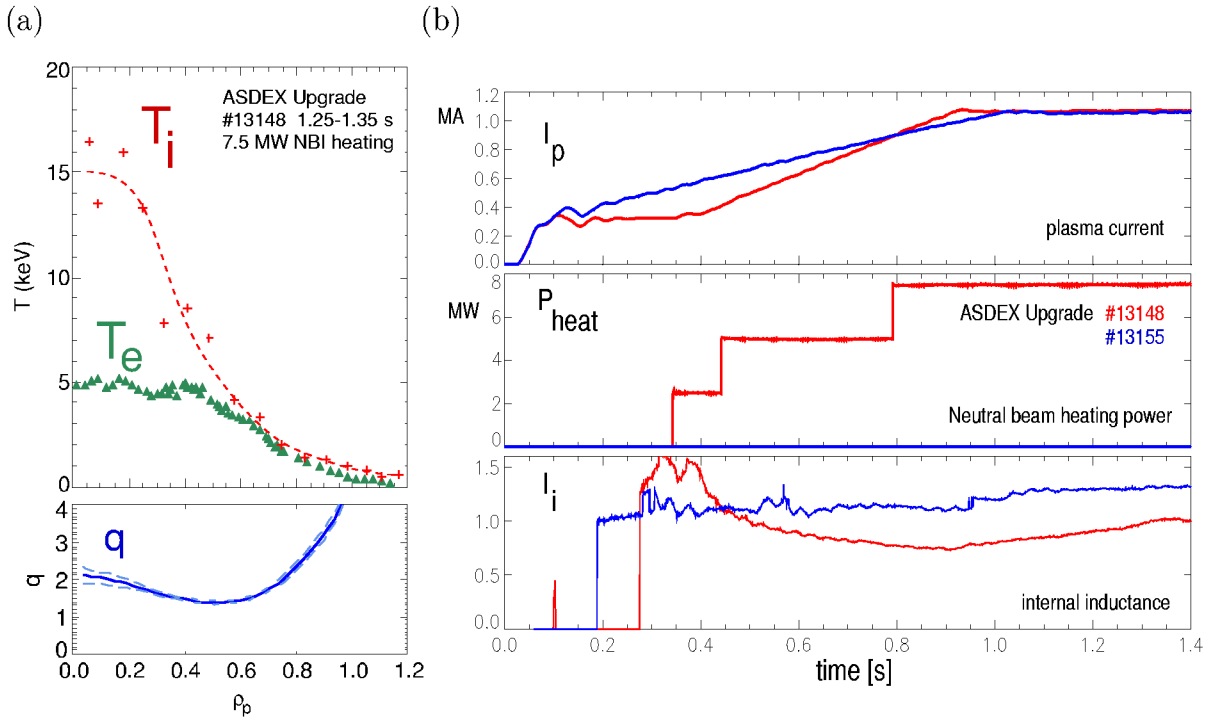

Figure 10.15: *Internal transport barrier example: (a) profiles of T_i, T_e and safety factor q, (b) Comparison of discharges with (13148) and without (13155): Early heating during the current ramp leads to broader current profile as seen by a reduced value of ℓ_i.*

cells by sufficiently fast sheared rotation is the origin of the transport reduction (cf. cartoon Fig. 10.14 b). However, although a number of possible mechanisms has been proposed the physics that drives the radial electrical field is still unknown and subject to ongoing research effort.

Internal Transport Barriers

Transport barriers can exist not only at the plasma edge, but also in the plasma core, causing steep temperature and/or density profiles, thereby increasing the central pressure. *Internal transport barriers* (ITB) arise from an influence of the magnetic shear $s = (r/q)\,\mathrm{d}q/\mathrm{d}r$ on the growth of micro-instabilities and thereby the heat diffusivity. In conventional tokamak plasmas without ITB, q increases monotonically from the center towards the edge, i.e. the magnetic shear is positive across the entire plasma radius. It is observed that heat transport can be reduced at low or negative magnetic shear. Fig. 10.15 (a) shows profiles of the electron and ion temperature and the safety factor q in a discharge with ITB in the ASDEX Upgrade tokamak. The q profile is flat or slightly reversed inside a normalized radius of $\rho = 0.6$. A strong ion temperature gradient is maintained around $\rho = 0.4$, leading to a central ion temperature of 15 keV. This temperature, obtained in a tokamak much smaller than an envisaged fusion reactor, is near the optimum temperature for D-T fusion reactions. Figure 10.15 (b) shows how this result is achieved. A conventional plasma (shot #13155) is compared with an ITB discharge (#13148). In the ITB pulse, heating power is applied early in the plasma current

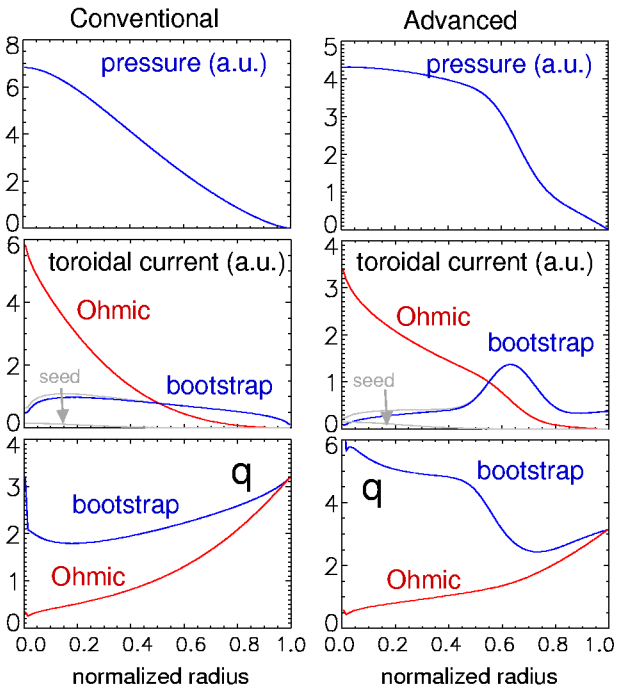

Figure 10.16: *Profiles of plasma pressure p, current density j and safety factor q comparing conventional and advanced scenarios. A conventional plasma has a monotonously rising q profile. Flat or reversed reversed q profile can lead to a transport barrier. In an ideal advanced scenario, the resulting steep pressure gradient creates a bootstrap current that maintains the q-profile non-inductively in steady state. Ohmic and bootstrap contributions to j and q are shown separately.*

ramp, resulting in higher T_e. Due to the increased resistive skin time the initial flat or slightly hollow plasma current profile remains "frozen" for the duration of the experiment. This is seen by the slow evolution of the *internal inductance* ℓ_i which indicates by its lower value after $t = 0.45$ s a broader (less peaked) current profile.

The "Advanced" Tokamak

For truly stationary tokamak operation the plasma current has to be driven entirely non-inductively, for example by the bootstrap effect due to the pressure gradient in the plasma. This leads to the interesting concept of the *Advanced Tokamak*, where the bootstrap current profile maintains the low or reversed shear profile required for the transport reduction which causes the ITB. Fig. 10.16 compares profiles of the pressure, toroidal current density and safety factor q (assuming pure ohmic or pure bootstrap current) for both a "conventional" (non-ITB) and an ITB plasma. In the conventional scenario the ohmic (inductively driven) current dominates. The ohmic current density profile is fixed by the conductivity (electron temperature) profile. A sufficiently strong transport barrier can, in principle, sustain a reversed shear profile. The strong pressure gradient produced by the transport reduction creates a strong off-axis bootstrap current. The resulting non-monotonic current profile maintains the weak or negative magnetic shear profile that allows to sustain the transport barrier. A tokamak reactor with an ITB and this type of "self-generated" plasma current could be built smaller than a conventional tokamak and would allow true steady-state operation. A crucial condition is the alignment of the reversed shear region with the region of actual strong pressure gradient, which if not matched, leads to rapid changes of the radial position of the transport barrier. A (small) current profile correction can be applied non-inductively by external current drive techniques, e.g. by electron cyclotron or lower hybrid wave heating with toroidal component of the wave vector. Advanced tokamak scenarios with

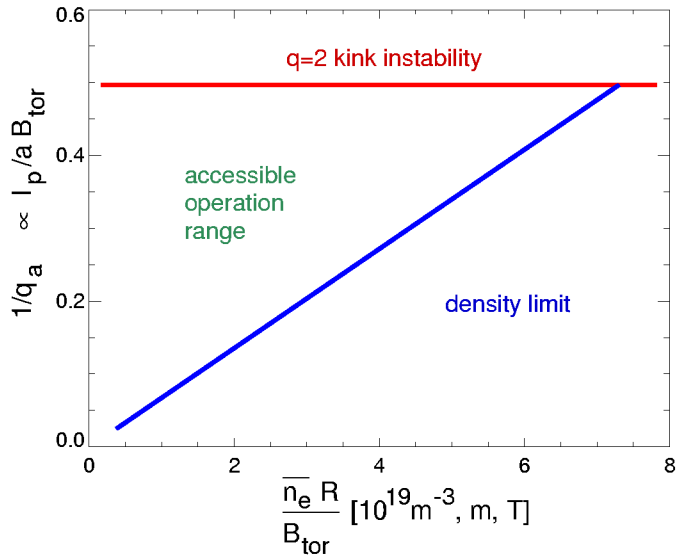

Figure 10.17: *Hugill-Diagram showing the basic tokamak operational range. An upper limit to the plasma current is given by the onset of* $n = 1, m = 2$ *kink instability for* $q = 2$ *at the plasma edge. A density limit exists at* $\overline{n}_e \propto B_t/(Rq) \propto I_p/a^2$

a variety of current drive methods are an important topic in most current tokamak research programs.

10.2.3 Stability and operational limits

Instability occurs if a plasma perturbation amplifies itself and grows until the plasma configuration is severely modified. Free energy sources for instability growth arise for instance from large gradients of pressure and currents present in a fusion plasma. Many instabilities involve displacements of magnetic surfaces (*MHD instabilities*), but also other types of instabilities exist, for example radiation instability originating from increased radiated power with decreasing temperatures. MHD instabilities are distinguished by their scale: Micro-instabilities occur on the gyro-radius scale and are relevant for radial particle and heat transport. Macrocoscopic instabilities affect the plasma on the scale of the plasma dimensions and can have large effects on confinement or even terminate a plasma discharge. In toroidal geometry one can characterize unstable modes by their integer toroidal (n) and poloidal (m) mode numbers. Most macroscopic MHD modes can become unstable only at "resonant" surfaces, i.e. magnetic surfaces where $q = m/n$, and n and m are small numbers. At finite aspect ratio, modes with different poloidal mode number m couple, giving rise to complex mode number spectra.

Instabilities are important as they define the accessible plasma parameter range for stable tokamak operation. Subsequently, we discuss the basic tokamak operation range and examine several important types of instabilities and their effects.

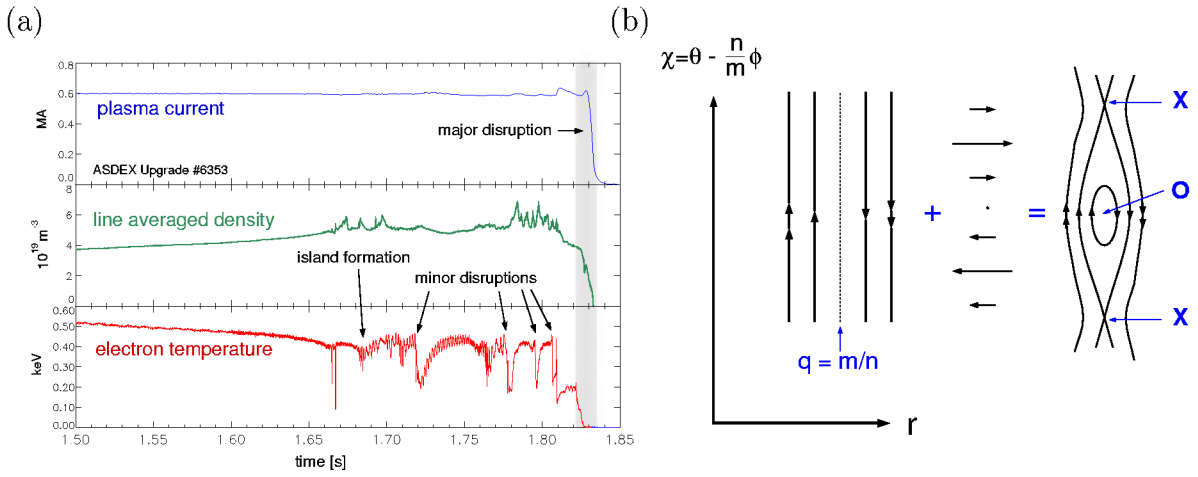

Figure 10.18: *(a) History of a density limit disruption. With increasing density the plasma edge is cooled and magnetic islands grow. Finally a "major" disruption occurs with thermal and plasma current quench. (b) Formation of magnetic islands by superposition of an unperturbed sheared magnetic field and a helical B_r field*

Tokamak operational limits

For stable tokamak operation, there are upper bounds for the plasma current and the plasma density. Figure 10.17 shows a schematic diagram of the accessible parameter range in a plot of $1/q_a$, the reciprocal edge safety factor vs. $\overline{n_e}R/B_t$ (known as *Hugill diagram*). We note that $1/q_a \propto I_p/B_t$, so the vertical axis is proportional to the plasma current. For $1/q_a \to 0.5$ the $q = 2$ surface approaches the plasma edge and a $m = 2$, $n = 1$ "kink" instability occurs. This is a fast-growing large scale ideal MHD mode which leads to a quick termination of the plasma discharge.

Empirically, a density limit is found which is proportional to the plasma current density. In the Hugill diagram (Fig. 10.17) this is expressed by a an upper bound of the line averaged density $\overline{n}_e R/B_t \propto I_p/aB_t$ or $\overline{n}_e \propto I_p/aR \propto I_p/a^2$ (for constant aspect ratio R/a). The physics of the density limit is quite complex, and some of its aspects are outlined in the next section.

The accessible operation range of tokamaks is bounded by these limits. High plasma density is desirable for good performance and to facilitate power exhaust with a divertor. For a tokamak reactor it is therefore desirable to operate at highest possible plasma current density. The maximum value of B_t is defined by technical limitations for toroidal field coil system. Hence, the $q = 2$ limit sets an upper bound to I_p. From these considerations, the optimum operation point is in the upper right corner of the Hugill plot.

Density limit disruptions

The density limit in tokamaks can assume quite complex phenomenology. A typical history of a density limit in a discharge with only ohmic heating is shown in Fig. 10.18

(a). In this experiment, the line averaged density is slowly raised by gas puffing. The edge electron temperature (bottom trace) reduces with increasing density. When the edge has sufficiently cooled down, *tearing mode* instability occurs which results in the formation of magnetic islands by reconnection.

Figure 10.18 (b) shows the structure of magnetic islands (in helical and radial coordinates). Magnetic islands result from helically periodical perturbation currents which give rise to a radial magnetic field with helical symmetry. They can grow only at resonant rational surfaces, i.e. where $q = m/n$. At the density limit, several islands with m/n = 4/1, 3/1 and 2/1 appear. Since heat transport is faster along magnetic field lines than perpendicular to the field, radial heat flux effectively bypasses the island interior (*O-point*) and concentrates near the X-point. Consequently the temperature is flat inside the island, while near the X-point a gradient is maintained. Plasma rotation makes this modulation visible as an oscillation of the temperature (bottom panel in Fig. 10.18 a).

After islands have grown to a certain radial extent, fast confinement loss events (*minor disruptions*) occur, which lead to a flattening of the temperature profile around a resonant surface. The volume inside this surface cools down and islands on inner resonant surfaces begin to grow. After several minor disruptions, several island chains can exist simultaneously and the rotation velocity reduces to zero (*mode locking*). A *major disruption* occurs, with a fast loss of plasma energy (*energy quench*) and subsequent quench of the plasma current. Because of the inductivity of the plasma, the plasma current quench results in *halo currents* in the vacuum vessel wall, which lead to very large forces on the material structure of a tokamak. The vacuum vessel and the support structure of all magnetic coils must be designed to withstand these forces.

Nevertheless, the disruptive termination of a plasma can be avoided or at least mitigated. If the density is kept below the density limit, the phenomenology described above does not occur. If the density limit is encountered, one can delay tearing mode growth by localized electron cyclotron current drive which replaces the missing helical current in the O-point. Several techniques have been successfully applied to delay or avoid mode locking. Finally, during a disruption the kinetic and magnetic energy in the plasma can be disposed by radiation from injected impurities leading to a more even distribution of energy deposition on the walls, and a reduction of halo currents.

The physics mechanism at the onset of the density limit are still under investigation. Several observations can be made depending on the confinement regime: Increase of radial transport at the edge leading to edge cooling and breakdown of the H-mode barrier; *detachment* of the divertor, i.e. loss of the parallel pressure balance between main chamber edge and divertor due to radial momentum transfer, and formation of a poloidally asymmetric condensation instability (*"MARFE"*) which leads to edge cooling. Several mechanisms can drive magnetic island growth: Deformations of the current profile, and helical current perturbations due to radiation losses from the island interior or loss of the bootstrap current because of pressure profile flattening around the O-point. The interplay of these mechanisms is being studied in experiments and by complex computer simulations.

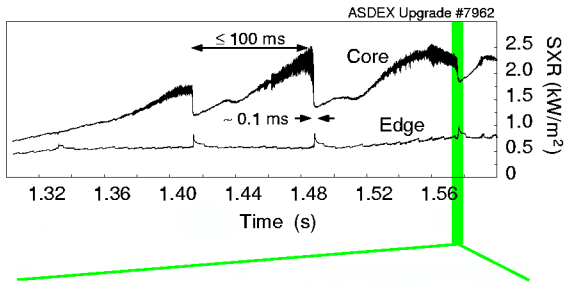

Figure 10.19: *(right) Sawtooth oscillations as seen by Soft X-ray measurements. Bottom right: Tomographic reconstruction of Soft X-ray emissivity before, during and after the sawtooth crash.*

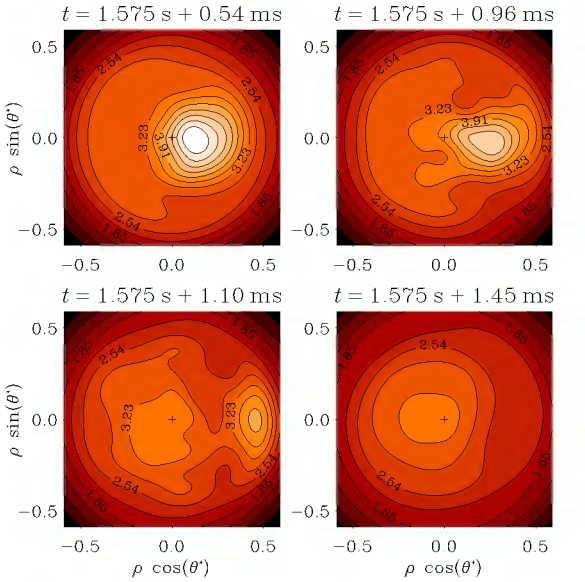

Figure 10.20: *(bottom) Profiles of j during a sawtooth cycle.*

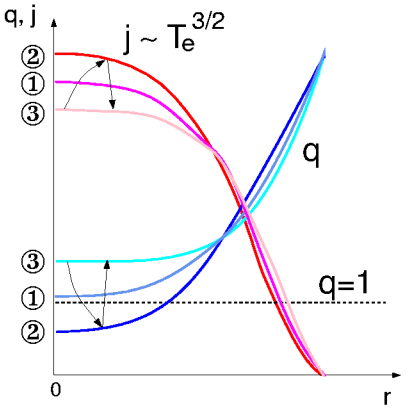

Sawtooth oscillations

In many tokamak discharge scenarios, the central temperature undergoes a characteristic oscillation: After a slow linear rise (of few to several 100 ms duration) the temperature crashes very quickly (within about 100 μs) and the cycle repeats. This behaviour has been first observed in the central soft x-ray emissivity and has been named "sawtooth" oscillations for its peculiar time history (Fig. 10.19, top panel). X-ray tomography can be used to reconstruct a two-dimensional image of the central emissivity which reveals the structure of the underlying perturbation. The lower part of Fig. 10.19 shows the reconstructed X-ray emissivity for four phases before, during and after the sawtooth crash. In between sawtooth crashes the plasma center is heated and the central temperature increases. If $q(0) < 1$, an $n = 1, m = 1$ kink mode is destabilised. Because of good radial confinement the interior of this region is hot ($t = +0.54$ ms). Because of the toroidal plasma rotation, the difference of temperatures inside and outside the kink structure appears as fast oscillations (black areas) in the X-ray signals (Fig. 10.19 top). With increasing central current density the structure becomes unstable and reconnection sets in ($t = +0.96$ ms and $t = +1.1$ ms). Hot plasma streams into a larger volume and the peak temperature and emissivity are reduced, but the 1/1 mode re-appears and the cycle starts over ($t = +1.45$ ms).

Figure 10.20 schematically shows the temporal evolution of the profiles of the central current density and associated safety factor q. In between sawtooth crashes, $j(0)$ (and $T_e(0)$) both rise, resulting in a drop of central q (1). Eventually $q(0)$ falls significantly

below unity (2). A quick reconnection event flattens the central j (and T_e) profile and q rises again above one; the cycle starts over.

Edge Localized Modes

Edge Localized Modes are instabilities that occur in H-mode where a transport barrier leads to a steep pressure gradient at the plasma edge. The edge temperature (shown in Fig. 10.21, top time trace) and edge density (not shown) increase until sudden heat and particle losses occur. These losses can be detected as a characteristic spike in the D_α line radiation intensity in the divertor due to increasing recycling particle flux and increasing ionisation because of the heat loss (Fig. 10.21, bottom trace). The particle and heat losses are also seen as a sudden partial erosion of the edge temperature and density profiles (Fig. 10.22). Steep profiles (A) in the edge barrier region before ELMs flatten within few 100 μ s (B) and recover slowly (c) by radial heat and particle transport from within the plasma core until the maximum pressure is reached again and a new ELM occurs. This results in a characteristic oscillation cycle which repeats itself many times, often hundreds of times in one plasma discharge. Along with hydrogen, also impurities are lost which otherwise tend to accumulate in the main plasma due to the very slow out-diffusion across the H-mode transport barrier. While this feature of ELMs allows for stationary H-mode plasmas, the fast energy loss during the collapse phase can present a large peak power load to the divertor structure which can cause significant erosion of the divertor structure. For this reason, ELMs with small losses occurring at a high frequency are preferred over slow and large ELMs.

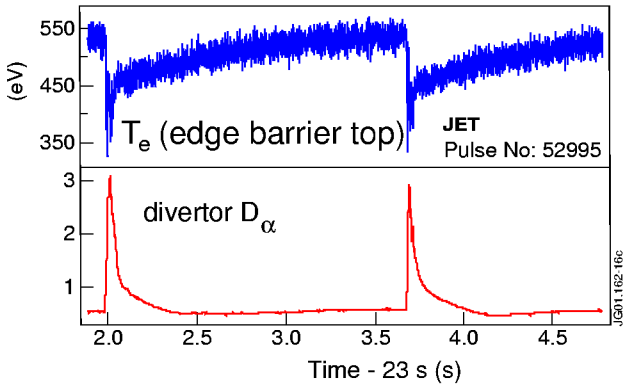

Figure 10.21: *(top) Time traces of edge electron temperature and divertor D_α showing repetitive losses at the edge and increased recycling during ELMs.*

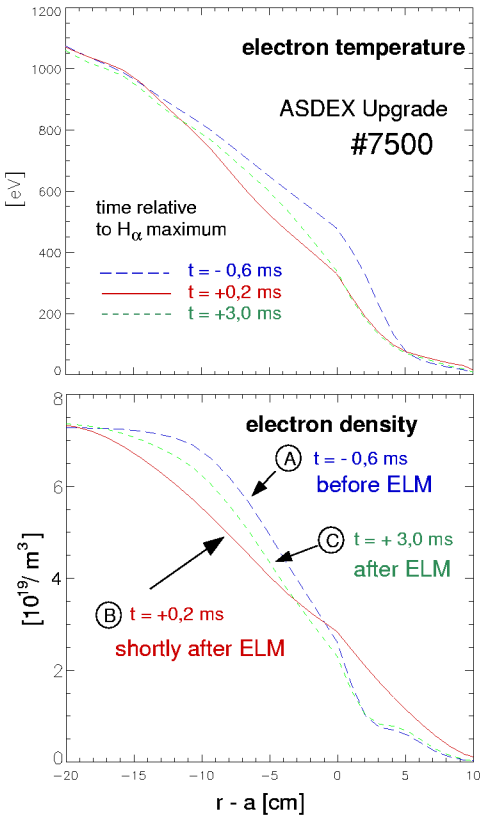

Figure 10.22: *(right) edge electron temperature and density profiles (A) before an ELM, (B) shortly after an ELM, (C) in the recovery phase in between ELMs.*

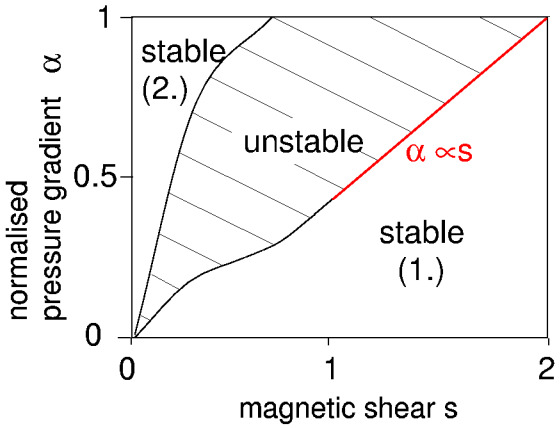

Figure 10.23: *Stability diagram for ballooning modes. Stability occurs for high magnetic shear ("first" stable regime) or very low magnetic shear ("second" stable regime). Access to the second stable regime is often blocked by an unstable region as shown.*

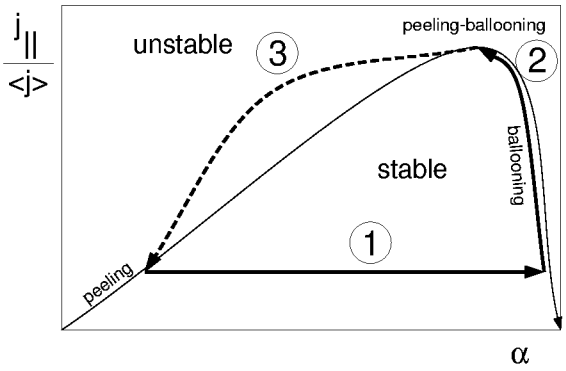

Figure 10.24: *Schematic model for the ELM cycle: Different time scales for evolution of edge pressure gradient α and edge current density $j_{||}$ result in several stability limitations during the cycle (see text).*

The precise physical origin of ELMs and the nature of the instability are still under investigation. The phase of enhanced transport during ELMs is characterized by a broad spectrum of MHD modes with a duration of about 100 μs. ELMs set in near values of the total edge pressure gradient where one expects *ballooning* instability, i.e. short wavelength modes driven by the pressure gradient at the magnetic low field side where the curvature of the magnetic field is not stabilizing. Fig. 10.23 shows a stability diagram for ballooning modes. The attainable normalized pressure gradient (first stability limit) $\alpha = 2\mu_0 R\,(\nabla p)\,q_a^2/B_t^2$ increases with magnetic shear $s = (r/q)\,\mathrm{d}q/\mathrm{d}r$. Interestingly, at low shear a second stable regime can exist. Low local shear at the magnetic low field side can be produced by suitable plasma shaping or by high edge current density.

Ballooning modes are typically small scale modes, most unstable for high mode numbers and thus do not explain the large perturbations associated with ELMs. Furthermore, it is often observed experimentally that the pressure gradient saturates well before an ELM occurs indicating a more complex physics process involved. Recent models for ELMs consider a variety of instabilities, including modes driven by the large toroidal current gradient at the plasma edge. A large edge current density originates from the bootstrap current driven by the large edge pressure gradient in the H-mode transport barrier. In this picture the ELM cycle can be described as follows (Fig. 10.24): In between ELMs (1) the (normalized) pressure gradient α rises on the transport time scale (few ms for heat and particle diffusion over a few cm) until the ballooning pressure gradient limit is reached. Small scale instability leads to enhanced losses, effectively clamping the pressure gradient while the edge current density $j_{||}$ builds up within the resistive skin time (10 to 100 ms for the edge of current tokamaks). Ultimately the stability limit for coupled peeling (i.e. medium-n kink) and ballooning modes is reached, leading to macroscopic instability, the ELM crash (3). Pressure and current are expelled and the cycle repeats itself. At present, the ELM cycle and stability limits are qualitatively and quantitatively

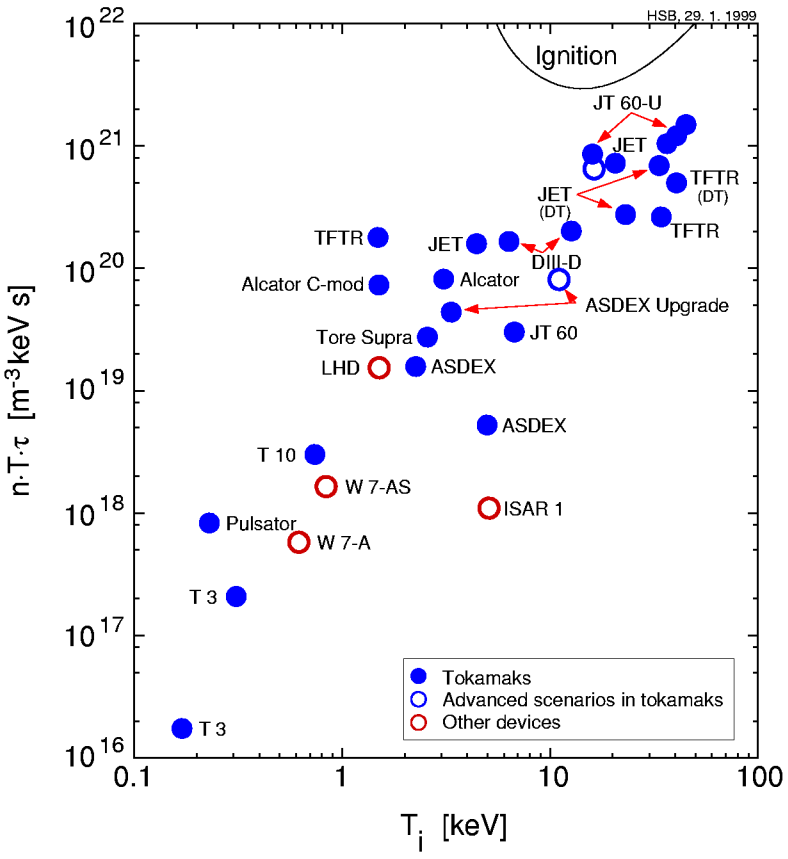

Figure 10.25: *Historical performance of tokamaks and other devices, fusion triple product* $n\,T_i\,\tau_E$ *as a function of* T_i.

described. Current theoretical and experimental work focuses to understand and predict the magnitude of the ELM losses and to tailor the plasma edge in order to reliably obtain ELM types with smaller energy losses.

10.3 Summary and Outlook

Tokamaks can confine a nuclear fusion plasma with a combination of external toroidal field and poloidal magnetic field created by an internal plasma current. The plasma current can be driven inductively by a magnetic flux ramp created with a central solenoid which limits the duration of tokamak discharges. Non-inductive current drive by externally driven current or bootstrap (pressure gradient current) current can extend the pulse duration and possibly allow stationary tokamak operation. Heat and particle transport in tokamaks is usually dominated by fluctuating $E\times B$ convection from micro-instabilities which are driven by the strong temperature gradients. However, transport barriers at the plasma edge and in the plasma interior can be produced which reduce the heat diffusivity to near a level expected for collisional transport. The strong pressure and current density gradients present in a well-confined tokamak plasma can also drive a range of macroscopical instabilities, which often take the form of limit-cycle oscillations. Examples are sawtooth oscillations, associated with central $m = 1, n = 1$ kink modes

that undergo fast reconnection events and a flattening of the central temperature, and Edge Localized Modes, driven by the steep pressure gradient of an edge transport barrier resulting in repetitive energy and particle losses. While these instabilities do not prevent stationary plasma operation and in some cases even help avoiding accumulation of impurities, other instabilities lead to severe confinement deterioration or even a termination of the plasma. The accessible tokamak parameter range is bounded by the conditions to avoid these instabilities.

The historical progress of nuclear fusion research can be measured by the fusion triple product $n\,T_i\,\tau_E$ which is plotted in Fig. 10.25 as a function of T_i for tokamaks and other magnetic confinement devices (mostly stellarators). The values of $n\,T_i\,\tau_E$ have increased over several orders of magnitude in the last few decades and plasma temperatures and densities needed for a fusion reactor are obtained in contemporary tokamaks. In order to reach ignition (self-sustained plasma heating by alpha particles resulting from fusion reactions) an increase of the energy confinement time to values of several seconds is needed. This can be achieved by a larger plasma size, such as that of the planned International Thermonuclear Experimental Reactor (ITER), a tokamak with major radius $R = 6.2$, about twice as large as that of the presently largest tokamak, JET ($R = 3$ m). The step to a reactor-scale experiment with large fusion power and significant neutron production will allow to study dominant plasma heating by fast alpha particles, confinement and plasma-wall interaction, and test first-wall and low-activation structural materials needed for an integrated power plant concept. Alternative confinement concepts such as stellarators will further develop and demonstrate their attractive potential in new experiments, for example for steady state operation. Nevertheless, one can expect that tokamaks will remain at least for some foreseeable future the reliable "workhorse" and universal test-bed for magnetic fusion research they have been in the last three decades.

Further reading

General

M. Kaufmann, Plasmaphysik und Fusionsforschung (in German), Teubner Verlag, Stuttgart, Leipzig, Wiesbaden 2002, ISBN 3-519-00349-X
F. F. Chen, Introduction to Plasma Physics, Vol. 1, second edition, Plenum Press, New York 1984, ISBN 0-306-41332-9
R. J. Goldston, P. H. Rutherford, Introduction to Plasma Physics, IOP Publishing, Bristol 2000, ISBN 0-750-30183-X
K. Miyamoto, Plasma Physics for Nuclear Fusion, MIT Press, Cambridge 1989, ISBN 0-262-13237-0
J. A. Wesson, Tokamaks, Oxford University Press 1987, ISBN 0-19-856328-0

Specific topics

F. Ryter *et. al.*, Empirical studies of electron transport, Plasma Phys. Control. Fusion **43** (2001) A323
R. J. Groebner, An emerging understanding of H-mode discharges in tokamaks, Phys.

Fluids **B 5** (1993) 2343
J. W. Connor and H. R. Wilson, a review of theories of the L-H transition, Plasma Phys. Control. Fusion **42** (2000) R1
H. Zohm, Edge Localized Modes, Plasma Phys. Control. Fusion **38** (1996) 105
J. W. Connor, A review of models for ELMs, Plasma Phys. Control. Fusion **40** (1998) 191
H. R. Wilson *et. al.* Ideal magnetohydrodynamic stability of the tokamak high-confinement edge region, Physics of Plasmas **6** (1999) 1925 J. P. Freidberg, Ideal Magnetohydrodynamics, Plenum Press, New York 1987, ISBN 0-306-42512-2
D. Biskamp: Nonlinear Magnetohydrodynamics, Cambridge University Press, Cambridge 1993, ISBN 0-521-59918-0
ITER: ITER Physics Base, Nuclear Fusion **39** (1999) 2137-2638, R. Aymar *et. al.*, The ITER design, Plasma Phys. Control. Fusion **44** (2002) 519 and `http://www.iter.org`
ASDEX Upgrade: `http://www.aug.ipp.mpg.de`

Chapter 11

Computational Plasmaphysics[1]

Ralf Schneider and Ralf Kleiber

11.1 Introduction

Physics in plasmas is determined in most cases by simple equations, namely the equations of motion for electrons, ions and neutrals including the effect of collisions and (self-consistent) electric and magnetic fields. An exact numerical model based on individual particles is nevertheless impossible due to the large number of particles involved and would need much too large computer resources. The simulation of plasma physics using of the most powerful computers available started in the fifties [1]. Modeling fusion plasmas is inherently difficult due to the need to include a range of space scales extending from the gyro radius of the ions (a few mm) and electrons (a few 10^{-5} m) to the machine size (a few m) and the range of time scales extending from 10^{-12} s for fast electrons to several seconds for steady-state discharges. To cover a good part of these ranges in a computational model for a fusion plasma about 10 physical variables are necessary (densities, velocities, temperatures). These have to be updated at approximately 10^{10} grid points for 10^8 time steps. Assuming 10^2 operations for a very simple numerical algorithm per grid point and time step this results in a total number of 10^{21} floating point operations (FLOP). The execution speed of a code on a computer is usually measured in mega-flops (10^6 FLOP/s), giga-flops (10^9 FLOP/s) or tera-flops (10^{12} FLOP/s). Assuming a realistic performance of 60 giga-flops for such a model (Cray T3E with 512 processors in parallel), one run would take some 500 years of computer time. Therefore, the brute force ansatz will not work and a hierarchy of models is necessary.

The task of computational plasma physics is to develop such methods in order to obtain a better understanding of plasma physics. For this, a close contact to theoretical plasma physics and numerical methods is necessary. Ideally, computational plasma physics acts

[1]to be published: © Springer Lecture Notes on Physics: Plasma Physics: Confinement, Collective Effects and Transport

as a pathfinder to guide the scientific and technical development and to connect experiment and theory. Therefore, it is an independent method in addition to the two traditional ones.

For low temperature plasmas it is sometimes still possible to use a full kinetic model, using so-called super-particles representing a large number of real particles. Similar methods are used in the gyrokinetic description of turbulence in high temperature plasmas or in astrophysical plasmas. For longer length scales fluid models are usually used leading to mixed conduction–convection problems. In fusion plasmas these methods are used e.g. for magnetohydrodynamics (MHD), optimization of stellarators and edge physics, but are also used in turbulence modeling. In terms of numerical methods the MHD problem also poses eigenvalue problems to be solved (e.g. for stability analysis). In astrophysical and dense plasmas, where many-body effects can get quite important, special integration methods are needed.

In the following, two examples of computational plasma physics will be presented: plasma edge physics and turbulence.

11.2 Plasma Edge Physics

The various aspects of plasma edge physics are discussed by presenting, as an example, a comprehensive suite of codes having applications from industrial plasmas to fusion devices. As mentioned before, the basic problem of plasma edge physics is the large range of length (see Fig. 11.1) and corresponding time scales.

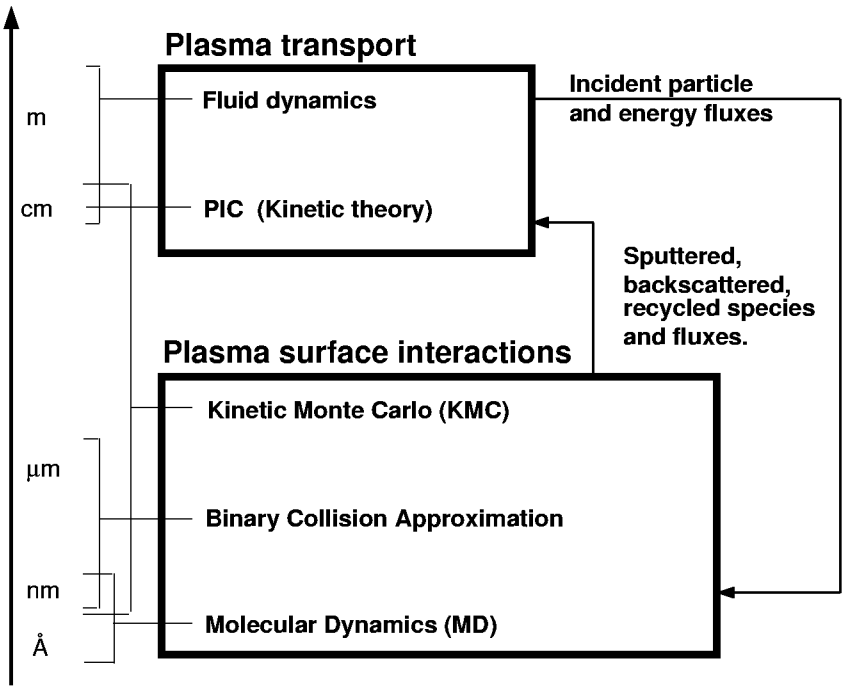

Figure 11.1: The different length scales and methods used for plasma edge modelling.

Plasma wall interaction effects introduce microscopic length scales (like the typical interaction distance of about 1 nm between atoms and molecules) and very short time scales

(fast momentum transfer processes determining the collision processes occur in 10^{-12} s). These processes are important for material changes in plasma wall facing materials and therefore also for the release of impurities into the plasma (e.g. physical or chemical sputtering). They are studied either by Molecular Dynamics (MD) or by a simplified binary collision model. The latter strongly reduces the computational effort, though at the price of drastically simplifying the physics. In addition, diffusion in such materials introduces length scales spanning from microns (size of the granules) up to centimeters (size of the tiles). These effects (e.g. diffusion in amorphous materials) are analyzed with Monte Carlo methods (kinetic Monte Carlo with input from molecular dynamics or experiment).

The plasma description again has different levels of complexity. A full kinetic description (including ions, electrons, neutrals and their collisions) is possible for some low temperature plasmas (e.g. electron cyclotron resonance heated methane plasmas) and for qualitative studies of edge plasma effects in fusion edge plasmas. Here, the limitations are given by the fact that the Debye length and the plasma frequency have to be resolved.

For the study of the physics of the edge of magnetically confined plasmas (2D tokamaks, tokamaks with ergodic perturbations, 3D stellarators) fluid codes are used for understanding the complex physics in such devices. Depending on the geometrical complexity (2D tokamaks, 3D stellarators) and on the additional effect of ergodicity, different numerical methods (finite volume, finite difference and Monte Carlo methods) are used.

The plasma surface interactions influence the plasma transport through sputtered, backscattered and recycled particles and fluxes. On the other hand, the incident particle and energy fluxes determine the plasma surface interaction.

The different codes not only describe different time and spatial scales, but also different parts of the plasma edge: codes describing plasma wall interaction processes and codes resolving the sheath in front of a wall are models for the near-wall physics, whereas the plasma transport fluid codes try to cover the whole scrape-off layer (SOL) replacing the near-wall physics by effective boundary conditions.

A typical example where a problem involves all the different scales mentioned before is the study of carbon as a wall material. The release of hydrocarbons from the walls [2, 3, 4] due to the influx of hydrogen ions and/or neutrals create, after break-up in the plasma, a source of carbon ions for the plasma. Due to its radiation characteristics, carbon is the ideal radiator for a divertor, because the radiation losses can be maximized, while minimizing the core dilution. However, the hydrocarbons also tend to form co-deposited layers far away from the plasma like in pump ducts. This results from additional transport through neutrals and/or low temperature plasmas in the periphery. These layers pose a severe safety problem for any reactor because they trap a huge amount of tritium. Therefore, understanding of such processes and plasmas is critical for reactor design and will strongly influence the choice of the wall material.

This paper describes codes which have been developed and used in one group to study many aspects of plasma edge physics.

11.2.1 Models

Plasma Wall Interaction

Molecular Dynamics A molecular dynamics (MD) code HCParcas (developed by K. Nordlund) is used to study the transport of interstitials in a graphite crystal. This code uses the semi-empirical Brenner potential [5] for treating the hydrogen and Carbon system and the Nordlund interlayer term [6] to simulate a graphite crystal. The interstitial trajectories (over a sample size of 100 Å for 100 pico-seconds) are analyzed to obtain input parameters for our Kinetic Monte Carlo (KMC) code [7]. A first study of the diffusion of hydrogen in porous graphite showed [8] Levy–flight–type behavior. The diffusion process proceeds via vacancy jumps towards neighboring atoms. These jumps are thermally activated processes with jump frequencies ω determined by $\omega = \omega_0 \cdot \exp(\frac{-\Delta E}{k_B T})$, where ω_0 is the jump attempt frequency and ΔE is the activation energy for this process. There exist two different channels of diffusion for hydrogen isotope interstitials in graphite crystallites: one is a high frequency, high migration energy channel which matches the graphite phonon frequencies, and the other is a low frequency, low migration energy channel which shows a $1/\sqrt{m}$ mass dependence for the jump attempt frequencies [8].

Binary Collision Code A computationally much less expensive technique is also successfully used for studies of the interaction of particles with (homogeneous) materials [9]. Here, only two-particle interactions are taken into account. A successful application of this code is the description of physical sputtering of surfaces including dynamical changes of the composition [10, 11, 12]. However, due to its simplification it fails as soon as chemical processes get important [2].

Kinetic Monte Carlo A KMC code DiG (Diffusion in Graphite) is being developed to treat hydrogen transport in graphite. It is designed to use the information from MD or from experiments to study the transport and interactions of hydrogen as it diffuses in a realistic porous graphite structure. The advantage of using a KMC scheme is that it allows us to model multiple scale lengths in time in an efficient way using the scheme described in [13]. It models graphite crystals ranging in from 100 Å across to graphite granules of a few microns, and with time scales ranging from pico-seconds to seconds (depending on the graphite temperature and the trap energies). Experimental results for diffusion in graphite were matched in the trapping/de-trapping dominant regime. It was shown that the diffusion coefficient depends on the structure of the graphite used (void sizes) and the trapping mechanism [8].

Plasma Modelling

Kinetic PIC Microscopic models of plasmas are conceptually easy: one has to solve the equations of motion and, self-consistently, the resulting fields, which again influence the particle motion. However, it is impossible to solve such a system directly due to the large number of particles. Therefore, a so-called Particle–in–Cell (PIC) method is used

[14, 15]. Here, we deal with "super-particles", which are collections of thousands of real particles. Since their charge mass ratio is the same as for normal particles they obey the same equation of motion as real particles. In most practical cases one is not interested in a spatial resolution smaller than the Debye radius. This allows one to compute electric and magnetic fields only at grid points separated by about one Debye length and thus considerably reduce computational time. A general multi-species electrostatic PIC code was developed including all collisions between electrons, ions and neutrals. This code was successfully applied to the study of low temperature methane plasmas [16] (which are model systems for chemical sputtering studies), capacitive RF discharges [17] and complex plasmas [18].

Plasmas which, in addition to electrons, ions and neutrals, also contain microscopic particles of nanometer — micrometer size are called dusty (complex) plasmas. The dust particles in such plasmas gain an electric charge, the sign and magnitude of which depends on the balance between different charging processes. The absorption of electron and ion fluxes, thermo-, photo- and secondary electron emissions are the most typical mechanisms of particle charging in complex plasmas. Such charged micro-particles substantially change plasma behavior and are responsible for the unusual properties of complex plasmas. In a capacitive RF discharge the gravitational force acting on the particles can be equilibrated by the electrostatic force acting in front of the lower electrode due to a strong repulsive electric field in the RF sheath. In this case particles are trapped in the discharge and form a cloud levitating above the lower electrode. The dust particles interact with each other through the repulsive Coulomb potential, screened by the plasma electrons and ions. In the case of strong electrostatic coupling, i.e. when the energy of the inter-particle interaction is large compared to the particle thermal energy, particles self-assemble into ordered structures, known as plasma crystals. Due to the large mass of the dust particles the characteristic relaxation time for the plasma crystals is usually of the order of seconds, making such structures easy to observe with ordinary video-observation techniques. The inter-particle distance in dusty plasma crystals is usually of the order of a fraction of millimeter, so that it is possible to observe such structures even with a naked eye. The plasma crystals represent a bridge connecting the atomic or molecular scale of matter with the macroscopic scale of a dusty particle system, giving a unique possibility to observe processes in the condensed matter on the kinetic level.

We have studied the formation of dust structures in a capacitive coupled RF discharge using a self-consistent particle simulation. For this purpose we have utilized the particle–in–cell (PIC) code with a Monte–Carlo collisions (MCC) package resolving 3 spatial dimensions and 3 velocity components [19]. The dust particles were introduced into the model as an additional charged species, using the Cloud–in–Cell weighting formalism [14], so that no finite size effects for dust particles were considered. In addition to the electrostatic force the gravitational and neutral gas friction forces were also considered for the dust particles.

In Fig. 11.2 we present the dust structure equilibrated over the lower electrode of a capacitive RF discharge.

We can see that the particles are divided in three horizontal layers with a separation of about one Debye length (for convenience we highlighted the layers with different

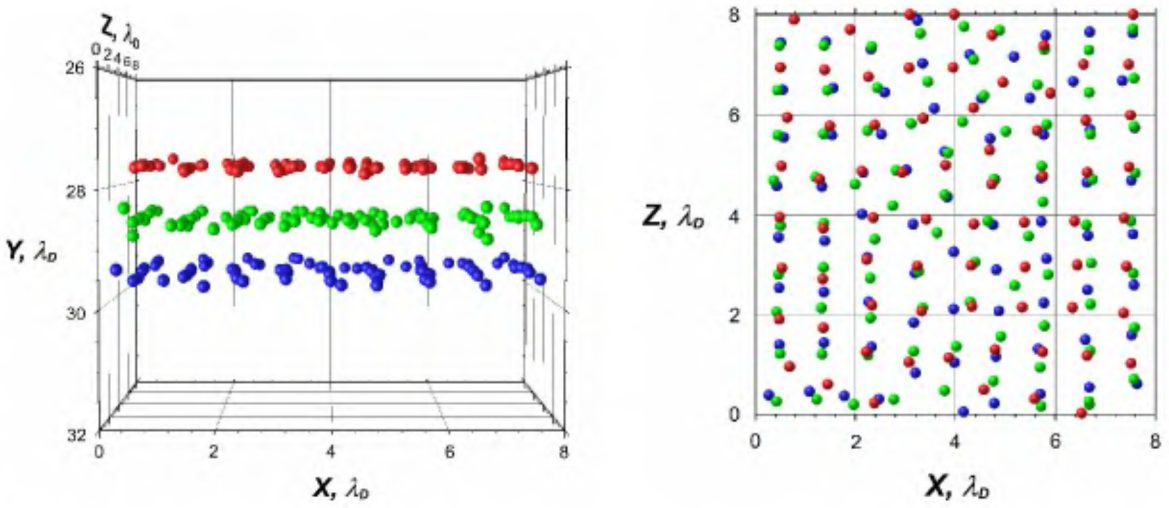

Figure 11.2: Side (left) and top (right) view of the 3D plasma crystal.

colors). When looking on the dust structure from above (Fig. 11.2) we can note that particles tend to form 'triads', as particles belonging to three different layers are aligned vertically. This type of alignment is caused by the polarization of the ion flow in the sheath region. Thus the dust formation in Fig. 11.2 shows a quasi–two–dimensional structure of vertically aligned horizontal layers, each with a similar structure.

Application of the PIC method for turbulence modelling will be discussed in the chapter 11.3.

2D Fluid Code (B2) The kinetic models also allow one to formulate effective boundary conditions at the plasma sheath, which is needed for multi-fluid models [20]. These models use the fluid equations derived as moments from the kinetic equations, including sinks and sources (like radiation or heating). Closing of the system is obtained by the proper transport coefficients [21, 22]. The applicability of these models is limited to collisional regimes, where all mean-free paths are smaller than the relevant system lengths, namely the temperature gradient length and the connection length along the field lines. Applying the fluid model can be problematic in front of the divertor where temperature gradients can become steep, resulting in non-local heat conduction. Further problems can arise on closed field lines near the separatrix, where for high temperatures the heat conduction of electrons has to be modified according to kinetic flux limits for periodic systems. Then, (gyro-)kinetic models are necessary for a complete and correct description. In addition, the effect of plasma turbulence has to be introduced by parametrization of the radial anomalous fluxes either by empirical fitting [23] or from ab-initio models [24]. The neutrals, which are quite important for many edge effects, are modelled either by fluid models are through Monte Carlo codes [25]. Numerically, a generalized finite volume scheme for mixed conduction–convection is used, where each individual equation (continuity equations, parallel momentum equations, electron and ion internal energy equations, potential equation) is solved by iterating through this coupled set of equations until convergence is obtained [26]. This code package has been successfully applied to many tokamaks, especially to ASDEX Upgrade, e.g. for the opti-

mization of the divertor [27]. The latest development was the completion of the physics regarding inclusion of drifts and currents, where the observed radial electric fields and flow patterns close to the separatrix was studied [28].

3D Fluid Code (BoRiS)

An extension of this finite volume scheme is necessary for stellarators, which are intrinsically 3D. BoRiS is a 3D SOL transport code under development which is designed to simultaneously solve a system of partial differential equations in three dimensions. Although developed in the framework of 3D edge modelling for the new W7–X stellarator, the code development follows a more general concept to allow for different applications. The main characteristics of BoRiS are:

1. finite volume method,
2. use of generalized (magnetic) coordinates,
3. general interpolation for mixed convection–diffusion problems and
4. Newton's method.

These features are strongly influenced by the experiences derived from edge physics modelling with model-validated 2D codes like B2-Eirene [29] and UEDGE [30]. The use of magnetic (Boozer) coordinates s, θ, ϕ allows for standard discretization methods with higher-order schemes to describe a complex 3D geometry (see Fig. 11.3). Therefore, the existence of intact flux surfaces is a prerequisite of this concept.

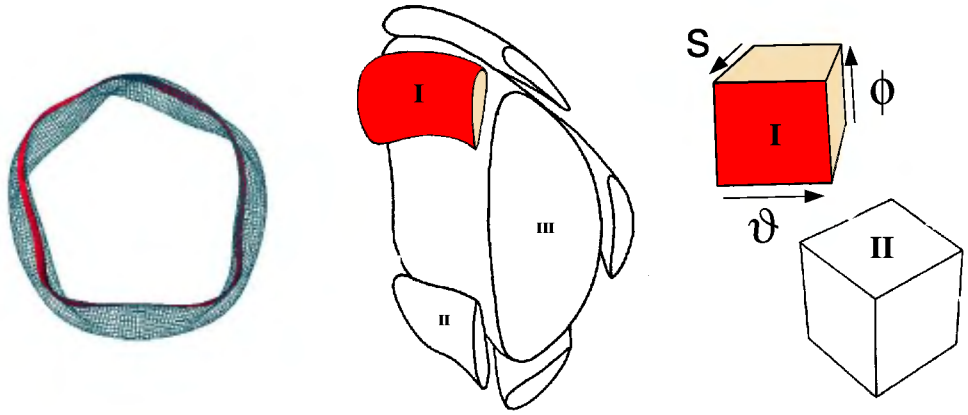

Figure 11.3: A set of seven sub-grids forms the complete W7–X grid (*five islands, core and outer SOL*).

With the Newton method, BoRiS utilizes a variety of sophisticated solvers (sparse direct, sparse iterative and matrix-free iterative) and preconditioners [31] which are available. In order to deal with large systems, a parallel version of the code was developed.

BoRiS was initially tested on the coupled Laplace equations for electron and ion temperatures in a W7–X island flux tube [32]. Several complexity levels (1D, 2D, 3D) were

benchmarked against UEDGE [33] and a 3D Monte Carlo code [34]. In addition, a complete Navier–Stokes neutral fluid model was also compared with simplified models [35].

Transport Codes for Ergodic Configurations A further complication appears as soon as ergodic configurations are studied. Here, like in TEXTOR-DED [36], a special set of coils is installed to give an additional control of the magnetic topology in the periphery. Indeed, the stronger the perturbation, the larger the islands on the resonance surfaces, until they overlap and build a so-called ergodic layer: the behavior of a field line becomes stochastic (two originally neighbouring field lines diverge from each other exponentially with a Kolmogorov characteristic length L_K), and we obtain a nonzero projection of the strong parallel heat transport onto the radial direction and, therefore, a flattening of the temperature profile.

Configurations of this kind are very general: they contain intact magnetic surfaces, islands, ergodic and open field lines, and are, in that respect, similar to the edge region of stellarators.

The main problem of the transport modelling in such mixed regions is as follows: the coordinate system must be aligned to the unstructured magnetic field. For realistic plasma edge conditions, the ratio between $\chi_{\|}$ and $\chi_{\perp}$ can be up to 8 orders of magnitude, and numerical diffusion becomes a severe problem.

If we choose a coordinate system in which the magnetic field has only one nonzero component, we guarantee the separation of the parallel and perpendicular fluxes. The question is how to build such a coordinate system. We begin by choosing a surface (called the reference cut) which intersects all field lines of interest and then draw some reasonable (say, Cartesian) mesh on this cut. We then trace field lines through the mesh lines. The surfaces we obtain are our coordinate surfaces. The metric of this system can be obtained by field line tracing. Indeed, the real space coordinates are linked with these magnetic coordinates by field line tracing, and we can extend this procedure to calculate the relevant transformation matrix. These Clebsch coordinates have a remarkable advantage: they can be used locally. By this, we mean that more than one reference cut (and, therefore, multiple coordinate systems) can be used, in order to keep the scope of a single system well below the Kolmogorov length. The price for such flexibility is clear: the system is non-periodic, i.e. the coordinate surfaces of neighbouring systems overlap arbitrarily at the interface between the two systems. Also we have a full metric tensor.

If we try to solve the problem by interpolation, we induce numerical diffusion of the same nature as before: a contribution of the parallel flux to the perpendicular fluxes. For instance, if one were to pass a beam (a δ-function) through such a system, one would obtain a response in all corners of the cell at the interface, and then on the next interface it would spread further. There are two possible ways of dealing with this phenomenon: The first is to optimize the mesh on the reference cut, i.e. to produce it by field line tracing itself. This idea is good for the field lines starting and ending on the wall, or for closed field lines.

Any other field line can be treated as "almost closed" as long as the following criterion is fulfilled (see Fig. 11.4): $\Delta \ll L_{\|}\sqrt{\chi_{\perp}/\chi_{\|}}$, where Δ is the excursion between the start

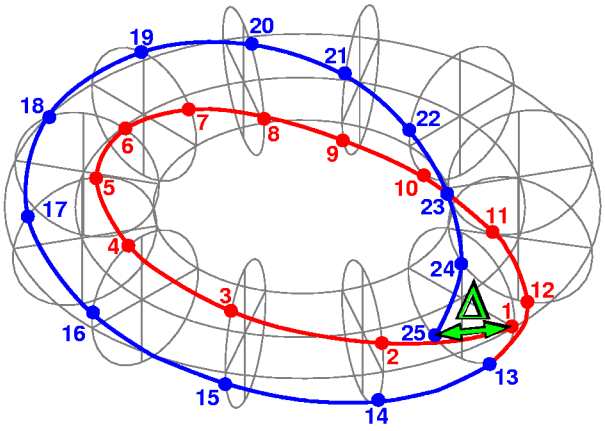

Figure 11.4: Grid construction criterion for the finite difference code.

and end points on the cut and $L_{\parallel} \approx 2\pi RN$ is the distance between the same points measured along the field line with $N \approx 100$ toroidal turns. We select only those field lines which come within $\Delta = 1$ mm of closing on themselves. These field lines are used in building the mesh. This minimizes the induced numerical diffusion to about $10^{-4}\,\mathrm{m}^2/\mathrm{s}$. The penalty one pays for this method is an unstructured mesh [37]. The local system is a moving patch covering three neighbouring reference cuts simultaneously, because one must be able to write and discretize the divergence of gradients within its scope.

For the parallel terms, we use only the three points in our scheme located along the same field line at its intersections with the reference cuts. The rest is more or less conventional work with an unstructured mesh: the perpendicular problem is quasi-isotropic, and the choice of the numerical method is uncritical. Normally, one uses so-called Delaunay triangulation to build the mesh – a method commonly used in finite elements. First successful studies were done for W7–X cases [38].

The second idea is to switch to a Monte Carlo method with an appropriate mapping technique (see chapter by D. Reiter).

11.3 Turbulence

In tokamak devices the observed transport is much higher than the neoclassical transport (transport caused by collisions in a toroidal confinement system) thus it must be due to transport caused by turbulence (anomalous transport). Observations suggest that Ion Temperature Gradient (ITG) driven instabilities and the subsequent turbulence are the main cause for anomalous transport in the plasma core of tokamaks.
For stellarator devices the situation is less clear. In most classical stellarator experiments the transport was dominated by neoclassical transport making it impossible to observe the anomalous contribution. For the newly designed advanced stellarators (e.g. Wendelstein 7-X, currently under construction in Greifswald) the neoclassical transport has been greatly reduced so that the anomalous transport may become detectable.

11.3.1 Gyrokinetic Theory

Gyrokinetic theory for ions is the standard theory used for describing the core (where temperature and density are high). It is a simplification of full kinetic theory where the Vlasov equation

$$\frac{\mathrm{d}f}{\mathrm{d}t} = \frac{\partial f}{\partial t} + \mathbf{v}\cdot\nabla_r f + \frac{q}{M}(\mathbf{E}+\mathbf{v}\times\mathbf{B})\cdot\nabla_v f = 0 \tag{11.1}$$

(q, M: ion charge, mass; $\mathbf{E}, \mathbf{B}$: electric, magnetic field) describes the time evolution of a six-dimensional distribution function $f(\mathbf{r}, \mathbf{v})$ in phase space. Solving this equation numerically should be avoided since it is very costly; thus approximations are required which are more feasible for numerical simulations.
For the general case the electric and magnetic field $(\mathbf{E}, \mathbf{B})$ are determined by Maxwell's equations where the density and current are obtained by taking velocity moments of f. In the following we will only look at the electrostatic case where a fixed magnetic field is prescribed externally and only the electric field $\mathbf{E} = -\nabla\phi$ is allowed to change.
The motion of a charged particle in a magnetic field can be decomposed into a fast gyration with the gyrofrequency $\Omega_\mathrm{i} := \frac{qB}{M}$ along a circle – called the gyroring – with radius $\rho := \frac{v_\perp}{\Omega_\mathrm{i}}$ centered at the slowly drifting gyrocenter $\mathbf{R}$. The position of the particle can thus be written as $\mathbf{x} = \mathbf{R} + \rho$ with $\rho = \rho\,(\cos(\alpha)\mathbf{e}_{\perp 1} + \sin(\alpha)\mathbf{e}_{\perp 2})$ and $\mathbf{e}_{\perp 1,2}$ two base vectors perpendicular to $\mathbf{B}$. The velocity $\mathbf{v}$ can then be decomposed into components parallel ($v_\parallel$) and perpendicular ($v_\perp$) to the magnetic field and the gyrophase α.

If the characteristic frequency ω of the processes one wants to describe is much smaller than Ω_i – this is the case for turbulence and ITG instabilities – it is possible (under assumptions on the space variation of the quantities) to average over the fast gyromotion. Due to the averaging procedure the gyrophase α disappears and the result is the gyrokinetic equation [39] now describing the evolution of a distribution function $f(\mathbf{R}, v_\parallel, \mu)$ in a five-dimensional phase space spanned by the gyrocenter position $\mathbf{R}$ and two velocity components (here the magnetic moment per unit mass $\mu := v_\perp^2/(2B)$ is used instead of $v_\perp$):

$$\frac{\mathrm{d}f}{\mathrm{d}t} = \frac{\partial f}{\partial t} + \dot{\mathbf{R}}\cdot\nabla f + \dot{v}_\parallel\frac{\partial f}{\partial v_\parallel} + \dot{\mu}\frac{\partial f}{\partial \mu} = 0 \tag{11.2}$$

with the equations of motion for the gyrocenter (for the reason of simplicity we assume a vacuum magnetic field in the following)

$$\dot{R} = v_\parallel\mathbf{b} + \frac{1}{B}\mathbf{b}\times\nabla\langle\phi\rangle + \frac{\mu B + v_\parallel^2}{B\Omega_\mathrm{i}}\,\mathbf{b}\times\nabla B \tag{11.3}$$

$$\dot{v}_\parallel = -\mu\,\mathbf{b}\cdot\nabla B - \frac{q}{M}\left(\mathbf{b} + \frac{v_\parallel}{B\Omega_\mathrm{i}}\mathbf{b}\times\nabla B\right)\cdot\nabla\langle\phi\rangle \tag{11.4}$$

$$\dot{\mu} = 0 \tag{11.5}$$

($\mathbf{b} := \frac{\mathbf{B}}{B}$). Equation (11.3) gives the motion of the gyrocenter as a parallel motion plus $\mathbf{E}\times\mathbf{B}$-drift and grad-B/curvature-drift; the first term in the equation for $\dot{v}_\parallel$ shows the mirror effect; finally, μ is a constant of motion.

The equations of motion do not depend on the electrostatic potential directly but on its average over the gyroring described by the gyroaveraging operator $\langle . \rangle$

$$\langle \phi \rangle (\mathbf{R}) := \frac{1}{2\pi} \int_0^{2\pi} \phi(\mathbf{R} + \rho)\, d\alpha \; . \tag{11.6}$$

The space density n_i of ions is given by the gyroaveraged ion density $\langle n_\mathrm{i} \rangle$ defined as

$$\langle n_\mathrm{i} \rangle (\mathbf{x}) := \int f(\mathbf{R}, v_\parallel, \mu)\, \delta(\mathbf{R} + \rho - \mathbf{x})\, d\mathbf{R}\, d\mathbf{v} \tag{11.7}$$

plus a correction term called the polarization density (n_0 denotes the equilibrium ion density and $\nabla_\perp$ the gradient perpendicular to the magnetic field)

$$n_\mathrm{i} = \langle n_\mathrm{i} \rangle + \nabla_\perp \cdot \left(\frac{n_0}{B\Omega_\mathrm{i}} \nabla_\perp \phi \right) \; . \tag{11.8}$$

Since the gyroradius of the electrons is much smaller than that of the ions the former can be described by a simple approximation called adiabatic electrons: $n_\mathrm{e} = n_0 + \frac{e n_0}{k_\mathrm{B} T_\mathrm{e}} \phi$. Together with charge neutrality $n_\mathrm{e} = n_\mathrm{i}$ this leads to the final Helmholtz equation determining ϕ

$$\frac{e n_0}{k_\mathrm{B} T_\mathrm{e}} \phi - \nabla_\perp \cdot \left(\frac{n_0}{B\Omega_\mathrm{i}} \nabla_\perp \phi \right) = \langle n_\mathrm{i} \rangle - n_0 \; . \tag{11.9}$$

Equations (11.2)-(11.7) and (11.9) constitute a closed system for ϕ and f.

Gyrokinetic theory may seem complicated but can be understood intuitively by a simple physical picture: Due to the time–scale separation between gyration and drift motion the ion can be replaced by a ring of charge with radius ρ centered around $\mathbf{R}$. f now becomes the distribution function of these rings located in space at the position $\mathbf{R}$. Equations (11.3)–(11.5) describe the movement of such a ring in 5dim. space. As a consequence the electric field does not act at the center of the ring $\mathbf{R}$ but on the ring itself; thus to get its action it must be integrated along the ring what is expressed by (11.6). Equation (11.7) can be understood by noting that the charge at one specific space point is the sum of the charge from all the rings with different ρ passing through it. Finally, the polarization density can only be understood by deriving the gyrokinetic theory rigorously using the theory of Lie transformations [39].

11.3.2 The PIC Method

The gyrokinetic equation can be solved as a partial differential equation on a 5dim. grid or by particle in cell (PIC) simulations. Since the PIC method combined with a δf approach has proven extremely powerful we restrict ourselves to this approach. Also we concentrate – as an example – on the line of PIC codes originating from the CRPP at the EPFL Lausanne. We do not want to delve into the details and problems of linear/nonlinear numerical implementation, geometry or extensions for non-adiabatic electrons and electromagnetic effects (see e. g. [40]–[44], [50]) but merely present some of the basic methods used in a modern PIC code.

The fluctuation amplitude of ITG turbulence in a plasma is much smaller than the magnitude of the equilibrium quantities. For a simulation using particles this means that most of the particles get wasted by representing the equilibrium and only a small number is left over for the description of the fluctuations. Since the numerical noise depends on the particle number N as $\frac{1}{\sqrt{N}}$ this leads to a bad statistical behaviour that can be overcome by employing the δf approach [45]–[47]; here the time dependent distribution function f is split into a fluctuating part δf and a time–independent part f_0 representing the equilibrium: $f(t) = f_0 + \delta f(t)$. If now f_0 is given analytically (usually it is assumed to be a Maxwellian distribution) all the particles can be used to represent the fluctuation δf resulting in highly improved statistics.

Using this ansatz in (11.2) one gets $\frac{\mathrm{d}}{\mathrm{d}t}\delta f = S$ (S is a source term resulting from the application of $\frac{\mathrm{d}}{\mathrm{d}t}$ on f_0). This PDE can be solved formally using the method of characteristics: Given an initial function $\delta f(t=0)$ integration of the ODE $\frac{\mathrm{d}}{\mathrm{d}t}\delta f = S$ along the characteristics determined by (11.3)–(11.5) gives the general solution $\delta f(t)$.

A gyrokinetic PIC code rests on four procedures subsequently executed at each time step:
1) particle pushing: Integrating the equations of motion for each particle in a given potential.
2) gyro-averaging: The gyroaverage $\langle\phi\rangle$ of the electrostatic potential ϕ needs to be calculated by numerically approximating the integral in (11.6).
3) charge assignment: the potential equation (11.9) is discretized on a grid but the particles are distributed irregularly; thus a prescription must be provided specifying how to generate from the particles (and their weights) a density defined on the grid (in gyrokinetics one has also to take into account that one does not deal with point particles but with gyrorings). Charge assignment can thus be regarded as the link connecting the Lagrangian (particles) with the Eulerian part (grid).
4) potential solver: given the gyroaveraged density on the grid the Helmholtz equation must be solved in order to obtain the potential.

Introducing N marker particles each one carrying a weight w_p the quantity δf is discretized by writing it as a sum of delta functions

$$\delta f = \sum_{p=1}^{N} \frac{1}{J} w_p(t)\, \delta(\mathbf{R} - \mathbf{R}_p(t))\, \delta(v_\parallel - v_{\parallel p}(t))\, \delta(\mu - \mu_p(t)) \tag{11.10}$$

($J = 2\pi B$ is the phase space Jacobian) resulting in the equation

$$\dot{w}_p = S|_{\mathbf{R}_p, v_{\parallel p}, \mu_p} \tag{11.11}$$

for the weights.

For the numerical integration of (11.3)–(11.5) and (11.11) with e.g. a Runge-Kutta– or a Predictor–Corrector–method $\nabla\langle\phi\rangle$ must be known at each time step. In order to compute this one uses $-\nabla\langle\phi\rangle \approx \langle\mathbf{E}\rangle$ and approximates the integral by an average over N_a points ρ_j evenly spaced on the gyroring:

$$\langle\mathbf{E}\rangle = \frac{1}{N_\mathrm{a}} \sum_{j=1}^{N_\mathrm{a}} \mathbf{E}(\mathbf{R} + \rho_j)\ . \tag{11.12}$$

ϕ is obtained by solving the Helmholtz equation (11.9) discretized on a grid; also the right hand side $\langle n_\mathrm{i} \rangle$ must be computed by the charge assignment process. An elegant way that combines the charge assignment and the discretization of the Helmholtz equation uses B-splines as finite elements[40]. The potential is discretized by writing it as a sum over the finite element basis

$$\phi(\mathbf{x}) = \sum_\nu \phi_\nu \Lambda_\nu(\mathbf{x}) \tag{11.13}$$

where Λ_ν is a tensor product B-spline of order k. B-splines are continuous non-negative functions with finite support piecewise defined by polynomials of order k. Their most interesting property here is that B-splines provide a partition of unity i. e. $\sum_\nu \Lambda_\nu(\mathbf{x}) = 1$ [48]; this guarantees the conservation of charge during charge assignment.

Using (11.13) and the particle discretization (11.10) in (11.9) one can derive the following matrix equation for the coefficient vector ϕ_ν

$$\sum_{\nu'} A_{\nu\nu'} \phi_{\nu'} = n_\nu \tag{11.14}$$

with the matrix

$$A_{\nu\nu'} = \int \left(\frac{n_0}{B\Omega_\mathrm{i}} \nabla_\perp \Lambda_\nu \cdot \nabla_\perp \Lambda_{\nu'} + \frac{e n_0}{k_\mathrm{B} T_\mathrm{e}} \Lambda_\nu \Lambda_{\nu'} \right) d\mathbf{x} \tag{11.15}$$

that is the same at each time step and thus can be precomputed.
The charge assignment process defines the vector n_ν

$$n_\nu = \sum_{p=1}^{N} w_p \frac{1}{2\pi} \int_0^{2\pi} \Lambda_\nu(\mathbf{R}_p + \rho_p) d\alpha \tag{11.16}$$

where the last integral is again discretized by an average over N_a points on the gyroring (analogously to (11.12)).

This completes the short description of the ingredients needed for a numerical solution of the gyrokinetic equation. We now demonstrate the application by a linear and a nonlinear example.

If $\delta f \ll f_0$ is assumed then the gyrokinetic equation can be linearized. The EUTERPE code [43] solves this equation globally in full three-dimensional geometry; thus it can be used to investigate stellarator configurations (e. g. Wendelstein 7-X [49]).
As a simple example the result of a calculation for a circular tokamak configuration is shown in Figure 11.5 (the ion temperature gradient driving the instability is chosen such that it is maximal near half the minor radius of the configuration). In this simulation one follows the time evolution of small initial fluctuations imposed onto an equilibrium plasma. In the beginning ($t \lesssim 4$) the plasma oscillates randomly but for $t > 4$ a coherently oscillating mode is established and grows exponentially in time. The slope of the blue line then gives the growth–rate while the frequency of the mode can be obtained from the red/black curve. The mode structure at the end of the simulation is presented in Figure 11.5, right (since the configuration is axially symmetric only one poloidal cut is depicted). The structure shown rotates poloidally but its envelope always has its maximum at the right hand side (corresponding to the low field side of a tokamak); thus

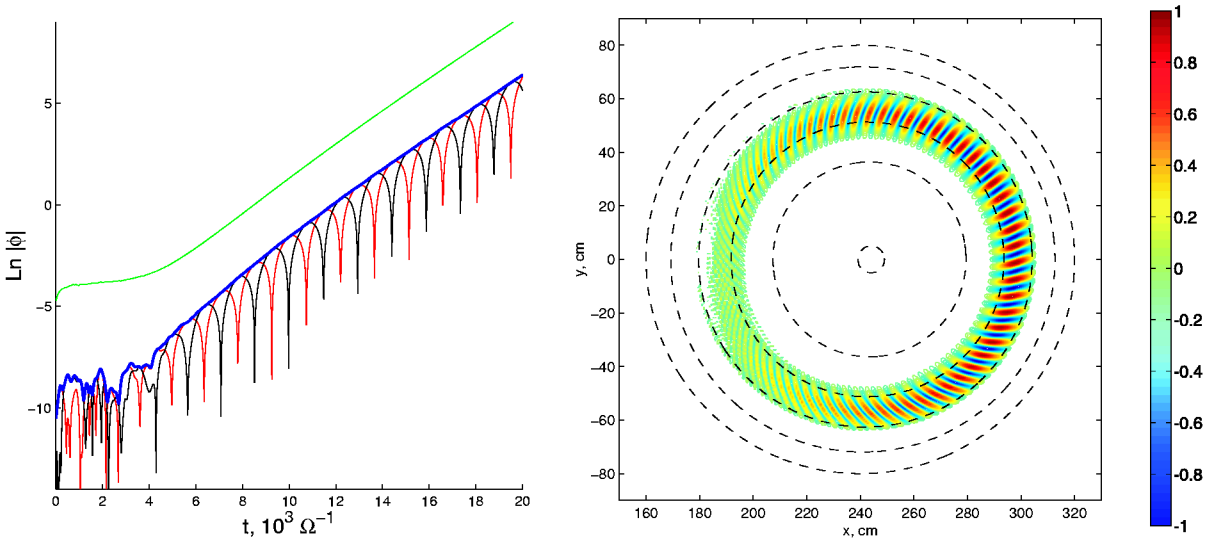

Figure 11.5: Linear ITG mode in a tokamak. Left: Time traces of $Re(\phi)$, $Im(\phi)$, $|\phi|$ (red, black, blue) and field energy (green). Right: $Re(\phi)$ (color coded) in the poloidal plane (courtesy of V. Kornilov).

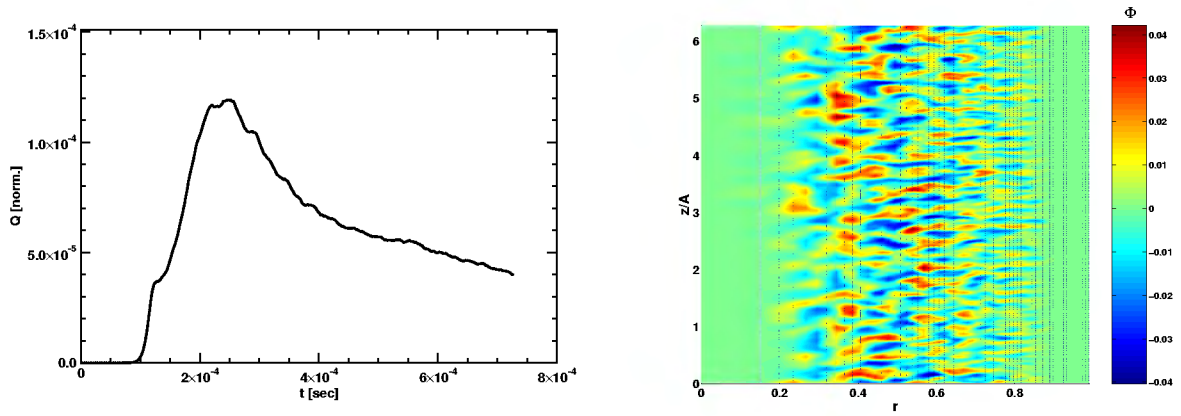

Figure 11.6: ITG turbulence in a θ–pinch. Left: Time trace of the (normalized) ion heat flux. Right: Potential fluctuations (color coded) in the $r-z$ plane of the cylinder (the magnetic field points in the z direction; also note that z has been scaled with $A = 10$) (courtesy of S. Sorge).

it is a typical toroidal ballooning mode. This kind of mode is characterized by small scale structures perpendicular to the magnetic field and long structures nearly following the field lines; this reflects the high anisotropy of the system caused by the magnetic field.

Linear calculations are important in many ways e. g. to identify parameter regions where the plasma becomes unstable. However, for the calculation of anomalous transport caused by turbulence, nonlinear calculations are necessary. Figure 11.6 presents results from the TORB code [41, 42] which solves the nonlinear global gyrokinetic equation for a straight cylinder geometry (θ–pinch). The left plot shows the ion heat flux as a function of time (in this simulation the formation of zonal flows, known to strongly suppress the turbulence, was artificially inhibited). The simulation starts from small

initial random noise. During the linear phase the perturbations grow exponentially until $t \approx 1.5 \times 10^{-4}$ sec. At this time the system saturates due to the nonlinearity but the transport increases because the turbulence spreads radially. After the flux reaches its maximum the transport induced flattening of the temperature profile leads to its slow decay. This is connected to the absence of an external source of energy maintaining the temperature profile. The space structure of the turbulence at $t = 3 \times 10^{-4}$ sec (Figure 11.6, right) is again characterized by very different length scales perpendicular and parallel to the magnetic field.

Bibliography

[1] C.K. Birdsall, "Particle-in-Cell Charged-Particle Simulations, Plus Monte Carlo Collisions With Neutral Atoms, PIC-MCC", *IEEE Transactons on Plasma Science* **19** (2) (1991) 65–85.

[2] J. Roth, "Chemical erosion of carbon-based materials in fusion devices", *Journal of Nuclear Materials* **266–269** (1999) 51–57.

[3] J. Küppers, "The hydrogen surface chemistry of carbon as a plasma facing material", *Surface Science Reports* **22** (1995) 249–321.

[4] E. Salonen, K. Nordlund, J. Keinonen and C.H. Wu, "Swift chemical sputtering of amorphous hydrogenated carbon", *Physical Review B* **63** (2001) 195415[1–14].

[5] D.W. Brenner, "Empirical potential for hydrocarbons for use in simulating the chemical vapor deposition of diamond films ", *Physical Review B* **42** (15) (1990) 9458–9471.

[6] K. Nordlund, J. Keinonen, and T. Mattila, "Formation of ion irradiation induced small–scale defects on graphite surfaces", *Physical Review Letters* **77** (4)(1996) 699–702.

[7] M. Warrier, R. Schneider, E. Salonen, and K. Nordlund, "Modelling of the diffusion of hydrogen in porous graphite", *Physica Scripta*, accepted for publication (2003).

[8] M. Warrier, R. Schneider, E. Salonen, and K. Nordlund, "Multi-scale modeling of hydrogen isotope diffusion in graphite", *Contributions to Plasma Physics*, to be published.

[9] W. Eckstein, "Computer simulation of ion-solid interactions", *Springer series in materials science 10*, Springer, Berlin, Heidelberg 1991.

[10] W. Eckstein, C. García-Rosales, J. Roth, W. Ottenberger, "Sputtering", IPP-Report **IPP 9/82**, *Max-Planck-Institut für Plasmaphysik, Garching, Germany* (1993).

[11] W. Eckstein, "Sputtering, reflection and range values for plasma edge codes", IPP-Report **IPP 9/117**, *Max-Planck-Institut für Plasmaphysik, Garching, Germany* (1998).

[12] W. Eckstein, "Calculated sputtering, reflection and range values", IPP-Report **IPP 9/132**, *Max-Planck-Institut für Plasmaphysik, Garching, Germany* (2002).

[13] A.B. Bortz, M.H. Kalos, and J.L. Lebowitz, "New algorithm for Monte Carlo simulation of Ising spin systems", *Journal of Computational Physics* **17** (1) (1975) 10–18.

[14] C.K. Birdsall, A.B. Langdon, "Plasma physics via computer simulation", McGraw–Hill, New York, 1985.

[15] R. Hockney, J. Eastwood. "Computer simulation using particles", McGraw–Hill, New York, 1981.

[16] K.V. Matyash et al., "Modeling of hydrocarbon species in ECR methan plasmas", *Journal of Nuclear Materials* **313–316** (2003) 434–438.

[17] K.V. Matyash, R. Schneider, "PIC–MCC modeling of a capacitive RF discharge", to be published in Contributions to Plasma Physics.

[18] K.V. Matyash, R. Schneider, " Kinetic modelling of dusty plasmas", to be published in Contributions to Plasma Physics.

[19] K. Matyash, R. Schneider, A. Bergmann, W. Jacob, U. Fantz and P. Pecher, J. Nucl. Matter. 313-316 (2003) 434.

[20] R. Chodura, "Plasma wall transition in an oblique magnetic field", *Physics of Plasmas* **25** (9) (1982) 1628–1633.

[21] S.I. Braginskii, "Transport processes in a plasma", *Reviews of Plasma Physics* **1** (1965) 205–311.

[22] V.M. Zhdanov, "Transport processes in multicomponent plasma", *Plasma Physics and Controlled Fusion* **44** (10) (2002) 2283 (re-edition of a Russian document, first published in 1982).

[23] D.P. Coster et al., "Automatic evaluation of edge transport coefficients with B2–SOLPS5.0", *Contributions of Plasma Physics* **40** (3–4) (2000) 334–339.

[24] X.Q. Xu et al., "Low to high confinement transition simulations in divertor geometry", *Physics of Plasmas* **7** (5) (2000) 1951–1958.

[25] D. Reiter, "The EIRENE Code, Version: Jan. 92 Users Manual", Jül-Report 2599, KFA Jülich, 1992.

[26] R. Schneider et al., "B2–SOLPS5.0: SOL transport code with drifts and currents", *Contributions to Plasma Physics* **40** (3–4) (2000) 328–333
V.A. Rozhansky et al., "Perpendicular conductivity and self-consistent electric fields in tokamak edge plasma", *Contributions to Plasma Physics* **40** (3–4) (2000) 423–430
B.J. Braams, "A multifluid code for simulation of the edge plasma in tokamaks", NET Report No. 68, January 1987 (EUR–FU/XII–80/87/68).

[27] R. Schneider et al., "Divertor geometry optimization for ASDEX Upgrade", *Journal of Nuclear Materials* **241–243** (1997) 701–706
R. Schneider et al., "Role of divertor geometry on detachment in ASDEX Upgrade", *Journal of Nuclear Material* **266–269** (1999) 175–181.

[28] V.A. Rozhansky et al., "The structure of the radial electric field in the vicinity of the separatrix and the L–H transition", *Contributions to Plasma Physics* **42** (2–4) (2002) 230–235
V.A. Rozhansky et al., "Impact of $\mathbf{E} \times \mathbf{B}$ drifts on the distribution of impurities in the tokamak plasma edge", *Journal of Nuclear Materials* **313–316** (2003) 1141–1149
V.A. Rozhansky et al., "Modelling of electric fields in tokamak edge plasma and L–H transition", *Nuclear Fusion* **42** (9) (2002) 1110–1115.

[29] R. Schneider et al., "B2–SOLPS5.0: SOL transport code with drifts and currents", *Contributions to Plasma Physics* **40** (3–4) (2000) 328–333
V. Rozhansky et al., "Perpendicular conductivity and self-consistent electric fields in tokamak edge plasma", *Contributions to Plasma Physics* **40** (3–4) (2000) 423–430.

[30] T.D. Rognlien et al., "A fully implicit, time dependent 2–D fluid code for modeling tokamak edge plasmas", *Journal of Nuclear Materials* **196–198** (1992) 347–351.

[31] M. Borchardt et al., "Numerics in BoRiS", in *Parallel Computational Fluid Dynamics* edited by K. Matsuno, A. Ecer, J. Periaux, N. Satofuka and P. Fox, (Elsevier Science, 2003) 459–465.

[32] M. Borchardt et al., "W7–X edge modelling with the 3D SOL fluid code BoRiS", *Journal of Nuclear Materials* **290–293** (2001) 546–550.

[33] J. Riemann et al., "Hierarchy tests of edge transport models (BoRiS, UEDGE)", *Journal of Nuclear Materials* **313–316** (2003) 1030–1035.

[34] A. Runov et al., "Benchmark of the 3–dimensional plasma transport codes E3D and BoRiS", *Contributions to Plasma Physics* **42** (2002) 169–174.

[35] J. Riemann et al., "Navier–Stokes neutral and plasma fluid modelling in 3D", *30th EPS Conference on Controlled Fusion and Plasma Physics, St. Petersburg* (2003) P–2.151.

[36] K.H. Finken et al., "Background, motivation, concept and scientific aims for building a dynamic ergodic divertor", *Fusion Engineering and Design* **37** (1997) 337–340
"Near field divertor structure of the helical perturbation current produced by the dynamic ergodic divertor", *Fusion Engineering and Design* **37** (1997) 379–383
"Considerations on diagnostics during operation with the dynamic ergodic divertor on TEXTOR–94", *Fusion Engineering and Design* **37** (1997) 411–415
"Particle, in particular helium removal experiments optimized by the dynamic ergodic divertor", *Fusion Engineering and Design* **37** (1997) 445–448.

[37] A. Runov et al., "Transport in complex magnetic geometries: 3D modelling of ergodic edge plasmas in fusion experiments", *Journal of Nuclear Materials* **313–316** (2003) 1292–1297.

[38] N.A. McTaggart, "Energy transport modelling including ergodic effects", *Contributions to Plasma Physics*, to be published.

[39] T.S. Hahm, "Nonlinear Gyrokinetic equations for tokamak microturbulence", *Physics of Fluids*, **31** (9) (1988) 2670–2673.

[40] M. Fivaz, S. Brunner, G. de Ridder, O. Sauter, T.M. Tran, J. Vaclavik, L. Villard and K. Appert, "Finite element approach to global gyrokinetic Particle-In-Cell simulations using magnetic coordinates", *Computer Physics Communication*, **111** (1998) 27–47.

[41] T.M. Tran, K. Appert, M. Fivaz, G. Jost, J. Vaclavic and L. Villard, "Global Gyrokinetic Simulation of Ion-Temperature-Gradient-Driven Instabilities using Particles", *Proceedings of the Joint Varenna-Lausanne International Workshop Theory of Fusion Plasmas 1998, ISPP–18, edited by J.W. Connor, E. Sindoni and J. Vaclavik, Bologna 1999*, 45–58.

[42] R. Hatzky, T.M. Tran, A. Könies, R. Kleiber and S.J. Allfrey, "Energy conservation in a nonlinear gyrokinetic particle-in-cell code for ion-temperature-gradient-driven modes in theta-pinch geometry", *Physics of Plasmas*, **9** (3)(2002) 898–912.

[43] G. Jost, T.M. Tran, W.A. Cooper, L. Villard and K. Appert, "Global linear gyrokinetic simulations in quasi-symmetric configurations", *Physics of Plasmas*, **8** (7) (2001) 3321–3333.

[44] S. Sorge and R. Hatzky, "Ion-temperature-gradient driven modes in pinch configurations within a linear gyrokinetic particle-in-cell simulation of ions and electrons", *Plasma Physics and Controlled Fusion*, **44** (11) (2002) 2471–2481.

[45] M. Kotschenreuther, "Numerical simulation", *Bulletin of the American Physical Society*, **34** (1988) 2107.

[46] S.E. Parker and W.W. Lee, "A fully nonlinear characteristic method for gyrokinetic simulation", *Physics of Fluids B*, **5** (1) (1993) 77–86.

[47] A.Y. Aydemir, "A unified Monte Carlo interpretation of particle simulations and applications to non-neutral plasmas", *Physics of Plasmas*, **1** (4) (1994) 822–831.

[48] C. de Boor, "A practical guide to splines", *Springer-Verlag* 2001.

[49] V. Kornilov and R. Kleiber and R. Hatzky and L. Villard and G. Jost, "Gyrokinetic global three-dimensional simulations of linear ion-temperature-gradient modes in wendelstein 7-X", *Physics of Plasmas*, submitted.

[50] S. Sorge, "Investigation of ITG turbulence in cylinder geometry within a gyrokinetic global PIC simulation: influence of zonal flows and a magnetic well", *Plasma Physics and Controlled Fusion*, **46** (3) (2004) 535–550.

Chapter 12

Plasma Technology

W. Jacob

12.1 Introduction

Apart from its basic physical importance as the "fourth state of matter", the plasma offers numerous technical or practical applications, which mostly are subsumed under the phrase **plasma technology**. Plasmas are used for, e.g. - *light production* (fluorescent lamps, arc light sources, gas lasers, plasma displays, etc.); - *electrical switches;* - *metallurgic applications* (melting and welding of metals); - *space propulsion;* - *chemical processing* and, as a major complex: - *treatment of surfaces by specific coatings or by erosion* (thin-film deposition, plasma spraying, dry etching).

The most widely used methods in surface treatment applications are the classical PCVD (plasma chemical vapor deposition) techniques for thin film deposition and dry etching in the patterning of silicon. Both fields rely heavily on the application of low-temperature plasmas.

Even a sketchily review of the basics of plasmas and some typical experimental set-ups would go far beyond the scope of this section. Therefore, the purpose of this section can merely be to discuss some basic concepts and point the reader to sources in the literature for further study.

A clear and comprising presentation of the basics of plasmas and their application in materials fabrication is given in the textbook by A. Grill [1]. Furthermore, a comprehensive introductory description of the basic glow discharge processes is provided in the textbook of B. Chapman [2]. A modern, in-depth discussion of the principles of plasma discharges and materials processing can be found in the textbook by Lieberman and Lichtenberg [3] or in the lecture notes of Chen and Chang [4]. RF discharges are discussed in in the textbook by Raizer et al. [5]. Recently, a compilation of lecture notes from a Summer School on *'Low-temperature Plasma Physics'* was published in the journal *'Plasma Sources Science and Technology'* containing among others a very nice compact introduction to gas discharges by Braithwaite [6], an introduction to RF discharges by W.J. Goedheer [7], and a review of various plasma sources by Conrads and Schmidt [8].

The following chapters give a short review of the various types of plasma discharges employed for technological plasma applications. Thereafter, a brief description of some

of these applications may illustrate the important role of low-temperature plasmas in modern industry.

12.2 Low-temperature Plasmas ("Gas Discharges")

In general, laboratory plasmas are produced and maintained by the input of electric power i.e. by the application of an electric field, which provides the acceleration of the charged particles. This electric field (applied voltage) can be either static (DC) or alternating (AC), where the latter could mean 'low' (e.g. standard line frequency 50 to 60 Hz) or 'high' (i.e. RF or microwave) frequency. The typical densities (i.e. neutral-, electron- and ion density) in gas discharges cover a wide range from very low values (e.g. 10^{14} m^{-3}) up to or beyond atmospheric particle density ($\sim$ a few times 10^{25} m^{-3}), corresponding to discharges approaching almost vacuum conditions (e.g. below microbar range) to more than 1 bar operational pressure. The electron temperatures remain low and are typically of the order of a few eV. For a definition of the basic plasma parameters see the chapter on *"Basic Plasma Physics"*. In the following, the most important types of different gas- or plasma discharges shall be shortly discussed.

12.2.1 Glow Discharge

A basic type of discharge is the **glow discharge**. Its immediate understanding may be obtained by the description of the breakdown process between two electrodes in a low-pressure (typically $\sim$ 1 mbar) gas background. This is the classical **Townsend** mechanism. If a high voltage is applied to these electrodes, an electron which might be produced by some external event (e.g. cosmic rays and natural radioactivity lead to $\sim 10^3$ ion-electron pairs in air) will be accelerated by the electric field towards the positive electrode. On its path, however, it permanently undergoes collisions with neutral gas molecules. These may be ionized, if the actual electron energy exceeds the ionization energy of the gas. This way, additional free electrons are produced and an avalanche process will result at sufficiently large electric field strength. This process is usually called *'gas amplification'*.

One electron at the cathode finally will produce N_e electrons, arriving at the anode. N_e is given by

$$N_e = 1 * e^{\alpha z} \tag{12.1}$$

where α denotes the **first Townsend coefficient** describing the number of ionization processes per unit length (meter) and z the path length of the electrons.

The avalanche processes now would occur one after the other - according to the external ionizing events - and the device would operate as a radiation counter only. Here we may ask, whether also a self-sustaining discharge could develop even from a single (first) avalanche. Such a continuous process indeed becomes possible by action of the $(N_e - 1)$ ions also produced in the avalanche. These ions are moving in a direction opposite to that of the electrons towards the cathode. The ionization of neutral gas atoms by ion impact (**second Townsend coefficient,** β is in most cases negligible because of the low ionization cross section of ions compared with that of electrons in the relevant kinetic energy range. Positive ions impinging on the cathode release in the average a number of

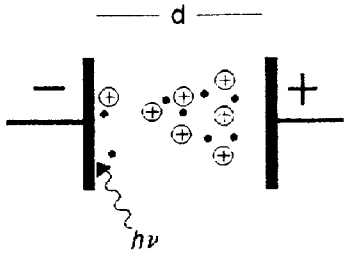

Figure 12.1: Schematic picture of a planar DC glow discharge.

γ new electrons. This process is named *'secondary electron emission"* (SEE). γ, i.e. the number of electrons per incident ion, is usually called the **third Townsend coefficient** (more generally it is known as *'secondary electron emission coefficient'*). Typical values for γ are of the order of 0.01 – 0.1. γ is a material constant; it depends on the cathode material, the energy fo the impinging ions, and the type of the ions, hence on the working gas. Figure 12.1 schematically shows the initiation process of such a glow discharge.

The avalanches can be visualized as a (continuous) flowing electric current through the electrode system, which can easily be formulated into:

$$I = I_0 \frac{e^{\alpha d}}{1 - \gamma(e^{\alpha d} - 1)} \tag{12.2}$$

where I_0 represents the externally (e.g. cosmic rays or radioactive decay) generated current. One recognizes the resonance denominator in the above equation, from which immediately the obvious breakdown condition

$$\left[1 - \gamma(e^{\alpha d} - 1)\right] \to 0 \quad \text{or} \quad \gamma e^{\alpha d} \approx 1 \tag{12.3}$$

can be derived.

In order to quantify this condition in more detail, the ionization coefficient α has to be analyzed. Here one has to notice first that the ionizing collision in a neutral gas background becomes a rather rare process for an electron: much more frequent are the encounters which occur **before** the electron has gained the energy needed for ionization. Expressed by a characteristic length for ionization $\lambda_{\text{ion}} = (n_0 \cdot \sigma)^{-1}, n_0$ neutral gas density and σ ionization cross-section, the respective length for inelastic encounters at lower energy like dissociation or excitation would be much shorter. The question of the remaining number of ionization events is then reduced to the probability problem: How many starting electrons are escaping such 'other' encounters and can achieve the full energy needed for ionization. The obvious result is that the number of ionizations per meter, i.e. the 'α-value', relates to the other encounters per meter, such as the exponential of the respective collision length (i.e. $\sim \exp - (\lambda_{\text{ion}}/\lambda_{\text{inel}})$).

The inelastic collision length λ_{inel} will depend on the kind of the gas and decreases inversely with gas density (or gas pressure p). Assuming further that ionization probability becomes unity for those (few) electrons which escaped other collisions (i.e. $\lambda_{\text{ion}} = E_{\text{ion}}/eE$; E_{ion} the ionization energy in eV), one obtains the relation for the Townsend coefficient α:

$$\alpha/p = k_1 \cdot e^{-\frac{\lambda_{\text{ion}}}{\lambda_{\text{inel.}}}} = k_1 \cdot e^{-\frac{k_2}{E/p}} \tag{12.4}$$

The characteristic dependence of the coefficient α as function of the electric field is to be seen in Fig. 12.2:

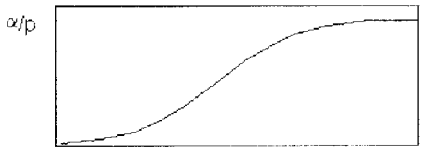

Figure 12.2: Characteristic dependence of the first Townsend coefficient $\alpha(/p)$ on the electrical field strength $E(/p)$.

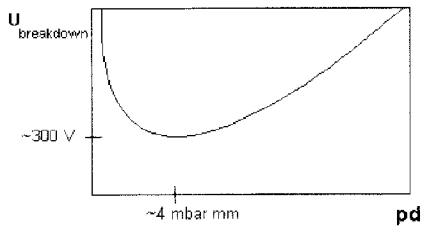

Figure 12.3: Breakdown voltage as function of the parameter pd for a typical working gas (e.g. hydrogen) $\longrightarrow$ **Paschen curve**.

Inserting α into the breakdown condition ($\gamma e^{\alpha d} \sim 1$) leads to the well known **Paschen law** for the breakdown voltage:

$$Ed = U_{\text{breakdown}} = \text{const} \cdot pd \cdot \frac{1}{lnp - lnln\gamma} \tag{12.5}$$

The corresponding **Paschen curve** is shown in Fig. 12.3:

According to the above simplified treatment of the breakdown process, the discharge current would go to infinity at breakdown condition (see eq. (12.3)). In reality, however, a stable discharge operation (**normal glow discharge**) may be achieved even at "zero" source resistance. This can be understood from the space charge effects which extinguish the applied electric field over a large region in front of the anode (**positive column**). The result is a strong potential drop between a "virtual anode" and the cathode (**cathode fall**), which is required in order to drive and accelerate the heavy ions for their two functions: 1) to carry almost the whole current near the cathode and 2) to release the electrons from the electrode surface ("γ effect").

The entire mechanism can best be explained by visualizing the process towards the **normal glow discharge** in a time sequence of increasing applied voltage or discharge current, as depicted in Fig. 12.4. Starting from a somewhat lower voltage (current) – point a_0, "virtual anode" not yet developed – this "anode" moves continuously towards the cathode $[t(a_0) < t(a_1) < t(a_2)]$) with the result of a corresponding increase of the E field in front of the cathode.

According to the above diagram the glow discharge obviously has two stationary operational points, where the "gas amplification" just balances the electron and ion losses to the electrodes (i.e. the value $\gamma e^{\alpha d^*}$ tends $-- > 1$). The first point at low current (a_0) is unstable and can be operated with an accordingly large series resistor only (**subnormal glow discharge**). The third point (a_2) corresponds to the situation where the "virtual anode" is already moved very close to the cathode. At this position the coefficient α is further increased, which, however, is overcompensated by the small effective electrode distance d^* to such an extent that the product αd^* is sufficiently reduced in order to provide $\gamma e^{\alpha d^*} = 1$. This behavior can directly be inferred from the S-shaped α over E curve shown in Fig. 12.2.

The operational point at the higher current has a positive characteristic (dU/dI>0) and is therefore stable. In this "normal glow" mode the discharge current varies strongly with even small voltage change (see Fig. 12.5) until the whole electrode area is covered

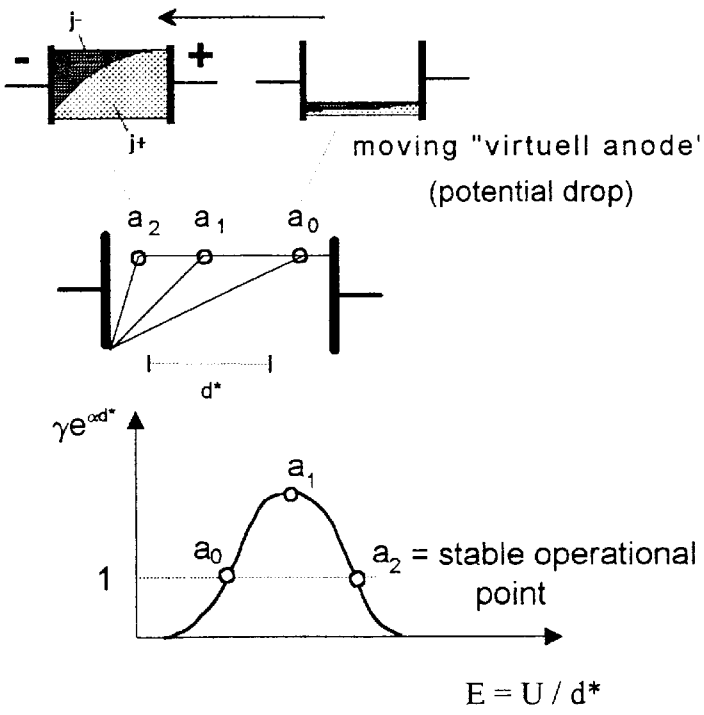

Figure 12.4: Formation of a "virtual anode".

"Gas amplification" as function of anode position d^*.

by the discharge. After that point a significant voltage increase is needed to increase the current further (region of **anomalous glow**). Finally the glow alters into the **arc discharge**.

12.2.2 Arc Discharge

The basic characteristic of the arc is the replacement of the secondary electron emission ("γ effect") by a much more efficient mechanism: the **thermal emission** of electrons from a sufficiently hot surface. The required cathode heating simply is the result of the increased current density at the transition from a glow discharge to a **low-pressure arc**. Arc discharges, however, can also be operated at very high densities (**high-pressure arc**). In this case the discharge can be produced by a transient contact of the electrodes or it may be initiated by an initial high-voltage breakdown (**spark discharge**) to be discussed later. A typical feature of the arc is its falling U/I-characteristic which requires a sufficiently large series resistor in order to provide a stable operational point.

12.2.3 Typical Plasma Parameters of Glow- and Arc Discharges

The typical operational range of both discharge types is shown by the U/I diagram of Fig. 12.5.

According to the figure the plasma current covers a range of 8 orders of magnitude for the transition of a *"subnormal"* – *"normal"* and *"anomalous glow discharge"* to the (low-pressure) *arc discharge*. Common feature for the entire regime is the **non-thermal** plasma state, i.e. a high temperature of the electrons – typically a few eV – and a low temperature of the ions (and neutrals) – a few hundred centigrade at most – in the bulk plasma. This is a result of the small energy transfer from the light electrons to the heavy particles, characterized by $\tau_{ei} \gg \tau_p$; (τ_{ei} the energy equiparticipation time and τ_p the

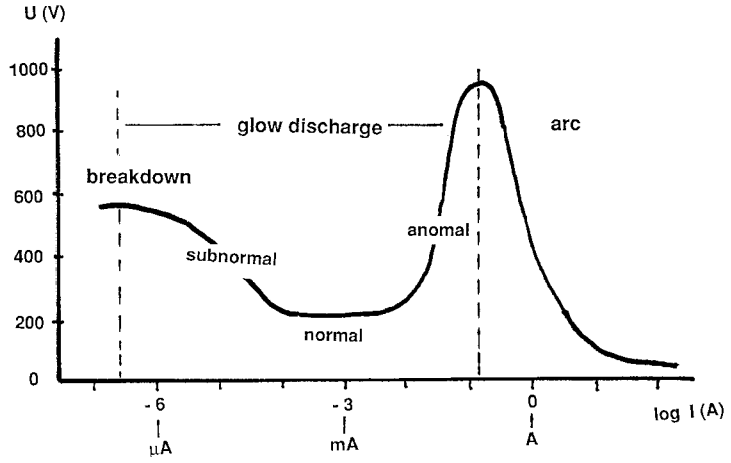

Figure 12.5: Current-voltage characteristic of a DC discharge.

heavy-particle confinement time). Energetic ions, however, are present at the cathode according to the respective cathode fall (as discussed before).

A **thermal** plasma, on the other hand, exists in the *high-pressure arc*, where the high collisionality (i.e. $\tau_{ei} \ll \tau_p$) provides almost equal temperatures of all species ($T_e \sim T_i \sim T_0 \sim 1 - 1.5$ eV).

12.2.4 Spark, Corona, and Barrier Discharge

These three types of discharges have the following three common characteristics:

- High (typically atmospheric) gas pressure
- high voltage,
- instationary (pulsed) mode of operation.

The common physical basis of these discharges is the **streamer mechanism**, which gives an alternative to the electron-induced avalanche of the glow discharge breakdown. Starting point of the streamer is similar, i.e. ionizing encounters by a single somehow produced electron. Owing to a (sufficiently) high gas density, however, the head of the avalanche achieves high plasma density and emits now a large amount of energetic photons. These photons are then reabsorbed in the dense gas where they provide new volume ionization and thus give the starting point of new "daughter avalanches". Electric field distortion due to ion accumulation in the streamer head thereby supports the mechanism (see specific literature).

As a result high-voltage breakdown between electrodes may be performed within the 10 nanosecond time scale. When the streamer channel is established, **spark breakdown** will be followed by a high-current discharge (arc) provided that the appropriate power source is available (e.g. capacitor, low impedance generator).

Somewhat different is the development in **corona-** and **barrier discharge**. In the first case a very inhomogeneous electric field (e.g. that of a high-voltage power line) is the prerequisite for the occurrence of a **corona**. In the high electric field of a peaked electrode (wire) breakdown conditions are given and streamers will start. Due to the

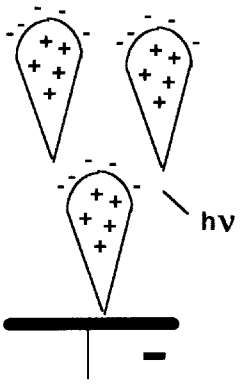

Figure 12.6: Schematics of streamer mechanism.

vanishing field in some distance, however, the streamer dies out. The electric current, nevertheless, continues to flow and is carried over the major part of the gap towards the ground by the generated ions. Corona discharges can occur between a positive or negative electrode and ground. Depending on polarity the heavy charge carriers then are *positive (molecular) ions* or *negatively charged molecules*, respectively (the latter formed by electron attachment).

Also in the **barrier discharge** a further development of a streamer into an arc is hindered, which in this case is achieved by an insulating coverage of one (or both) high-voltage electrodes. The discharge now forms a current channel (typically few ampères) but is terminated when the (insulating) surface is charged up after a few ten nanoseconds. Well-known example of a barrier discharge is the small sparking which usually appears when combing (dry) hair. It is interesting to note that due to the short discharge duration a **non-thermal, but dense** plasma is formed in this way in spite of the high collisionality at atmospheric pressure. This feature, i.e. high plasma density and electron temperature ($T_e \sim 5 - 10$ eV) in combination with cold ions and neutrals ($\sim$ "room temperature"), makes the barrier discharge very interesting for plasma chemical applications (see section 12.4).

12.2.5 RF- and Microwave Discharges

A further important and interesting variety of low-temperature discharges can be produced by RF- or microwave application. For an easy insight into this specific field we may consider the RF energy input into plasma, or – more precisely – into the plasma electrons, which follows immediately from their equation of motion in the presence of an oscillating electric field:

$$m_e\ddot{x} + \nu_{\text{coll}}\ (m_e\dot{x}) = e \cdot E_0 \cdot \exp(i\omega t) \tag{12.6}$$

where collision frequency ν_{coll} multiplied by the momentum $(m_e\dot{x})$ represents the frictional force acting on the electrons. The equation can easily be integrated to give the (complex) electron velocity $\dot{x}$. Multiplied by charge e and electron density n_e yields the (also complex) current density j. The power input per volume then results from the product of the real parts of current density and electric field $Re|E| = Re|E_0 \exp(i\omega t)|$. After short calculation there results:

$$P_{\text{abs}} = Re[j] \cdot Re[E] = \frac{n_e e^2}{m_e}\frac{E_0^2}{2\nu}\left\{\frac{\nu^2}{\nu^2+\omega^2}\right\} \tag{12.7}$$

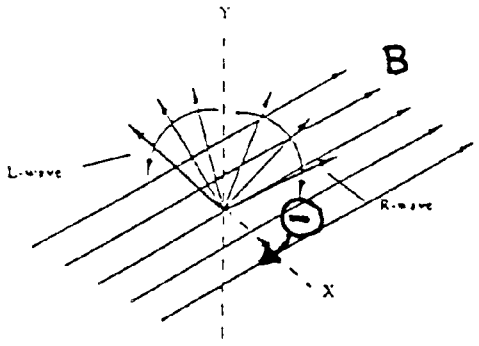

Figure 12.7: Right- and left-hand polarized wave and electron gyromotion.

From this relation one recognizes a few features of (collisional) RF power absorption:

- The absorbed power increases quadratically with the electric field present in the plasma volume.
- Absorption needs a finite number of collisions with a maximum at $\nu \sim \omega$. For ν below this optimum P_{abs} decreases $\sim \nu$ and above – at high collisionality – $\sim 1/\nu$, respectively.
- At low collision rates (i.e. $\nu^2 \ll \omega^2$) high frequency becomes inefficient due to the ω^2 term, which now determines the denominator. (It has to be noted, however, that microwaves can produce much larger electric fields in a plasma volume, see chapter on wave propagation!)

Microwave application is of specific interest in combination with a magnetic field superimposed on the plasma. The most interesting case, where the microwave is propagating in the direction of the magnetic field, may be considered here. For these conditions a primarily linearly polarized wave splits into the two pertaining eigenmodes, i.e. a left- and right–hand polarized wave (see "wave propagation in a magnetized plasma"). The electric field vector of the right-hand wave **("R-wave")** rotates in the same direction as the also righ-hand gyrating electrons, which now "see" the E-field at reduced frequency $\Delta\omega = (\omega - \omega_{ce}), \omega_{ce}$ the electron gyrofrequency ($= eB/m_e$) (Fig. 12.7).

In the denominator of eq. 7 ω^2 has to be replaced by $\Delta\omega^2$ and of particular interest now becomes the resonance condition $\Delta\omega = 0$ (electron cyclotron resonance (**ECR**). One recognizes that the resonant power absorption, $P_{\text{abs,ECR}}$, increases in proportion to $1/\nu$ providing rather effective plasma production and heating in a low-density plasma.

This becomes evident from Fig. 12.8, where the power absorption is as function of the normalized collision frequency is compared for resonant and non-resonant (i.e. no magnetic field) conditions. Also shown in the figure are cases with various distances $\Delta\omega/\omega$ from resonance. The pressure scale below corresponds to the most convenient microwave frequency of 2.45 GHz, i.e. 875 mT resonance field. This quite efficient resonant electron heating, by the way, can be understood from the fact that the gyrating electrons become accelerated by a DC-field in its frame of reference.

This acceleration (and resulting energy gain) continues until the electron is stopped by a collision. This also explains why the ECR effect vanishes when the collision already occurs after one cycle (i.e. $\nu \sim \omega$).

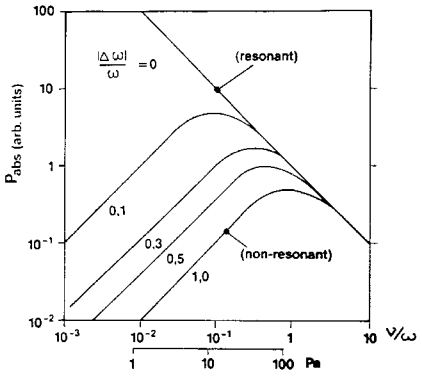

Figure 12.8: Microwave power absorption at ECR and various distances $\Delta\omega/\omega$ from resonance.

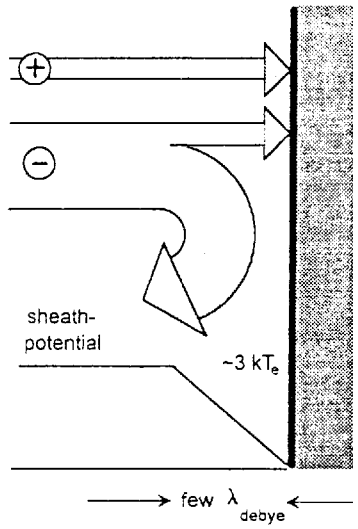

Figure 12.9: Schematics of edge fluxes and edge potential.

12.3 Plasma Boundary, Plasma-Surface Transition

Any laboratory gas discharge is bounded by some material wall where the hot plasma comes in contact with a cold (solid) surface. At this transition the plasma parameters are changing drastically, and a so-called **sheath** is being formed. The "sheath effects", especially the resulting acceleration of the plasma ions onto the (substrate) surface are of extreme importance for plasma-surface and thin-film technologies and have thus to be discussed at least briefly. Here we may start with the simple picture of a solid conductive body instantaneously inserted into a plasma. In the first moment a strong flux of electrons will hit its surface due to their much larger velocity compared to that of the ions.

($v_e/v_i = (m_i T_e/m_e T_i)^{1/2}$, i.e. $\sim$ 0(100) at least). After a short time, however, the plasma will become positively charged to such an extent that electron and ion fluxes are equal. From now on an **ambipolar** flux of particles leaves the plasma consistent with the request of **quasi-neutrality** $n_e \sim n_i$. In order to adjust both fluxes, a potential drop must appear which retracts the major part of electrons and allows further outflow above a certain velocity $v_{\min}$ only. The resulting edge potential immediately follows from the electron distribution function $f(v_e)$ in the direction normal to the surface, e.g. in the x-direction.

$$\Gamma_i = n_i v^i_{\text{bulk}} \tag{12.8}$$

$$\Gamma_e = n_e(x) \int_{v_{\min}}^{\infty} (v^e_x) dv^e_x \tag{12.9}$$

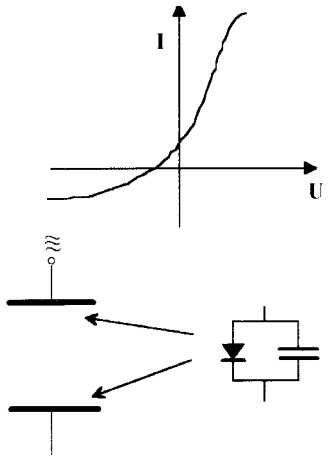

Figure 12.10: Langmuir characteristic and the resulting electric equivalent circuit of the RF boundary.

e.g. with Maxwell distribution results for the sheath potential:

$$U_s = \frac{kT_e}{2e} ln\left\{\frac{1}{2\pi}\frac{m_i}{m_e}\right\} \approx 3\ldots4 \cdot kT_e \qquad (12.10)$$

At typical electron temperatures of a few eV a potential of typically 20 – 30 V will appear at a plasma-surface transition acting as efficient ion accelerator towards a substrate. The corresponding low-energy ion fluxes are important for many technical applications. If the substrate surface simultaneously acts as DC- or RF electrode, the situation changes and ions with much higher energies will occur. In the first case (DC-discharge) the cathode fall leads to ion energies in the 100 eV range at the negative electrode. In an RF discharge the "sheath rectification" also yields a potential of the order of the applied RF voltage.

This latter effect can be understood by the diode characteristic of the plasma-surface transition at frequencies below the ion plasma frequency. (Theory of a Langmuir probe; for explanation see also Fig. 12.10.)

In summary, the plasma-solid transition exhibits a wide range for the actual value of surface potential, depending on the mode of operation, i.e. the "ambipolar potential" of $\sim 3 - 4\mathrm{kT}_e$, in a field-free or microwave ($\omega > \omega_{pi}$) plasma, and a high potential drop in the cathode fall of a DC or in an RF discharge (typically in the several 100 V range). This variety opens the possibility for different important technical applications of plasma surface treatment, as discussed in the next chapter.

12.4 Examples of Technical Plasma Applications

Low-temperature plasmas presently are already being used in numerous technical and practical applications, for example (TP = thermal NTP = non-thermal plasma):

Light production

high-pressure arcs (TP)	.....for intense light sources
low-pressure arcs (NTP)	for room illumination, e.g. modern fluorescent lamps
gas lasers (NTP)	.....e.g. CO_2-, ion-excimer lasers
plasma display (NTP)	..... flat screens for PC's

Electric switching

vacuum switch (NTP) ..... ~ 10 kA circuit breakers in HV systems
high-pressure switches (TP) .... e.g. SF_6 switch in high-power transmission lines
"standard" switches,
automatic fuses (TP) .....domestic applications

Space propulsion

RF plasma sources (NTP) .....engines with low mass consuming propulsion
.....meanwhile used for fusion plasma heating
.....(NBI ion sources)
....also used for ion implantation in semiconductors

Thermal treatment

plasma arcs, "torches" (TP) ..... welding, melting in large-scale applications
.....(up to 150 MW units for steal production)
..... **new** toxic waste disposal

Electro filtering

corona discharge (NTP) .....dust filtering in fossil power stations

Plasma Chemistry and Plasma Surface and Thin-Film Technology:
Because of their specific importance, these two fields of plasma technology shall be discussed in some more detail.

Plasma Chemistry:
This topic involves chemical reactions which in some cases can only be achieved via the plasma state. The plasma chemical process can be performed in **two ways:**

- Molecules to be modified are fed into a **thermal plasma** (e.g. high-pressure arc or RF plasma) and are completely destroyed. After having left the plasma zone the atoms (ions, radicals) are cooled down in a specific way ("quenched") in order to give the desired reaction (product), i.e. the chemical reaction happens outside the plasma. The process inherently allows a **large mass throughput**. (Example: acetylene production from methane in ~ 10 MW high-pressure arcs).

- Chemical reactions are performed **within** a low-pressure **non-thermal plasma**. In this case the energetic plasma electrons initiate chemical reactions with high efficiency ($kT_e \sim$ chemical binding energy!), created compounds need, however, to be sufficiently stable in order to be extracted from the system. Such dry chemical process gives access to a new, more sophisticated chemistry. As a major drawback, on the other hand, the production rate usually remains quite small due to the low-density operation.

Here the specific combination of a **dense but non-thermal plasma** has to be noticed, which is achieved in the ultra-short pulses of a barrier (or corona) discharge at high pressure. Such barrier discharge reactors (in MW units) are already in operation for large-scale ozone production (e.g. for the sterilization of drinking water). The principle arrangement of a single subunit is shown in Fig. 12.11:

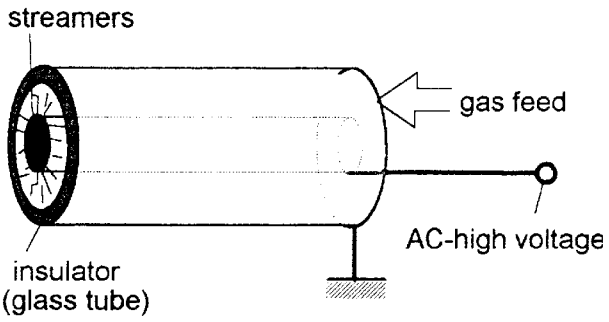

Figure 12.11: Schematics of a coaxial barrier discharge reactor for ozone production.

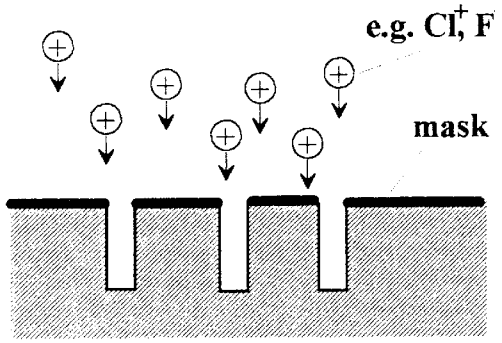

Figure 12.12: Anisotropic etching by energetic ions.

High-frequency (several 10 kHz) high-voltage reversal provides a large number of individual streamers per area and time and thus a rather high production rate of ozone. Such dense non-thermal plasmas seem to have a large potential for other chemical applications too, since the – in most cases – insufficient production rates of (non-thermal) low–pressure plasmas may be increased substantially by this technology.

Plasma Surface and Thin-Film Technology

Surface treatment by non-thermal plasma presently offers the obviously most important technical plasma applications. These techniques include surface modifications by **erosion** or **etching** and thin-**film** deposition as well and the world market of the resulting products already has exceeded a several 100 billion $ range. In the following a few most important applications of plasma surface treatment can be given only:

- Plasma etching meanwhile is a prerequisite in the area of modern microelectronics since it provides the tool for the desired sub-micron structuring necessary for highly integrated circuits. The basic principle relies on the impact of ions (see Fig. 12.12) accelerated in the plasma-edge potential towards the substrate, as discussed in the previous section. Reactive ions hit the surface and remove material at positions which are not shielded by the mask (i.e. material of less erosion). Important for the desired 1-dimensonal etching is the highly directed velocity of the ions normal to the surface. (In practice the desired highly anisotropic etching of submicron structures additionally needs the transient coating (= passivation) of the sidewalls by a hydrocarbon layer, which is achieved by an appropriate gas mixture.)

- Depending on process gas and parameters **material** can also be **deposited** by plasma discharge treatment. Such thin-film deposition has numerous areas of application, for example:

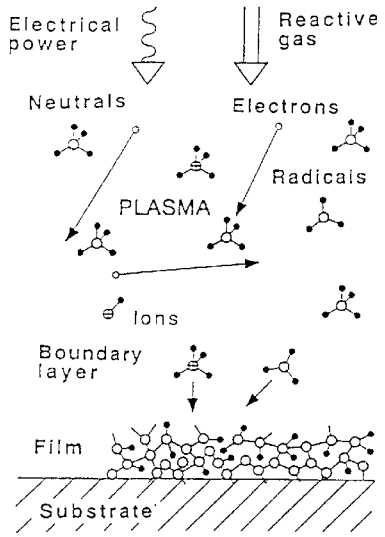

Figure 12.13: Particle fluxes onto a plasma exposed surface (for the example of an CH_4 discharge.

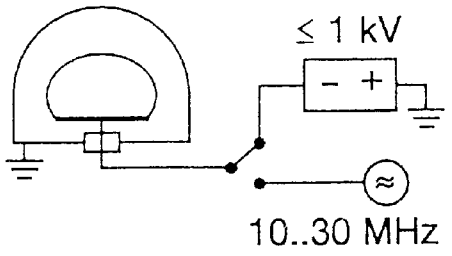

Figure 12.14: (a) Standard setup of a DC-/RF reactor

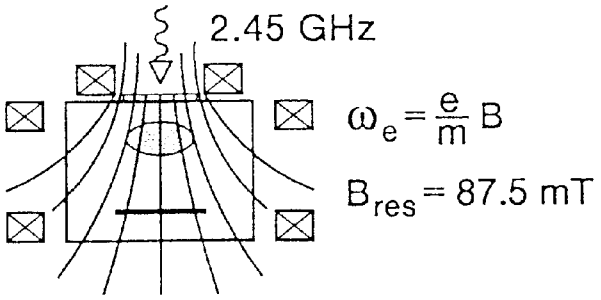

Fig. 12.14 (b) ECR microwave reactor.

- hard coatings for surface protection (e.g. hard carbon (a-C:H), diamond layers)
- corrosion protective layers (e.g. SiO_2, SiON)
- decorative layers (e.g. TiN "gold layers")
- coatings for reduced friction ("tribological layers")

and so-called *"functional layers"*:

- membrane layers (e.g. for alcohol-water separation)
- diffusion barriers (e.g. for food packaging)
- resistive, capacitive layers
- optical transparent, conductive layers
- (indium-tin-oxide (ITO) layers in photo cells)
- photovoltaic layers (e.g. a-Si:H)
- layers for magnetic data storage, etc.

The growth of films of specific composition and features is a quite complicated and in many examples not yet completely understood process. Basic element is the synergism

of chemically active radicals and energetic ions impinging the surface. Especially the ion energy is important for the individual process and its optimum value may range from some 100 eV (for amorphous hard carbon films) to a few 10 eV (e.g. a-Si:H) or a few eV (e.g. diamond, SiO_2, SiON).

The appropriate plasma conditions can be achieved with the various types of DC-, RF- and microwave discharges, where the latter especially allows the production of (for many processes required) low-energy ions in combination with a high plasma density. (In DC and RF discharges ion energies are above the 100 eV range and are further increasing if the plasma density is pushed by higher voltage operation.)

The sheath growth itself in most cases then becomes a result of a possibly small difference between erosion and deposition. In specific examples, such as diamond deposition, an enormous re-etching (in this case of the transiently bond hydrogen) is necessary for the desired process result.

Figure 12.14 finally shows typical examples of process reactors for DC-/RF- (Fig. 12.14a) and microwave applications (Fig. 12.14b), in this case with superimposed magnetic field to provide ECR condition.

For many applications, however, the standard devices are not satisfactory with respect to deposition velocity, homogeneity, and/or substrate size. Here intensive research is necessary in order to transfer a laboratory process to industrial large-scale application without quality reduction. Some newly developed plasma configurations seem to promise success in that direction (e.g. film deposition with 200 m^2 per hour at 2 – 3 m substrate dimensions). Their detailed discussion would exceed the scope of this brief introduction into plasma technology.

Bibliography

[1] A. Grill, *'Cold Plasmas in Material Fabrication, from Fundamentals to Applications'* IEEE Press, New York, 1994.

[2] B. Chapmann, *'Glow Discharge Processes'*, Wiley, New York, 1980.

[3] M.A. Lieberman, A.J. Lichtenberg, *'Principles of Plasma Discharges and Materials Processing'*, Wiley, New York, 1994.

[4] F.F. Chen, J.P Chang, *'Lecture Notes on Principles of Plasma Processing'*, Plenum/Kluwer Publishers, Dordrecht, 2002 (ISBN 0-306-47497-2).

[5] Y.P. Raizer, M.N. Shneider, N.A. Yatsenko, *'Radio-frequency Capacitive Discharges'*, CRC Press, Boca Raton (USA), 1995.

[6] N.St.J. Braithwaite, *'Introduction to Gas Discharges'*, Plasma Sources Sci. Technol. **9** (2000) 517-527.

[7] W.J. Goedheer, *'Lecture Note on RF Discharges DC Potentials, Ion and Electron Energy Distributions'*, Plasma Sources Sci. Technol. **9** (2000) 507-516.

[8] H. Conrad, M. Schmidt, *'Plasma Generation and Plasma Sources'*, Plasma Sources Sci. Technol. **9** (2000) 441-454.

Chapter 13

Plasma Wall Interaction in Nuclear Fusion Devices

Karl Krieger

13.1 Overview

A major issue for design and construction of a nuclear fusion reactor with a magnetically confined plasma is the interaction of the hot plasma with the material components of such a device. On the one hand, the plasma facing vessel components represent a sink for energy and particles released by the plasma. On the other hand, the particle bombardment of the material surface may lead to release of wall atoms and of previously implanted fuel atoms which in turn may enter the plasma.

The contamination of the plasma by impurities released from the vessel structure is one of the main problems caused by plasma wall interaction processes. An additional problem is the alteration of the material structure by the particle bombardment and the high energy flux which may limit the lifetime of the plasma facing components significantly. These problems must be solved under the constraint that the generated power has to pass through the vessel components at some location. The wall may further act as a reservoir for the hydrogen fuel isotopes leading to an uncontrollable additional source of fuel atoms, which may cause problems in maintaining stationary discharge conditions.

In the following we will first introduce a basic model of the edge plasma region in contact with the walls, the so-called scrape-off layer (SOL). Then the basic interaction processes between plasma and material walls will be discussed. This includes in particular wall erosion processes leading to impurity production and mechanisms involved in the formation of hydrogen wall inventories and the corresponding recycling processes. Finally, the main diagnostic methods for investigation of plasma wall interaction processes will be discussed.

13.1.1 Plasma facing components

In a fusion reactor, we find several components facing the plasma directly. The largest surface consists of the first wall which surrounds the bulk region of the plasma torus. The plasma shape may be restricted by additional limiters to protect the vessel wall or equipment like antennas for radio-frequency heating which cannot withstand excessive heat loads. Finally, a very important part of the plasma facing components in current and future fusion devices are the divertor target plates. In a diverted plasma configuration these plates provide the main plasma-surface interaction zone. The fraction of the fusion power carried by the produced α-particles is coupled out to a large extent through these areas.

Fig. 13.1 shows poloidal cross-sections of a limiter type (a) and a divertor type (b) plasma configuration. In a divertor configuration the distance of the plasma wetted surface areas to the confined plasma region is much larger than for limiter configurations. Due to the correspondingly lower penetration probability of eroded material, it is much easier to maintain a low impurity level in diverted plasma discharges.

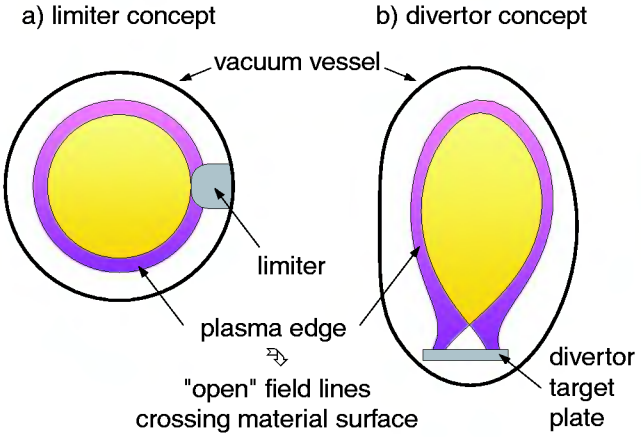

Figure 13.1: Poloidal cross-section of a limiter type (a) and a divertor type (b) plasma configuration with principal plasma facing wall components.

13.1.2 Bombardment of the walls with plasma particles

If the plasma is in direct contact with wall components, electrons and ions will hit the surface. This particle bombardment leads to release of atoms by collisions and, for certain materials by chemical reactions. In addition the wall material will be heated by the corresponding energy transfer. Finally, electron impact may produce secondary electrons which are reemitted back into the plasma.

The incident plasma ions will be neutralized with a fraction of them being reflected, while the remaining part will be implanted and may be released with some delay. Neutralized particles entering the plasma are ionized again by electron impact or by charge exchange processes with plasma ions. Charge exchange processes in hot plasma regions will produce neutral particles at high energies, which can escape the plasma hitting also plasma facing components without direct plasma contact. high energetic particles and about one half of these will hit the walls again and might be reemitted with some probability.

In fusion plasmas facing components are also subject to intense irradiation by neutrons, which leads to modifications of the material structure and to corresponding degradation of mechanical stability and thermal conductivity.

Wall atoms eroded by the particle bombardment and, in case of excessive heat loads, by evaporation processes, will enter the plasma as impurities with detrimental effects on plasma performance. The erosion of wall surfaces will also limit the lifetime of the respective components. The eroded material will, however, migrate through the plasma until it is finally redeposited, which may balance the erosion to a certain extent.

13.2 The scrape-off layer

As shown in Fig. 13.1 the plasma edge in a magnetically confined plasma is either defined by a material limiter or, in the case of a diverted plasma, by a magnetic separatrix (see Fig. 13.2). Inside the so defined boundary, the magnetic surfaces are closed while in the region between the boundary and the wall surface, the so called scrape-off layer, the field lines intersect material components. The particle exhaust and the α-particle fraction of the produced power (as well as the additional heating power during start-up) are coupled out to a large extent through this region and transferred to the limiters or divertor plates.

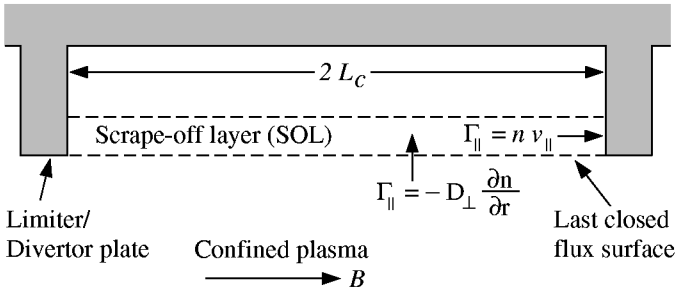

Figure 13.2: Schematic view of the scrape off layer in a magnetically confined plasma [J. Wesson, Tokamaks, 1996, p.424]. a is the minor plasma radius, B is the magnetic field, L_c is the connection length, $\Gamma_{\perp}$ is the diffusive flux of particles perpendicular to B and $\Gamma_{\|}$ is the flux of particles streaming along B.

The variation of plasma density and temperature in the scrape-off layer as a function of the minor radius can be approximately described by an exponential decay. Using a simple model of particle balance with purely diffusive transport perpendicular to the magnetic field and sonic flow along the field lines, one can estimate the decay length λ_n as a function of the perpendicular diffusion coefficient, $D_{\perp}$, and the ion sound velocity, c_s. The rate $\dot{N}_{\perp}$ of particles per unit poloidal length W diffusing across the separatrix into the SOL must be equal to the rate $2\dot{N}_{\|}$ of particles per unit poloidal length streaming along the magnetic field lines towards the 2 limiters or target plates. $\dot{N}_{\perp}$ and $\dot{N}_{\|}$ are given by

$$\begin{array}{lllll} \dot{N}_{\perp} = D_{\perp} \frac{\partial n}{\partial r}\big|_{r=a} L_c W & = D_{\perp} \frac{n(a)}{\lambda_n} L_c W & = \Gamma_{\perp} L_c W & \text{and} \\ \dot{N}_{\|} = \int_a^{\infty} n(a) exp(-(r-a)/\lambda_n)\, dr\, c_s W & = n(a) c_s \lambda_n W & = \Gamma \lambda_n W & \end{array} \qquad (13.1)$$

where $2L_c$ is the connection length and $c_s = \sqrt{(T_e + T_i)/m_i}$. Solving $\dot{N}_\perp = 2\dot{N}_\parallel$ one obtains an exponential decrease of n with a characteristic decay length of $\lambda_n = \sqrt{D_\perp L_c/c_s}$. A similar analysis holds for the temperature assuming convective energy transport. Inserting typical parameters ($D_\perp = 1\,\mathrm{m}^2/\mathrm{s}$, $L_c = 10 - 100\,\mathrm{m}$, $T_{e,i} = 10 - 100\,\mathrm{eV}$), one obtains a decay length in the range from 1–5 cm which is in good agreement with measured values. The decay length of the power flux is smaller because it is determined by the product of n and T.

Since the total energy and particle flux leaving the plasma is concentrated in a very narrow region of the target plates, the incident flux will be strongly amplified over the flux across the plasma boundary. Assuming a circular shaped plasma torus with major radius R and minor radius a, one obtains a torus surface of $4\pi^2 aR$. The plasma wetted surface of a divertor or limiter in contact with the plasma boundary is $2\pi R\lambda$. The radial flux crossing the boundary of the confined plasma is therefore amplified by the ratio of these surfaces $\pi a/\lambda \simeq 100$ with $a = O(1\,\mathrm{m})$ and $\lambda = O(1\,\mathrm{cm})$. For a fusion machine like ITER, the α-particle heating power is $\simeq 200\,\mathrm{MW}$. With a major plasma radius of $\simeq 6\,\mathrm{m}$ one obtains a heat flux at the target plates of $\simeq 100\,\mathrm{MW/m^2}$, which exceeds by far the engineering limits of any material. It is therefore necessary, to distribute the power to a larger area of the vessel, for example by increasing edge radiation from impurities and charge exchange processes.

13.3 Electric coupling of plasma and wall

When the magnetic field intersects a solid surface, the surface will charge up negatively with respect to the plasma. Consider a small plasma cube with one side limited by a wall and with electrons and ions in thermodynamic equilibrium i.e. with a Maxwellian velocity distribution. For the particle flux to the wall one obtains $\Gamma_e = n\bar{v}_e/4$ and $\Gamma_i = n\bar{v}_i/4$. With $\bar{v} = \sqrt{8kT/\pi m}$ one sees readily that $\Gamma_e = \Gamma_i\sqrt{m_i/m_e} \gg \Gamma_i$. A repelling potential for the electrons will build up until the fluxes are balanced which is necessary to maintain the quasi neutrality of the plasma. Because of the screening effect of the plasma, the potential is restricted to a sheath with a width of some Debye lengths $\lambda_D = \sqrt{kT_e/4n_e^2}$.

To determine the value of the potential, we consider the balance of ion and electron flux along the field lines. The ions enter the electrostatic sheath with ion sound velocity, thus $\Gamma_i = nc_s$. The electron flux to the wall is modified by the sheath potential:

$$\Gamma_e = \frac{n_e}{4}\sqrt{\frac{8kT_e}{\pi m_e}}\,\exp\,(-e\Phi/kT_e). \tag{13.2}$$

The electron hitting the wall material will produce secondary electrons which reenter the plasma with a flux $\Gamma_{es} = -\gamma\Gamma_e$ with γ being the secondary electron emission coefficient. From the balance of ion and electron flux $\Gamma_i = (1-\gamma)\Gamma_e$ we obtain

$$e\Phi = -\frac{kT_e}{2} ln\left(\frac{2\pi m_e}{m_i}\left(1+\frac{T_i}{T_e}\right)\frac{1}{(1-\gamma)^2}\right). \tag{13.3}$$

For a cold hydrogen plasma ($\gamma \ll 1$) with $T_i \simeq T_e$ one obtains $\Phi \simeq 3kT_e/e$. Obviously, if γ increases, the argument of the logarithm will increase as well and become undetermined

for $\gamma = 1$. In reality, for $\gamma \geq 0.8$, an electron space charge layer will form at the surface inhibiting any further secondary emission. In that case, the equation above does not hold anymore.

Because only the fast electrons will reach the wall, the electrons are cooled in the sheath. The ions, however, gain additional energy because they are accelerated in the sheath potential. For a Maxwellian plasma the energy flux in one direction is given by $Q = 2kT\Gamma$. The convective energy fluxes to the wall surface are then given by

$$Q_e = 2kT_e\Gamma_e = 2kT + e\frac{\Gamma_i}{1-\gamma} \qquad Q_i - \left(2kT_i + \frac{kT_e}{2} - e\Phi\right)\Gamma_i \tag{13.4}$$

where the contribution of $kT_e/2$ for the ions has it's origin by an additional acceleration in a pre-sheath potential drop. Obviously, the major part of the energy flux is deposited by the ions because of the acceleration by the sheath potential. With increasing edge temperatures the secondary electron emission may come closer to 1, thus leading to very high energy fluxes to the wall through the electron channel.

In addition the energy deposition is increased by the neutralization energy of the ions and, for hydrogen, by the recombination energy of the hydrogen atoms.

13.4 Hydrogen fuel cycle

The hydrogen isotopes used as fuel for nuclear fusion interact with most of the relevant reactor materials. This is important in particular because of:

- radiological reasons: the storage of tritium in the first wall is responsible for the major fraction of the tritium inventory in fusion reactors;
- engineering aspects: hydrogen in solids may alter their mechanical properties in an unfortunate way;
- density control of the plasma: the hydrogen inventory in the walls during a stationary discharge will be much higher than the hydrogen content of the plasma itself, leading to possible difficulties in maintaining a stable plasma density.

At low plasma temperatures, neutral atoms and ions hitting the wall will usually be reflected after transferring a part of their kinetic energy to the material.

For high plasma temperatures, the particles can penetrate deeply into the material. In this case, the recycling of the particles will be determined by kinetic reflection, but in addition, the particles may be implanted and reemitted after diffusion back to the surface. In the following, these processes will be discussed in more detail.

13.4.1 Reflection

Ions and neutral particles hitting the wall material will not be reflected right at the solid surface. Usually they will penetrate the material and be scattered by the atoms and electrons in the crystal lattice. Collisions with nuclei will lead to energy transfer and deflection while collisions with electrons will only lead to energy loss. If the path of the

penetrating particles leads them back to the surface, they will be reemitted. The particle reflection coefficient R_n and energy reflection coefficient R_E defined by

$$R_n = \frac{\text{number of reflected particles}}{\text{number of incident particles}} \quad \text{and} \quad R_E = \frac{\text{energyofreflectedparticles}}{\text{energyofincidentparticles}} \tag{13.5}$$

can be determined by computer simulations where the particle trajectory and the energy transfer in the scattering processes is calculated assuming binary collisions. Experimental results are obtained from backscattering experiments, which are, however, very difficult at energies below 10eV due to strongly decreasing detector sensitivities.

Figure 13.3 shows the reflection coefficients of hydrogen for two reactor relevant materials, carbon and tungsten, as a function of the energy of the incident hydrogen atoms. The reflection is mainly determined by backscattering processes and therefore increases with the target atom mass. With increasing energy the incident particles will penetrate more deeply into the bulk material, which leads to the observed decrease of the reflection coefficients towards higher energies. The simulations assume an attractive surface potential, which leads to the strong decrease of the reflection coefficients at energies below 1 eV. The determination of the precise form of the surface potential is, however, a very difficult problem. In addition, adsorbed hydrogen at the surface will strongly modify the surface potential function.

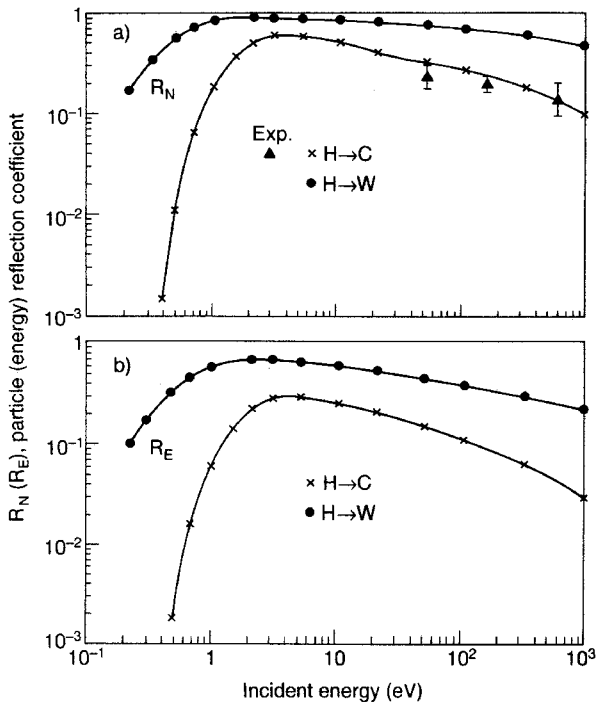

Figure 13.3: Particle (a) and energy reflection coefficients (b) for hydrogen ions incident on carbon and tungsten solid surfaces as a function of the impact energy.

13.4.2 Implantation, diffusion and reemission

The fraction of implanted hydrogen ions which are not reflected, i.e. which do not find their way back to the surface right after penetration, are slowed down by subsequent scattering and will eventually be trapped, either at grain boundaries or at vacancies in the bulk. In addition they may be bound in form of a metal hydride.

When the ions enter the solid surface they recombine to atoms and the fraction which is not trapped within the course of the thermalization process may then travel through the material by diffusion. If the atoms reach a surface, they will recombine to molecules and may be released by thermal desorption.

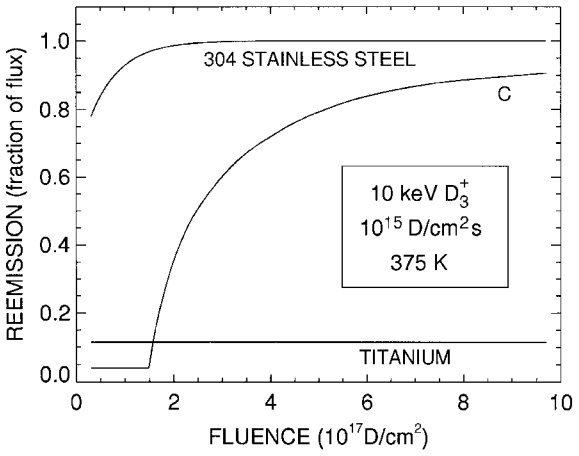

Figure 13.4: Reemission as a function of fluence (total number of implanted atoms) for different materials. The reemission is expressed in units of the implantation flux.

Metals

Diffusive propagation of neutral hydrogen in a metal is described approximately by a transport equation for the concentration $c(x)$ of free atoms in a depth x

$$\frac{\partial c}{\partial t} = D\frac{\partial^2 c}{\partial x^2} + Q - \frac{\partial c_T}{\partial t} \tag{13.6}$$

where Q is the source function of implanted hydrogen atoms and c_T is the concentration of trapped atoms. The maximal concentration will be found in a depth approximately equal to the mean ion range R_p. From there, the atoms diffuse back to the surface as well as deeper into the bulk material. At the surface, the rate of release is determined by the recombination rate coefficient to H_2 because energetically only molecules can be released. For the H_2-flux one obtains

$$\Gamma_{H_2} = -D\frac{\partial c}{\partial x}|_{x=0} = Kc(x=0)^2 \tag{13.7}$$

where K is the molecular recombination rate constant.

The final equilibrium distribution depends further on the solubility of the hydrogen in the material. For metals in which hydrogen dissolves exothermically like titanium, the surface is a potential barrier. Therefore, the reemission of hydrogen will be very low, the hydrogen is collected in Ti, forming TiH_2 (see Fig. 13.4).

In metals like steel, where hydrogen is dissolved endothermically, the reemission depends on the temperature. At low temperatures the diffusion coefficient is small and the reemission is determined by the diffusive transport. A steady state concentration builds up until the flux of implanted atoms is equal to the reemission flux (see Fig. 13.4). After stopping the implantation process, the hydrogen inventory in the material will be

reemitted. This situation is typical for present fusion experiments with steel walls where the wall temperature remains low because of the short discharge times.
With higher temperatures 500^0 for steel) the diffusion increases strongly. In that case, the reemission is mainly determined by the recombination to H_2 at the surface. This situation would occur in a fusion reactor and is important with respect to the tritium fuel. The tritium inventory in the wall will be small but on the other hand, a considerable fraction of the tritium atoms will diffuse through the wall and must be captured for example by a double wall structure with a pumped interspace.

Carbon

For carbon as wall material, the situation is different to the metals. For temperatures 400^0 C like in present fusion experiments with graphite as wall material, there is practically no diffusion. Implanted hydrogen will be collected until a saturation level of 0.4 H/C is reached. If the implantation continues, the additional hydrogen will be reemitted immediately (see Fig. 13.4). After stopping the implantation, the reemission will be much smaller than for metals. In present fusion experiments, the saturation level is reached after some discharges which may cause problems in controlling the plasma density. With so called conditioning discharges using helium, one can decrease the hydrogen inventory if necessary.
In a fusion reactor with wall temperatures above 500^0 C, diffusion and recombination to H_2 become important also for carbon with similar problems for the tritium handling as for the metals.
A further process leading to trapping of hydrogen in carbon will occur in devices with divertor plates made of carbon. Carbon atoms produced by erosion of the plate surfaces may be deposited at other locations where they will collect more hydrogen. This leads to a further increase of the hydrogen inventory in the vessel.

13.5 Impurity production

As mentioned in section 13.1, the bombardment of the wall elements by particles escaping the plasma or streaming along field lines which intersect a solid surface will produce in turn a source of neutral atoms from the wall material. Depending on the location of the surface and the plasma properties in the vicinity of the source, a certain fraction of the wall atoms will penetrate the plasma becoming ionized there. The presence of these impurities may degrade severely the plasma properties necessary for nuclear fusion. In this section, we will discuss the most important processes responsible for the contamination of the plasma.

13.5.1 Sputtering

When an ion or neutral atom is hitting a solid surface, it follows a complicated trajectory because of collisions with the lattice atoms in the solid. During this collision cascade the incident particle will be reflected or trapped as described in the previous section. In addition, if a surface atom receives sufficient energy from a collision, it is sputtered away

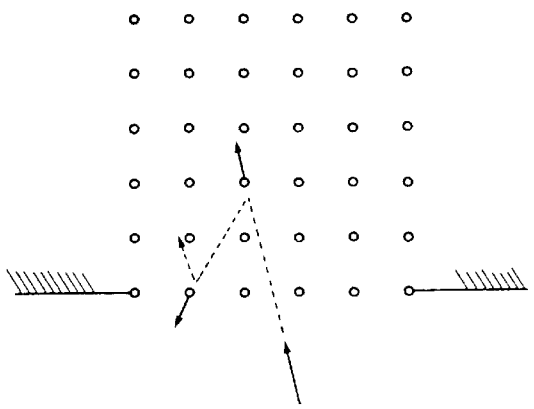

Figure 13.5: Schematic view of the physical sputtering process. The ion incident from the left is reflected in a first collision to the surface where it releases a lattice atom in the second collision.

from the solid (see Fig. 13.5). This is only possible if the energy of the incident particle is above a certain threshold E_{th}. The sputtering yield Y is defined by

$$Y = \frac{\text{average number of sputtered particles}}{\text{incident ion}}. \tag{13.8}$$

For central collisions, the fraction of the kinetic energy E_0 of an incident particle with mass m_1 which is transferred to a target atom with mass m_2 is given by $\gamma = 4m_1m_2/(m_1+m_2)^2$. For light projectiles sputtering will occur only if the incident particle is reflected in a first collision towards the surface as shown in Fig. 13.5. It's energy after the collision is $E_0(1-\gamma)$. To sputter a surface atom, the transferred energy in the following collision $E_0\gamma(1-\gamma)$ must be high enough to exceed the surface binding energy E_s. This leads to a threshold energy of

$$E_{th} = \frac{E_s}{\gamma(1-\gamma)} \tag{13.9}$$

For most materials E_s is in the range 3.5 - 9 eV. Therefore, for the same projectile mass, the threshold energy is mainly determined by the mass of the target atoms. However, if $m_1 m_2$, e.g. if the projectile and the target atoms are the same (self sputtering), the collision cascades are much larger and the model described above does not hold any longer. In that case, the threshold energy is $E_{th} = 4E_s$.

The left part of Fig. 13.6 shows the sputtering yields Y of different targets for bombardment with D atoms. Apart from the described dependence of the threshold energy from the mass of the target atoms the position of the maximum in Y increases to higher target masses.

To determine the sputtering yield of a material exposed to a plasma, one has to integrate the sputtering yields over the energy distribution function of the incident plasma ions. In the plasma the ions usually are close to a Maxwellian distribution. Ions impinging on a solid surface are, however, accelerated by the sheath potential, which significantly increases their impact energy. The right plot of Fig. 13.6 shows results for a D-plasma. The ions from the high energy tail of the temperature distribution and the effect of the sheath acceleration lead to significant sputtering even at plasma temperatures fairly below the monoenergetic sputtering threshold energy.

For heavy projectiles, in particular in the case of self sputtering, the yield may even become greater than 1 which will lead to an unlimited increase of the impurity content in the plasma.

For light projectiles $Y_{\max}$ is always < 1. This is, however, only true for normal incidence. If the angle of incidence increases from the normal, the sputtering yield increases as well and may become > 1.

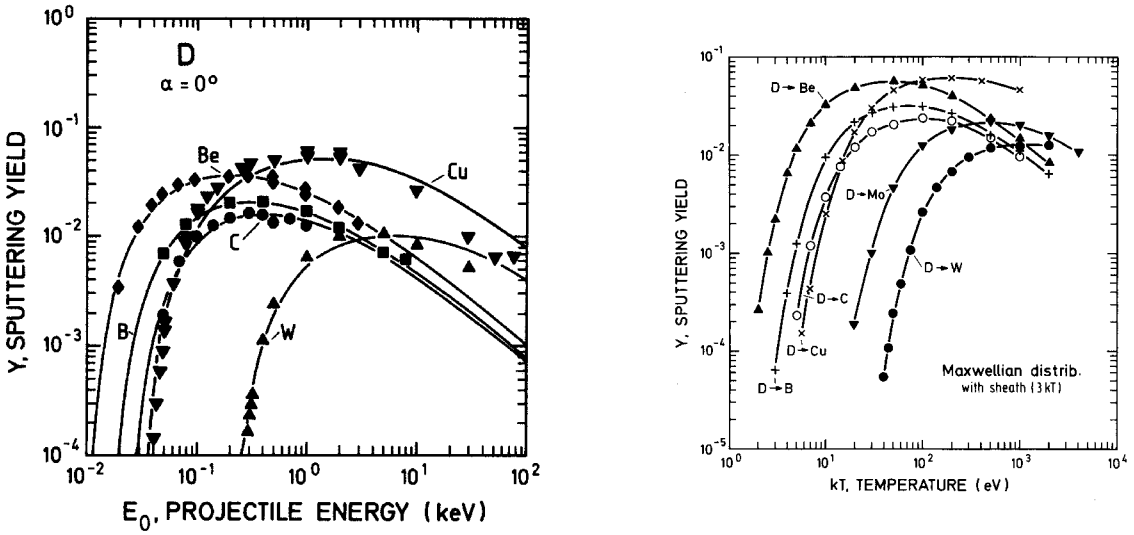

Figure 13.6: Calculated sputtering yield Y of various target materials for bombardment by D ions as a function of impacy energy (left) and sputtering yields for exposure to a D-plasma as a function of the plasma temperature including acceleration by the sheath potential (right).

The sputtered wall particles are practically all neutral. Except for single crystal targets their angular distribution is given approximately by a $\cos(\theta)$ distribution. Their energy distribution has typically a maximum at $0.5E_s \simeq$ 2-3 eV. Therefore, they can deeply penetrate the plasma before they become ionized which gives them a high probability to become confined in the plasma.

13.5.2 Chemical erosion

Another erosion process will be found if the incident particles produce volatile compounds with the target material. This is observed in particular for carbon surfaces with hydrogen plasmas or with oxygen as a plasma impurity. In the first case, methane and higher carbohydrates are produced while in the latter case, production of carbon monoxide (CO) can be observed. These gases are set free very easily from the surface by thermal desorption or collisions.

For the most important case $D^+ \rightarrow C$, chemical erosion by high energy particle bombardment will occur mainly at surface temperatures in the range $500 - 600^0$ C. However, if the energy of the incident deuterons is smaller than 100 eV, chemical erosion processes will dominate the physical sputtering processes. Figure 13.7 shows sputtering yields for hydrogen, deuterium and helium impact on a carbon surface. The solid lines represent results from calculations with a simulation code for physical sputtering. Obviously, for

hydrogen and deuterium sputtering/erosion occurs even below the threshold energy for physical sputtering.

E results from ASDEX Upgrade which is equipped with graphite wall tiles and divertor plates, confirm that the carbon content of the plasma is indeed to a large extent produced by chemical erosion of the main chamber graphite tiles.

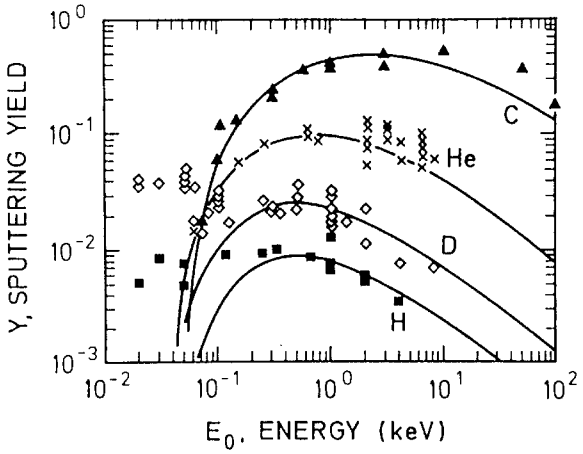

Figure 13.7: Dependence of the sputtering yield of graphite for H, D, He and C ions at normal incidence. The solid curves represent results from simulations of physical sputtering.

13.5.3 Sublimation, evaporation

In a closed system, sublimation from a solid surface or evaporation of fluid material is in equilibrium with the condensation from the gas phase. The equilibrium is determined by the temperature and the steam-pressure of the material. For steam pressures above 10^{-6} mbar, sublimation or evaporation will be the dominant process. For beryllium which is considered as a possible wall material, the corresponding temperature is 800^0 C while sublimation of carbon will only occur for temperatures $> 2000^0$ C.

Furthermore, laboratory experiments show that in carbon exposed to high levels of particle influx, interstitial atoms are produced which can reach the surface by diffusion where they sublimate. This process starts at much lower surface temperatures $> 800^0$ C) and could lead to increased carbon production in a fusion reactor.

13.5.4 Desorption

The surfaces inside the vacuum vessel are covered with thin layers of water, cleaning agents and residue of manufacturing processes. Depending on their surface binding energy, they will be released from the wall by the particle bombardment from the plasma thus producing an additional source of plasma impurities. It is possible to remove the weakly bound layers by glow discharges, however, the remaining oxide layers and adsorbed water molecules cannot be removed and are the main source for the oxygen contamination of the plasma.

13.5.5 Arcing and melting

If metals are used as wall material, the surface can be destroyed by melting, if the heat load from the plasma becomes so high that it cannot be removed by conduction and

cooling. Droplets of molten material from the upper vessel regions can fall into the plasma where the sudden rise of the radiation losses may cause a break down of the discharge.

As less spectacular erosion process can be observed under certain discharge conditions. Because of the potential difference between edge plasma and wall, electric arcs are ignited by field emission from ridges and peaks in the surface which last for times $1\mu s$ with a size of some mm. After ignition the cathode spot on the material surface is heated up by ion bombardment from the arc and cooled by the melting and conduction. The cathode spot grows because of the increasing erosion and after reaching a critical size the arc breaks down and may ignite again in the vicinity.

13.5.6 Positive and negative aspects of impurity contamination

The impurity contamination of the plasma in a fusion reactor can only be tolerated below a critical level which depends mainly on the charge number of the impurity atoms. However, if one can restrict the zone with higher impurity concentration to the plasma edge and the divertor plasma, the presence of impurities can also have a beneficial effect as described below.

High-Z - cooling of the central reaction zone

Heavy impurities like tungsten, molybdenum and to a certain extent nickel and iron are not fully ionized in a fusion plasma. The power loss by their line radiation is a function of the plasma temperature which has for high-Z elements a maximum in the temperature range of $10^6 - 10^7$ K relevant for nuclear fusion. Therefore, concentrations higher than 0.01% (for W, Mo) and higher than 0.1 - 1% (for Fe, Ni) will lead to a power losses which inhibit the ignition of the plasma.

Fuel dilution

Light impurities like beryllium, boron and carbon and also helium as a product of the fusion process will be fully ionized in the plasma core. Therefore, they do not emit line radiation in the central region in contrast to the cooler edge regions. The radiation losses in the outer plasma zone will not inhibit the ignition and the burning of the plasma. However, they still can degrade the overall energy balance of the fusion reactions. A further negative effect is the dilution of the fuel ions in the core because of the quasi neutrality of the plasma which will decrease the fusion rate. For these reasons, the concentrations of light impurities in the confined plasma must not be higher than 2 - 5%.

Edge cooling and power exhaust

Under certain plasma conditions, in particular at high densities, it turned out that it is possible to confine the impurities in the divertor region of a tokamak plasma. There are attempts to use the intense line radiation produced by light impurities in this cooler zone as a means to spread the power flux generated from the plasma onto a larger area of the vessel surface thus decreasing the power load of the divertor target plates. The

impurities can be introduced into the divertor plasma either by sputtering from the walls or by additional puffing of impurities in gas form. This concept is known as *radiative divertor.*

Another concept to make use of radiation to decrease the power load of the divertor plates consists basically in trying to increase the divertor density to very high values and to puff in additional gas. Then, a cold plasma zone will establish above the divertor plates in which the plasma ions streaming towards the plates are cooled by charge exchange radiation. However, in these processes, as mentioned above, fast neutral atoms are produced which may increase the wall sputtering. This concept is known as *cold gas target.*

13.6 Diagnostics for plasma surface interaction

Many diagnostics are needed to provide the information for a more detailed understanding of the edge plasma and plasma-wall interaction. A detailed description would break the size limit for this manuscript, therefore only a short overview is given over diagnostics used directly in fusion experiments and diagnostic methods used in laboratory experiments for example to analyze wall materials and surfaces.

13.6.1 In situ diagnostics

- *Electron density and temperature* are measured by Thomson scattering and from spectral emission of neutral atom beams injected into the plasma edge. A further possibility is the use of electrical Langmuir probes which allow the measurement of n_e and T_e and in addition the *floating potential* of the plasma.

- *Impurity densities and fluxes* and the *densities of molecules* are measured by spectroscopy and laser resonance fluorescence. With good spectral resolution, *impurity temperatures* can be measured as well. However, there is no good method to obtain the *temperature of the plasma ions.*

- *The composition of the neutral gas* is determined by mass spectrometry. This gives valuable information for example on the molecules produced by chemical erosion.

- *Velocity spectra of escaping neutrals* are measured by time of flight spectrometers. These provide information on the ion temperature in the plasma and allows to estimate the effects of the neutral wall bombardment.

- *Surface temperatures and heat flux deposited on surfaces* are measured by infra red cameras.

- *Surface erosion and deposition* are investigated with long term marker probes where materials are vaporized as thin layers onto surface elements. To analyze single discharges, collector probes are used which allow in addition the determination of *impurity flux, mean energy and mass* and *plasma ion fluxes and mean energy.* After exposure to the plasma for a certain time, the probes are removed and analyzed by surface analytical techniques described in the next paragraph. As a further method

to measure *erosion and redeposition of thin material layers* one can measure the thickness of such layers by interferometric methods.

13.6.2 Laboratory experiments

- *Analysis of collector probes and long term exposition probes.* The surface structure of the probes is examined by raster electron microscopy. The electron beam of the microscope will produce bremsstrahlung when hitting the examined surface which is characteristic for each element and allows the determination of the material composition. A quantitative determination of the distribution of an element in the material is possible by scanning the surface with high energy ion beams (in the MeV range) of protons, deuterons or α-particles. One can measure the energy distribution of the ions from R utherford backscattering processes (RBS) or, in case of a proton beam, the spectrum of the proton-induced X-ray emission (PIXE). A further possibility is the detection of products of nuclear reactions induced by the incident ion beam which are also characteristic for a certain element. To measure the erosion of the probe surface, a trace element is implanted in a surface layer with known thickness. The erosion rate is determined by measuring the thickness of the remaining layer after exposition of the probe.

- *Hydrogen recycling* is studied by implanting protons or deuterons in materials until steady state is reached and measuring the pressure of the reemitted atoms as a function of time after switching off the beam.

- *Sputtering coefficients* can be measured by bombarding a probe with an ion beam and measuring the weight loss after a certain exposition time. In addition, the sputtered material can be analyzed by laser resonance fluorescence.

- *Reflection coefficients* are determined by estimating the amount of trapped atoms or by detecting the reflected particles using ion spectroscopy.

Bibliography

[1] W. Hofer, J. Roth (Ed.), *Physical Processes of the Interaction of Fusion Plasmas with Solids*, San Diego (1996).

[2] R. Behrisch and D. E. Post (Ed.), *Physics of Plasma Wall Interactions in Controlled Fusion*, Proceedings of a NATO Advanced Study Institute, New York (1985).

[3] P. C. Stangeby, *The Plasma Boundary of Magnetic Fusion Devices*, Bristol (2000).

[4] O. Auciello, D. L. Flamm (Ed.), *Plasma Diagnostics - Surface Analysis and Interactions*, San Diego (1989).

[5] J. C. Vickermann (Ed.), *Surface Analysis - The Principa Techniques*, West Sussex (1997).

Chapter 14

Astrophysical Plasmas

Harald Lesch

14.1 Introduction

99% of the luminous matter in the Universe is in plasma state, i.e. it consists of ions and electrons with some degree of ionization larger than 10^{-6}. This simple statement already proves the importance of plasma physics for astronomy. Astropyhsical plasma systems appear everywhere in space: There are extragalactic jets made of relativistic particles and magnetic fields, flowing with almost the velocity of light, originating in the centres of quasars, which are 10^5 lightyears long, with pinch like magnetic field configurations. There are disk galaxies are magnetized spirals which rotate with a few hundred km per secondof size of 10^5 lightyears. Supernovae explode with velocities of a few 10^4 km/sec, leaving a tiny nucleus of about 1.5 solar masses of 10 km in form of a strongly magnetized rapidly rotating neutron star. The interstellar medium is a highly filamented magnetized medium in which shear motions compress, stretch and twist the magnetic field within a highly conducting collisionless plasma. The intergalactic medium is a very thin (1 particle per m^3) , very hot plasma ($T \simeq 10^{7-8}$ K). The sun is surrounded by a corona which is hundred times hotter than its surface! The Earth ionosphere glows from time to time since plasma curtains emit the Aurora. We really live in a plasma universe!

14.2 Typical parameters of astrophysical plasmas

Typical examples for astrophysical plasmas are

- all the stars (about10^{11} stars per galaxy)
- the interstellar medium in galaxies (about 10^{11} objects)
- the intergalactic medium between galaxies and galaxy clusters

The particle number density covers an enormous range: from about one particle per cubicmeter in the intergalactic medium up to 10^{30} in the central regions of hydrogen burning solar like stars. The plasma temperature is only a few hundred Kelvin in cold, but still significantly ionized gas clouds in which stars form up to a few 10^8 Kelvin in the

X-ray halos of galaxy clusters, emitting thermal bremsstrahlung. Every plasma in the universe is magnetized! The smallest magnetic field strengths of about 10^{-11} Tesla have been deduced from the low-frequency radio emission in the intergalactic medium, which is due to synchrotron emission of relativistic electrons. The strongest magnetic fields at the surface of neutron stars are about 10^{8-10} Tesla, measured by the cyclotron emission line in the X-ray regime. Neutron stars are only 10 km in size, the intergalactic medium has a typical size of millions of lightyears. One lightyear is about 10^{16} m. The length at which intergalactic magnetic fields are ordered is about a few thousand lightyears. Beside the population of thermal particles, astrophysical plasmas contain ultrarelativistic particles, electrons and nuclei, as well. This population is known as cosmic rays, although it consists of particles. The relativistic electrons radiate via synchrotron emission and if they are in compact systems with intense photon fields via inverse Compton scattering. We will discuss the different radiation processes in the next section. From observations of the electromagnetic spectrum we can estimate the electron energies required to provide the observed radiation. Especially from the most recent X-ray satellites CHANDRA and XMM it became clear that in active galactic nuclei, in extragalactic jets and in supernova remnants the electrons have energies up to 100 TeV! Typically at least a few hundred MeV electron population fills the space between the stars and galaxies. In most galaxies the electron population is energized globally up to 10 GeV.

Concerning the hadronic population our knowledge is not as complete, since these partilcles (protons and nuclei) do not undergo intense energy losses by radiation processes like the electrons. We know only the energy distribution of the cosmic ray hadronic population which encounters the earth. From cascades induced by cosmic rays hitting the earth atmosphere we can deduce maximum energies of about 10^{20} eV for the protons. Typical energies are in the range of MeV to GeV.

As stated in the introduction the velocity fields of astrophysical plasmas exhibit motions at all velocities. The plasma velocities are determined by gravity and rotation mainly. The interplay of these two forces explains the main part of astrophysical streamings. This is true for accretion disks around black holes and neutron stars, which accelerate plasmas alomost to the speed of light. Close to galactic nuclei plasma clouds move with a few 10^{3-4} km/sec. In the interstellar medium clouds move with a few $10-100$ km/sec. Due to stellar explosions there are also plasma flows escaping with 20.000 km/sec. In any case the velocity fields contain spatial gradients, i.e. they are always shear motions.

After that brief introduction we can already formulate the central issues of modern plasma astrophysics:

- Where do the magnetic fields come from?
- What is the origin of magnetized, relativistic jets?
- How are the particles accelerated to the ultrahigh energies?
- What is the interplay of acceleration processes and the radiative loss mechanisms?
- How do the astrophysical plasmas respond to the distortions by unsaturated externally driven shear flows?
- How do we have to describe such thin and highly conducting magnetized plasmas?

In that contribution we give an overview about the basic theoretical procedures and constituents necessary to tackle plasma astrophysical problems. Let us start with the source of information about the physical state of astrophysical plasmas the electromagnetic radiation.

14.3 Radiation processes

The electromagnetic radiation is the cosmic newspaper, thus we a must know what kind of mechanism may responsible for the photons which hit our detectors or telescopes. We observe the Universe in practically all bands of the electromagnetic spectrum, starting with the radio regime with which important information can be gained about the magnetic field strength and structure since most of the radio emission in space is of nonthermal origin, i.e. it is synchrotron radiation. Radio waves tell us about relativistic electrons gyrating in magnetic fields. The infrared photons mostly originating in star-forming regions are produced by scattered light from dust particles and by direct emission due to the rotational and vibrational transitions of molecules. IR-radiation is the indicator for star formation. Optical photons are due stellar energy production. It is still the backbone of modern astrophysics oberserved by the largest ground based telescopes with mirrors up to 15 m and alos in space with the Hubble Space Telescope. UV-photons can be observed only by satellites. They come from very hot stars and indicate young stars, since massive, hot stars which are 10–50 times heavier than the sun have lifetimes of only a few million years, whereas our sun lives 10 billion years. The X-ray astronomy developed very rapidly in the last decade and gave deep insights into the hot plasmas in the intergalactic and interstellar medium, as well as about stellar X-ray sources and nonthermal X-ray emission from extragalactic jets. Finally the highest energies are now also available from the MeV-range up to 100 TeV. Here we gain information how particles are accelerated to the highest energies in the Universe. For example, the Crab nebula, the rest of a supernova explosion observed by chinese astronomers in 1054, this supernova remnant emits gamma rays at energies of about 50 TeV, requiring electrons at least at this energy.

It is the central subject of astrophysics to translate the received electromagnetic radiation into models by using the theory of electromagnetic radiation.

There are in principle two classes of radiation mechanisms: the thermal and nonthermal processes. The latter are mechanisms like synchrotron radiation and inverse Compton scattering, where relativistic electrons emit photons due to the interaction with magnetic fields or external radiation fields. Nonthermal radiation is produced by particles with nonthermal energy distributions, mainly with power law distribution functions or almost monoenergetic distributions.

In the case of thermal radiation the energy distribution of the particles is a Maxwellian which defines a temperature. The particles will either emit lines (atomic transitions) or continuum radiation (free-free emission, i.e. bremsstrahlung). From the blue and/or redshifts of the recombination lines we get knowledge about the plasma velocities and densities We will not discuss the numberless line emission or absorption mechanisms but rather concentrate on the emission of a fully ionized plasma without recombination lines, etc.and we will also not consider the case of black-body radiation. This leads us

to the mechanism of thermal bremsstrahlung, which gives information about the plasma temperature **T** and the electron density $\mathbf{n_e}$.

14.3.1 Thermal Bremsstrahlung

When a charge is accelerated or decelerated it emits electromagnetic radiation, and bremsstrahlung is the radiation emitted in all electromagnetic encounters between the charge and the nuclei of substance through which it passes. Of special importance is the thermal bremsstrahlung, where free electrons with a kinetic energy $1/over2m_e v_e^2$ equal to the thermal energy $k_B T_e$ move in a hydrogen plasma (k_B denotes the Boltzmann constant). The radiated energy is then a direct measure of the plasma temperature and the plasma density, since the energy loss rate of the plasma is

$$\left(\frac{dE}{dt}\right)_{brems} = 1.435 \times 10^{-27} T_e^{1/2} n_e n_i \ [\mathrm{erg\,cm^{-3}\,s^{-1}}] \tag{14.1}$$

For quasineutral plasmas with $n_e = n_i$, bremsstrahlung measures the electron temperature and electron (ion) density.

Its spectrum is characterized by a flat curve in the optically thin regime followed by an exponential break at $h\nu \simeq k_B T_e$. In the optically thick regime the spectrum rises proportional to ν^2.

Thermal bremsstrahlung is an important radiation process for very hot gases radiating thermal X-rays (like supernova remnants and gas halos of galaxy clusters). Flat and Optically thick bremsstrahlung is emitted by HII-regions close to the regions of star formation in the radio regime.

14.3.2 Synchrotron Radiation

Synchrotron emission is the radiation of a high energy particle gyrating in a magnetic field. It was originally noted in some early betatrons where high energy particles were first accelerated to ultrarelativistic energies. This same mechanism is responsible for the radio emission from the Galaxy, from supernova remnants and extragalactic radio sources. It is also responsible for the nonthermal optical and X-ray emission in the Crab Nebula and for the optical continuum emissionof quasars and jets.

For nonrelativistic velocities the complete nature of the radiation is simple and is called cyclotron radiation. The frequency of emission is simply the frequency of gyration in the magnetic fields

$$\omega_g = \frac{zeB}{m_e}. \tag{14.2}$$

A useful figure to remember is that the gyrofrequency of an electron is

$$\nu_g = \frac{eB}{2\pi m_e} = 28\,\mathrm{GHz} B[T]. \tag{14.3}$$

Particles emit only if their pitch angle θ (which is the angle between the particle velocity and the magnetic field line) is not zero. The energy loss rate of an electron is ($\sigma_T = 6.65 \times 10^{-29}\,\mathrm{m^2}$ denotes the Thomson cross section and γ is the particles Lorentz factor)

$$-\left(\frac{dE}{dt}\right) = 2\sigma_T c \gamma^2 \frac{B^2}{2\mu_0} sin^2\theta. \tag{14.4}$$

Ths result applies for electrons of a specific pitch angle θ. To get the average loss rate for particles of all pitch angles, we must average over solid angle, i.e. $P(\theta)d\theta = \frac{1}{2}sin\theta d\theta$

$$-\left(\frac{dE}{dt}\right)_{average} = 2\sigma_T c\gamma^2 \frac{B^2}{2\mu_0}\frac{1}{2}\int_0^\pi sin^3 d\theta = \frac{4}{3}\sigma_T c\gamma^2 \frac{b^2}{2\mu_0}. \tag{14.5}$$

The typical frequency emitted by an electron is the nonrelativistic gyrofrequency times γ^2

$$\nu_{syn} \simeq \gamma^2 \nu_g sin\theta. \tag{14.6}$$

The emitted radiation spectra depend on the energy distribution of the relativistic electrons. An almost monoenergetic (beam-like) distribution of relativistic electrons emit an optically thin synchrotron spectrum

$$I(\nu) \propto \nu^{1/3} \quad (\nu \ll \nu_{syn} \tag{14.7}$$

and

$$I(\nu) \propto exp(-\frac{\nu}{\nu_{syn}} \quad (\nu \gg \nu_{syn}), \tag{14.8}$$

with a maximum frequency $\nu_{max} \simeq 0.29\nu_{syn}$. Such a spectrum has been detected in several galactic nuclei and especially in the centre of our galaxy (Sgr A*)and its immediate surrounding the arc. There the synchrotron emission is concentrated in long (150 light years) and thin (0.5 light years) highly polarized magnetic filaments. The magnetic field strengths in these filaments is estimated to be about 10^{-7} T, with the maximum frequency of about 100 GHz this indicates that some process has produced an electron energy distribution which is almost mononenergetic with a characteristic energy of about 40 GeV (Lesch and Reich 1992). In the central light year of the galactic centre, in SgrA* the monoenergetic electrons are at about several MeV (Lesch et al. 1988, Duschl and Lesch 1994).

Such monoenergetic spectra are rare, more typical are energy distributions of power law form

$$N(E)dE = \kappa E^{-x} dE, \tag{14.9}$$

where $N(E)dE$ refers to the number of particles per unit volume.

Such energy spectra emit optically thin radiation power lwas in form of

$$I(\nu) \propto \nu^{(x-1)/2}. \tag{14.10}$$

The important rule is that *if the electron energy spectrum has a power law index x, the spectral index of the synchrotron emission of these electrons is* $\alpha = (x-1)/2$. Such spectra are found in supernova remnants with $\alpha \simeq 0.5$ indicating an energy distribution of E^{-2}, in galaxies with $\alpha \simeq 0.83$, i.e. $E^{-2.66}$.

Synchrotron radiation is linearly polarized perpendicular to the magnetic field. Its degree of polarization in case of a power law is

$$\Pi = \frac{x+1}{x+\frac{7}{3}}, \tag{14.11}$$

giving a maximum linear polarisation of about 72%.

The optically thick synchrotron spectrum does not depend on the energy distribution and has a form of

$$I(\nu) \propto \nu^{5/2}. \tag{14.12}$$

Such optically thick synchrotron spectra are observed in nuclei of quasars which evolve at higher frequencies into a $\nu^{-\alpha}$ optically thin spectrum.

14.3.3 Inverse Compton Scattering

Relativistic electrons lose energy when they collide with photons because the photons are scattered to much higher energies. This process is called *inverse Compton scattering* because in the usual Compton scattering interaction the photon gives energy to a particle initially at rest and thereby loses energy in the collision. The situation most often encountered in astrophysical plasmas is the limit in which the energy of the photon in the centre of momentum frame of the collision is much less than the rest mass energy of the electron, i.e. $\gamma h\nu \ll m_e c^2$. The energy loss rate due to inverse Compton scattering is

$$\left(\frac{dE}{dt}\right)_{IC} = \frac{4}{3}\sigma_T c \gamma^2 c U_{rad}, \tag{14.13}$$

where U_{rad} denotes the energy density of the external photon field.

Note the great similarity of this result to that for synchrotron radiation all the way down to the factor of 4/3. The reason for this is that in both cases, the partilces being accelerated by the electric field which it sees. A partilce does not care about the origin of this electric field. Due to this similarity it is clear what the typical emitted frequency in inverse Compton scattering must be

$$\nu_{IC} \simeq \gamma^2 \nu_0 \tag{14.14}$$

where ν_0 denotes the photon frequency of the external radiation.

In the limit $\gamma h\nu \ll m_e c^2$ inverse Compton scattering is Thomson scattering. If instead the Doppler shifted photon energy $\gamma h\nu$ in the rest frame of the electron is equal to the electrons rest mass energy $m_e c^2$ the cross section is given by the Klein Nishina cross section which is approximately $\sigma_{KN} \propto \frac{1}{\gamma}\sigma_T$.

IC-process is important for compact objects like active galactic nuclei, in which very intense radiation fields are produced by accelerated plasma streams, for example accretion disks around black holes with masses of a few million solar masses. The disks are heated to temperatures of about 10^5 K, which can be deduced from line emission and thermal continuum radiation. Such disks emit intense radiation in the optical and UV at about 10^{13-15} Hz. Some active galactic nuclei are intense emitters of TeV- radiation, i.e. 1000 GeV! The only mechanism to produce such a high energy radiation without intense pair production (remember the rest mass of an electron plus a positron is about 1MeV) is with optically thin inverse Compton scattering. One requires electrons with energies of several TeV, their corresponding Lorentz factor is about 10^6 which adds up $\nu_{IC} \simeq \gamma^2 \nu_0 \simeq 10^{25}$ Hz! This scattering works efficiently only for the low energy photons of the external radiation. For UV photons the Klein-Nishina limit holds and the cross section drops with $1/10^6$! since the photon energy in the rest frame of the electrons is comparable to the rest mass energy of the electrons.

Finally we give some interesting figures for the loss time scales of inverse Compton scattering and synchrotron radiation
For the IC-case we have a loss time

$$t_{loss}^{IC} = \frac{5 \times 10^8 \text{sec}}{\gamma U_{rad}}, \tag{14.15}$$

with U_{rad} in erg/cm^3.
For synchrotron radiation we have

$$t_{loss}^{SYN} = \frac{3 \times 10^7 \text{sec}}{\gamma B^2}, \tag{14.16}$$

with B in 10^{-4} T.
For more information about radiation processes we refer to Rybicki and Lightman.

14.4 Cosmical Magnetohydrodynamics

Since astrophysical plasmas are highly conductive the ideal magnetohydrodynamics (MHD) may be an appealing description for such magnetized gases. For large spatial scales this statement is correct, i.e. in cosmical plasmas magnetic fields obey the frozen in condition that the magnetic flux $\Psi = BR^2$ is conserved globally. In terms of Ohm's law an ideal MHD-plasma obeys $\mathbf{E} = -\mathbf{v} \times \mathbf{B}$, i.e. induced electric fields force plasma and magnetic field to corotation and frozen-in flux. Large volumes in space like the interstellar medium in galaxies, the intergalactic medium or extragalactic jets can be almost perfectly described by ideal MHD.
It is not valid locally, i.e. for small spatial scales, in which magnetic boundary layers are build up by external forces like gravity, rotation or explosions. There the magnetic field is sheared, twisted and compressed leading to antiparallel field structures, that is to current sheets. Locally the ideal nondissipative MHD-description cannot be applied to cosmical plasmas. In the boundary layers often such strong electrical currents flow that collective processes provide a local reduction of the conductivity that dissipation sets in via magnetic reconnection. According to Ohm's law the deviation from idealness is equivalent to a parallel electric field which may accelerate plasma particles to ultrarelativistic energies as it is required by the observations.
Let us start with the ideal MHD description and its consequences for the dynamics of astrophysical plasmas.

14.4.1 The Ideal MHD Equations

One important equation of ideal MHD describes the time evolution of magnetic fields due induction ($\mathbf{v} \times \mathbf{B}$). It can be derived from the Maxwell equation $\nabla \times \mathbf{E} = -\frac{\partial \mathbf{B}}{\partial t}$, and Ohms law $\mathbf{E} = -\mathbf{v} \times \mathbf{B}$, leading to

$$\frac{\partial \mathbf{B}}{\partial t} = \nabla \times (\mathbf{v} \times \mathbf{B}) \tag{14.17}$$

According to this equation it is only the induction which changes the field strengths with time. This equation is synonymous with the frozen-in condition of the magnetic flux.

An equation which has profound implications for the energy transport in ideal MHD systems like astrophysical plasmas is

$$\nabla \times \mathbf{B} = \mu_0 \mathbf{j}, \tag{14.18}$$

which can be rewritten as

$$\nabla \cdot \mathbf{j} = 0. \tag{14.19}$$

In ideal MHD-plasmas the displacement-term $\frac{1}{c^2}\frac{\partial \mathbf{E}}{\partial t}$ can be neglected because the conductivity is assumed to be high that electric fields are always much weaker than magnetic fields, i.e. $E \ll B$ and all velocities are smaller than the velocity of light. The condition that the divergence of the current density vanishes means that the current circuit has to be closed. If for example we distinguish between currents runnibg parallel to the magentic field $\mathbf{j}_\parallel$ and currents perpendicular to the magnetic field lines $\mathbf{j}_\perp$ than Eq. (19) presents an important relation between a generator, a load and the conductive wires:

$$\nabla \cdot \mathbf{j}_\parallel = -\nabla \cdot \mathbf{j}_\perp. \tag{14.20}$$

Eq. (20) means that the perpendicular currents are sources for parallel currents and vice versa! If for example in a magnetized plasma forces are present which drive plasma motions perpendicular to the magnetic field, such a situation stores energy in the plasma. This region can be taken as a generator. It is connected with the outside material by magnetic field-aligned currents, which are force free (supposed that the external medium is of smaller density, i.e. the pressure forces outside of the generator are weaker than inside the generator). Force free currents are perfect for energy transport! They induce a filamentary magnetic field structure which stabilizes the plasma flow along the magnetic field and allows energy deposition far away from the generator. Such a scenario depends on the pressure gradients which may stabilize a given magnetic configuration. In the denser generator region pressure gradients will be definitely important.

In the external medium, which may the corona of a star or the atmosphere of a galaxy or of an accretion disk around a black hole, the pressure may be weak and the pressure gradients small. The strong shear of the magnetic fields in the generator may be transported into that external medium by Alfven waves, i.e. the magnetic field strengths can be enhanced by the kinetic energy of the plasma in the generator. The weakness of the pressure and the stronger magnetic field will both help to develop force-free filaments which are energetically preferred stages of magnetized plasmas in which currents are driven. Such force-free filaments should be a natural ingredients of any astrophysical plasma with low pressure.

In any case at least partially the stored energy in the filaments will be dissipated by either plasma heating or particle acceleration, both mechanisms should be observable in terms of thermal radiation in heated plasmas (like the solar corona) or in terms of nonthermal radiation where particles have been accelerated (like in solar flares). But the dissipation of the energy is not described by ideal MHD. We will discuss that important subject in the subsequent sections.

Here we list typical examples of such configurations in which an external force agitates a plasma perpenedicular to the magnetic field lines, stores energy and transports this stored energy via magnetic field-aligned electric currents, thereby inducing magnetic filaments

Solar Flares - Solar Prominences - Earth Aurora - Interstellar Filaments - Stellar Jets - Extragalactic Jets.

This list is time dependent in that sense that it depends on the actual state of the observational techniques in astrophysics. The typical experience is the higher the spatial resolution of the instruments is the more spatial structures, i.e. inhomogenities are detected. The more advanced astrophysical instruments are the more plasma physics becomes relevant for the interpretation of the observations!

For astrophysicsts the plasma structure and the magnetic field structure is of course important for the understanding of stability and inhomogeneity. However, as mentioned above, the most important subject of plasma astrophysics concerns the electromagnetic radiation which can be expected from dynamical plasma processes in terms of plasma heating and particle acceleration. To investigate such problems we have to extend ideal MHD to resistive MHD, including the effects of a finite electrical conductivity.

14.4.2 The resistive MHD Equations

The MHD equations taking into account the role of a finite electrical conductivity σ are quite different from the set of ideal MHD equations in many ways.

First of all for a stationary current density $\mathbf{j}$ Ohm's law is now

$$\mathbf{j} = \sigma(\mathbf{E} + \mathbf{v} \times \mathbf{B}). \tag{14.21}$$

The electrical conductivity in its most simplest form is given by

$$\sigma = \frac{n_e e^2 \tau_{ei}}{m_e} \tag{14.22}$$

whereτ_{ei} denotes the collision time $\tau_{ei} \simeq 0.266 \times 10^6 T_e^{3/2} n_e^{-1} (ln\Lambda)^{-1}$ (with the *Coulomb logarithm* $ln\Lambda$ which is generally between 5 and 20 and has a weak dependence on temperature and density). In case of Coulomb collisions the conductivity is $\sigma = 1.53 \times 10^{-2} T^{3/2} n^{-1} (ln\Lambda)^{-1}$. For temperatures higher than 10^3 K the conductivity is so high that the frozen-in condition is fulfilled. Nevertheless even in case of only Coulomb collisions the conductivity is finite and has to be taken into account if the plasma is known to be dissipative.

The ideal induction equation (17) changes now into

$$\frac{\partial \mathbf{B}}{\partial t} = \nabla \times (\mathbf{v} \times \mathbf{B}) - \nabla \times (\eta \nabla \times \mathbf{B}), \tag{14.23}$$

where $\eta = 1/(\mu_0 \sigma)$ is the *magnetic diffusivity* (which must not be confused with the electrical resistivity (σ^{-1} which is just the inverse of the electrical condcutivity σ. If the magnetic diffusivity is uniform the we get the equation usually used as induction equation

$$\frac{\partial \mathbf{B}}{\partial t} = \nabla \times (\mathbf{v} \times \mathbf{B}) + \eta \nabla^2 \mathbf{B}). \tag{14.24}$$

Eq. 14.24 for a vanishing plasma velocity describes the pure diffusion of magnetic field lines due to finite resistivity, i.e. finite conductivity. Eq. 14.23 with a spatial dependent diffusivity describes localized dissipation of magnetic field energy. Since most

astrophysical plasmas are globally ideal and dissipative only on small spatial scales, we will continue with the consequences of Eq. 14.23.

What does that equation mean? According to the non-ideal Ohm's law a localized resistivity corresponds to a localized electrical current distribution. Strong currents imply strong gradients in the current induced magnetic fields. As long as only Coulomb collisions are the source for resistivity the field lines move with the plasma, since collisions are rare, i.e. the plasma is collisionless and behaves in an ideal way.

However, if the magnetic field lines are subject to strong plasma motions, the situation changes drastically. The frozen-in field lines may be twisted, stretched, compressed etc.., and thereby strong currents are induced. Especially in the case of shear motions (like in the case of differential rotation), or turbulent gas flows, the magnetic energy is heavily dissipated via **magnetic reconnection**.

Reconnection is an intrinsic property of a magnetized plasma with shearing and/or turbulent motions. The encounter of magnetic field components with different polarity corresponds to parallel electric currents, which attract each other. In that sense any kind of plasma motion can trigger reconnection.

If the plasma pressure between opposite fields $\pm B$ is insufficient to keep the fields apart (e.g. by pushing the different flux systems apart), the plasma squeezed from between them and the two fields approach each other. The field gradient steepens and eventually the current density $\frac{c}{4\pi}\nabla \times B$ becomes so large that there is strong dissipation. The problem of reconnection is to know how the dissipation of the currents with density $j = en_e v_d$ is provided (e is the charge and v_D denotes the drift velocity of the electrons). If the current density is constant, enhanced dissipation is equivalent to the reduction of the electrical conductivity σ.

Thus strong dissipation not only means an enhancement of the current density but also a reduction of the conductivity. Indeed both effects support each other. This can be understood as follows: when the conductivity is high, the magnetic field lines are "frozen into" the plasma. Field lines embedded within a volume element of plasma are carried along by the moving plasma. Any two plasma elements that are threaded by the same lines of force will remain threaded in this way, i.e. two plasma elements that are threaded by different lines of force can never be threaded together. Thus a high conductivity prevents the field lines from merging. Reconnection occurs only in those plasma regions where the electrical conductivity is drastically reduced below its classical Coulomb value. The reduction of the electrical conductivity is provided by plasma instabilities, driven by the induced current. If the plasma is locally unstable, i.e. if the current density exceeds a critical value $j > j_{crit}$ or $v_d > v_{crit}$ (e.g. Huba 1985) microscopic instabilities will excite waves which enhance the collision frequency by wave-particle interactions; they lead to *anomalous conductivity*. The effective σ becomes anomalously low, greatly enhancing the dissipation and reconnection of the lines of force. Then the concept of "frozen in" field lines is no longer valid and the plasma moves relative to the field lines. When this occurs, strong electric fields along the reconnection length L are induced. It is the dissipation of the electric field E which transforms the current energy into particle energy.

Schindler et al. (1988, 1991) have shown that in three dimensions the reconnection process is always related to with a magnetic field aligned electric potential $U = -\int E_{\|} ds$. The induced electric field is always parallel to that field component which is not directly

involved in the reconnection process. This result was used to consider the acceleration of particles in cosmical plasmas and it was concluded that parallel electric fields associated with nonideal plasma flows can play an important role in cosmic acceleration. The actual value of $E_{\|}$ depends on the details of the microscopic instability, which is responsible for the deviations of the plasma from the ideal high conductivity state. It has been shown that in the case of the slow reconnection mode first proposed by Parker (e.g. Parker 1979) it is possible to get an estimate of the maximum Lorentz factor particles can attain via parallel electric potentials (Lesch and Reich 1992; Lesch and Birk 1997, 1998; Schopper et al. 1998, 1999).

Starting from the assumption of a stationary Ohmic dissipation in a three-dimensional reconnection sheet with an area $\sim L^2$ and a thickness l, the dissipation surface density in the sheet lj^2/σ is just to devour the influx of magnetic energy $uB_0^2/8\pi$. u is the approaching velocity of the field lines. Conservation of fluid requires that the net magnetic field inflow balances the outflow

$$uL = v_A l. \tag{14.25}$$

In terms of the magnetic Reynolds number $R_{\rm M} = \frac{2Lv_{\rm A}}{\eta}$, where $\eta = \frac{c^2}{4\pi\sigma}$, one gets (Parker 1979)

$$l = \frac{2L}{\sqrt{R_{\rm M}}} \tag{14.26}$$

and

$$u = \frac{2v_{\rm A}}{\sqrt{R_{\rm M}}} \tag{14.27}$$

The thickness of a reconnection sheet is also defined by Maxwell's equation $\nabla \times \mathbf{B} = \frac{4\pi}{c}\mathbf{j}$, which means $l \simeq \frac{cB}{4\pi j}$. The accelerating electric field is given by $E \simeq \frac{u}{c}B$. Now the whole problem is shifted to the microscopic level of description. As mentioned above the particle collisions are not efficient enough to produce a significant magnetic diffusivity (or to decrease the electric conductivity). The collision frequency is too small. Current driven plasma instabilities are involved, whose excited frequency depends on the drift velocity between electrons and ions. We choose in the following the wave mode which has the lowest instability threshold where the drift velocity $v_{\rm d}$ is equal to the ion thermal velocity $v_{\rm thi} = \sqrt{\frac{k_{\rm B}T_{\rm i}}{m_{\rm i}}}$ *the lower hybrid (LH) wave* $\omega_{\rm LH} \simeq 4.2 \cdot 10^5 B$. LH waves depend on the magnetic field strength, which means they are also suitable for three-dimensional reconnection where the magnetic field is not zero in the reconnection zone. A fully developed LH-instability results in an effective collision frequency of the order of $\omega_{\rm LH}$ (Sotnikov et al. 1978). We note that the central role of LH-waves in reconnection zones has been established for magnetospheric activity (e.g. Shapiro et al. 1994)

Inserting u into the electric field

$$E = \frac{\mathbf{v} \times \mathbf{B}}{c} \sim uB/c \tag{14.28}$$

and l into L, using $\nu_{\rm coll} \simeq \omega_{\rm LH}$ and with

$$\gamma m_{\rm e} c^2 \simeq eEL \tag{14.29}$$

one obtains the maximum Lorentz factor electrons can achieve in a three-dimensional reconnection zone, where the conductivity is determined via lower-hybrid waves (Lesch

1991)

$$\gamma_{\rm LH} \simeq 6 \cdot 10^3 B \simeq 6 \cdot 10^5 \left[\frac{B}{100\,G}\right]. \tag{14.30}$$

In the last years we have performed numerical simulations to create via three-dimensional MHD-calculations reconnection regions. We used a self-consistent description of the localized reduced current dependent conductivity and investigated by fully relativistic test-particle simulations within the MHD-structures the effiency of such dissipative structures in terms of particle acceleration to relativistic energies, including energy losses via synchrotron and inverse Compton radiation (Lesch and Birk 1997, 1998; Schopper et al. 1998, 1999; Birk et al. 1999).

Our results can be summarized within one sentence: *Magnetic reconnection is a very efficient acceleration mechanism.* In reconnection regions due to sheared magnetic fields the radiation losses do not influence the acceleration, simply because the acceleration is much faster than the losses. Depending on the initial injection position particles experience different electric field strength and power laws appear. Depending on the isotropy of the injection spectrum, more less all low-energetic particles which enter the reconnection region are accelerated. In case of an anisotropic injection, the resulting energy distribution function of the electrons will be quasi-monoenergetic since the achievable energy depends on the length of the reconnection zone, i.e. it is a linear accelerator. Since the final energy distribution will show an accumulation of particles either at the maximum energy or at the energy where radiation losses and acceleration exactly cancel, we obtain an energy distribution which exhibits pronounced low and high energy cutoffs, i.e. a relativistic electron beam (REB) (Lesch and Schlickeiser 1987).

The energy given by Eq. 14.30 is close to the required energies for TeV-radiation. The particles would not lose their energies via synchrotron radiation in the strong magnetic field simply because they flow along the field lines, i.e. the energy distribution is highly anisotropic (Crusius-Wätzel and Lesch 1998).

In this section we have used conventional reconnection in terms of an enhanced collision frequency via plasma waves, excited by some phase- space instability. In a relativistic plasma the excitation of waves is much more difficult, the plasma is very stable due to the high energy of the particles. That is, if we still have external shear flows which twist and compress the magnetic field lines, thereby enhancing locally the current density the system starts to become *filamentary* (Wiechen et al. 1998; Lesch and Birk 1998). The plasma is now completely collisionless, there are even no plasma fluctuations to reduce the conductivity, i.e. we have no dissipation at all. In such a case, like for example in jets, where the plasma density is very low and only magnetic fields and relativistic particles react to the externally driven differential rotation of the disk, then the system reacts via strong filamentation and the inertia of the particles plays a very important role. We describe *the inertia-driven -reconnection* in the next section.

14.4.3 Inertia-driven -reconnection in AGN

How reacts an ideal collisionless, magnetized plasma which is strongly distorted by externally driven shear flows? The magnetic fields will be twisted more and more until tube like structures appear, in which at same spatial scale the magnetic field gradients will be so strong that magnetic reconnection sets in, which is equivalent to a current sheet.

The magnetic field aligned electric field appearing in a reconnection zone is driven by the reduction of the local electrical conductivity. In principle the field strength of such a field cannot exceed the convective electric field, which is responsible for the shear, twist, etc.., given by Equation (27). The maximal shear velocity is the Alfvenic speed v_A.
Thus we get

$$E_{\parallel} = \zeta \frac{v_A}{c} B, \tag{14.31}$$

where ζ denotes the effiency of the conversion of the generated electric field energy to particle energy.
The necessary condition for magnetic reconnection to operate is the local violation of the ideal Ohm's law

$$\mathbf{E} + \frac{1}{c}\mathbf{v} \times \mathbf{B} = \mathbf{R}, \tag{14.32}$$

where $\mathbf{R} \neq 0$ is some unspecified nonideal term that gives rise to a nonvanishing electric field component parallel to the magnetic field.
Since the relativistic plasmas in AGN and especially inside the jets from AGN are highly collisionless, i.e. the dissipative term in Equation (21a) $\mathbf{j}/\sigma = \eta \mathbf{j}$ (where η is the resistivity (inverse of the conductivity) that would otherwise contribute to $\mathbf{R}$ is negligible. Therefore, the question arises concerning the nature of the nonidealness and also about the effectiveness ζ in a completely collisionless plasma. High energy plasmas are very stable against the excitation of plasma waves since the wave excitation condition $v_{drift} > v_{the} \sim c$ is hardly to fulfill for relativistic energies.
If a plasma is completely collisionless only the particle inertia is left to introduce some resistance. With a time dependent current density Ohm's law reads as

$$\frac{m_e}{n_e e^2} \frac{\partial \mathbf{j}}{\partial t} = \mathbf{E} - \frac{\mathbf{j}}{\sigma_{coll}}, \tag{14.33}$$

where σ_{coll} denotes an assumed collisional condctivity.
From dimensional analysis we see from Equation (32) that the inertial term is of order

$$\frac{m_e}{n_e e^2} \frac{\partial \mathbf{j}}{\partial t} \simeq \frac{m_e}{n_e e^2} \frac{\mathbf{j}}{\tau}, \tag{14.34}$$

where τ is the characteristic time of the system. Thus the inertial term can be large compared to the collisional term if $\tau \ll \tau_{coll}$, where $\tau_{coll} \simeq \nu_{coll}^{-1}$.
We can solve Equation (33) explicitely (assuming zero initial current)

$$j = \sigma_{coll} \left[1 - exp \left[\frac{-\tau}{\tau_{coll}} \right] \right] E. \tag{14.35}$$

We therefore define an effective conductivity due to the inertia of the particles σ_i, as

$$\sigma_i = \sigma_{coll} \left[1 - exp \left[\frac{-\tau}{\tau_{coll}} \right] \right]. \tag{14.36}$$

The time τ in Equation (35) is regarded as the lifetime of the particle in the system, that is the time during which the electric field can be effective in accelerating the particles. If $\tau \gg \tau_{coll}$ then the intertial conductivity σ_i,approaches the collisional conductivity σ_{coll}.

In a system with $\tau \ll \tau_{coll}$ in which the characteristic time scales are much smaller than the collision time, i.e. in thin relativistic plasmas for example, then

$$\sigma_i(\tau) = \frac{\sigma_{coll}\tau}{\tau_{coll}} = \frac{ne^2\tau}{m_e}, \tag{14.37}$$

and σ_i *becomes arbitrarily small for* $\tau \to 0$. Thus the lifetime of the particle in the system replaces τ_{coll} in the conductivity expression leading to this effective conductivity. Consequently the inertial term in Ohm's law, usually ignored in MHD becomes important when the lifetime of the particle in the system is small compared to a mean time between collisions.

The field aligned electric field supported by electron inertia is (e.g. Vasyliunas 1975)

$$E_{\|} \simeq \frac{m_e}{ne^2}\frac{\partial j}{\partial t} \simeq \frac{c}{\omega_{pe}^2}\frac{B}{L_{shear}\tau_A} = \frac{\lambda_{skin}^2}{L_{shear}^2}\frac{v_A}{c}B, \tag{14.38}$$

where L_{shear} and λ_{skin} denote the thickness of the current sheets of the filamentary current carrying magnetic flux tubes and the electron skin length, respectively. We now have a measure for the conversion effiency ζ in Equation (30)

$$\zeta \propto \frac{\lambda_{skin}^2}{L_{shear}^2}. \tag{14.39}$$

Since there are no collisions, the only characteristic time scales involve energy losses by radiation. For the central part we have strong inverse Compton losses (Birk et al. 1999) and for regions further away from the center and along the jets it is synchrotron radiation (Lesch and Birk 1998). The latter case allows a satisfying explanation for extended optical synchrotron emission in jets (Meisenheimer 1996) which requires continuous reacceleration along the jet flow until $\gamma \sim 10^6$!. The first case gave us first hints toward a self-consistent accretion model for particles in the very centre of an active galactic nucleus towards TeV-energies.

Finally, some general comments may be appropriate. The fact that active galactic nuclei are magnetized plasma containing relativistic and nonrelativistic plasma streams which transport energy from a galactic nucleus into the jets, hot spots and lobes, together with the Ghisellini request for a nondissipative energy transport in the very centre (see Introduction) suggests that force-free magnetic structures are very important for the plasma dynamics in AGN. Force-free means that no Lorentz force is exerted onto the plasma since the currents are "field-aligned", i.e. they flow parallel to magnetic field lines: $\mathbf{j} \times \mathbf{B} = \nabla \times \mathbf{B} \times \mathbf{B} = 0$. This condition can be satisfied in three ways: $\mathbf{B} = 0$, $\nabla \times \mathbf{B} = 0$, i.e. $\mathbf{j} = 0$ or $\nabla \times \mathbf{B} = \phi\mathbf{B}$, where the scalar $\phi = \phi(r)$ in general. Such configurations tend to have a twisted or sheared appearance and represent the lowest state of magnetic energy that a closed system can achieve (Taylor 1986). This has two important consequences. It proves the stability of force-free fields with constant ϕ and shows that in a system in which the magnetic forces are dominant and in which there is a mechanism to dissipate the fluid motion, force-free fields with constant ϕ are the natural final configuration.

The advantages of force-free magnetic field systems are obvious: Force-free structures are globally stable and thus allow an almost unperturbed transport of energy from the

generator region up to some volume in which dissipation takes place (only shearing instabilities at the edge of plasma streams with the ambient medium will distort the energy transport) until the jet energy is dissipated in the hot spots. The internal energy overshoot of the plasma in such a flux tube is disspated via continuous particle acceleration. Since the currents flow parallel to magnetic field lines they will evolve into a filamentary structure simply by inducing local toroidal magnetic fields which isolate one filament from the other. In the context of acceleration it is then important to recognize the fact that the jets are collisionless. A probable shear of current carrying filaments cannot be opposed by some resistivity since the particles do not collide. The current filaments shrink to a size where the particle inertia becomes important, i.e. to filament with thicknesses of the order of c/ω_e. It is within these filaments the kinetic energy of the shear is dissipated via particle acceleration as described in our paper.

To summarize, the proposed highly filamentary structure of the plasma in AGN is a natural configuration of magnetohydrodynamic flows under the influence of external forces. The lowest energy state of force-free magnetic fields allows a simple explanation of the continuous dissipation via particle acceleration in the thin filaments along the jet flow. Since no collisional resistance can be build up in the flows only radiation losses of the relativistic particles can limit the acceleration.

14.5 References

Birk, G.T., Lesch, H., Schopper, R., Wiechen, H., 1999, Astroparticle Physics 11, 63

Björnsson , C.-I., 1985, MNRAS 216, 241

Björnsson , C.-I., 1990, MNRAS 242, 158

Blandford, R.D., 1990 in *Active Galactic Nuclei*, Saas-Fee Advanced Course 20, 57, Springer, Berlin

Blumenthal, G.R., Gould, R.J., 1970, Rev. Mod. Phys. 42, 237

Camenzind, M., 1996, in *Solar and Astrophysical Magnetohydrodynamical Flows* , ed. K.C. Tsinganos, NATO ASI Series 481, 699, Kluwer, Dordrecht

Celotti, A., Ghisellini, G., Fabian, A.C., 1991, MNRAS, 251, 529

Collmar, W., Schönfelder, V., 1998, Lecture Notes in Physics, 514, 37

Crusius-Wätzel, A., Lesch, H., 1998, A&A, 399, 404

Dermer, C.D., Schlickeiser, R., 1992, Science, 257, 1642

Dermer, C.D., Schlickeiser, R., 1993, ApJ, 416, 458

Gaidos, J.A., et al., 1996, Nature, 383, 319

Ghisellini, G., in BL Lac Phenomenon ASP 159, 311 (1999)

Ghisellini, G., Madau, P, MNRAS 280, 67 (1996)

Huba, J.D., 1985, in *Unstable Current Systems and Plasma Instabilities in Astrophysics*, IAU **107**, eds. M.R. Kundu, G.D. Holman, Reidel, Dordrecht, p. 315

Kunieda, H., et al., 1990, Nature, 345, 786

Lesch, H., Schlickeiser, R., Crusius, A., 1988, A&A, 200, L9

Lesch, H., 1991, A&A, 245, 18

Lesch, H., Schlickeiser, R., 1987, A&A, 179, 93

Lesch, H., Appl, S., Camenzind, M., 1989, A&A, 225, 341
Lesch, H., Reich, W., 1992, A&A, 264, 493
Lesch, H., Birk, G.T., 1997, A&A, 321, 461
Lesch, H., Birk, G.T., 1998, ApJ 499, 167
Meisenheimer, K., 1996, Lect Notes Phys., 471, 57
Netzer, H., 1990 in *Active Galactic Nuclei*, Saas-Fee Advanced Course 20, 57, Springer, Berlin
Parker, E., 1979, *Cosmical Magnetic Fields*, Clarendon Press, Oxford
Priest, E., 1987, Solar Magnetohydrodynamics, Cambridge University Press
Quinn, J., in BL Lac Phenomenon ASP 159, 239 (1999)
Rees, M.J. 1966, Nature, 211, 468
Rees, M.J. 1987, MNRAS, 228, 47p
Reuter, H.P., Lesch, H., 1996, A&A, 310, L5
Schlickeiser, R., 1996, Space Sci. Rev., 75, 299
Schindler, K., Birn, J., Hesse, M., 1988, JGR, 93, 5547
Schindler, K., Birn, J., Hesse, M., 1991, ApJ, 380, 293
Schopper, R., Lesch, H., Birk, G.T., 1998, A&A, 335, 26
Schopper, R., Lesch, H., Birk, G.T., 1999, PoP (submitted)
Shapiro, V.D., Shevchenko, V.I., Cargill, P.J., Papadopoulos, K., 1994,JGR, 99, 23.735
Sotnikov, V.I., Shapiro, V.D., Shevchenko, V.I., 1978, Sov. J. Plasma Phys.,4, 252
Svensson, R., 1994, ApJS,92, 585
Standtke, K.J., et al., 1996, A&A, 306, 27
Taylor, J.B., 1986, Rev. Mod. Phys., 58, 741
Vasyliunas, V.M., 1975, Geophys. Space Phys. 13, 303
Wagner, S.J., Witzel, A., 1995, ARAA, 33, 163
Wiechen, H., Birk, G.T., Lesch, H., 1998, PoP, 5, 3732

Chapter 15

Interaction of Heavy Ions with Dense Plasma

D.H.H. Hoffmann and M. Stetter[1]

Abstract

Experiments to study interaction processes of heavy ions and ionized matter are discussed. A Monte-Carlo code to simulate charge exchange and energy loss processes in a plasma environment has been developed to plan the experiments, to analyze the results, and to investigate the influence of magnetic fields on the particle trajectories inside the plasma target. Results of beam plasma interaction experiments are:

- The stopping power of ionized matter is increased compared to that of cold, non-ionized matter. This effect is especially pronounced at low ion energies (E $\ll$ 100 keV/u) where an enhancement factor of up to 40 has been observed. At higher energies (E $\gg$ 1 MeV/u) this effect is less dramatic, but is still on the order of 2 - 3, depending on the ion species.
- The charge state of ions traversing a fully ionized plasma is increased due to reduced capture cross sections of free plasma electrons.
- It is possible to focus intense heavy ion beams of high magnetic rigidity using a plasma lens. This ideal focusing device achieves a high focusing power for ion beams almost comparable to optical systems for intense beams from high power lasers.
- Energetic ion beams are very well suited to heat cylindrical target volumes and to create a dense plasma. Cryogenic krypton and xenon crystals were irradiated with intense heavy ion beams, leading to beam driven hydrodynamic motion of the heated target volume, and shock waves inside the target were induced.

[1]GSI-Darmstadt, D-64220 Darmstadt

15.1 Introduction

Investigation of interaction processes of ionizing radiation with matter is a classical research topic of nuclear physics. A wide and divers field of applications has developed from this basic research effort, ranging now from the construction of sophisticated particle detectors to very effective methods in tumor treatment. The target material in all these cases is what we call ordinary, cold matter, e.g. solids, fluids, gases, and organic material. The most frequently occuring form of matter in our universe is, however, the plasma state. It is therefore an obvious and logical step to extend the investigation of interaction processes of ions to include ionized matter. Plasmas, as we find them in nature, for example as very low density interstellar plasma, or as very dense plasma in the interior of massive stars, do also span a large range of temperature, and differ therefore greatly in their fundamental physical properties. Thus arises the interest to investigate properties of matter under extreme conditions of density, pressure, and temperature.

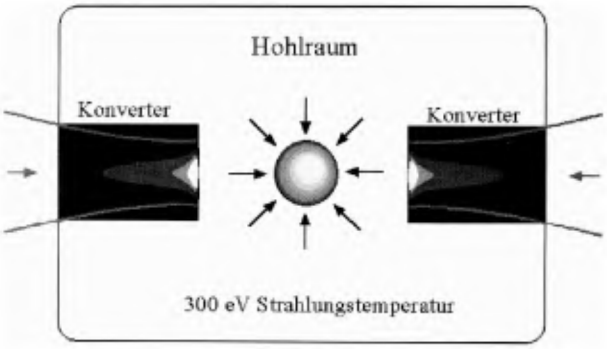

Figure 15.1: *Schematic diagram of a fusion target driven by heavy ions. For reasons of symmetry, two converters are used to turn the kinetic energy of the heavy ions into radiation energy. Located in the center of the hohlraum the fusion pellet is compressed by the ablation pressure of the evaporized surface. A spark ignition is achieved at high temperature but low density in the center, which then spreads into the surrounding cold fuel which is compressed to approximately 1000 times the density of solid hydrogen. The symmetry requirements of the radiation field are achieved here by first heating the hohlraum surrounding the fusion pellet. This is called an indirect drive inertial fusion scheme.*

One of the applications of this field is also the ultimate goal of plasma physics in general: the production of energy through controlled nuclear fusion. Here we are concerned with the principle of inertial confinement fusion. In this process the deuterium and tritium fuel mixture is contained at cryogenic temperatures in a small fusion pellet. The surface of this pellet is heated very rapidly by an intense radiation field, thereby evaporating the ablation layer of the pellet. Through this process the fuel mixture is accelerated towards the center and is finally compressed to approximately a 1000 times solid density. Due to mass inertia this state remains long enough to fulfil the ignition condition set by the Lawson citerion.

The intense radiation field required to evaporate the pellet surface and to compress the fuel with a high degree of symmetry is very hard to achieve by direct irradiation of the target with intense laser- or heavy ion beams. Indirectly driven targets are therefore proposed. For heavy ion beams the principle is layed out in fig. 15.1 schematically. In this

scheme it is necessary to convert the kinetic energy of the ions into soft x-ray radiation at a temperature of about 300 eV, by interaction processes in a converter target. The converter will turn into a dense plasma during this process, and its radiation then heats up the hohlraum, where the symmetry and homogeneity requirements for the pellet surface can be achieved. Detailed knowledge of the conversion efficiency of heavy-ion beam kinetic energy into soft x-ray radiation is necessary to ensure an efficient inertial fusion process. The conversion efficiency in turn depends on the details of the interaction processes of heavy ions with dense plasma.

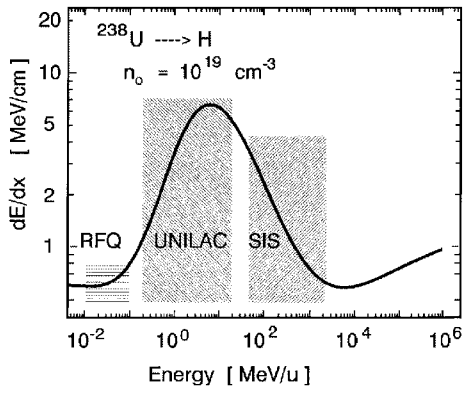

Figure 15.2: *Stopping power of hydrogen for U-ions. The accelerator facilities at GSI consisting of a radio frequency quadrupole (RFQ) accelerator a linac (UNILAC), and a synchrotron (SIS) allow to perform energy loss measurements in a large energy range extending up to the energy loss minimum at approximately 1 GeV/u.*

At least for simple collision systems a basic understanding for atomic and nuclear interaction mechanisms has been achieved. Systematic compilations of experimental data helped to develop and to test theoretical models. Data tables are now available for arbitrary projectile target combinations and for a large range of energies [1, 2, 3]. The maximum deviations between the predictions of these tables and experimental data are of the order of 30% [4]. The current level of understanding energy loss processes of heavy ions in ordinary cold matter is summarized in fig. 15.2. Inelastic collisions with bound target electrons are the dominating energy loss processes to slow down energetic heavy ions in matter under normal conditions. Only at very low energies below 100 keV/u elastic collisions with atomic nuclei gain some importance. The broad energy range extending just beyond the energy loss maximum, is dominated by charge exchange processes between target and projectile. The energy regime extending down to the energy loss minimum is characterized by an almost constant or very slowly varying projectile charge state, and the energy loss scales as $dE/dx \propto 1/\mathrm{v}^2$, where v is the projectile velocity. At energies above the energy loss minimum relativistic effects cause a rise in the observed energy loss.

First theoretical studies of energy loss mechanisms of ions in ionized matter at high temperatures [5, 6, 7] have initiated experimental work in this field. Two effects mainly have been predicted, which were confirmed later by experiments:

- Contrary to inelastic collisions with bound target electrons, there is no lower limit for the energy transfer in collisions of ions with free plasma electrons. The large number of collisions at large impact parameters and small energy transfer contribute to the total stopping power of ionized matter and thus result in an enhanced stopping power of fully ionized plasmas.

- The dynamic equilibrium of ionization and electron capture processes in the projectile is different in ionized and cold matter due to the effect that electron capture processes of free electrons have a much lower cross section than bound electron capture. The reason for this is that in a collision with a free electron it is difficult to fulfil simultaneously the conservation laws of energy and momentum, since a third partner taking up the recoil is generally missing in such collision systems. The net result is that the equilibrium charge state of the projectile shifts to a higher degree of ionization, thus contributing to an enhanced energy loss of the particle traversing a fully ionized plasma target.

There is, however, also published theoretical speculation, that under certain conditions in high density plasmas in some temperature regime, also a range lengthening effect may be expected [8, 9]. Therefore it remains to be shown by experiments, as described here, which effects govern the energy loss processes of heavy ions traversing a fully ionized plasma target.

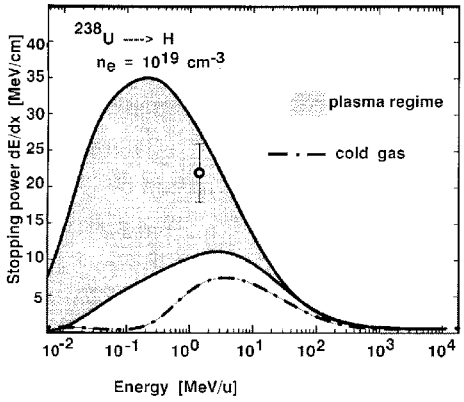

Figure 15.3: *Stopping power of cold hydrogen and fully ionized hydrogen plasma (Te ≈ 5 eV). Also shown is the experimental result taken at 1.4 MeV/u.*

In fig. 15.3 the effect of enhanced stopping of ions in plasma is demonstrated for U-ions in hydrogen. The lower curve (dash dotted) shows the respective energy loss in cold hydrogen gas. The plasma stopping regime of fully ionized hydrogen is the hatched area above the cold stopping curve. The lower limit of the plasma regime arises if only the enhanced stopping due to the more effective energy transfer in collisions with free electrons is taken into account keeping the same effective charge state of the heavy ion as in the cold hydrogen case. The upper limit of the plasma stopping is achieved if a new plasma - equilibrium charge state is reached. This aspect will be discussed in more detail later, but the experimental data point already shows that the assumptions made by the theory are more or less valid and that experiments indeed show a considerable enhancement of the energy loss of heavy ions in a plasma.

15.2 Numerical simulation of heavy ion energy loss processes in plasmas

In the following theoretical models underlying our Monte-Carlo code for the well-known case of ions penetrating through cold hydrogen gas and through fully ionized hydrogen plasma are presented. A comprehensive description of the theoretical aspects involved

can be found in refs. [10, 11, 12]. The work described there has partly been developed in parallel to the experimental program and has strongly influenced it.

The first case discussed here is when the velocity of the beam is much larger than the thermal velocity of the free plasma electrons or the orbital velocity of bound hydrogen electrons. This is the case for most of the energy regime under consideration here. Therefore the stopping power models underlying the experiments are the simple high energy theories given by Bohr and Bethe (see e.g. [7]):

$$\begin{aligned} \textit{Cold gas}: \quad -\left(\tfrac{dE}{dx}\right)_{gas} &= \left(\frac{Z_{eff}\cdot e\cdot \omega_H}{v}\right)^2 \cdot ln\left(\frac{2\cdot m\cdot v^2}{I}\right) \\ \textit{Plasma}: \quad -\left(\tfrac{dE}{dx}\right)_{plasma} &= \left(\frac{Z_{eff}\cdot e\cdot \omega_e}{v}\right)^2 \cdot ln\left(\frac{0.764\cdot m\cdot v^3}{Z_{eff}\cdot e^2\cdot \omega_e}\right) \end{aligned} \tag{15.1}$$

Here $Z_{eff}(v,x,T)$ is the effective charge of the ion beam during the passage through the target; e, m are electronic charge and mass I is the average ionization potential; and $\omega_{e,H}$ is the plasma frequency.

For an evaluation of eq. 15.1 the x -dependence, that is the variation of Z_{eff} along the interaction path has to be known. The value of the effective charge is, as stated already earlier, a result of the competition between different atomic collisional recombination and ionization processes governing the population of the projectile electronic shells. For the cases considered here the most important atomic cross sections can easily be estimated:

15.2.1 Collisional ionization by ions (CII)

The binary encounter model of Gryzinski [13] describes the collisional ionization cross section:

$$\sigma_{CII} = \sum_n \sigma_n = \sum_n N_n \cdot \pi \cdot \left(\frac{Z_t\cdot e^2}{U_n}\right)\cdot G\left(\frac{v_p}{v_n}\right) \quad [cm^{-2}] \tag{15.2}$$

with

$$G(V) = \frac{\alpha^{3/2}}{V^2}\cdot[\alpha + \frac{2}{3}\cdot(1+\beta)\cdot ln(2.7+V)]\cdot(1-\beta)\cdot(1-\beta^{(1+V^2)})$$

and

$$\alpha = \frac{V^2}{1+V^2} \qquad \beta = \frac{1}{4\,V}\cdot(1+V).$$

In this equation N_n, U_n, v_n are, respectively, the population number, ionization energy, and orbital velocity of electrons in the n-th shell of the projectile, Z_t is the target atomic number and v_p the projectile velocity. In the Monte-Carlo code the ionization cross section is calculated in each step as a function of ion energy and charge state. The main contribution to the ionization cross section arises from the weakly bound outer electrons.

Collisional ionization with free plasma electrons or quasi free electrons of outer electron shells of the target atoms is treated by the well known Lotz formula [14] :

$$\sigma_{CEI} = \sum_n N_n\sigma_n = 4\cdot 10^{-14}(eVcm)^2\cdot\sum_n N_n\cdot\frac{ln(E_r/U_n)}{E_r\cdot U_n}. \tag{15.3}$$

Here E_r is the kinetic energy of the electron in the projectile rest frame and can be approximated by the following relation

$$E_r = \frac{1}{2} \cdot m_e v_r^2 \approx \frac{1}{2} m_e (v_p^2 + v_{th}^2) \approx \frac{1}{2} m_e v_p^2 \text{ for } v_p \gg v_{th} \tag{15.4}$$

This process, however, contributes to the total ionization cross section only for the outermost projectile electrons in a low ionization state, since the kinetic energy of the electrons is low for our experimental conditions.

15.2.2 Recombination by electron capture (BEC)

The cross section for bound electron capture (BEC) is rather high. High target densities therefore require much computing time in simulation programs based on Monte-Carlo methods. A simple semi-empirical formula by Schlachter et. al [15] is therefore especially suited to treat electron capture processes over a large energy range and arbitrary projectile target combinations:

$$\sigma_{BEC} = 4.4 \cdot 10^{-23} cm^2 \cdot Z_p^{3.9} \cdot Z_t^{4.2} \cdot E^{-4.8} \tag{15.5}$$

A comparison with experimental results measured at GSI [16] shows, however, deviations up to a factor of three. For hydrogen targets we therefore use in our simulation program the recombination cross section in the OBK-approximation [17]:

$$\sigma_{OBK} = 4.1 \cdot 10^4 \cdot \sum_{n_f} N_j \cdot a_{Chan} \cdot \frac{(Z_{eff} \cdot e^2)^2 \cdot E_i^{5/2} \cdot E_f^{3/2} \cdot E_r}{[E_k^2 + 2E_r \cdot (E_i + E_f) + (E_i - E_f)^2]^5} \tag{15.6}$$

where Ei and Ef are the binding energies in the initial and final state, and Er is the kinetic energy of the electron in the center of mass system, and Ni is the population number of the n-th shell. Final state interaction of the collision partners reduces the capture probability. This effect is taken into account by the Chan-Eichler factor aChan [18, 19] which ranges between 0.1 and 0.3 .

15.2.3 Radiative recombination (REC)

We treat the cross section for radiative electron capture σ_{REC} according to Spitzer's theory [20] :

$$\sigma_{REC} = (1 - \frac{N_m}{2m^2}) \cdot \sigma_m + \sum_{n=m+1}^{\infty} \sigma_n \text{ with } \sigma_n = 2.1 \cdot 10^{-22} \text{cm}^2 \cdot \frac{n \cdot U_n^2}{(U_n + E_r) \cdot E_r} \tag{15.7}$$

To obtain the total cross section the summation is carried out over all unoccupied shells. The outermost eventually partly occupied shell carries the index m and the respective occupational number is Nm. Compared to bound electron capture the cross section for radiative capture is lower by approximately 2 orders of magnitude for our experimental conditions.

15.2.4 Dielectronic recombination (DR)

Dielectronic recombination is a resonant process and it has been pointed out by Peter et. al. [10] that this process may be dominant under certain conditions in our experiments. The resonance condition is fulfilled, when the sum of the electron kinetic energy Er and the binding energy En is equal to the excitation energy (Ei - Ej) of a second projectile electron.:

$$E_r + E_n = E_i - E_j \tag{15.8}$$

An analytical approximation for dielectronic recombination cross sections for fast ions moving in a plasma which we use in our simulation code, has been given by Peter [11]:

$$\sigma_{DR} = \begin{cases} 9.6 \cdot 10^{-20} cm^2 \cdot \frac{(Z_p+1)^{11/2}}{(v_p/v_0)^9} \cdot \frac{1}{m^5} & \text{if 15.8 is valid} \\ 0 & \text{else.} \end{cases} \tag{15.9}$$

Three body recombination is not of concern for our experiments, hence we neglect this process. A typical example for U-ions interacting with hydrogen is given in fig. 15.4. The dominating ionization cross section in this case is due to collisions with target ions, protons for the hydrogen plasma under consideration. With increasing projectile charge state the binding energy increases thus reducing the ionization probability. Closed shell configurations (K-, L-, and M-shell) show up through large changes in the respective cross sections. As discussed earlier ionization by free electrons plays a minor role in this scenario. The dominating electron capture process is bound electron capture, however, at high projectile charge states also dielectronic recombination contributes and may even be the dominating process at high charge states.

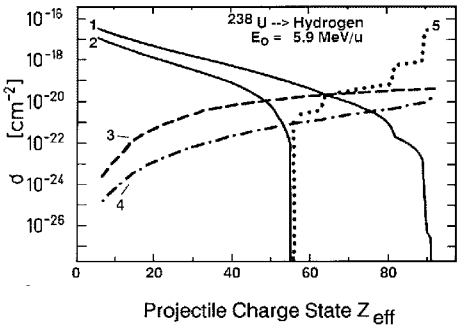

Figure 15.4: *Ionization and capture cross sections for U-ions in hydrogen. 1: Collisional ionisation by ions; 2: Coulomb collisions with free electrons; 3: bound electron capture; 4: radiative electron capture; 5: dielectronic recombination.*

15.3 Energy loss and charge state measurements

Different kinds of plasmatargets have been developed to cover a target density range from $10^{17} \ll n_e \ll 2 \times 10^{19}$ cm^{-3}. For the low density regime discharge plasmas were sufficient [21], whereas for the very high density above 10^{19} cm^{-3} a z-pinch plasma target [22, 23] was employed. These targets were then integrated into the high vacuum system of the accelerator beam line at GSI. Details of the experimental set-up are given in ref. [24]. Typical target areas for beam plasma experiments are schematically shown in fig. 15.5. The ion beam is injected into the plasma target during the time of the plasma discharge. A stripper foil in front of the target serves to strip the incoming ion to a higher charge state, and thus a variation of the incoming projectile charge state is

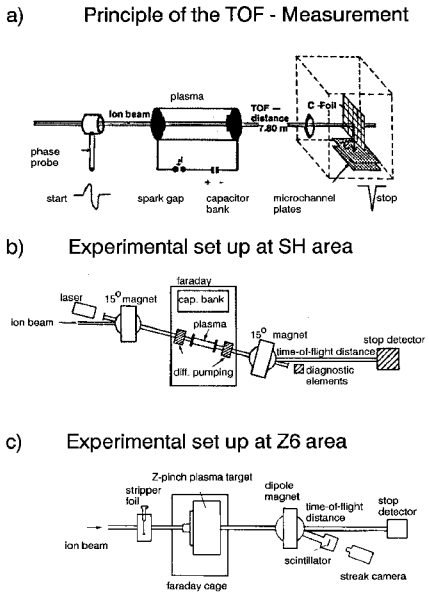

Figure 15.5: *Experimental set-up for energy loss and charge state measurements.*

possible. The energy loss is measured by time-of-flight techniques using a 12 m time-of-flight distance. Due to the rf acceleration the beam carries the inprinted time structure of the accelerator rf. This results in beam bunches approximately 2 ns wide, following each other in time intervals of 37 ns. The ion charge state after beam target interaction is measured with a combination of a dipole magnet to separate the charge states and a fast detector system consisting of a scintillator coupled to a streak camera for high time resolution (lower part of fig. 15.5). This detector allows to take charge state spectra with a data rate exceeding 1012 Hz for time intervals up to several microseconds, which is long enough to cover the complete plasma target discharge time.

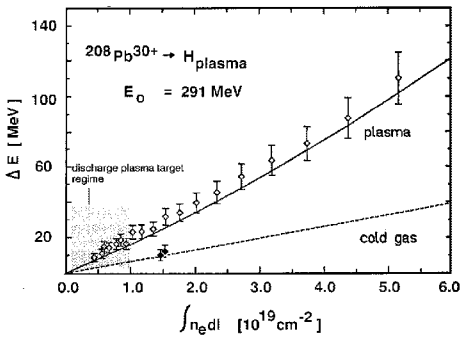

Figure 15.6: *Energy loss of Pb-ions in a z-pinch plasma target as a function of target areal density.*

The experimental program was aiming at the highest available plasma target density to investigate the interaction processes of heavy ions with dense plasma. A z-pinch plasma target finally made even the density regime above $n_e \gg 10^{19}$ cm^{-3} accessible for target experiments. The areal density in this case is so high, however, that Pb ions with a total energy of 291 MeV are completely stopped inside the target.In the case shown in fig. 15.6 time-of-flight techniques allowed to do energy loss measurements up to an target areal density of $5.2\times$ 10^{19} cm^{-2}. The energy loss data taken in the fully ionized hydrogen plasma clearly exceed the cold gas energy loss by approximately a factor of 3. Moreover the data cannot be fitted by a straight line, assuming a constant charge state. In order to consistently interpret the data we have to assume that the effective projectile charge state rises from 30+ to 38+ while ploughing through the dense plasma. A direct charge

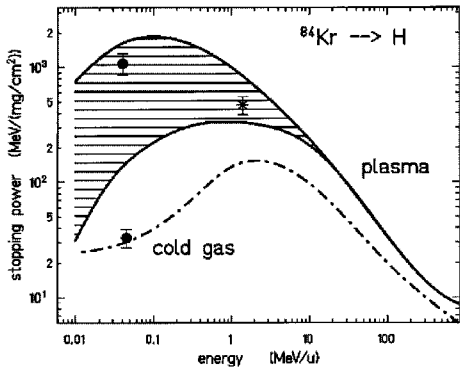

Figure 15.7: *Stopping power of hydrogen plasma for Kr-ions. The full data point at 30 keV/u shows a stopping power enhancement of a factor of 40 compared to cold hydrogen gas (dash-dotted curve). This is in part due to a high effective charge state of the projectile in plasma environment. Also at higher energy (1.4 MeV/u, open data point) the increase of stopping power compared to cold gas is clearly visible beyond experimental uncertainties. The effect of higher charge states is less pronounced due to the fact that at higher energy also cold gases strip more effectively.*

state measurement will be discussed below. The result for an energy loss measurement of Kr-ions at different energies (1.4 MeV/u and 45 keV/u) is given in fig. 15.7. As discussed already in the introduction the data clearly are within the plasma regime predicted by theory. For the lowest available energy at the GSI accelerator facilities (45 keV/u) the measured enhancement of the plasma stopping power compared to cold target gases is almost a factor of 40. This large increase in stopping power is in part due to the fact that a high charge state is achieved. From the accelerator the ions are delivered at charge state 1+ and are stripped to 8+ in the plasma. We were able to perform charge state measurements which confirm this result. In cold hydrogen gas we observe at the same target density only charge states 1+ and 2+ for Kr-ions at 45 keV/u. Ionized matter is therefore a very effective stopping medium for heavy ions. Moreover, since capture cross sections of free electrons are very low, a plasma is also very efficient to strip heavy ions to high charge states.

Direct charge state measurements were performed with the detector system shown in the lower part of fig. 15.5. For two different ion species (Ar-ions at 4.8 MeV/u, and Xe-ions at 5.9 MeV/u) the charge state was determined after the passage through the plasma. The plasma target for this experiment was the z-pinch with which also the energy loss measurements were performed. For typical discharge parameters (pressure 2.5 mbar, voltage 32.5 kV) we find a maximum plasma density of 1.5×10^{19} cm^{-3}. This means that through the pinch effect compression occurs to more than hundred times the initial density. After the pinch time the plasma column expands and the density decreases by two orders of magnitude within 1 μs. The density calculated from the energy loss agrees nicely with interferometric measurements of our earlier experiments. The fast detector system enabled us to measure the charge state distribution as a function of the fast varying plasma density [27].

Figure 15.8 shows in the top part the results for 4.8 MeV/u Ar-ions with initial charge state 10+ and 15+. With increasing plasma density the ions are stripped to higher charge states reaching an equilibrium at $Z_{eff} = 16.2$. We compare this result to the respective value of the Betz formula [25] for cold gas amounting to $Z_{eff}^{cold} = 15.8 \pm 0.5$ (dotted

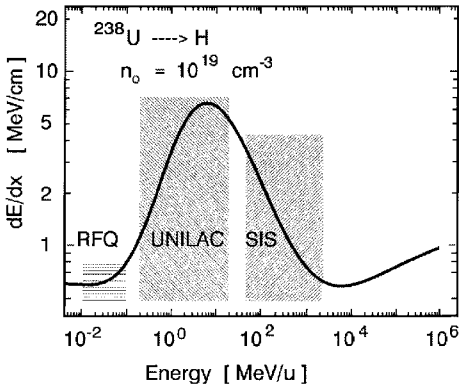

Figure 15.8: *Charge states of Ar-ions (top) and Xe-ions (bottom) after interaction with a dense hydrogen plasma.*

line in fig. 15.8). Martin and Northcliffe determined this value experimentally [26] with a result of $Z_{eff}^{cold} = 16.2 \pm 0.35$, which is in good agreement with the semiempirical formula of Betz. Thus the value of the effective charge for Ar-ions at 4.8 MeV/u is equal in plasma and cold hydrogen gas. This is due to the fact that an Ar-ion at charge state 16 is a very stable He-like configuration and the high binding energy of the K-shell electrons prevents further ionization in the gas and in the plasma case. This situation is somewhat different for Xe-ions at 5.9 MeV/u. The respective data are displayed in the bottom part of fig. 15.8 for initial charge s tates 37+ and 40+. In the plasma the effective charge increases up to $Z_{eff} = 43$ which is five charge states higher than the corresponding value for cold gas, which again has been calculated by the Betz formula which has a general accuracy of one charge state. Our data thus provide experimental evidence for an enhanced effective charge of fast heavy ions in plasma. The data are compared to theoretical predictions of our Monte-Carlo code which is based on the work of Peter and Meyer-ter-Vehn [10]. As can be seen, this theory is in excellent agreement with the data. Not only the equilibrium charge state but also the evolution from the initial charge state to its equilibrium value are reproduced correctly, even though simple atomic models are involved in the calculations.

15.4 High energy density in matter with heavy ion beams

High-energy heavy ion beams are excellently suited to generate dense plasmas. The high kinetic energy enables them to penetrate deep into the target material and to deposit energy along the interaction path during the deceleration process. Through this mechanism it is possible to directly heat a macroscopic volume of several cubic millimeters in a cylindrical geometry. This property is very specific to heavy ion beams and distinguishes them from all other sources of intense radiation. A schematic comparison of the energy deposition characteristics of heavy ion beams and laser radiation is given in fig. 15.9.

The potential of heavy ion beams to heat matter to extreme conditions of temperature and pressure is expressed by the specific energy deposited in matter:

$$E_s = 1.6 \times 10^{-19} \cdot \frac{dE/dx \cdot N}{\pi \cdot r^2} \quad [J/g] \tag{15.10}$$

Here dE/dx [eV/g cm^{-2}] is the energy loss of heavy ions in matter, N is the beam particle number and πr^2 [cm2] is the focal spot area. As was shown before, the energy

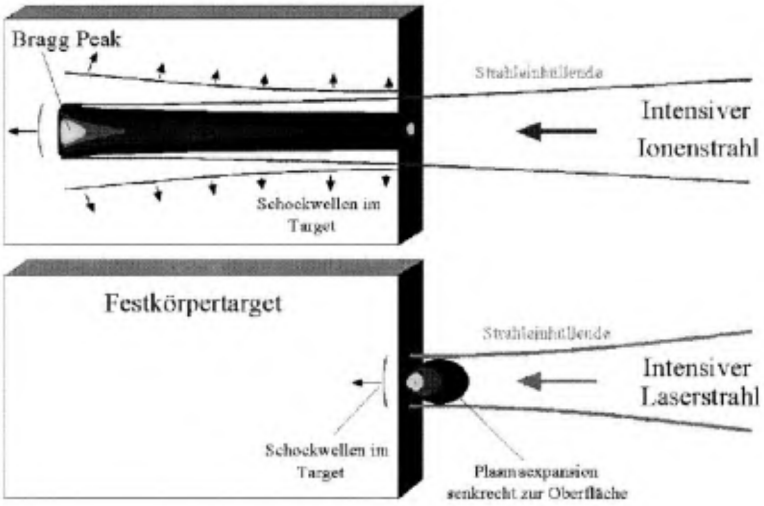

Figure 15.9: *Schematic comparison of the energy deposition of an intense heavy-ion beam and that of intense laser radiation in a solid target. Ion beams penetrate deep into the material, whereas laser radiation is absorbed at close to the surface at the critical density of the ablating surface plasma. The critical density is obtained when the plasma frequency equals the laser frequency. At a wavelength of* $\lambda = 1\mu m$ *the critical density is approximately* $n_e = 10^{21}\ cm^{-3}$.

loss can be expected to be enhanced in a plasma, as compared to cold matter. The energy deposition inside the target is very homogeneous, but is significantly intensified at the end of the range, where the so called Bragg-peak is observed.The precise energy distribution depends on the ion species, the energy and the intensity of the ion beam, as well as the properties of the target material and its equation of state. From equation 15.10 it is also obvious that the energy distributed inside the target volume depends not only on the physics of the interaction processes involved in the ion stopping process, but also on the area to which the ion beam can be focused. A powerful focusing device for high energetic ion beams has turned out to be the plasma lens.

15.5 Plasma lens focussing

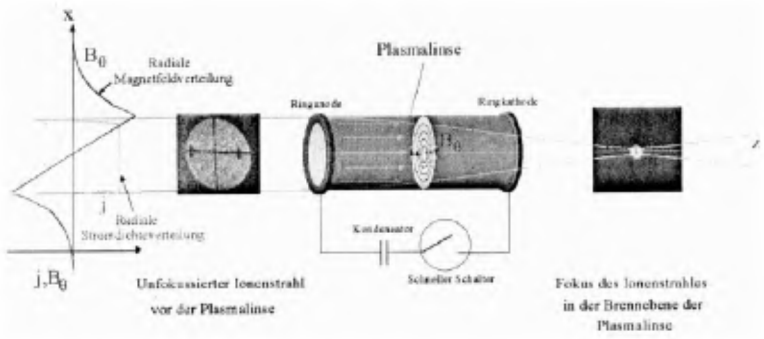

Figure 15.10: *The plasma lens principle.*

Intended as a focusing system for high-energy heavy ions, the plasma lens consists of a magnetic field which concentrates parallel ion beams on a small focal spot. In contrast to magnetic quadrupole lenses, a plasma lens focuses in all planes and thus enables extremely short focal length. To generate the magnetic field shown in the diagram of fig. 15.10, a gas discharge is triggered between two hollow electrodes in the plasma lens. A cylindrical insulator containing a noble gas at a pressure of 1 to 10 millibar is located between the electrodes. The discharge process gives rise to a plasma column carrying a high discharge current up to several hundred kA. If done properly, the radial current distribution is very homogeneous and results in an azimuthal magnetic field with a linearly rising flux density as a function of the radius. An ion passing through this field configuration is then deflected towards the axis. The plasma lens installed at the experimental area at GSI achieves peak currents of 400 kA. This is sufficient to focus a parallel beam of 12 mm diameter to a focal spot of roughly 190 μm radius. This makes it possible to increase the specific energy deposited inside the target volume by one order of magnitude, compared to conventional focussing systems. In recent experiments this energy deposition is above 1 kJ/g, which is enough to overcome the lattice binding energy of some solid materials.

15.6 Hydrodynamics of dense plasmas

Targets from frozen noble gas crystals were developed to study beam induced hydrodynamic motion in solids. The advantage of xenon and krypton crystals is the low lattice binding energy, which is about one order of magnitude lower than in metallic targets. For these kind of crystals about 100 J/g of deposited energy is sufficient to start hydrodynamic response of the target. In addition, these targets are transparent to visible light, which allows optical diagnostic methods to be employed. Figure 11 displays the temporal development of the target expansion in a xenon krystal with a sequence of six frames. The first frame shows the direct interaction of the beam with the target. The following frames were taken with a Xe flashlamp to backlight the target. After 40 μs the crystal shows first signs of hydrodynamic response and the destruction of the target begins. The energy deposition profile with the Bragg peak is clearly reproduced in the target response. The energy deposition in this region is roughly 100 J/g. The maximum observed velocity of the expanding material is 200 m/s. Therefore the pressure inside the heated target volume amounted to some kilobar.

With the increasing beam intensity available from the accelerator at GSI it will soon be possible to increase the specific energy deposition above 100 kJ/g with temperatures in the 10 eV regime. Therefore it will be possible to study properties of dense plasmas at solid state density and pressures ranging up to some megabars. The primary cooling process in this case is not electronic heat conduction, but hydrodynamic expansion.

Detailed studies of hydrodynamics provide an insight into material properties under these extreme conditions. Computer codes have been developed in recent years for this purpose and are used to predict the rate and spatial distribution of the expansion

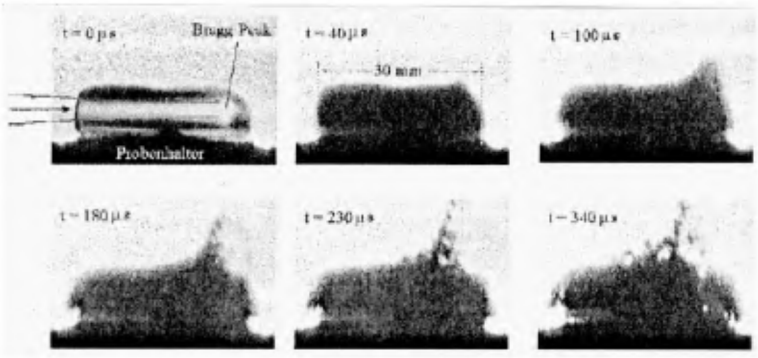

Figure 15.11: *Development of target expansion in a xenon crystal. The first frame shows the energy deposition zone and the Bragg peak. This is followed by expansion due to induced shock waves as well as extreme temperature and density gradients. The processes are fastest in the Bragg peak zone.*

15.7 Studies with dense plasma in Europe

Heavy-ion accelerators are regarded as the most feasible method to drive reactors based on the inertial confinement fusion principle. The beam intensity and quality requirements are, however, considerably higher than those of existing systems. In view of this a joint European project has been initiated to systematically examine important aspects such as the dynamic behavior of heavy-ion beams under extreme space charge conditions. GSI-Darmstadt is one of the leading partners in this European collaboration, accompanied by various institutes such as ENEA Frascati, FZ Karlsruhe, and DENIM Madrid. The purpose of the study group formed by these institutions and experts from various university groups is to investigate the feasibility of a heavy ion driver and to determine the parameters essential for its implementation.In the course of the present discussion of the long term perspectives of GSI, a further massive increase in intensity is considered as a new option. Apart from the fundamental nuclear structure physic, the plasma research would be among the main supporters of this high current option. Although the beam parameters aimed at with a new accelerator facility at GSi will not be sufficient for the ignition of a fusion target, the facility should be designed in a way which allows significant progress in this research field. This will undoubtedly be one of the forthcoming challenges for high current heavy ion accelerator development.

Bibliography

[1] J.F. Ziegler; Handbook of Stopping Cross Sections for Energetic Ions in All Elements,Vol. 5, Pergamon Press, New York (1980)

[2] F. Hubert, A. Fleury, R. Bimbot D. Gardes; Ann. Phys. (Paris) **55** (1980), p. 1

[3] F. Hubert, R. Bimbot and H. Gauvin; At. Data Nucl. Data Tables **46** (1990), p. 1

[4] H. Geissel; Ph. D. thesis, Giessen University, GSI-Report-82-12-1982

[5] E. Nardi, E. Peleg, and Z. Zinamon; Phys. Fluids **21** (1978), p. 574

[6] E Nardi and Z. Zinamon; Phys. Rev. Lett. **49** (1982), p. 1251

[7] T.A. Mehlhorn, J. Appl. Phys. **52** (1981), p. 6522

[8] M. Basko, Sov. J. Plasma Phys. **10** (1984), p. 689

[9] Th. Peter and B. Kärcher, J. Appl. Phys. **69** (1991), p. 3835

[10] Th. Peter Dissertation, MPQ Report, MPQ 137, 1988

[11] Th. Peter and J. Meyer-ter-Vehn, Phys. Rev. **A43** (1991), p. 1998 and
Th. Peter and J. Meyer-ter-Vehn, Phys. Rev. **A 43** (1991), p. 2015

[12] C. Deutsch, Laser and Part. Beams **2** (1984), p. 449 and
G. Maynard and C. Deutsch Phys. Rev **A 26** (1982), p. 665 and **A27** (1983), p. 574.

[13] M. Gryzinski, Phys. Rev. **A138** (1965), p. 305, 322, 336

[14] W. Lotz, Z. Phys. **206** (1967), p. 205

[15] A.S. Schlachter, J.W. Stearns, W.G. Graham, K.H. Berkner, R.V. Pyle, and J.A. Tanis, Phys.Rev. **A27** (1983), p. 3372

[16] W. Erb, *Umladung schwerer Ionen nach Durchgang durch Gase und Festkörper im Energiebereich 0.2 - 1.4 MeV/u*, GSI Report, GSI-P-7-78, (unpublished), and
B. Franzke, Ann. Israel. Phys. Soc. **4** (1981), p. 111

[17] J.R. Oppenheimer, Phys. Rev. **31** (1928),p. 349.

[18] J.K.M. Eichler and F.T. Chan, Phys.Rev. **A 20** (1979), p. 104

[19] J.K.M. Eichler, A. Tsuji, and T. Ishihara, Phys. Rev. **A 23** (1981), p. 2833

[20] L. Spitzer, Jr., Astrophys. J. **107** (1948), p. 7

[21] K. Weyrich, D.H.H. Hoffmann, J. Jacoby, H. Wahl, R. Noll. R. Haas, H. Kunze, R. Bimbot, D. Gardes, M.F. Rivet, C. Deutsch and C. Fleurier, Nucl. Instr. Meth. **A 278** (1989), p. 52

[22] R. Noll, H. Kunze and C.R. Haas, Nucl. Instr. Meth. **A 278** (1989), p. 85

[23] H. Kunze, R. Noll, C.R. Haas, M. Elfers, J. Hertzberg and G. Hertziger, Laser Part. Beams **8** (1990), p. 595

[24] D.H.H. Hoffmann, K. Weyrich, H. Wahl, D. Gardes, R. Bimbot, and C. Fleurier, Phys. Rev. **A42** (1990), p. 2313

[25] H.-D. Betz, Rev. Mod. Phys. **44** (1972), p. 465

[26] F.W. Martin and L.C. Northcliffe, Phys. Rev. **128** (1962), p. 1166

[27] K.-G. Dietrich, D.H.H. Hoffmann, E. Boggasch, J. Jacoby, H. Wahl, M. Elfers, C.R. Haas, V.P. Dubenkov, and A.A. Golubev, Phys. Rev. Lett. **69** (1992), p. 3623

Chapter 16

Safety and Environmental Aspects of Fusion

H.-W. Bartels

16.1 Introduction

Future fusion reactors will operate with radioactive materials: Tritium is radioactive and very mobile and the neutrons produced in the fusion reactions will activate the components near the plasma. To assess the radiological hazards of fusion, the inventories and possible release mechanisms are discussed. The behaviour of the plant during normal operation and accident situations is analyzed together with the waste management. The control of the mobile tritium is a key issue in reducing the effluents in normal operation. Associated with this is the design goal of minimizing the tritium inventories which can be released in accidents. The absence of chain reactions and the moderate decay heat densities in a fusion reactor are inherent safety-enhancing differences to fission plants. Since the neutron-induced radioactivity strongly depends on the materials used in a fusion-reactor, appropriate material selection offers the possibility of significantly influencing the amount of radioactivity produced. Generally, the decay times of fusion waste are much shorter than those of fission waste. Recycling of reactor materials after 50 to 100 years of cooling time is a potential waste management option instead of geological disposal.

16.2 Inventories

The safety implications of nuclear fusion can immediately be seen from the fundamental reaction equation:

$$D + T \longrightarrow He + n$$

Two distinct classes of radioactive inventories follow from this:

- Tritium as part of the fuel is radioactive.
- Neutrons leaving the plasma do not just produce tritium by nuclear reactions with lithium (breeding). They also perform nuclear reactions with other materials in

the reactor, mainly those of structures near the plasma (first wall). Many of these reactions lead to radioactive end-products.

Tritium

The expected tritium inventory of a fusion plant amounts to a few kg. Although just 0.5 g of tritium will be inside the hot plasma, much larger amounts will be present in other systems such as the blanket, pumping system, tritium processing plant and storage.

Tritium is a weak β^- emitter with a half-life of 12.3 years. Its mean β^- energy is 5.7 keV, its maximum energy 18.5 keV. Due to the rather low energy, its mean range in organic matter is below 6 μm, whereas the human skin is covered by a horny layer which is 70 μm thick. Thus tritium does not pose any hazard as an external radiator. The situation changes when tritium is incorporated into the body via ingestion, inhalation, or skin absorption. The most common chemical species of tritiated molecules are HTO (tritiated water) and HT (tritiated hydrogen gas). Boths forms are very mobile since their behaviour is similar to the non-tritiated species H_2O and H_2. Especially HTO can easily be absorbed into the human body. Once in the body it is rapidly dissolved in the human water cycle.

Figure 16.1 shows the decrease of tritium in the body of a technician working in a tritium laboratory who accidentally inhaled a significant amount of HTO. The measurements show a decay with three time constants. The dominating decay time of about 10 days reflects the recycling in the water compartment of the human body. A reference person weighing 70 kg has a water compartment of 42 l and a daily water exchange of about 3 l leading to a biological half-life of 10 days. The longer components of about 30 and 300 days in figure 16.1 pertain to the exchange between water and the organic compartment. On the average the slow component accounts for roughly 10% of the tritium dose. Thus the *effective* biological half-life of tritium in the human body is 11 days.

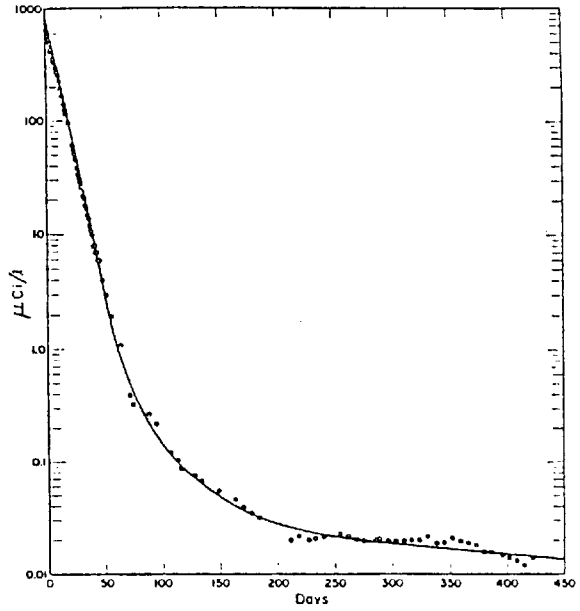

Figure 16.1: Time-dependent tritium concentration in a human after a single accidental incorporation of HTO

Table 16.1: Dose conversion factors for different isotopes

Isotope	**Dose Conversion Factor**	**Pathway**	**Relation to Tritium**
Tritium	$1.8 \cdot 10^{-11}$ Sv/Bq	ingestion	1
	$1.8 \cdot 10^{-11}$ Sv/Bq	inhalation	1
Cs-137	$1.4 \cdot 10^{-8}$ Sv/Bq	ingestion	800
Pu-239	$1.0 \cdot 10^{-7}$ Sv/Bq	ingestion	5 500
	$1.0 \cdot 10^{-4}$ Sv/Bq	inhalation	5 500 000

The intake of a certain amount of tritium measured in activity A (unit: Bq = decays per second) leads to the following energy deposition in the human body:

$$\epsilon = A \cdot \tau \cdot < E_{\beta^-} > \cdot m^{-1}$$

ϵ:	energy density	[J/kg]
A:	activity	[Bq]
τ:	effective biological lifetime	[s]
$< E_{\beta^-} >$:	average β^- energy	[J]
m:	mass of reference person	[kg]

Generally, the energy dose has to be multiplied with a quality factor to account for radiation forms more hazardous than γ-rays, e.g. α-radiation is assigned a quality factor of 20. The resultant quantity is the radiation 'dose' measured in units of Sievert (Sv) and allows quantification of radioactive radiation hazards to humans. For tritium the international consensus is to use Q=1, but some experiments tend in the direction of Q = 2 – 3 for tritium since the low β-energy leads to localized ionization.

With Q = 1, the intake of 1 Bq HTO leads to a dose of $1.8 \cdot 10^{-11}$ Sv. Intake of tritium in organic form, e.g. by eating contaminated food, would increase the dose by a factor of 2.5. This is due to a larger fraction of tritium transfered into the body compartments with longer biological lifetimes. For a given air concentration, tritiated gas (HT) is 10,000 times less hazardous than HTO since the uptake and incorporation into the body is strongly reduced. Table 16.2 shows a comparison of doses for different radioisotopes. It can be clearly seen that the amount of radioactivity measured in units of activity (Bq) is not a good indicator of the associated hazard. Tritium produces smaller radiation doses per Bq because the average energy per release is much smaller than for other isotopes and the effective lifetime in the human body is also shorter.

The special concern with tritium is its high volatility and the associated problems in keeping it inside the fusion plant. Once released, tritium is still very volatile. In figure 16.2 the specific tritium activity in soil surface water is shown versus time after a controlled release experiment in Canada. In the first year the tritium concentration dropped by a factor of 1000 and reached the background values which were measured

before the experiment. Thus strong contamination of large areas which lasts for many decades is not expected in the event of a major tritium release. Instead, most tritium will end up in the oceans, which carry a natural tritium inventory of a few kg. This tritium is formed by nuclear reactions of cosmic rays entering the earth's atmosphere (e.g.: n + ^{14}N $\rightarrow$ ^{12}C + T). During the period of extensive nuclear weapon testing in the fifties and sixties, the earth's inventory was increased to about 500 kg. Today the residual inventory has been reduced by decay of tritium to about 80 kg.

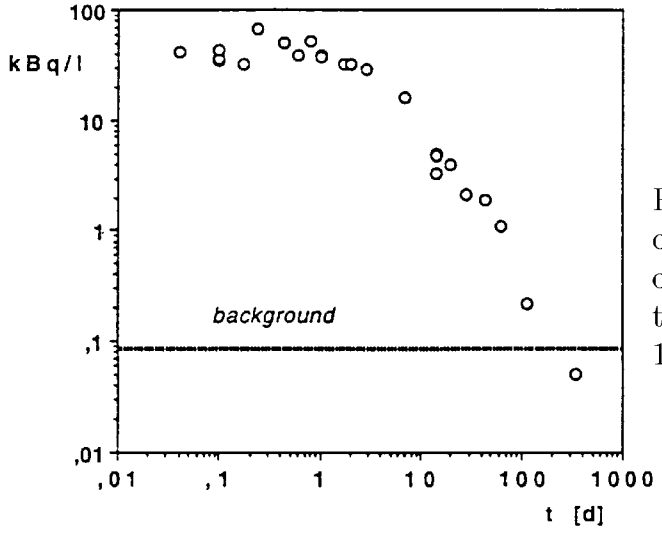

Figure 16.2: Time-dependent specific activity in the soil humidity of the top 20 cm after a controlled tritium release experiment (Canada 1987)

Activation products

The expected neutron wall loading is in the range between 2 and 5 MW/m^2, which will lead to considerable radiation damage of the components near the plasma. Thus a regular exchange of these components after 2.5 to 5 years of operation is envisaged. A target for fusion materials is a possible neutron fluence of about 12.5 MWa/m^2. The development of such materials is a very challenging task.

The amount of activation products in future fusion reactors strongly depends on the choice of materials. Figure 16.3 shows the dose rates of some elements in the first wall. The total amount of radioactivity in a fusion plant will be governed by the activation products. If conventional steels are used, a level of about 50% of the radioactivity in fission plants is reached.

There is a clear distinction between the inventories of tritium and activation products, i.e. the volatility. The radioactivity inside the structural material is very hard to mobilize by definition since the structure has to withstand large forces during normal operation. Special attention has to be given to the first-wall dust eroded by the plasma, because it can easily be mobilized. The use of very low activation materials such as carbon, beryllium, or boron would strongly reduce the hazard of this dust (see figure 16.3 for the dose rate of C). If high-Z materials have to be used in the plasma facing components (e.g. tungsten in the divertor), the dust inventory could pose problems similar to those of the tritium inventory. As indicated, a main issue of the activation products is waste management, which will be treated later. The environmentally most attractive elements for structural materials in a fusion plant are vanadium, chromium, and titanium.

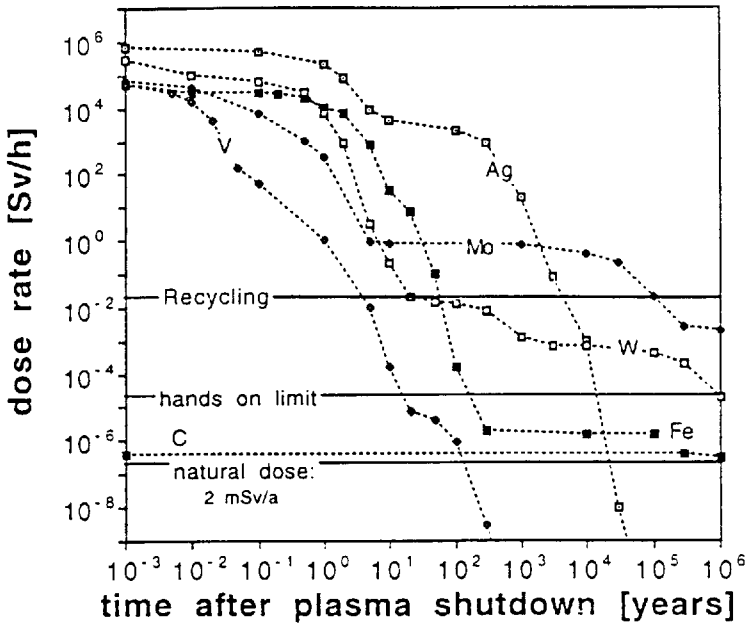

Figure 16.3: Dose rate of several elements after neutron irradiation of 12.5 MWa/m^2

16.3 Normal operation effluents

During normal operation, it is the volatile tritium which has to be properly controlled. Experience of tritium handling in large facilities is available from a special type of fission reactor working with natural uranium and heavy water as moderator, the Canadian 'CANDU' reactors. In this type of fission reactor, inventories of a few hundred grams are produced from n-capture in D_2O. Experience with these CANDU reactors allows the extrapolation that with present technology tritium effluents can be limited to 2 g per year or 50 Ci/day (1 Ci = 3.4 10^{10} Bq). In Los Alamos, USA, the largest fusion-oriented tritium laboratory, with a maximum inventory of 200 g, is in operation. The experience from this laboratory (TSTA, Tritium Systems Test Assembly) has demonstrated that one might even do better than the extrapolation above. This laboratory was closed for three month after an unexpected release of 0.4 Ci HT, which demonstrates the high safety level of the plant.

If we assume a daily release of 50 Ci in the more hazardous form HTO from a 100 m high stack, the resultant dose to the most exposed individual (MEI) living at the fence has to be calculated. It is assumed that food and sometimes also water originate from the location of the MEI. A conservative estimation of the dose to the MEI is very simple: The source term S [Bq/s] will be diluted by atmospheric dispersion. For a 100 m high stack, the plume will reach the ground at about R_{max} = 1000 m, leading to a maximum ground level air concentration c_{air} of:

$$c_{air} = S \cdot \frac{1}{v_{wind}} \cdot \frac{f}{2\pi R_{max}} \cdot \frac{1}{2h_{stack}}$$

with S being the source term in [Bq/s], v_{wind} the wind speed in [m/s], f a factor accounting for nonuniform wind rose, R_{max} the downwind distance from the source in [m], and h_{stack} the height of the source in [m].

Table 16.2: Energy inventories and characteristic time scales for their release in a fusion reactor

Source	Energy [GJ]	Time Scale
Plasma	2	< 1 s
DT in Plasma	250	1 min
Coils	100	1 min
Cooling Water	300	10 min
Decay Heat	80	1 hour
	550	1 day
	2000	1 week

Water volume in the primary loop: 400 m^3
Heat of evaporation at 1 bar: 900 GJ

A conservative assumption is f=3 and a typical average wind speed is 6 m/s at a height of 100 m. Given the air concentration, one can transform this to a concentration in the air humidity:

$$c_{H_2O,air} = c_{air}/\rho_{H_2O,air}$$

$\rho_{H_2O,air} = 10$ g/m^3 is a typical value for the Central European growing season.
Assuming complete equilibration of the specific tritium activity of the air humidity with that of soil water, plant water, animals, and humans, the average tritium concentration in the MEI is equal to $c_{H_2O,air}$ leading to a dose rate D of

$$D = c_{H_2O,air} \cdot < E_{\beta^-} >$$

For a source term of 50 Ci/d this simple approach results in an annual dose of 23 μSv/a, which is about 1% of the dose received from natural sources of radioactivity. More sophisticated models predict doses to the MEI which are 2 – 3 times smaller.

16.4 Accidents

With respect to safety in the event of accidents, the most important characteristic of fusion is self-termination of the fusion process under such conditions. So-called 'passive safety' appears to be achievable in fusion power plants because of the absence of chain reactions. The energy sources that could drive accidents are low compared with those in fission, whereas the volumes and surface areas are large. Table 16.4 lists some relevant energy inventories together with typical time scales of release.
After shutdown of the reactor, the decay of radioactive nuclei constitutes a heat source, known as decay heat. Passive removal of the decay heat is a key safety feature. In the event of loss of coolant accidents ('LOCA'), the core of a fission reactor is prone to melting if no additional cooling can be applied. In the case of fusion, the decay heat is much smaller and is distributed over large surfaces. If all cooling media are lost, just thermal conduction and radiation are left as heat removal mechanisms. Figure 16.4

shows a detailed analysis of such a situation for the ITER device. This is a good example of passive safety since the removal of the decay heat is managed by physical mechanisms that do not rely on engineering systems, which can always fail with a certain probability. Thermal radiation will never fail. The maximum temperatures in the fusion device stay well below the melting point of the steel structures (1400°C).

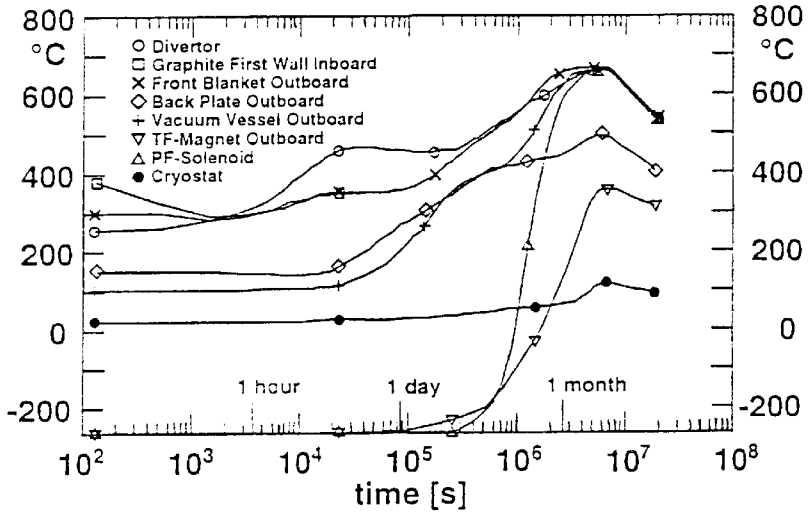

Figure 16.4: Temperature transient up to seven months for loss of all active cooling accident in ITER

The safety studies in fusion are prompted by the large radioactive inventories involved, but the fundamental difference between fusion and fission reactors is the fact that in the former major accidents are not driven by the nuclear system itself. Instead most safety studies focus on conventional hazards. The most important accident initiators are:

- loss of vacuum accidents with air ingress into the plasma chamber;
  concerns: chemical reactions (fire), transport of tritium
- loss of coolant accidents;
  concerns: pressurization, formation of hydrogen (explosion hazard)
- loss of offsite electric power;
  concerns: loss of coolant flow, quench of magnets
- electric arcs in the coil system;
  concerns: melting of adjacent systems, tritium release to the building
- coil deformation and displacement;
  concerns: damage of adjacent components, loss of vacuum, missile generation
- volume change of cryogenic helium;
  concern: pressurization
- explosions in the hydrogen isotopic separation system;
  concerns: damage of building, tritium release
- fire in the long-term tritium storage beds;
  concern: tritium release

The most detailed analyses have been performed for the ITER conceptual design phase. One example is air ingress into the plasma chamber, which is of concern since then one major confining barrier is breached. For a design where the majority of the first wall is covered by carbon, chemical reactions of this material were investigated. No self-sustained fire can develop in such a case since the plasma would definitely extinguish and the first-all cooling would very effectively reduce the carbon temperatures. Even if the active cooling was simultaneously, the inertia of the cooling system would be sufficient to cool the carbon below its ignition temperature. The mobilized material, mainly tritium in the carbon dust and pumping system, would be released into the adjacent rooms. Here it would be confined in the second of three confinement barriers.

Generally, the aim of fusion safety studies is to ensure that future fusion plants are designed so that any internal accident and all conceivable external events should entail consequences confined inside the fusion plant by passive means. No internal accident should be able to destroy the buildings. The strategy is to provide a robust multi-confinement system, reduce all radioactive and energy inventories as far as possible, apply passive safety features and use high-quality nuclear components. Active systems can also play an important role to reduce any damage inside the plant.

In fusion reactors large amounts of lithium will be used to breed the necessary tritium. This could be done very efficiently by using liquid lithium. In this case the lithium could also serve as coolant since it has very good thermal properties which would simplify the design. Technical problems are still presented by the large pressure losses of liquid metals flowing in magnetic fields (MHD effect). Another serious drawback are safety concerns arising from violent chemical reactions of liquid lithium with air, water, nitrogen, and concrete. The potential energy release of the lithium inventory is about 7000 GJ. Any contact with water produces large amounts of hydrogen with the unpleasant tendency to trigger detonations, which can seriously threaten the confinement buildings.

An alternative approach is the use of lithium ceramics such as Li_2O, Li_4SiO_4, Li_2ZrO_3, and other candidates which eliminate the chemical hazard caused by elemental lithium. Unfortunately, the need for a self-sufficient tritium breeding ratio calls for the neutron multiplier, beryllium [^{9}Be(n,2n)2He], in almost all ceramic breeder designs. Beryllium is a very toxic material which builds up significant tritium inventories during neutron irradiation. In addition, there are questions about the abundance of beryllium on earth. At temperatures above 600–700°C some violent chemical reactions can also occur with air and water. Consequently, attempts are being made to push the design of ceramic breeder blankets to the extreme so as to eliminate the beryllium. Li_2O is the best candidate for these studies since is has the highest lithium atom density of all lithium ceramics. The lithium density in Li_2O is even higher than in metallic lithium. In addition the neutron activation of Li_2O is extremely small.

Another option is to use $Li_{17}Pb_{83}$, which has a melting point of 235°C and is thus a suitable liquid metal. Its chemical reactivity is much smaller than that of liquid lithium, but the use of lead poses technical problems because of its weight and there are safety concerns because of the neutron activation of lead.

The final choice of the breeder material will strongly influence the safety and environmental properties of future fusion plants.

Table 16.3: Specific dose to the most exposed individual of the public (MEI) at a distance of 1 km from the release point

Source	Specific Dose	Type of Dose
tritium as HTO	0.5 mSv/g-T	early
	2.5 mSv/g-T	chronic
tritium as HT	0.04 mSv/g-T	early
AISI-316 first-wall steel	0.03 mSv/g	early
ITER conditions	2 mSv/g	chronic

Accidental doses to the public

The early dose is defined as the dose received during the first week after an accident, excluding the ingestion pathway. This dose definition is the basis for considering evacuation. Above 100 mSv evacuation is triggered in many countries. The chronic accidental dose integrates over 50 years of exposure time and includes all pathways. In Germany 50 mSv is the legal upper limit for public exposure after 'design basis accidents', i.e. accidents which have to be controlled by design.

Detailed studies for atmospheric accidental tritium and activation product releases have been performed. Specific doses for the most exposed individual of the public (MEI) at a distance of 1 km from the release point are presented in table 16.4. The dose due to inhalation and skin absorption is 0.5 mSv/g-T (early dose) for ground level releases in the chemical form of HTO. If ingestion is included, the dose values are about 5 times times higher (chronic accidental doses). For gaseous releases (HT), doses are at least a factor of 10 lower. The earlier mentioned difference in radiotoxicity of 10,000 between HTO and HT is levelled out by the fact that HT released to the environment will diffuse into the soil, where it is rapidly oxidized my micro-organisms and subsequently re-emitted as HTO. Specific doses for steel dust envisaged during the conceptual design of ITER are about one order of magnitude below the tritium values, but for the chronic accidental doses similar values result.

Under the German licensing procedure, it has to be shown that in design basis accidents the releases stay below 20 g for tritium in the form of HTO for ground level releases. This is achievable as long as the confinement building remains intact. To avoid evacuation, tritium releases have to be kept below 200 g in all circumstances. This is the reason for setting up the safety target of keeping the tritium inventory below 150 g for all single components.

If we compare the potential hazard of the tritium and steel dust of a fusion plant with the hazard of the J-131 and Cs-137 inventories of a fission plant, fusion is 500 times more benign.

16.5 Waste management

The majority of the radioactive waste in a fusion reactor will arise from replacement of divertor, first wall, and blanket segments and decommissioning of the whole tokamak, including the vacuum vessel and the magnets. These components will be activated by the intense flux of 14 MeV neutrons. Due to the shielding effect of the materials involved, there will be a steep gradient in the activation when going away from the plasma.

The relatively short life of the majority of the radioisotopes produced and the absence of very toxic actinides (α-emitters) causes the ingestion hazard index of the fusion waste to be more than 1000 times less than for fission waste after 100 years of cooling time. The basis of comparison is the total waste produced during the lifetime of the plants.

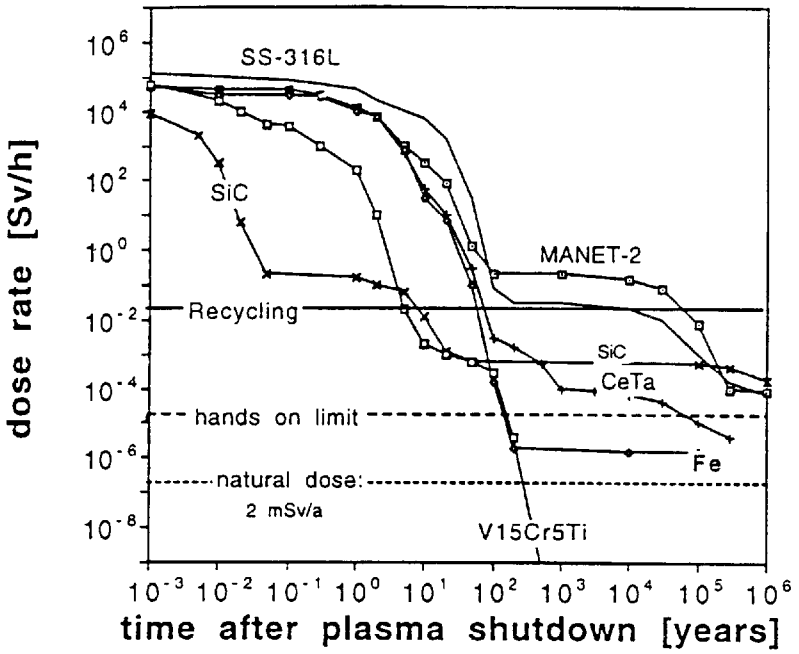

Figure 16.5: Time-dependent dose rates for technologically important materials irradiated by a neutron fluence of 12.5 MW/m^2; a standard steel (SS-316L), a fusion optimized steel (CeTa, KfK), the theoretical lower limit for iron based steels (Fe), a ceramic (SiC), and a vanadium alloy (V15Cr5Ti) are shown.

The volume of packed waste is estimated to add up to about 25,000 m^3 for a fusion reactor life. This is comparable to the amount of packed waste from a typical PWR plant life, including reprocessing. Without reprocessing the volume of packed fission waste will be 30 to 50% smaller. The fission waste still requires much more repository consumption due to the significantly larger heat production in the waste, which limits the packing density in geological repositories.

Figure 16.4 shows the dose rates of some technologically important materials irradiated at the first wall. Given moderate progress in the development of fusion-optimized materials, the reuse of activated material in new reactors is a potential option of waste management. For reduced-activation steels, recycling of components is estimated to be feasible up to contact dose rates of 25 mSv/h by remote handling techniques. The most activated

component, which is the first wall of the plasma chamber, would reach this level 50 to 100 years after being dismantled from the reactor.
If new classes of low-activation materials, such as vanadium alloys, could be used in fusion reactors, 'hands-on recycling' might be feasible after a few decades of cooling time. The benefit will be strong simplification of recycling procedures and thus greater economic attractiveness. However, great care must be taken to keep undesirable impurities to a low level in order to retain the radiological attractiveness, e.g. below 0.1 ppm for silver (see figure 16.3).

16.6 Conclusion

A board of independent scientists from different fields are regularly asked to review the European Fusion Programme. The following extract from the last 'Fusion Programme Evaluation Board' (Colombo report, July 1990) is quoted to conclude this overview:

'It is essential to expand the effort on technology, not only on the Next Step, but also on longer term issues, particularly in relation to the new emphasis on environmental and economic constraints. Environmental and safety criteria should as of now be considered as essential elements in governing the evolution of the Fusion Programme. Problems concerning materials, the use of tritium, the maintainability of the reactor should all be faced in time avoiding freezing of design or engineering concepts which might lead to environmentally unacceptable fusion reactors or make their design excessively complex.

Environment and safety must assume high priority in the European Fusion Programme and in its wider international extension.

. . .

It would be particularly important for fusion to qualify in two respects:

(i) it must be clearly shown that the worst possible fusion accident will constitute no major hazard to populations outside the plant perimeter that might result in evacuation;

(ii) radioactive wastes from the operation of a fusion plant should not require isolation from the environment for a geological timespan and therefore should not constitute a burden for future generations.'